WOODHEAD PUBLISHING SERIES IN CIVIL AND STRUCTURAL ENGINEERING

Transport Properties of Concrete

Measurement and Applications

Peter A. Claisse

WP
WOODHEAD PUBLISHING

Transport Properties of Concrete

Related titles:

Understanding the tensile properties of concrete
(ISBN 978-0-85709-045-4)

Handbook of recycled concrete and demolition waste
(ISBN 978-0-85709-682-1)

Understanding the rheology of concrete
(ISBN 978-0-85709-028-7)

Woodhead Publishing Series in Civil and Structural Engineering:
Number 53

Transport Properties of Concrete

Measurement and Applications

Peter A. Claisse

AMSTERDAM • BOSTON • CAMBRIDGE • HEIDELBERG • LONDON
NEW YORK • OXFORD • PARIS • SAN DIEGO
SAN FRANCISCO • SINGAPORE • SYDNEY • TOKYO
Woodhead Publishing is an imprint of Elsevier

Woodhead Publishing is an imprint of Elsevier
80 High Street, Sawston, Cambridge, CB22 3HJ, UK
225 Wyman Street, Walthan, MA 02451, USA
Langford Lane, Kidlington, OX5 1GB, UK

Notice
No responsibility is assumed by the publisher for any injury and/or damage to persons or property as a matter of products liability, negligence or otherwise, or from any use or operation of any methods, products, instructions or ideas contained in the material herein. Because of rapid advances in the medical sciences, in particular, independent verification of diagnoses and drug dosages should be made.

British Library Cataloguing-in-Publication Data
A catalogue record for this book is available from the British Library

Library of Congress Control Number: 2014933287

ISBN 978-1-78242-306-5 (print)
ISBN 978-1-78242-319-5 (online)

Typeset by Toppan Best-set Premedia Limited

Printed and bound in the United Kingdom

Contents

Author contact details

Professor Peter Claisse
JL Building
Coventry University
Priory Street
Coventry
CV1 5FB
UK

Email: pete@claisse.info

This page intentionally left blank

Woodhead Publishing Series in Civil and Structural Engineering

1 **Finite element techniques in structural mechanics**
C. T. F. Ross

2 **Finite element programs in structural engineering and continuum mechanics**
C. T. F. Ross

3 **Macro-engineering**
F. P. Davidson, E. G. Frankl and C. L. Meador

4 **Macro-engineering and the earth**
U. W. Kitzinger and E. G. Frankel

5 **Strengthening of reinforced concrete structures**
Edited by L. C. Hollaway and M. Leeming

6 **Analysis of engineering structures**
B. Bedenik and C. B. Besant

7 **Mechanics of solids**
C. T. F. Ross

8 **Plasticity for engineers**
C. R. Calladine

9 **Elastic beams and frames**
J. D. Renton

10 **Introduction to structures**
W. R. Spillers

11 **Applied elasticity**
J. D. Renton

12 **Durability of engineering structures**
J. Bijen

13 **Advanced polymer composites for structural applications in construction**
Edited by L. C. Hollaway

14 **Corrosion in reinforced concrete structures**
Edited by H. Böhni

15 **The deformation and processing of structural materials**
Edited by Z. X. Guo

16 **Inspection and monitoring techniques for bridges and civil structures**
Edited by G. Fu

17 **Advanced civil infrastructure materials**
Edited by H. Wu

18 **Analysis and design of plated structures Volume 1: Stability**
Edited by E. Shanmugam and C. M. Wang

19 **Analysis and design of plated structures Volume 2: Dynamics**
Edited by E. Shanmugam and C. M. Wang

20 **Multiscale materials modelling**
Edited by Z. X. Guo

21 **Durability of concrete and cement composites**
Edited by C. L. Page and M. M. Page

22 **Durability of composites for civil structural applications**
Edited by V. M. Karbhari

23 **Design and optimization of metal structures**
J. Farkas and K. Jarmai

24 **Developments in the formulation and reinforcement of concrete**
Edited by S. Mindess

25 **Strengthening and rehabilitation of civil infrastructures using fibre-reinforced polymer (FRP) composites**
Edited by L. C. Hollaway and J. C. Teng

26 **Condition assessment of aged structures**
Edited by J. K. Paik and R. M. Melchers

27 **Sustainability of construction materials**
J. Khatib

28 **Structural dynamics of earthquake engineering**
S. Rajasekaran

29 **Geopolymers: Structures, processing, properties and industrial applications**
Edited by J. L. Provis and J. S. J. van Deventer

30 **Structural health monitoring of civil infrastructure systems**
Edited by V. M. Karbhari and F. Ansari

31 **Architectural glass to resist seismic and extreme climatic events**
Edited by R. A. Behr

32 **Failure, distress and repair of concrete structures**
Edited by N. Delatte

33 **Blast protection of civil infrastructures and vehicles using composites**
Edited by N. Uddin

34 **Non-destructive evaluation of reinforced concrete structures**
Volume 1: Deterioration processes
Edited by C. Maierhofer, H.-W. Reinhardt and G. Dobmann

35 **Non-destructive evaluation of reinforced concrete structures**
Volume 2: Non-destructive testing methods
Edited by C. Maierhofer, H.-W. Reinhardt and G. Dobmann

36 **Service life estimation and extension of civil engineering structures**
Edited by V. M. Karbhari and L. S. Lee

37 **Building decorative materials**
Edited by Y. Li and S. Ren

38 **Building materials in civil engineering**
Edited by H. Zhang

39 **Polymer modified bitumen**
Edited by T. McNally

40 **Understanding the rheology of concrete**
Edited by N. Roussel

41 **Toxicity of building materials**
Edited by F. Pacheco-Torgal, S. Jalali and A. Fucic

42 **Eco-efficient concrete**
Edited by F. Pacheco-Torgal, S. Jalali, J. Labrincha and V. M. John

43 **Nanotechnology in eco-efficient construction**
Edited by F. Pacheco-Torgal, M. V. Diamanti, A. Nazari and C. Goran-Granqvist

44 **Handbook of seismic risk analysis and management of civil infrastructure systems**
Edited by F. Tesfamariam and K. Goda

45 **Developments in fiber-reinforced polymer (FRP) composites for civil engineering**
Edited by N. Uddin

46 **Advanced fibre-reinforced polymer (FRP) composites for structural applications**
Edited by J. Bai

47 **Handbook of recycled concrete and demolition waste**
Edited by F. Pacheco-Torgal, V. W. Y. Tam, J. A. Labrincha, Y. Ding and J. de Brito

48 **Understanding the tensile properties of concrete**
Edited by J. Weerheijm

49 **Eco-efficient construction and building materials: Life cycle assessment (LCA), eco-labelling and case studies**
Edited by F. Pacheco-Torgal, L. F. Cabeza, J. Labrincha and A. de Magalhães

50 **Advanced composites in bridge construction and repair**
Edited by Y. J. Kim

51 **Rehabilitation of civil metallic infrastructure using fiber-reinforced polymer (FRP) composites**
Edited by V. Karbhari

52 **Rehabilitation of pipelines using fiber-reinforced polymer (FRP) composites**
Edited by V. Karbhari

53 **Transport properties of concrete: Measurement and applications**
P. A. Claisse

The fundamental equations

The transport properties of concrete measure the ability of fluids to move through it. The equations for them were first documented by the end of the nineteenth century (Fick 1855; Darcy, 1856) and applied to concrete by the middle of the twentieth century (Powers *et al*., 1954). However, they remain difficult to measure, particularly if the common *in situ* tests are used.

Interest in these properties has increased as many structures built in the second half of the twentieth century have suffered durability problems, particularly corrosion of reinforcement. This corrosion was investigated by Knudson (1907) and was soon discovered to be caused by chloride transport through the cover layer (Rosa *et al*., 1912). All of the major deterioration mechanisms are controlled by the transport properties. This is the main application for them and is discussed in Chapter 13. Other applications in waste containment are discussed in Chapters 14 and 15.

This book is intended to give an improved understanding of the transport mechanisms that take place during testing. The particular emphasis of the work is to show how the fundamental transport properties may be obtained. Two different types of solution to the equations are presented: analytical solutions and computer models. In general, it is found that analytical solutions are useful up to a point, but full solutions require a computer model. In many cases, the analytical solutions are only used to check the computer models by running them for a special case.

The work will be of interest to researchers who are measuring or modelling durability of concrete structures and to practitioners who are evaluating concrete structures or designing containment structures for fluids or wastes and require to know the permeability as part of the design. The analysis methods which are presented may also be used to confirm the reliability of any individual test.

The importance of this work was stated by Whitmore and Ball (2004) as follows:

> 'According to a recent study completed by the US Federal Highway Administration, the annual direct cost of steel corrosion to the US economy is estimated at $276 billion, or 3.1% of the US Gross Domestic Product. If indirect costs such as loss of productivity are included, the annual cost is conservatively estimated at $552 billion, or over 6% of GDP. While these

> statistics are specifically related to the overall cost of corrosion, some estimates indicate that up to 30% of this total is related to corrosion in concrete structures.'

It is shown in Chapter 13 that this corrosion is directly controlled by the transport properties.

Computer codes

The computer code that was used for the models in this book is written in the Basic computer language. This language has been in use for at least 40 years and has been made far easier to use by being adopted as the macro language in Microsoft Excel. The way in which the fundamental equations are expressed as code is explained in Chapter 2. Due to the improvements in processing speed of common computers, very little attempt is made to optimise the code, but they all still run in a few minutes.

These simple programmes are quick to develop and very versatile. In recent work, the author has also used them to model heat evolution in concrete. The reader is referred to Walkenbach (2010) for a guide on how to write programmes in Excel. The full spreadsheets, including the code in the macros for the two main programmes, are free to download from the author's website (http:www.claisse.info/Landfill.htm and http:www.claisse.info/Coulomb.htm) for use as examples of the type of code used.

The derivation of equation (6.2) in Chapter 6 was an excellent example of using analytical methods in combination with numerical modelling. The author used numerical computer modelling while Dr Harris (lead author of the paper – see Appendix 1) used analytical methods. Work continued until agreement was reached. This is an approach that the author recommends. In particular, computer code should be checked with analytical solutions even if this can only be done for special cases as described in section 2.3.

Structure of this book

The fundamental equations are presented in Chapter 1. Chapter 2 explains how simple computer programmes can be written to use the equations in models. Chapters 3, 4 and 5 look at the surface tests for transport, showing analytical solutions for the transport equations and discussing how the tests can be improved to obtain values for the permeability. Chapters 6, 7 and 8 discuss gas migration and, in particular, how it is affected by moisture. Chapter 9 presents data showing factors affecting the measurement of water permeability at high pressure. Chapters 10, 11 and 12 are about electrical tests. It is shown that the commonly used solution to Fick's law is highly inaccurate in these tests even if there is no applied voltage. Finally, Chapters 13, 14 and 15 discuss applications of which the most common is durability of reinforced concrete in Chapter 13.

Experimental data

The experimental data and analytical derivations presented in this book have been taken from a number of journal papers published by the author. These papers are listed in Appendix 1 and full copies are available on the author's website (http:www.claisse.info/Publish.htm).

Summary of contents

This book explains:

- What the transport properties are and how they move ions and fluids through concrete.
- How to write computer models for the transport processes.
- How to choose a method to measure surface absorption of concrete – and how much of the sample it actually tests.
- How to prepare the concrete surface for testing – particularly if it is wet.
- How water vapour moves during the drying of concrete.
- How porosity affects the transport processes.
- What happens in the concrete if you apply a voltage for rapid testing of chloride migration.
- Why chloride migration generates a voltage in a test even if you don't apply one – and why this affects the results.
- How transport properties control the durability of structures.
- How to use transport properties to model waste containment structures.
- How to prepare cracked samples for permeability testing that don't fall apart (see photograph on front cover).

References

Darcy (1856) *Les fontaines publiques de la ville de Dijon*, Victor Dalmont, Paris.

Fick A (1855) On liquid diffusion, *Philosophical Magazine*, **10**, 30.

Knudson A A (1907) Electrochemical corrosion of iron and steel in concrete, *Transactions of the AIEE*, **26**, pp. 231–245.

Powers T C, Copeland L E, Hayes J C and Mann H M (1954) Permeability of Portland cement paste, *ACI Journal*, **51**, pp. 285–298.

Rosa E B, McCullom B and Peters P (1912) Electrolysis of concrete, *Engineering News*, **68**, pp. 1162–1170.

Walkenbach J (2010) *Excel VBA Programming for Dummies*, Wiley, Hoboken NJ.

Whitmore D W and Ball J C (2004) Corrosion management, *Concrete International*, **26** (12), pp. 82–85.

This page intentionally left blank

Acknowledgements

I would like to acknowledge the major contribution to the work published in this book made by the co-authors of the papers listed in Appendix 1. All of their research was significant; however, particular mention must go to Esmaiel Ganjian, Juan Lizarazo Marriaga and the late Joe Cabrera.

I would also acknowledge the financial support for the work from UK Nirex, the Engineering and Physical Sciences Research Council, ENTRUST (landfill tax), the Waste Resources Action Programme, the Minerals Industry Research Organisation and the European Union.

This page intentionally left blank

1

The transport properties of concrete and the equations that describe them

DOI: 10.1533/9781782423195.1

Abstract: In this chapter the main transport processes that take place in concrete are described. For each process a brief introduction to the physical mechanism is developed and then the basic equations are presented. The main transport processes are pressure driven flow (controlled by the permeability), diffusion and electromigration. These processes are controlled by adsorption and driven by capillary suction, osmosis and electro-osmosis. For the process of adsorption the water-soluble and acid-soluble concentrations are discussed together with the capacity factor (or distribution ratio) which may be used to calculate them using a linear isotherm. Equations are then developed to combine adsorption and diffusion.

Key words: permeability, diffusion, electromigration, adsorption, capacity factor.

1.1 Introduction

1.1.1 Molecular and ionic transport

The transport processes move materials such as salt or water through concrete. Before considering the processes in detail, the exact nature of what is being transported must be defined. Many molecules will dissociate into two separate parts (ions) when they are in solution with each part carrying an opposite charge. For example common salt (sodium chloride, NaCl) will dissociate into Na^+ and Cl^- and hydrated lime (calcium hydroxide, $Ca(OH)_2$) will dissociate into Ca^{++} and OH^-. These ions may move in two different ways. The water itself will move with the ions in it or the ions may move through the water. Thus the transport processes may cause damage both by movement of water (such as pressure-driven flow controlled by permeability) or by ionic movement in the water (such as diffusion or electromigration).

1.1.2 Variability in the properties of the materials

In analytical solutions, it is normally assumed that properties such as permeability, diffusion coefficient and capacity factor remain constant. However, it is well known (Luping *et al.*, 2012) that this is only an approximation. For example, the diffusion coefficient changes with age and

the capacity factor with pH (due to carbonation). Including these variations in analytical solutions is difficult and frequently impossible; however, they may be included in numerical solutions if the data is available.

Engineers who normally work with data for the strength of materials will be used to obtaining accurate results from their design calculations and finite element models. The deflection of a structure when loaded in the laboratory or on site will often be within 3 % of that predicted by modelling. This is rarely possible for transport properties. For example, when considering results for permeability testing, Neville (2011) states

> it is important to note that the scatter of permeability test results made on similar concrete at the same age and using the same equipment is large. Differences between, say, 2×10^{-12} and 6×10^{-12} are not significant so that reporting the order of magnitude, or at the most the nearest 5×10^{-12} m/s, is adequate. Smaller differences in the value of the coefficient of permeability are not significant and can be misleading.

The same issues with accuracy apply to diffusion coefficients. While laboratory trials are a necessary first step in work of this kind (in particular for mix design), these results indicate that large site trials are a necessary second step.

1.2 The transport processes

1.2.1 Permeability (advection)

Permeability is defined as the property of concrete which measures how fast a fluid will flow through it when pressure is applied. This flow is often referred to as advection (the term permeation is used to refer to a range of different transport processes and can cause confusion). In some types of structure, such as dams and tunnel lining, there may be an external water pressure, but in others it may be capillary suction which creates pressure differentials. The flow is measured as the average speed of the fluid through the solid (the Darcy velocity, V_F).

The volumetric flow is given by:

$$F_v = \frac{dV}{dt} = AV_F \qquad m^3/s \qquad [1.1]$$

where:

V is the volume in the reservoir and
A is the cross-section area of flow.

If the flux F is defined as the mass in solution flowing per unit area per second:

$$F = CV_F \qquad \text{kg/m}^2\text{/s} \qquad [1.2]$$

where C is the concentration (kg/m^3).

The **coefficient of permeability** k (also known as the hydraulic conductivity) has the units of m/s and is defined from Darcy's law (Darcy, 1856):

$$V_F = \frac{k(h_1 - h_2)}{x} \qquad \text{m/s} \qquad [1.3]$$

where the fluid is flowing through a thickness x (m) with pressure heads h_1 and h_2 (m) on each side. The coefficient of permeability is only applicable to water as the permeating fluid and is used in civil engineering because it is used extensively in geotechnology.

The flow rate will depend on the viscosity of the fluid and for this reason the intrinsic permeability is calculated using the viscosity. The **intrinsic permeability** K has the units of m^2 and is defined from the equation:

$$V_F = \frac{K(P_1 - P_2)}{ex} \qquad \text{m/s} \qquad [1.4]$$

where:

e is the viscosity of the fluid (= 10^{-3} Pa s for water) and
P_1 and P_2 are the pressures on each side (Pa).

The intrinsic permeability is theoretically the same for all different fluids (liquid or gas) permeating through a given porous solid and is thus normally used by scientists.

The pressure from a fluid is given by:

$$P = \rho g h \qquad [1.5]$$

where:

g = 9.81 m/s^2 (the gravitational constant)
ρ is the density = 1000 kg/m^3 for water and
h is the fluid head (m).

Equating (1.3) and (1.4) thus gives:

$$k = \frac{K\rho g}{e} \qquad \text{m/s} \qquad [1.6]$$

A typical value of k for water in concrete is 10^{-12} m/s and thus for K it is 10^{-19} m^2.

Differential forms of the equations

For analytical solutions the permeability equations should be expressed in differential form:

$$V_F = k\frac{dh}{dx} = \frac{K}{e}\frac{dP}{dx} \qquad \text{m/s} \qquad [1.7]$$

Thus:

$$F = \frac{KC}{e}\frac{dP}{dx} \quad \text{kg/m}^2\text{/s} \qquad [1.8]$$

and, in terms of volumetric flow:

$$F_V = \frac{dV}{dt} = \frac{KA}{e}\frac{dP}{dx} \quad \text{m}^3\text{/s} \qquad [1.9]$$

Equations for gas transport

These equations apply to both liquids and gases; however, the analysis of gases is complicated by their compressibility. In order to take account of this, it is necessary to define one 'mol' of a material as 6.02×10^{23} molecules and, from this, the mass of 1 mol of a material with an atomic mass of m is m grams. We now assume that the gas is 'ideal' and then the relationship between pressure and volume may be expressed as:

$$PV = nRT \qquad [1.10]$$

where:

n is the number of mols of gas present
R = 8.31 J/mol/K (the gas constant) and
P,V,T are the pressure (Pa), volume (m^3) and temperature (K).

Thus, at a given temperature and pressure, one mol of any gas will occupy the same volume.

If the flow is expressed as a change in volume dV/dt, equations (1.9) and (1.10) combine to give the molecular flow rate:

$$\frac{dn}{dt} = \frac{KAP}{eRT}\frac{dP}{dx} = JA \qquad \text{mol/s} \qquad [1.11]$$

where:

J is the flux (mol/m^2/s) and
A is the area through which the fluid is flowing (m^2).

This shows that for a compressible fluid the flow rate will depend on the absolute pressure as well as the pressure gradient.

Knudsen flow at low pressures

The permeability K of a given solid material is assumed to be constant for any fluid with viscosity e transporting through it. However, it has been observed that the permeabilities for liquids and gases are often different. The major reason for the differences between water and gas permeability is the theory of gas slippage. The theory suggests that the permeability will be affected by pressure, which will affect the mean free path of molecules. This gas slippage or 'Knudsen' flow becomes significant if the mean free path is of the same order or greater than the size of the capillary through which it is flowing (Knudsen, 1909). The contribution of Knudsen flow to the flow of a given gas is characterised by the Knudsen number, the ratio of the mean free path to the radius of the pores in which the gas is flowing. A Knudsen number significantly greater than unity indicates that Knudsen flow will be important.

Klinkenberg derived an equation relating water and gas permeability to the mean pressure, for oil sands, as follows:

$$K_l = \frac{K_g}{\left(1 + \frac{b}{P_m}\right)} \qquad [1.12]$$

where:

K_l is the water intrinsic permeability of concrete (m^2)
K_g is the gas intrinsic permeability of concrete (m^2)
P_m is the mean pressure at which gas is flowing (atmospheres) and
b is a constant known as the Klinkenberg constant.

It may be seen that this indicates that the permeability of a gas will rise significantly at low pressures. Experimental observations of this effect are reported in Chapters 6, 7 and 8.

1.2.2 Diffusion

Diffusion is a process by which an ion can pass through saturated concrete without any flow of water. The process is driven by concentration gradient. If a strong solution is in contact with a weak solution they will both tend towards the same concentration. Thus, for example, if a pile of salt is placed in one corner of a container full of water, diffusion will be the process that ensures that when the salt has dissolved it will assume a uniform concentration.

In Fig. 1.1 we intuitively know that as the salt dissolves into the water it will assume an equal concentration at all points throughout the liquid. By the same mechanism, ions which are present in the pore water of the

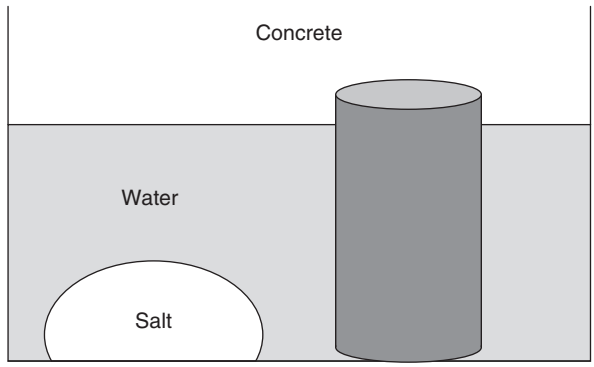

1.1 Schematic diagram of diffusion.

concrete will diffuse out and also assume an equal concentration throughout the liquid. Note that it is assumed that the water does not move.

Moisture diffusion will take place in a gas when the concentration of water vapour is higher in one region than another. This mechanism will enable water to travel through the pores of unsaturated concrete (but may be considered as permeability caused by a vapour pressure – see below in this section). The ions will generally diffuse in pairs with equal and opposite charges. If they do not do this they will build up an electrical potential which will cause them to electromigrate back together (see Section 1.2.3 below).

Diffusion is normally defined in terms of flux F which is the flow per second per unit cross-sectional area of the porous material. Flux may be measured in kg/m^2/s although a unit of mol/m^2/sec (designated J) is also common. The diffusion coefficient is defined from the equation (1.13) which has been known empirically since 1855 as Fick's first law (Fick, 1855):

$$F = D\frac{\mathrm{d}C}{\mathrm{d}x} \qquad \mathrm{kg/m^2/s} \qquad [1.13]$$

where D is the diffusion coefficient (m^2/s). This equation also applies if flux is measured in mol/m^2/s and concentration in mol/m^3.

Considering a small element of the system, the rate at which the concentration changes with time will be proportional to the difference between the flux into it and the flux out of it:

$$V\frac{\mathrm{d}C}{\mathrm{d}t} = A\Delta F \qquad [1.14]$$

where:

V is the volume of the element
A is the cross-sectional area and
$L = V/A$ is the length.

$$\Delta F = L\frac{\mathrm{d}F}{\mathrm{d}x} \qquad [1.15]$$

Thus:

$$\frac{\mathrm{d}C}{\mathrm{d}t} = \frac{\mathrm{d}F}{\mathrm{d}x} \qquad [1.16]$$

and:

$$\frac{\mathrm{d}C}{\mathrm{d}t} = D\frac{\mathrm{d}^2C}{\mathrm{d}x^2} \qquad [1.17]$$

Considering a system with concentrations C_1 and C_2 on each side (see Fig. 1.2), looking first at the long-term solution, the system will eventually reach a state where the concentration stops changing. Thus $\mathrm{d}C/\mathrm{d}t = 0$ and therefore $\mathrm{d}C/\mathrm{d}x$ is constant. Before this happens, the rate of change of concentration with time ($\mathrm{d}C/\mathrm{d}t$), and thus the curvature of the concentration vs position curve ($\mathrm{d}^2C/\mathrm{d}x^2$), will progressively decrease. $\mathrm{d}C/\mathrm{d}t$ will also increase with D, i.e. the system will reach a steady state sooner if the diffusion coefficient is higher (the flux will also be greater).

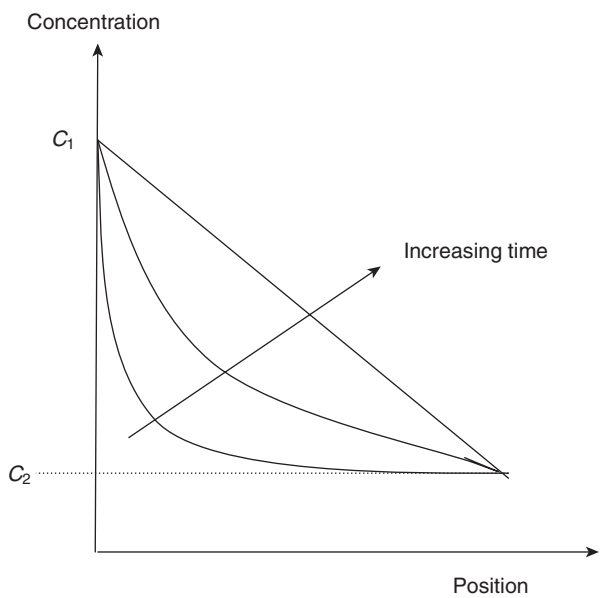

1.2 Typical shape of concentration profiles.

Comparing diffusion coefficients and permeability

When considering the movement of a gas or vapour which is mixed with another gas (e.g. water vapour in air), it is instructive to compare the equations for permeability and diffusion. Equation (1.10) shows that the concentration is proportional to the pressure.

For a fluid with atomic mass m:

$$C = \frac{mn}{V} \qquad [1.18]$$

Substituting this into equations (1.8), (1.10) and (1.13) gives:

$$D = \frac{KCRT}{me} \qquad [1.19]$$

Thus the coefficients for permeability and diffusion are exactly related and this transport may be considered as either diffusion or advection and the equations will give the same answer.

1.2.3 Electromigration

Electromigration (often called migration) occurs when an electric field (voltage difference) is present. This may be derived from an external source such as leakage from a direct current power supply but is also frequently caused by the electrical potential of pitting corrosion on reinforcing steel. If an electric field is applied across the concrete in Fig. 1.3, the negative ions will move towards the positive electrode.

Electromigration can be measured from the electrical resistance of the concrete because it is the only mechanism by which concrete can conduct electricity. The flux due to electromigration is given by equation (1.20):

$$F = \frac{DzECF_a}{RT} \qquad \text{kg/m}^2\text{/s} \qquad [1.20]$$

where:

z is the valence of the ion (i.e. the charge on it divided by the charge of an electron)
F_a is the Faraday constant = 9.65×10^4 C/mol
E is the electric field (V/m)
R = 8.31 J/mol/K and
T is the temperature (K).

The flux can be expressed as an electric current:

$$I = zFF_aA \qquad \text{A} \qquad [1.21]$$

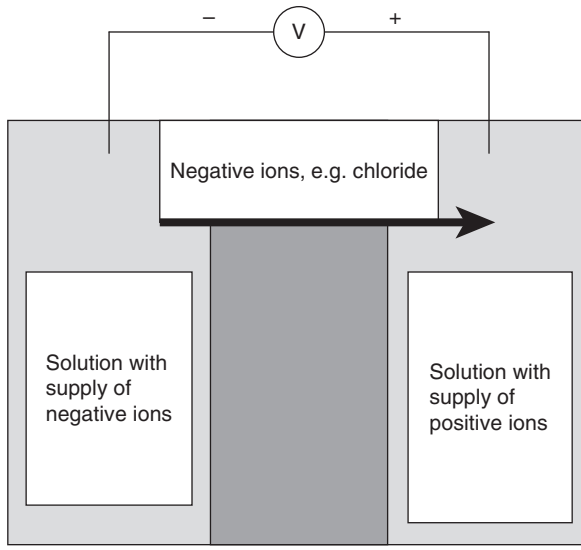

1.3 Schematic diagram of electromigration.

Ohm's law states that:

$$R = \frac{\phi}{I} \qquad \Omega \qquad [1.22]$$

where ϕ is the voltage. The electric field is the voltage gradient and thus:

$$E = \frac{\phi}{x} = \frac{IR}{x} = \frac{zFF_a AR}{x} \qquad \text{V/m} \qquad [1.23]$$

where x is the distance (m). The resistivity ρ is defined from the equation:

$$R = \frac{\rho x}{A} = \frac{x}{A\sigma} \qquad \Omega \qquad [1.24]$$

where σ is the electrical conductivity in $(\Omega\text{m})^{-1}$, the inverse of the resistivity.

Rearranging equations (1.20), (1.23) and (1.24) gives the Nernst–Einstein equation:

$$D = \frac{RT\sigma}{z^2 F_a^2 C} \qquad [1.25]$$

Note that if this is to be measured, an alternating current must be used to prevent polarisation. These phenomena are discussed in detail in Chapters 10, 11 and 12.

1.2.4 Combining diffusion and electromigration

The general law governing the ionic movements due to the chemical and electrical potential is obtained by combining equations (1.13) and (1.20) and is known as the Nernst–Planck equation:

$$F = D\frac{\partial C}{\partial x} + \frac{zF_a}{RT}DC\frac{\partial \phi}{\partial x} \qquad [1.26]$$

1.2.5 Thermal gradient

Water will move from hot regions to cold regions in solids. The rate at which it moves will depend on the permeability of the solid. This process is independent of and additional to the drying process (evaporation) which will take place on exposed surfaces which are hot. Similarly, in saturated concrete, ions in hotter water will migrate towards colder regions. The mechanism is shown in Fig. 1.4 and depends on probability. At a microscopic level, the temperature of a solid is a measure of the kinetic energy of the atoms and molecules within it. An ion or molecule which is moving faster on the hot side has a greater probability of crossing the sample than one on the cold side.

The most obvious situation when this process may occur is when a concrete structure which has been contaminated with de-icing salt heats up in sunlight. The salt saturated water in the surface pores will migrate rapidly into the structure. Even if this does not reach the steel by this mechanism, the salt may diffuse the remaining distance.

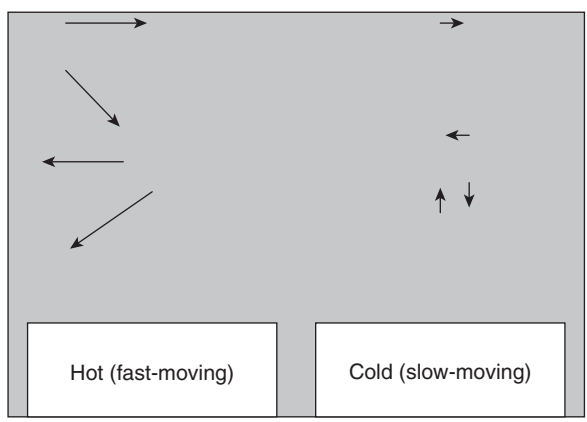

1.4 Schematic diagram of thermal migration. The longer arrows indicate the greater movement of ions in the hot region.

1.3 Processes which increase or reduce the transport

1.3.1 Adsorption

When considering transport of ions in a porous material, it is essential to consider adsorption at the same time because in many situations the bulk of the ions which enter into a barrier will be adsorbed before they reach the other side. Adsorbed ions are bound into the matrix in various ways and are unable to move and therefore unable to cause any deterioration.

We define:

C_l kg/m^3 is the concentration of ions per unit volume of liquid in the pores (i.e. the mobile ions)

and

C_s kg/m^3 is the total concentration (including immobile adsorbed ions) per unit volume of the solid.

It is necessary to make a clear distinction between absorption and adsorption. The term absorption is used to describe processes such as capillary suction and osmosis which may draw water into concrete. Adsorption is the term used for all processes which may bind an ion (temporarily or permanently) in the concrete and prevent it from moving. These processes may be chemical reactions or a range of physical surface effects.

When the ionic concentration in a concrete sample is measured there are various different systems that can be used:

- If the 'acid soluble' concentration is measured by dissolving the sample in acid, this will extract all of the ions including those adsorbed onto the matrix (this measures C_s).
- If the 'water soluble' concentration is measured by leaching a sample in water, only the ions in solution will come out (assuming the test is too short for adsorbed ions to dissolve). Alternatively, 'pore squeezing' or 'pore fluid expression' can be used to squeeze the sample like an orange using very high pressures (this measures C_l) (see Section 15.3.4).

The ratio of the solid to liquid concentrations is known as the capacity factor α. In concrete, the adsorption of chloride ions is normally on the cement (binding on the aluminate phases). Thus the capacity factor will be proportional to the cement content. It will probably also be higher if pulverised fuel ash or GGBS is used.

A simple approximation of the amount of material which is adsorbed onto the matrix may be obtained by assuming that at all concentrations it is proportional to the concentration of ions in the pore fluid (note that this implies that the adsorption is reversible). Thus the capacity factor is a

constant for all concentrations. This approximation is useful for modelling, but it works best for low solubility ions, unlike chlorides, which have a solubility of about 10 %. For chlorides, there will still be a good link between the number in solution and the number adsorbed, but it will not be a completely linear relationship. There are many other ways of analysing adsorption, for example the 'Langmuir isotherm' gives a more complex relationship between C_s and C_l. These more complex isotherms could be used in computer modelling but are difficult to use in analytical solutions (Luping *et al.*, 2012).

Using the linear isotherm, the ratio of the two concentrations is constant and is the capacity factor:

$$\alpha = \frac{C_s}{C_l} \qquad [1.27]$$

Equation (1.16) for the rate of change of concentration will be for the total concentration:

$$\frac{dC_s}{dt} = \frac{dF}{dx} \qquad [1.28]$$

Thus:

$$\frac{dC_l}{dt} = \frac{1}{\alpha}\frac{dF}{dx} \qquad [1.29]$$

From this, it may be seen that a high value of α will make the concentration change much more slowly – i.e. if chlorides are penetrating into a wall it will delay the start of corrosion of the steel.

1.3.2 Diffusion with adsorption

Because there are two different ways of measuring concentration in an adsorbing system, there are also two different ways of measuring diffusion: (i) using the apparent diffusion coefficient D_a (also known as the 'effective' diffusion coefficient; and (ii) using the intrinsic diffusion coefficient D_i.

The apparent diffusion coefficient D_a (which is what can be measured by testing the solid using measurements of total concentration) is defined from measurements of total concentration:

$$F = D_a \frac{dC_s}{dx} \qquad \text{kg/m}^2/\text{s} \qquad [1.30]$$

The intrinsic diffusion coefficient D_i (which is the diffusion coefficient for the pore solution) is defined from measurements of the water soluble concentration:

$$F' = D_i \frac{dC_l}{dx} \qquad \text{kg/m}^2\text{/s} \qquad [1.31]$$

where F' is the flux per unit cross-sectional area of the liquid in the pores.

Thus:

$$F = \varepsilon D_i \frac{dC_l}{dx} \qquad \text{kg/m}^2\text{/s} \qquad [1.32]$$

where ε is the porosity.

By integrating these (or by inspection) it may be seen that:

$$\frac{\alpha}{\varepsilon} = \frac{D_i}{D_a} \qquad [1.33]$$

For a typical concrete $D_i = 5 \times 10^{-12}\,\text{m}^2\text{/s}$.

1.3.3 Capillary suction

Capillary suction occurs in fine voids (capillaries) with wetting surfaces and is caused by surface tension. In the experiment shown in Fig. 1.5, water rises higher up a smaller diameter glass capillary tube and this shows how this mechanism has greatest effect in systems with fine pores. This leads to the situation that concretes with finer pore structures (normally higher grade concretes) will experience greater capillary suction pressures. Fortunately, the effect is reduced by the restriction of flow by generally lower permeabilities.

A good demonstration of the power of capillary suction in concrete can be observed by placing a cube in a tray of salt water and simply leaving it in a dry room for several months. The water with the salt in it will be drawn up the cube by 'wicking' until it is close to an exposed surface and can evaporate. As this happens, the near-surface pores fill up with crystalline salt which will eventually achieve sufficient pressure to cause spalling. This mechanism of damage by salt crystallisation is common in climates where there is little rain to wash the salt out again.

The capillary suction will create a pressure:

$$P = \frac{2s}{r} \qquad [1.34]$$

where:

s is the surface tension of the water (N/m) (= 0.073 N/m for water) and
r is the radius of the pores (m).

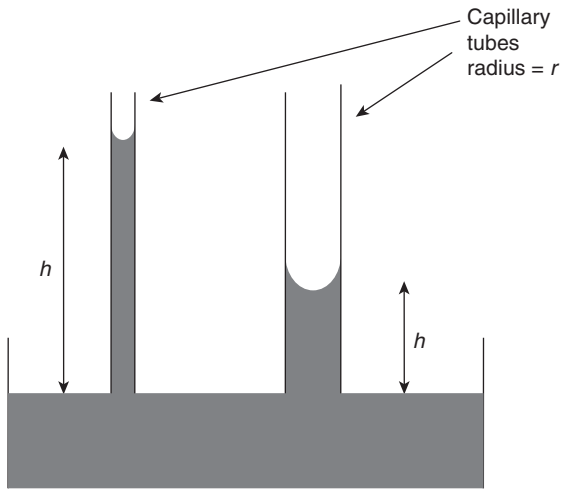

1.5 Capillary suction heights.

Thus, since the pressure from a fluid $P = \rho\, g\, h$, the height of the column of water in a fully wetting capillary is given by:

$$h = \frac{2s}{r\rho g} \quad \text{m} \qquad [1.35]$$

A typical pore in concrete has a radius of 10^{-8} m. Putting this into the equation gives a height of 1460 m indicating that damp should rise up concrete to this height. The reason why it does not is the irregularity of the pores (see Fig. 1.6). Water will be drawn up through the neck of the pore but will then reach the point where the radius is much larger and the capillary suction pressure thus much lower and will stop at that point.

1.3.4 Osmosis

Osmosis depends on what is called a semi-permeable membrane. This is a barrier through which the water can pass but material dissolved in it cannot pass as easily. An example is the surface layer of concrete which will permit water to enter but restrict the movement of the lime dissolved in the pore water. The osmotic effect causes a flow of water from the weak solution to the strong solution. Thus water on the outside of concrete (almost pure, i.e. a weak solution) is drawn into the pores where there is a stronger solution. The process is illustrated in Fig. 1.7. If two solutions were placed either side of a barrier as shown, the level in one of them would rise, although in

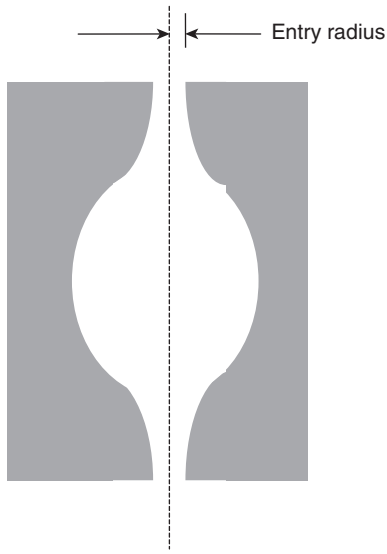

1.6 'Ink bottle' pore.

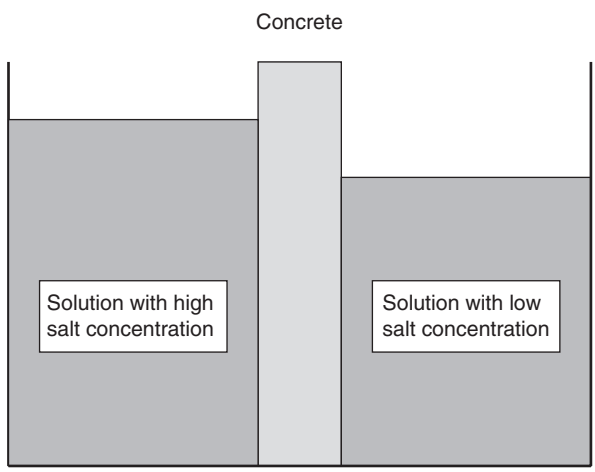

1.7 Schematic diagram of osmosis.

practice this would be very difficult to observe because concrete is permeable and the liquid would start to flow back as soon as a pressure difference developed.

If different solutions are present on each side of the sample, osmosis will still take place even if the concentrations are the same. The direction of flow will depend on their relative 'osmotic coefficients'. Osmosis could be a significant process for drawing chlorides and sulphates into concrete. Having entered the concrete they may move further in by diffusion.

1.3.5 Electro-osmosis

If a solid material has an electrically charged surface, the water in the pores will acquire a small opposite charge. Clay, both in soil and bricks, has a negatively charged surface so the pore water will have a positive charge. The water will thus move towards a negatively charged plate and away from a positively charged one. This system is used in one of the commercially available systems for removing damp from existing buildings (the more common one is resin injection to block the pores).

1.4 Conclusions

There are numerous mechanisms for the transport of fluids through concrete and several processes which promote or inhibit the transport. Equations have been presented for the following processes which are considered in detail in later chapters of this book:

- permeability (pressure-driven flow)
- diffusion
- electromigration
- adsorption
- capillary suction.

1.5 References

Darcy (1856) *Les fontaines publiques de la ville de Dijon*, Victor Dalmont, Paris.

Fick A (1855) On liquid diffusion, *Philosophical Magazine*, **10**, p. 30.

Knudsen M (1909) The law of the molecular flow and viscosity of gases moving through tubes, *Annals of Physik*, **28**, pp. 75–177.

Luping T, Nilsson L and Basheer P (2012) *Resistance of Concrete to Chloride Ingress*, Spon Press, London.

Neville A M (2011) *Properties of Concrete* (5th edn), Pearson, Harlow.

2

Computer models to predict the transport processes in concrete

DOI: 10.1533/9781782423195.17

Abstract: In this chapter, the basic methods used to develop computer models are explained by considering an example. It is shown that the models use the simple equations given in Chapter 1 rather than their integrated forms. A model for pressure-driven flow and diffusion through a waste containment barrier is considered. The lines of code correspond exactly to the equations that are being applied and the key equations and their corresponding code are discussed. Example calculations from the model are presented which show the key influence of adsorption on transport.

Key words: permeability, diffusion, computer model, finite difference, finite step.

2.1 Introduction

Having defined the basic physical equations in Chapter 1, there are two possible ways to make use of them: they may be integrated either analytically or numerically. Both approaches are used in different chapters of this book. In this chapter, a simple approach to numerical integration using BASIC computer code is described. This numerical integration may also be described as finite step modelling. The computer modelling was carried out using code written in Visual Basic running as a macro in Microsoft Excel on a standard desktop computer.

There are many different software packages available which can be used for modelling of this type. However, the author is not aware of any that can model the particular complexities that arise in the transport processes in concrete. In particular for the electromigration model, which is used in several of the later chapters of this book, there do not appear to be any packages that can adequately account for charge conservation. Also when considering pressure-driven flow combined with diffusion in a multilayer containment barrier, no packages were found that could be used for modelling. It must also be observed that a simple model for, say, pressure-driven flow combined with diffusion can be written in a few hours and will run on any computer with Microsoft Excel without the need to locate and purchase a package. The main limitation of this type of programme is that

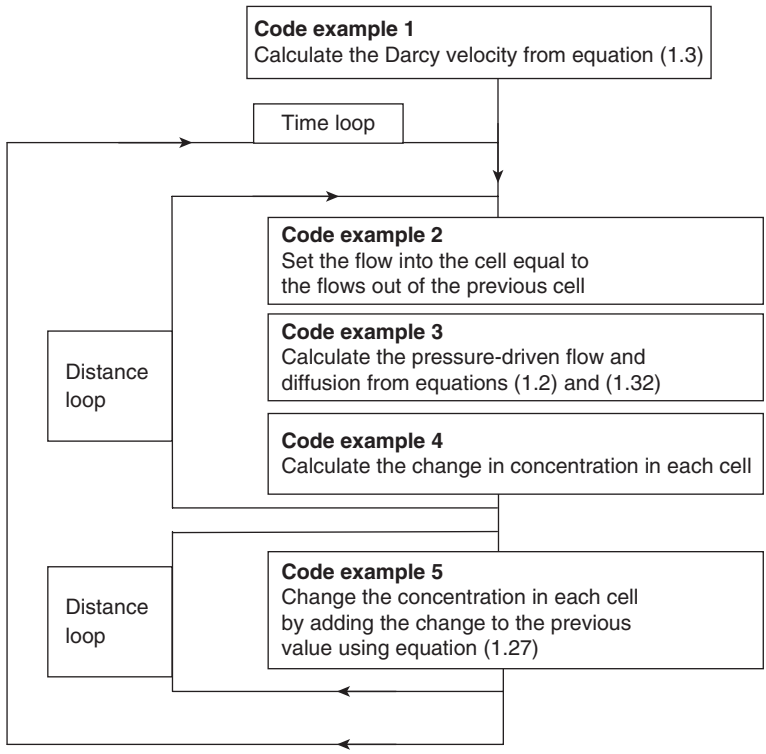

2.1 Block diagram of the computer code.

it is one-dimensional and can only model situations in which the flow is linear or there is, for example, circular, cylindrical or spherical symmetry.

To give an example of how the code can be written, combined pressure-driven flow and diffusion through a barrier is considered. The use of this particular model is described in Chapter 15 which also explains the purpose of the three layers. The same programme was used to analyse the three-layer barriers used in the site trials and the single-layer samples tested in the laboratory.

The structure of the programme is shown in Fig. 2.1; it loops through the sample in time and space. Examples of the code are discussed in Section 2.2.

2.2 Expressing the basic equations as computer code

2.2.1 Input data

The barrier is constructed with up to three layers. Each layer is characterised with parameters as follows. For any layer *j*:

layer thickness = x_j
capacity factor = α_j
permeability = k_j
intrinsic diffusion coefficient = D_j
porosity = ε_j

Within the programme, each layer is divided vertically into a large number of cells. The calculation is carried out for a unit cross-sectional area ($1\,m^2$) so the cell volumes are numerically equal to their thicknesses.

2.2.2 Code example 1: calculation of Darcy velocity

The computer code is complicated by the fact that this code was written for a multi-layer barrier. The Darcy velocity is calculated as follows:

$$V = \frac{k_1 \times (h + x_1 + x_2 + x_3)}{x_1 + \left(\frac{x_2 \times k_1}{k_2}\right) + \left(\frac{x_3 \times k_1}{k_3}\right)} \qquad [2.1]$$

where h is the total height of the water column on the sample which is added to the height (thickness) of the sample itself if the flow through it is vertical, but not if it is horizontal (as in lab tests).

The variables are expressed in the computer code as follows:

k_1	**PERM(1)**	element 1 in an array of permeabilities
$H + x_1 + x_2 + x_3$	**tHeight**	the total height (thickness) of the barrier
x_1	**THICK(1)**	the thickness of layer 1

Thus the code for equation (2.1) becomes:

```
V = PERM(1) * (tHeight) / (THICK(1) +
(THICK(2) * PERM(1) / PERM(2)) + (THICK(3) *
PERM(1) / PERM(3)))                    [Code example 1]
```

2.2.3 Code example 2: updating input to cell

The sample is divided up into cells as shown in Fig. 2.2, where **cin** and **cout** are the total flows due to pressure-driven flow during the time step and **din** and **dout** are the flows for diffusion. As the programme moves to consider the next cell, the flow out of the previous one becomes the flow into the next. The code for this is:

```
cin = cout
din = dout                             [Code example 2]
```

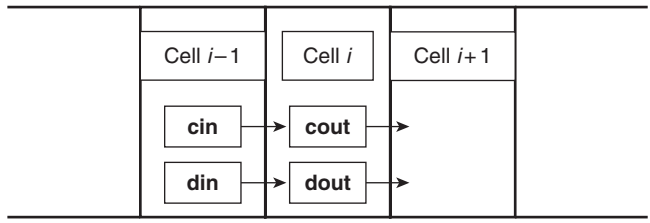

2.2 Schematic diagram of programme for cell *i*.

2.2.4 Code example 3: advection and diffusion calculation

Advection calculation

The advection from cell i to cell $i + 1$ during a single time step dt is calculated as:

$$F \times \mathrm{d}t = \mathrm{d}t \times V \times Cl_i \qquad [2.2]$$

The variable dt is expressed as **dtd** in the code so it becomes:

```
cout = V * dtd * CL(I)          [Code example 3a]
```

where:

CL(I) = Cl_i, the concentration in the liquid in cell i
V is the Darcy velocity of the flow and
dtd is the time step.

Diffusion calculation

The cells may be in different layers of the barrier with different porosities, diffusion coefficients and cell thicknesses. The formula assumes that cell sizes have been set so all cells are entirely in a single layer and thus do not have a layer boundary in them.

The diffusion from cell i to cell $i + 1$ during a single time step dt is calculated as:

$$F\mathrm{d}t = \mathrm{d}t \frac{C_{\mathrm{l}_i} - C_{\mathrm{l}_{(i+1)}}}{\left(\dfrac{Ct_i}{(2D_i\varepsilon_i)} + \dfrac{Ct_{i+1}}{(2D_{i+1}\varepsilon_{i+1})}\right)} \qquad [2.3]$$

where Ct_i is the cell thickness.

For the code, **clayer** is the layer in which the current cell **(I)** is located and **nlayer** is the layer in which the next cell **(I + 1)** is located. **IDIF(clayer)**, **POR(clayer)** and **CTHICK(clayer)** are the intrinsic

diffusion coefficient, porosity and cell thickness for the layer in which the cell **I** is located. The code for equation (2.3) therefore becomes:

```
dout = dtd * (CL(I) – CL(I + 1)) /
((CTHICK(clayer) / (2 * IDIF (clayer) *
POR(clayer))) + (CTHICK(nlayer) / (2 *
IDIF(nlayer) * POR (nlayer))))
```

[Code example 3b]

For the upper and lower cells (numbers **1** and **n**), the diffusion is doubled because the diffusion path to the centre of the cell only runs through half the distance of solid.

2.2.5 Code example 4: calculating change in contents of cell

change(I) is the change in concentration in cell **(I)** during the single time step. Thus the code is:

```
change(I) = (din – dout + cin – cout) /
CTHICK(clayer)
```

[Code example 4]

Where **CTHICK(clayer)** is the cell thickness in the layer in which the cell is located and is equal to the volume because a unit cross-sectional area is considered.

2.2.6 Code example 5: updating concentration in cell

The total concentration C_s in cell **(I)** is **CS(I)** and is increased by **change(I)**. The concentration C_l in the liquid **CL(I)** is then calculated using the capacity factor α, **CAP(clayer)**. Thus the code is:

```
CS(I) = CS(I) + change(I)
CL(I) = CS(I) / CAP(clayer)
```

[Code example 5]

A few additional lines of code (probably in a subroutine) could be used for a non-linear adsorption isotherm (i.e. α varying with concentration).

2.3 Other elements of the code

2.3.1 Checking the code

Transport by advection alone reaches a steady state when the concentration throughout the barrier C_{s_i} = the concentration above it C_{s_0}. Thus:

$$F = V \times C_{s_0} \qquad [2.4]$$

Transport by diffusion alone reaches a steady state when there is a linear concentration gradient through the barrier. The flux is given by:

$$F = \frac{C_{l_0}}{\left(\frac{x_1}{D_1 \times \varepsilon_1}\right) + \left(\frac{x_2}{D_2 \times \varepsilon_2}\right) + \left(\frac{x_3}{D_3 \times \varepsilon_3}\right)} \quad [2.5]$$

These values are calculated at the start of the programme and can be used for checking purposes.

The steady state values were checked by hand calculation and, for a number of different configurations, the programme was run for long enough to reach an effective steady state and the output checked for agreement. For a single layer, the model was checked for agreement with the PHREEQE transport code (Parkhurst *et al.*, 1990) for a single element.

2.3.2 Time step

The time step dt for the programme is set to an estimated value and the time to breakthrough is calculated. The time step is then halved and the process is repeated. A change of less than 5 % in the breakthrough time is taken to indicate stability (this could be reduced for greater accuracy – with each generation of faster computers the accuracy can be improved without extending the run time.)

The relationship between the time step and the cell size is initially determined by the advection calculation. This can mean that, if the diffusion flux is high, the concentration in the cell can change substantially during a single time step (it is assumed to remain approximately constant). This is checked and, if the resulting change in concentration in the cell exceeds 25 % of the concentration, the time step is reduced. In order to save time, the time step can be increased by 2 % in each loop and this check will then reduce it if it becomes too large; however, with increasing time the concentration will tend to change less.

2.4 Example: calculations for a waste containment barrier

This code was used to calculate the flow through a multilayer concrete barrier 1 m thick. The full details of this project are given in Chapter 15, but results are presented here for a single layer barrier to demonstrate the effect of the different material properties.

Figure 2.3 shows the base case which is a 1 m head of leachate on a 1 m thick concrete barrier with a permeability of 10^{-9} m/s, a diffusion coefficient of 5×10^{-10} m^2/s and a capacity factor of 10 (typical values for concrete). The graph shows the concentration of contaminants across the barrier at

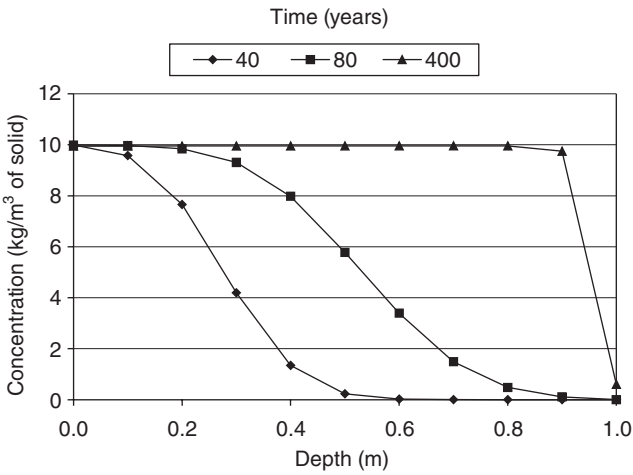

2.3 Concentrations of contaminants for base case.

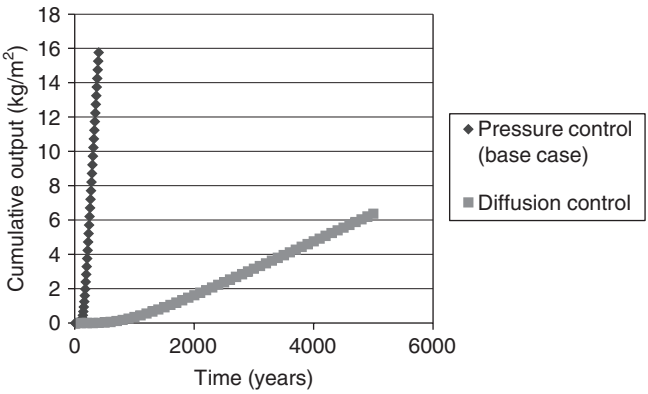

2.4 Output of contaminants from the base of the barrier.

different times. It may be seen that in the steady (final) state, the concentration is at its maximum level throughout the barrier. This occurs because the flow is driven by pressure gradient, and water with a high concentration of contaminants will flow all of the way through the barrier.

Figure 2.4 shows the output of ions from the base of the barrier against time. The breakthrough time (158 years) is obtained by extrapolating the linear part of the curve back to the axis. The second line on the graph (diffusion control) shows the situation with the permeability reduced to 10^{-12} m/s (typical value for a very good concrete). The breakthrough time has only increased to 1049 years for the three order of magnitude decrease in the permeability. The reason for this can be seen in Fig. 2.5 where the

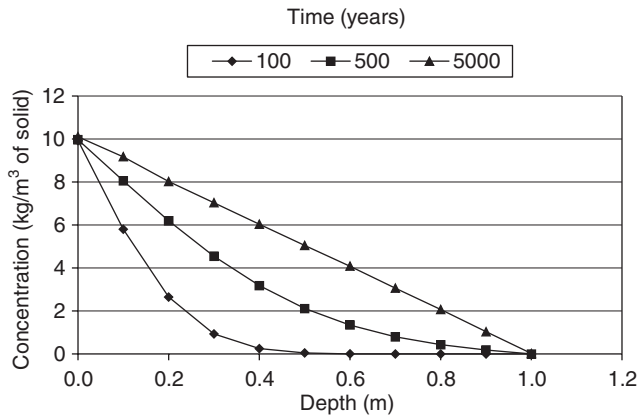

2.5 Concentrations of contaminants for diffusion control.

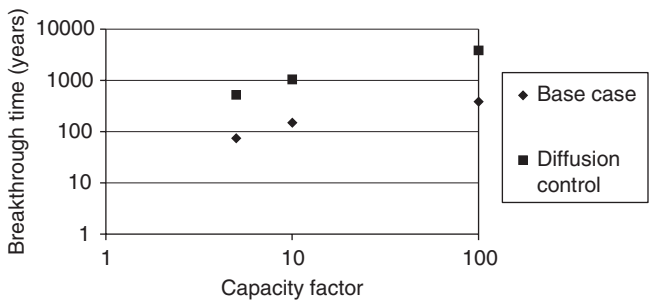

2.6 The effect of capacity factor.

steady state concentration can be seen to show a linear decrease across the sample because diffusion is driven by the concentration gradient and can therefore never cause the concentrations to rise above these values.

Figure 2.6 shows the effect of changing the capacity factor for each of the examples shown above. It may be seen that this increases the breakthrough time far more effectively than reducing the permeability, which was 10^{-9} for the base case and 10^{-12} for the diffusion control case.

Chapter 15 describes how this model was validated by constructing trial cells, filling them with leachate and extracting samples of pore solution at various depths over a period of three years. With this validation, it was then possible to use the knowledge of the transport properties to predict the performance of the barrier throughout its life. This made it possible to select materials for the concrete which will achieve the containment performance required by the regulatory authorities.

2.5 Conclusions

- If it is possible to model the transport processes in one dimension (e.g. with linear flow or circular or cylindrical symmetry); simple computer programmes may be written to simulate them.
- The basic transport equations from Chapter 1 may be used in the programmes. It is not necessary to use integrated forms.
- The programmes apply these equations repeatedly by looping through time and position.
- The time step may be adjusted to reduce run times, but with modern computers only simple tests for this are necessary because run times are normally very short.
- A simulation of pressure-driven flow and diffusion in a concrete barrier shows the significance of adsorption in the results.

2.6 Reference

Parkhurst D L, Thorstenson D C and Plummer L N (1990) *PHREEQE – a computer program for geochemical calculations*, Water-Resources Investigations Report 80–96, US Geological Survey, Reston, VA.

3

Surface tests to determine transport properties of concrete – I: the tests

DOI: 10.1533/9781782423195.26

Abstract: In this chapter, non-destructive surface permeability tests for *in situ* use are presented together with a 'vacuum preconditioning' method to make them more accurate. The main tests are the initial surface absorption test (ISAT) and the Figg test, and these are described. The ISAT measures water transport through the surface of concrete and the Figg measures air transport into a drilled hole. Additional tests are also described. A method for preconditioning the concrete by drying it with a vacuum and using indicating silica gel to monitor the progress is described. Experimental results are presented to show this is very effective.

Key words: initial surface absorption test (ISAT), Figg test, vacuum preconditioning, vacuum drying.

3.1 Introduction

A great number of permeability tests are available in the literature. These tests can be used for quality control and compliance testing, during and immediately after construction, or to check the residual durability of existing structures. Four different ones are considered in this book: the standard ISAT and Figg described in Sections 3.2 and 3.3 and two variations on them, the APNS and CAT, which are described in Section 3.4. Table 3.1 shows that these cover four basic generic types.

3.2 The initial surface absorption test (ISAT)

The test method was developed first by Levitt (1970) as a quality control test for precast concrete units. It is described in detail in BS 1881: Part 208 (BSI, 1996).

A cap of known area is clamped to the test surface (Fig. 3.1). Two pipes lead from the cap with one connecting to a reservoir, which can be isolated by a tap. The other is connected to a calibrated capillary tube, to measure the rate of absorption of water into the concrete below the cap by closing the tap (see Fig. 3.1). The initial surface absorption (ISA) is defined as the rate of flow of water into concrete per unit area at stated intervals from the start of the test. ISA_{10}, which is the value at 10 min, is often quoted.

Table 3.1 Summary of test methods

Test procedure	Test geometry	
	Surface	Drilled hole
Apply vacuum and measure time for decay	Air permeability of near surface (APNS)	Figg air permeation index
Apply water and measure flow into concrete	Initial surface absorption test (ISAT)	Cover concrete absorption test (CAT)

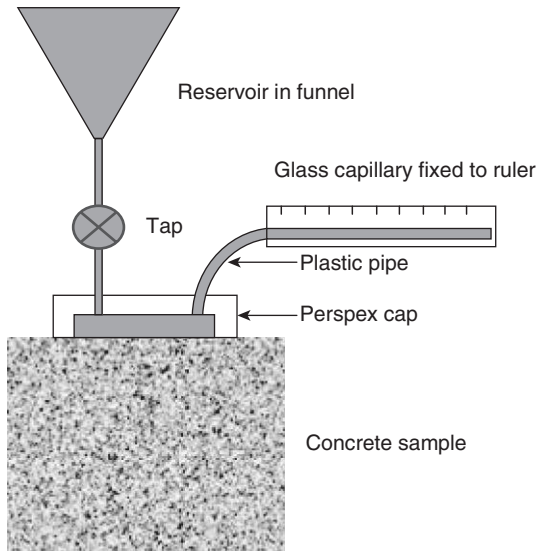

3.1 Schematic arrangement of ISAT.

The standard specifies that the water head (i.e. the height of the funnel above the cap) should be 200 mm, but the author has found that it makes no difference if this is as much as a metre. It may be seen from the analysis presented in Chapter 4 that this head is not considered relevant because the capillary suction pressure is much larger.

3.3 The Figg air permeation index

Figg (1973) developed a test for air and water permeability which involved a hole drilled into the concrete surface. Figg's air permeability test method is based on reducing the pressure in the drilled hole in the concrete through

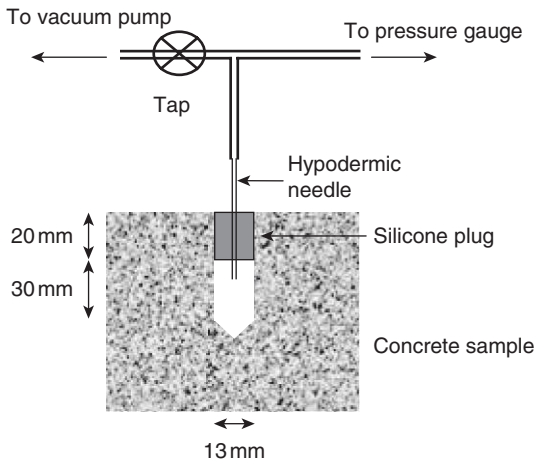

3.2 Schematic arrangement of Figg test.

a hypodermic needle using a vacuum pump. The rate at which the pressure subsequently returns to atmospheric gives a measure of the permeability of the concrete through which the air then flows.

For the tests reported here, a test hole of 50 mm depth and 13 mm diameter was drilled into the concrete. After thorough cleaning, the hole was plugged to a depth of 20 mm from the outside surface by polyether foam and then sealed with a catalysed silicon rubber. When the rubber had set, a hypodermic needle was pushed through the plug (Fig. 3.2). The vacuum applied was 0.45 bar and the permeation index was taken as the time elapsed for the decay of the applied vacuum from 0.45 bar to 0.55 bar with the tap closed.

3.4 Other tests

3.4.1 The cover concrete absorption test (CAT)

This test uses the water measurement system of the ISAT test in a drilled hole similar to the Figg test. A hole of 13 $\phi \times 50$ mm is drilled into one of the surfaces (not the cast surface). A basic ISAT set-up is used but with a 13 mm internal diameter cap. An inlet tube located inside the sealed hole is used to supply water to the concrete test cavity as shown in Fig. 3.3. The procedure of carrying out CAT is the same as that for ISAT. The results are normally quoted as a flow per unit area where the area is the surface of the drilled hole. The water pressure is maintained at 200 mm head above the centre of the hole (but this is not critical, as noted above for the ISAT). The cover concrete absorption index CAT_{10} is the absorption at 10 min.

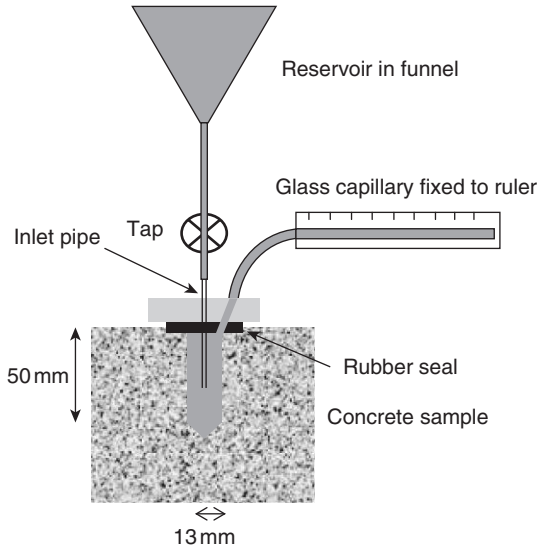

3.3 Schematic arrangement of CAT.

3.4.2 The air permeability of near surface (APNS) test

This test makes use of the cap from the ISAT test but measures vacuum decay in a similar manner to the Figg test. The APNS index is defined as the time in seconds for the pressure in the cap to rise from 0.01 to 0.9 bar.

At this point in the discussion, it may be observed that the water tests measure volumes rather than pressures. In the analysis that is developed in the next chapter it is shown that this means that they can be used to obtain values for permeability, while the gas tests, in their basic form as presented here, cannot. A solution to this problem is presented in Chapter 5.

3.5 Vacuum preconditioning: a development of the ISAT test

The major difficulty in applying all these tests *in situ* is that their measurements are substantially affected by the amount of water already present in the concrete. It has been shown that any uncertainties about the original moisture content lead to poor reproducibility of the results. The effect of moisture on gas migration is discussed in detail in Chapter 6 and it is shown to be very significant. For the water tests, any water already in the pores will clearly have a significant effect on subsequent absorption by capillary suction. There are two possible approaches to overcoming this

problem. The first is to measure the moisture content and compensate for it in the results, and the second is to precondition the sample by removing the moisture.

Measurement of the moisture content of *in situ* concrete may be achieved by measuring the electrical impedance or radiation attenuation or by establishing hygral equilibrium between the *in situ* concrete and a specimen of which the moisture content may be established by weighing. When the relative humidity is below 90 %, some indication of the moisture content may be obtained by using a humidity probe in a drilled hole, although difficulties may be found in calibration. After establishing the moisture content, an extensive system of correction factors, taking into account the concrete grade, age, cement replacement materials, etc., would be used to calculate standard base values. The results could then be inaccurate, owing to errors arising from the test measurement itself, the measurement of moisture content or the correction factors. Thus the method of removing the moisture is considered to be a better solution.

Water will remain in concrete pores with entry diameters which are sufficiently small to sustain a meniscus. The conditions for this are given by the Kelvin equation:

$$r \ln(RH) = \frac{2ms}{\rho RT} \qquad [3.1]$$

where:

r is the pore radius (m)
RH is the relative humidity
m is the molecular weight of water = 0.018 kg
s is the surface tension of water = 0.073 N/m
ρ is the density of water = 1000 kg/m^3
R is the gas constant = 8.3 J/mol/K and
T is the temperature = 290 K.

Applying this equation indicates that, at a typical external humidity of 70 %, no pores with radii greater than 3 nm will sustain a meniscus. The volume of pores in concrete with radii less than 3 nm is very small, so if concrete is in equilibrium with air at normal humidities in the UK it will be virtually dry. The practical difficulty for the purpose of preparing samples for permeation testing is the time taken to reach equilibrium. This will depend on the permeation properties of the concrete and the air flow at the surface.

The two possibilities for fast removal of water are raising the temperature and lowering the pressure. Raising the temperature of any part of an *in situ* sample, except for the immediate surface layer, would be difficult without a risk of damage from overheating. Lowering the pressure is, however, an

attractive option. The maximum stress which may be applied in this way is one atmosphere, which is 0.1 N/mm^2, and this is not likely to affect a typical concrete.

3.5.1 Use of indicating silica gel desiccant

The essential requirement for sample preconditioning is that it should be simple to replicate in order to give reproducible *in situ* ISAT results. The time required to extract the moisture with a vacuum will depend on the pressure and the initial moisture content, as well as the permeation properties of the sample. Similarly, the depth to which the moisture should be removed will depend on the depth of penetration in the ISAT test, and this in turn will depend on the permeation properties (and the amount of moisture in the sample). Attempting to establish fixed times for vacuum treatment would therefore be exceptionally difficult. Monitoring weight loss (which is used for oven drying) is obviously not possible for *in situ* work.

The vacuum was applied to the concrete surface using the cap from an ISAT apparatus, and the method chosen to determine the required application time of the vacuum was to place some silica gel indicator desiccant in the ISAT cap and to wait until the colour change was observed. Silica gel desiccant is widely available in the form of crystals which have been treated with an indicator which turns pink when moisture is present and blue when it is not. The time taken for the colour to change when in the vacuum on the concrete surface will depend on the pressure and humidity. The humidity in the vacuum depends upon the rate of moisture loss from the concrete, which in turn depends on the moisture content of the concrete surface as well as the pressure and the permeation properties. The time taken for the gel to change colour is therefore dependent on the same parameters which determine the time required for preconditioning.

3.5.2 Development work

The basic procedure using silica gel was established when laboratory work started, but it was necessary to develop the apparatus to ensure that the pressure was low enough to make it work at a practical rate. As an initial trial to determine whether the laboratory vacuum pump was performing adequately, it was tested to see if it could boil water at room temperature. The pump was unable to do this and was replaced, but even with the new pump the gel took 6–18 h to turn blue. A high vacuum gauge was then fitted to the system and this revealed numerous leaks in the pipework, the ISAT heads and the seals against the samples. When these leaks had been rectified the vacuum time was reduced to 1–6 h. It is the opinion of the author that

Table 3.2 Mix designs

Concrete grade (N/mm^2)	Constituent materials (kg/m^3)					w/c
	PC	Water	Aggregate			
			20 mm	10 mm	Sand	
35	290	190	800	400	715	0.66
60	425	190	800	400	600	0.45

w/c: water to cement ratio.

the use of such a gauge is essential for this technique in order to monitor and minimise leakage. In order to enable work to proceed faster, a manifold was built to apply the vacuum to six specimens at the same time. However, this can only be used if the samples are relatively impermeable. The flow rates through permeable concrete decrease the vacuum head unacceptably.

3.5.3 Preparation of test samples

Two concrete mixes with mean strengths of 35 and 60 N/mm^2 were used (Table 3.2). The test specimens, 100 mm cubes, were cast and kept under wet hessian for 1 day before demoulding. Two curing conditions were used: water curing at 20 °C and air curing at 20 °C, 55 % RH, until testing at 28 days.

3.5.4 Time for silica gel to indicate drying

As ISAT cap containing pink silica gel was placed against a dry impermeable acrylic surface and the time required for the gel to turn blue was recorded. The pressure was then adjusted by bleeding air into the system and the pressure–time relationship shown in Fig. 3.4 was developed. This shows that the relationship is linear starting from about 3 mbar. It was observed that, especially at low pressures, the times were greater if the oil in the vacuum pump was substantially contaminated with water. In order to achieve rapid drying, it is essential to remove this water and change the oil regularly. This problem may also be solved with a water-trap fitted to the inlet of the vacuum pump.

The times recorded using a dry impermeable surface represent the minima for preconditioning at the different pressures; moisture loss from a concrete surface always extended them. In practice, the vacuum pressure was determined by the permeability of the concrete; thus the time was less for concretes with low water to cement (w/c) ratios (in comparison with

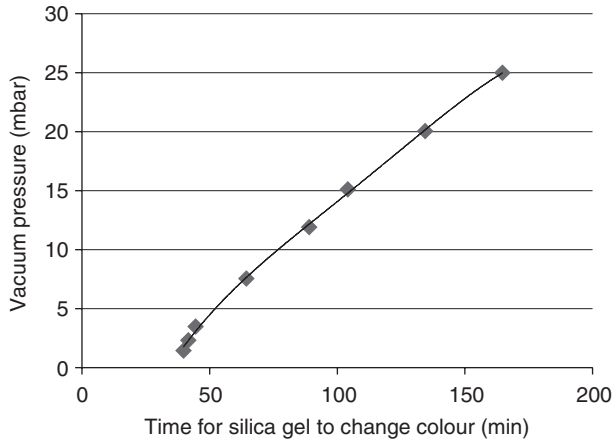

3.4 Time required for silica gel to turn blue on dry impermeable surface.

Table 3.3 Times for gel to turn blue (samples taken directly from curing)

Concrete grade (N/mm^2)	Curing (20 °C)	Time (h)	Pressure (mbar)
35	Air	1.5	8
60	Air	1.0	5
35	Water	6.0	3
60	Water	4.0	2

other mixes with the same initial moisture content). Typical times are given in Table 3.3. The air-cured samples are representative of site concrete, and the conditioning times of 30 and 90 min taken for 35 and 60 N/mm^2 mixes, respectively, are acceptable for site application.

3.5.5 Progressive change of ISAT values

The 10 min ISAT results were plotted in Fig. 3.5. It can be seen that the ISAT value was virtually stabilised prior to the colour change of the silica gel.

3.5.6 Comparison with BS 1881 methods

The two preconditioning methods described in BS1881-208 (BSI, 1996) for laboratory use are drying for two days in air and drying in an oven at 105 °C to constant weight. For site use, the test may only be carried out after a

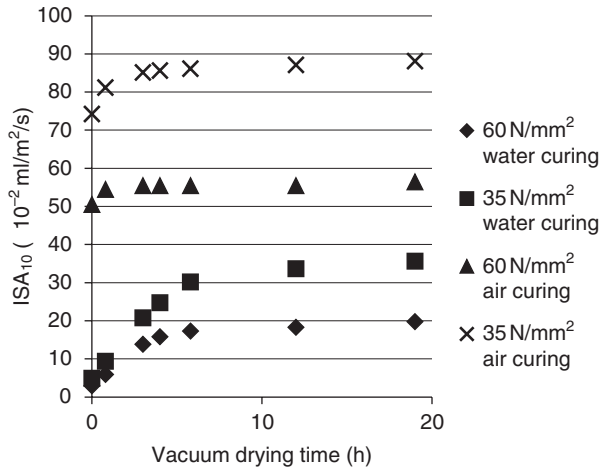

3.5 ISAT values after different drying times.

period of at least 48 h during which no water has fallen onto the test surface. The criterion for a preconditioning method to be effective is that it should give similar ISAT results on similar samples, regardless of the initial moisture content. The experimental design to test this was therefore based on sets of samples which had been cured in an identical manner and then brought to different moisture contents. The effectiveness of the new preconditioning system in giving similar results from each set was then compared with the BS 1881 laboratory methods.

The statistical *F*-test is used to compare the variability in the set preconditioned by vacuum with that in the sets preconditioned in the oven or in the laboratory for 2 days. Because the means of the sets were not equal, the coefficient of variation was used to calculate the variance ratio (*F*-ratio) (Kennedy and Neville, 1986). The two sided *F*-test was applied on the null hypothesis that the variation in results caused by the different moisture contents was the same for the different preconditioning methods. The critical value for the variance ratio is called the *F*-statistic. The *F*-statistic for 95 % confidence limits is 7.15 (both degrees of freedom being 5).

In addition, a fourth preconditioning treatment, in which a vacuum was applied for twice the time taken for the gel to turn blue, was used in order to see if further improvements could be obtained (this preconditioning is referred to as 'twice vacuum').

The following three methods were used to produce samples with a range of different moisture conditions:

1. vacuum-saturate for 2 h at 10–15 mbar (typical weight gain from dry curing 2 %);

Table 3.4 Comparison between different preconditioning methods

Concrete grade (N/mm^2)	Curing	Preconditioning	Mean ISA_{10} ($\times 10^{-2}$ $ml/m^2/s$)	*V* of ISA_{10} (%)	*F*-statistic
35	Air	Vacuum dry	80.7	8.4	1.0
		2 day air	69.9	40.4	22.9
		Oven dry	122.8	6.7	1.6
		Twice vacuum	86.3	8.4	1.0
35	Water	Vacuum dry	31.3	16.2	1.0
		2 day air	17.9	65.7	16.6
		Oven dry	53.0	6.9	5.5
		Twice vacuum	34.6	16.0	1.0
60	Air	Vacuum dry	44.9	15.2	1.0
		2 day air	24.5	54.9	13.0
		Oven dry	65.1	7.7	3.9
		Twice vacuum	46.3	15.0	1.0
60	Water	Vacuum dry	21.5	23.0	1.0
		2 day air	14.0	66.2	8.3
		Oven dry	48.7	10.9	4.5
		Twice vacuum	28.1	22.9	1.0

2. 6 h in water (typical weight gain from dry curing 1 %);
3. dry in laboratory air for 28 days.

For each of the two mixes, two curing conditions, three different moisture contents and four preconditioning methods, two samples were tested, giving a total of 96 samples. The results are given in Table 3.4.

The coefficient of variation (*V* = the standard deviation divided by the mean) has been calculated from the ISA_{10} results from two samples from each moisture condition, i.e. a total of six samples in each case. For each of the four mix/curing combinations, it is therefore indicated that the coefficient of variation of the vacuum-dried samples is significantly less than for the 2-day room-dried samples, i.e. the null hypothesis that all the data is from the same population is rejected. For all other cases, the null hypothesis is accepted (i.e. there is no significant statistical difference), although it may be seen that the coefficient of variation is lowest for the oven-dried samples in each set, indicating that this is the best way of overcoming the effect of the three different moisture conditions.

In Fig. 3.6, the standard deviations are shown as error bars. It may be seen that the standard deviations of the oven-dried sets of samples are no larger than those for the vacuum-dried samples. This results in coefficients of variation being lower for oven drying because the means are higher, possibly due to micro-cracking caused by the heating.

3.5.7 Discussion

As expected, oven drying gives highest ISAT values and lowest coefficients of variation. It can be argued that oven drying is the most efficient method, since it gives consistent results regardless of the moisture history of concrete. Unfortunately, this method cannot be used *in situ*. It is interesting to note from Fig. 3.6, by comparing the bars for the same drying conditions from the different groups, that the vacuum drying results are the only ones in which the four different mix/curing combinations chosen for this study have been fully resolved, in that the error bars do not overlap. The graph indicates that the results from this preconditioning are better than the others at distinguishing between the different concrete 'qualities' and would thus be of greater practical use. Preconditioning by air drying is the only method currently used for *in situ* ISAT testing and the results show that changing to vacuum drying would give a significant improvement in the reproducibility of the results. The presence of moisture is normally beneficial to concrete, and absorption should therefore be measured in naturally occurring conditions. This would give lower values of absorption, indicating higher durability for structures in moist conditions. The author suggests that drying prior to absorption testing is essential, since porous or cracked concrete would have a high moisture content. This would yield low absorption values (indicating high durability) if the concrete had not been dried before testing.

The 'twice vacuum' samples which were subjected to the vacuum for twice the time taken for the gel to turn blue were not significantly different

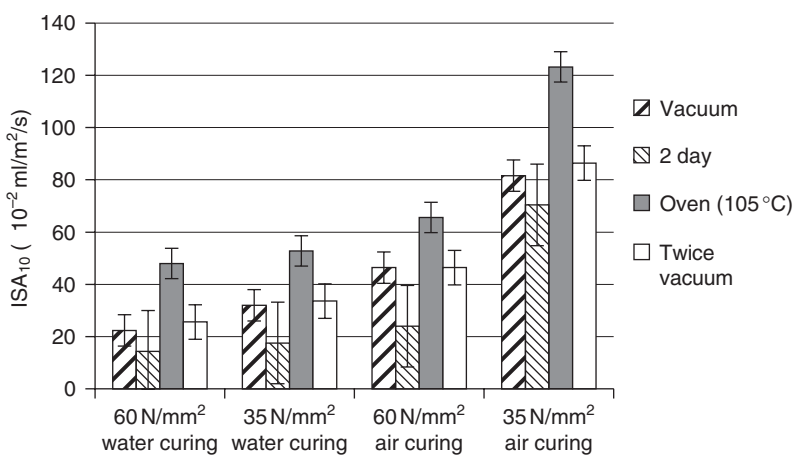

3.6 Standard error bars for ISAT results. (Author's note: When originally published (see paper 4 in Appendix 1) all of the error bars on this graph were of different lengths. This is statistically incorrect.).

from the 'vacuum dry' samples which were tested when the colour change occurred. This result indicates that minor increases in vacuum time will not have a significant effect on the results. This is important because the colour change is a gradual process which takes place over about 10 or 20 min, and observing an exact time for it is not possible.

The mean ISAT values were higher for the lower grade of concrete and less efficient curing, i.e. decreasing quality, as expected. Although the coefficient of variation remained significantly lower for the vacuum-dried samples relative to the 2-day dried samples, the difference decreased with increasing concrete quality. The 60 N/mm^2 water-cured samples, however, probably exceed the quality found on most existing structures. As the quality decreased towards more typical site concretes, the difference became more significant and the vacuum-dried results were comparable with the oven-dried ones.

3.5.8 Proposed test procedure

The testing procedure which was used in this project and is recommended for site is as follows:

1. modify the head of an ISAT apparatus by blocking one pipe connection and connecting the other to a vacuum pump (the ISAT head must be made from transparent material);
2. expose some silica gel to air until it turns pink;
3. place the ISAT head against the area of concrete to be tested with the silica gel inside it (note that clamping is not necessary);
4. start the pump and check that the pressure is 10 mbar or less;
5. run the vacuum pump until the majority of the gel turns blue;
6. carry out a normal ISAT test starting within 10 min of the release of the vacuum.

The components of the apparatus used for this work are shown in Fig. 3.7; they are very simple and robust and may readily be used on site. A single-stage mechanical vacuum pump (Edwards Speedivac) was connected to an ISAT cap with 12 mm PVC braided tube. A 0–25 mbar vacuum gauge was used (Capsule dial type, also supplied by Edwards).

3.6 Vacuum preconditioning for other tests

In Section 3.5 it was found that for the ISAT test a vacuum up to 10 mbar was suitable for drying in a reasonable time period, and 3 g of silica gel is sufficient as a drying indicator. Pilot trials were conducted in order to test the vacuum system prior to CAT and Figg. The vacuum technique was used for preconditioning test concrete (100 mm cubes) by drilling holes 13 mm

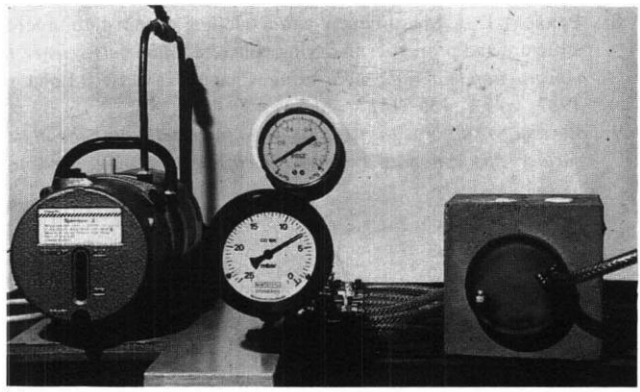

(a)

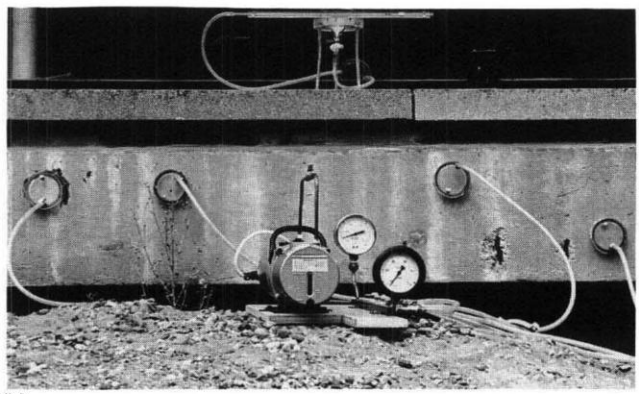

(b)

3.7 Improved *in situ* ISAT method: (a) vacuum apparatus; (b) application on site (note the additional high vacuum gauge).

diameter by 50 mm depth and subjecting the test specimens to different moisture conditions. The vacuum was applied as described in Section 3.5 and the preconditioned concrete specimens were tested using both CAT and Figg tests immediately after the silica gel colour turned blue. The results obtained from both CAT and Figg test were not reproducible (i.e. the vacuum preconditioning method failed to give similar results regardless of the moisture history of the test concrete).

Reproducibility was improved by applying the vacuum directly to the hypodermic needle prior to the Figg test (Fig. 3.8) and to the CAT cap prior to CAT. This is probably because of the concentration of vacuum on the immediate test area compared to the larger area under the ISAT cap and subsequent reduction of the leakage around the cap. Splitting cubes after preconditioning by vacuum showed that the drying front shape (see Fig.

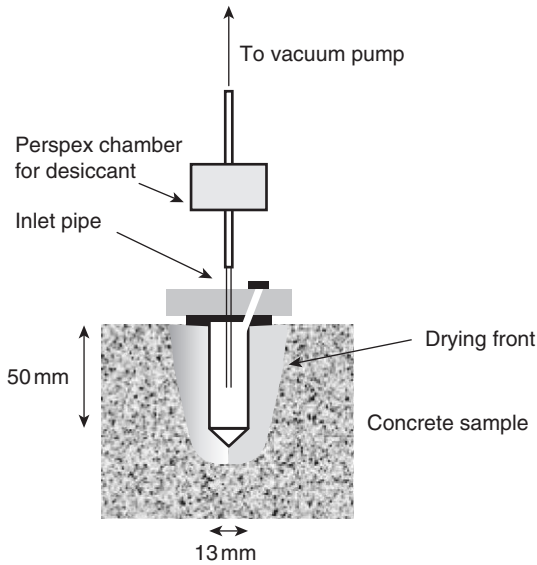

3.8 Schematic of vacuum drying front shape for CAT.

3.8) is similar to the wetting front shape obtained by applying the absorption test (discussed in Section 4.4). Therefore, preconditioning the test area using CAT cap or the hypodermic needle of the Figg test leads to a drying of the concrete volume which will be tested by the specific permeation test.

3.6.1 Further development of the test apparatus

A separate perspex silica gel chamber was developed for placing in the vacuum line in order to monitor the progress of drying since it was not possible to use the same arrangement as in the larger ISAT cap.

3.6.2 Experimental procedure

The mixes, curing and experimental design were the same as those used for the ISAT test except that the 'twice vacuum' condition was not used. For each grade, curing condition, moisture content and drying method, two samples were tested giving a total of 72 samples for each test (CAT and Figg).

3.6.3 Results and discussion

The results for Figg and CAT test are shown in Tables 3.5 and 3.6 and Figs 3.9 and 3.10. The coefficient of variation V% has been calculated from the

Table 3.5 Figg test results for different preconditioning methods

Concrete grade (N/mm^2)	Curing	Preconditioning	Mean index (s)	*V*% of index	*F*-statistic
35	Air	Vacuum dry	8	14.0	1.0
		2 day air	14	63.0	20.3
		Oven dry	7	12.0	1.4
35	Water	Vacuum dry	61	20.5	1.0
		2 day air	121	60.0	7.2
		Oven dry	38	8.0	6.6
60	Air	Vacuum dry	57	19.0	1.0
		2 day air	112	56.0	10.0
		Oven dry	30	8.4	5.1
60	Water	Vacuum dry	227	23.0	1.0
		2 day air	400	43.0	3.5
		Oven dry	150	9.5	5.9

Table 3.6 CAT results for different preconditioning methods

Concrete grade (N/mm^2)	Curing	Preconditioning	Mean $CAT_{10} \times 10^{-2}$ ml/m^2/s	*V*% of index	*F*-statistic
35	Air	Vacuum dry	121.4	19.5	1.0
		2 day air	106.5	59.5	9.3
		Oven dry	185.0	12.5	2.4
35	Water	Vacuum dry	58.3	15.0	1.0
		2 day air	38.0	51.0	11.6
		Oven dry	110.0	11.0	1.9
60	Air	Vacuum dry	63.5	12.0	1.0
		2 day air	41.5	39.0	10.6
		Oven dry	115.0	8.0	2.3
60	Water	Vacuum dry	16.0	10.0	1.0
		2 day air	14.0	24.0	5.8
		Oven dry	85.0	5.0	4.0

CAT_{10} and Figg permeation index results from each of the three moisture conditions, i.e. a total of six samples in each case.

The *F*-ratios are shown in Tables 3.5 and 3.6 for each of the four mix/curing combinations. It can be seen that the coefficients of variation of the vacuum dried samples were significantly less than those for the 2 day room-dried samples except for water-cured concrete (60 N/mm^2). Thus the null hypothesis that all the results are from the same population cannot be rejected for concrete of grade 60 (cured in water) but can for the other grades and curing conditions. The sensitivity of the tests to changes in concrete decreases with the increase of concrete grade.

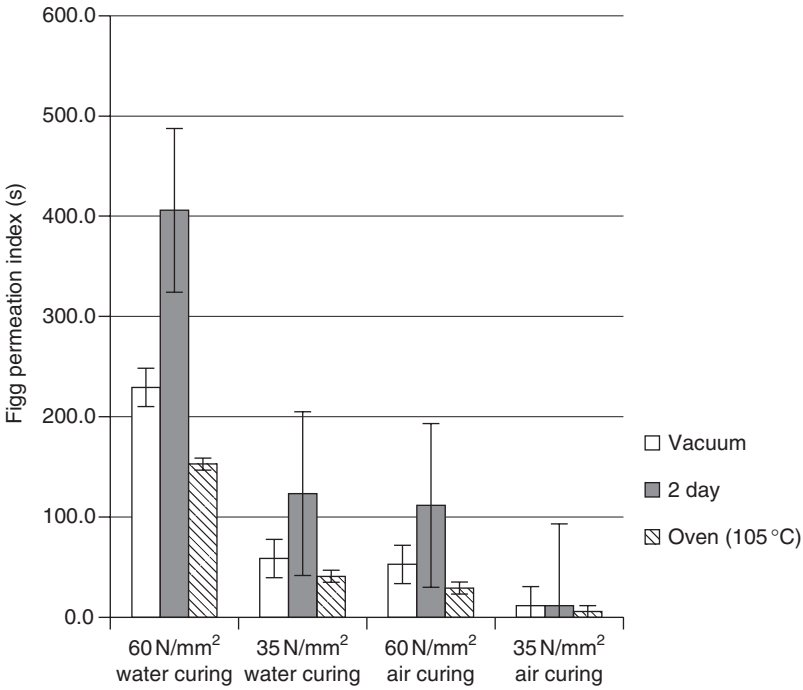

3.9 Effect of preconditioning method on Figg results.

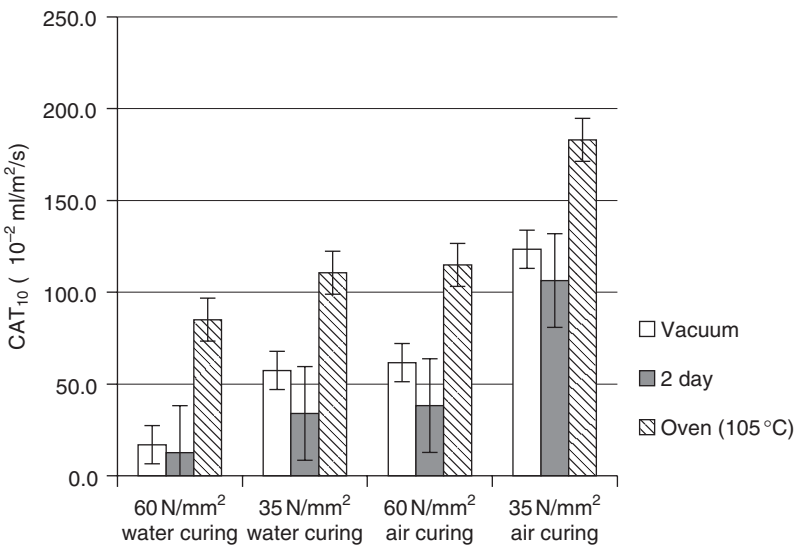

3.10 Effect of preconditioning method on CAT results.

Figures 3.9 and 3.10 show that the oven drying method produces highest CAT and lowest Figg values. The oven drying method gave lowest coefficients of variation for CAT. However, coefficients of variation for Figg values obtained after oven drying were comparable to those obtained after vacuum preconditioning. It is clear from Figs 3.9 and 3.10 that the error bars, representing the mean ± standard deviation, are overlapped for water-cured concrete (grade 35) and air-cured concrete (grade 60) regardless of the preconditioning method used, so they do not cast doubt on the new method. It is thus concluded that vacuum preconditioning should also be used with these tests.

3.7 Conclusions

- There are four generic types of surface permeability tests working with either water or vacuum either on the surface or drilled into it.
- All of these tests suffer from problems with application in environments where the concrete surface becomes damp. The vacuum drying system provides a good solution to these problems.

3.8 References

BSI (1996) *BS1881-208:1996 Testing concrete. Recommendations for the determination of the initial surface absorption of concrete*, British Standards Institute, London.

Figg J W (1973) Methods of measuring air and water permeability of concrete, *Magazine of Concrete Research*, **25** (85), pp. 213–219.

Kennedy J B and Neville A M (1986) *Basic Statistical Methods for Engineers and Scientists* (3rd edn), Harper & Row, New York.

Levitt M (1970) The ISAT – A non-destructive test for the durability of concrete, *British Journal of Non-destructive Testing*, **13**, pp. 106–112.

4

Surface tests to determine transport properties of concrete – II: analytical models to calculate permeability

DOI: 10.1533/9781782423195.43

Abstract: This chapter presents theoretical models for the four tests described in Chapter 3. These are analytical models which use integrated forms of the equations presented in Chapter 1. Two additional tests are described to be used to assess the accuracy of the models; these are a sorptivity test and a high pressure permeability test. The models are used to calculate the sensitivity of the different tests to changes in concrete properties. For practical use the results indicate that the water tests give better results than the gas tests. No clear advantage of either drilled hole or surface tests was observed.

Key words: initial surface absorption test (ISAT), Figg test, analytical models, sorptivity test, high pressure permeability test.

4.1 Introduction

The modelling of all four tests is based on the Darcy equation for pressure-driven flow (equation 1.1). For the vacuum decay tests the applied pressure is atmospheric and for the water absorption tests it is capillary suction.

4.2 Additional tests

For comparison with the surface tests two additional tests were used: sorptivity and a high pressure test.

4.2.1 The sorptivity test

This test is shown in Fig. 4.1. The water rises into the concrete sample with capillary suction and the increase of mass is plotted against time. Measurements were carried out using specimens (50ϕ × 150 mm) which were oven dried and then rested on rods in water containers to allow free access of water to the inflow surface (see Fig. 4.1). The water level was maintained to remain at no more than about 5 mm above the base of the specimens. The lower areas on the sides of the specimens were coated with

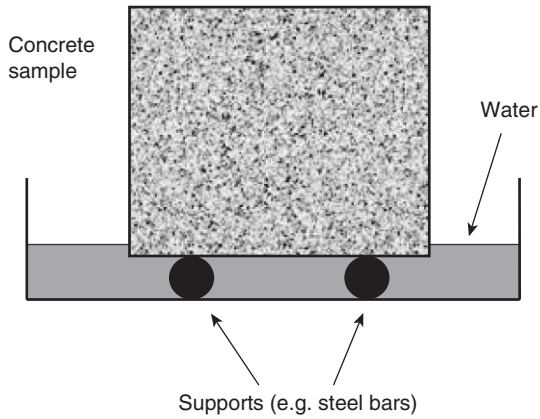

4.1 Schematic diagram of sorptivity test.

grease to achieve unidirectional flow. The cumulative water absorbed was recorded at different time intervals up to 2 h by weighing the specimens after removing the surface water using a dampened tissue.

The sorptivity is defined as the slope of the cumulative volume of water absorbed per unit area against the square root of time:

$$\frac{1}{A}\int F \, \mathrm{d}t = St^{1/2} \qquad [4.1]$$

where S is the sorptivity ($\mathrm{m\,s^{-0.5}}$).

4.2.2 The high pressure permeability apparatus

The permeability of the samples was measured with water using 54 mm or 100 mm diameter cylindrical sections approximately 30 mm long in modified 'Hoek' triaxial cells (Figs 4.2–4.4).

Pressures up to 10 MPa were used depending on the compressive strength of the particular specimen. These high pressures were chosen in order to give results in a practical timescale. Measurements of the effect of pressure on the results were made to relate them to the site application (see Chapter 9). The water pump was operated by a pressurised air supply.

To maintain the structural integrity of the sample, and prevent flow past its sides, a confining (triaxial) pressure was applied around an impermeable sleeve surrounding the sample. By maintaining the pore solution pressure below that of the confining pressure, the internal structure of the material was maintained. Note that with this apparatus, if the confining pressure is

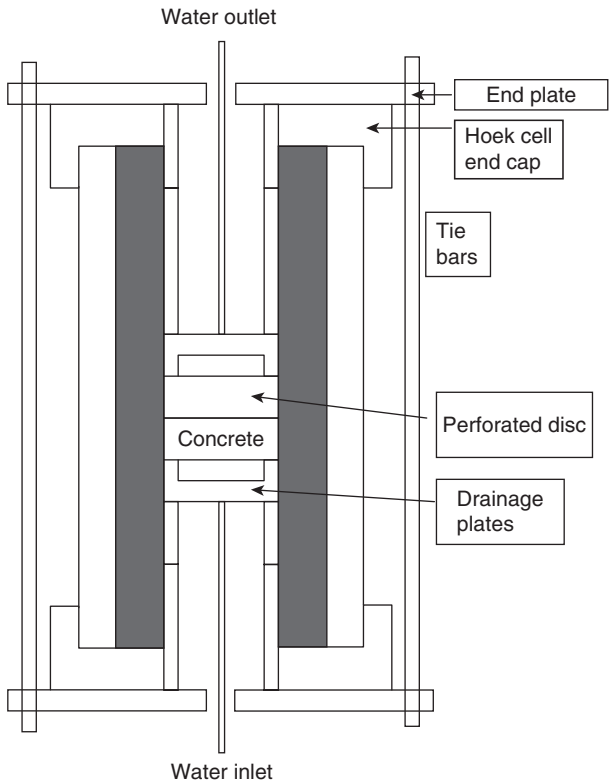

4.2 The high pressure test cell.

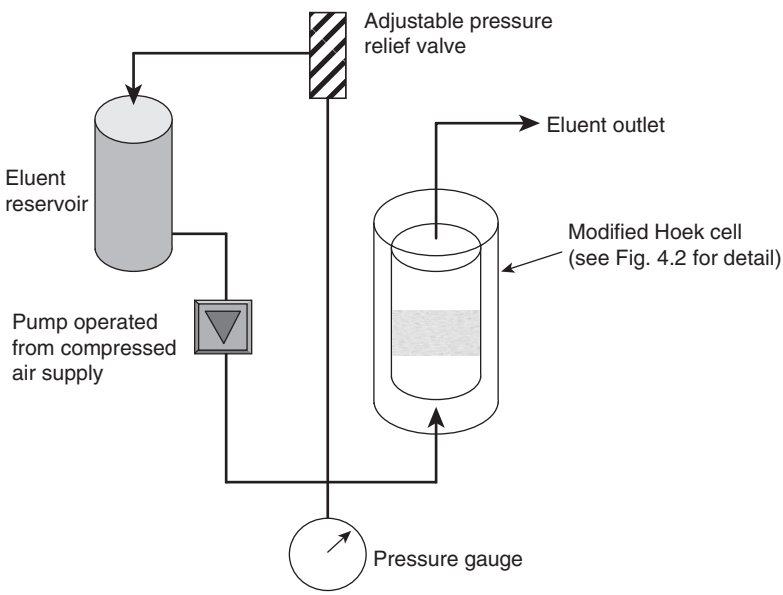

4.3 Schematic view of high pressure permeability apparatus.

4.4 High pressure apparatus at Coventry, showing one small cell (for 54 mm diameter samples) and one big cell (for 100 mm diameter samples) together with the frame for the second small cell, the liquid pump and pressure gauge.

released rapidly during a high pressure test the pressure in the pores will cause concrete samples to break up.

The modifications to the Hoek cells were designed to provide a fluid supply to, and drain from, the samples and to contain the axial load to permit use without an external compression frame. On the downstream (top) face of the sample, this load could have caused spalling from the surface due to the high pressure in the pores so it was carried through a thick perforated disc. A porous (sinter) disc was placed against the sample to permit free flow across the face. From the perforated disc the load was carried by the drainage plates and then through load-bearing spacers to a substantial (20 mm thick) end plate with tie bars around the circumference.

The pressure was controlled by adjusting a pressure relief valve which recirculated fluid back to the reservoir (Fig. 4.3). This method was chosen because the pump maintained a more constant pressure when some flow was permitted, and also because it ensured safe operation. All of the components and pipework were made with stainless steel to permit the use of corrosive leachates in the experiments as an alternative to water.

Water was collected to approximately equate to one sample size, then the time required to collect 10 ml of water was recorded to calculate the intrinsic permeability from equation (1.4) as follows:

$$K = \frac{V_F x e}{P} \qquad [4.2]$$

where:

K is the intrinsic permeability (m^2)
V_F is the velocity of Darcy flow (m/s), obtained as volume/(cross-sectional area × time)
x is the sample thickness (m)
P is the applied water pressure (Pa) and
e is the viscosity (Pa s).

4.3 Modelling of the absorption tests

There are numerous mechanisms which may contribute to the movement of water through concrete, including pressure-driven flow, capillary suction, osmosis, electro-osmosis and thermal migration. For simplicity, this model assumes that the flow is driven by capillary suction and controlled by permeability. The rate of capillary suction is initially high but decreases as the water filled volume of capillaries increases. Levitt (1970) derived equation (4.3) for the ISAT test (see Section 3.2) based on the mathematical formula from the Pouseille equation for a liquid travelling through a single capillary tube:

$$ISA = \frac{F_V}{A} = at^{-n} \qquad [4.3]$$

where:

ISA is the initial surface absorption ($m^3/m^2/s$)
t is the absorption time (s)
a, n are regression parameters
A is the area under cap (m^2) and
F_V is the flow rate (m^3/s).

Thus, integrating:

$$\int F_V dt = \frac{Aat^{(1-n)}}{1-n} \qquad m^3 \qquad [4.4]$$

4.3.1 The general model for water flow

The pressure head from capillary suction is given by equation (1.34). (The 200 mm head of water in the ISAT and CAT tests is assumed to be substantially less than P.)

In the model, it is assumed that, at any given time t after the start of the test, a volume V of the concrete is saturated with water and there is no water outside it. This assumption of a well-defined front to the water

penetration is in agreement with the observations on samples which had been broken open during the test. Thus:

$$F_V = \varepsilon \frac{dV}{dt} \quad [4.5]$$

where ε is the porosity.

The flow through the concrete to the penetration front will be limited by the permeability (equation 1.4).

4.3.2 Modelling the ISAT and absorption

For the absorption test and the ISAT, the flow may be considered as one-dimensional (i.e. the curved wetting front is assumed to be flat, see experimental observations in Fig. 4.4). The area is thus constant and from equations (1.34) and (1.9):

$$F_V = \frac{KA}{e}\frac{P}{X} = \frac{2sKA}{erX} \quad [4.6]$$

where:

X is the distance in m from the reservoir to the wetting front and
A is the constant area.

Also:

$$V = XA \quad [4.7]$$

Differentiating equation (4.6) with respect to t and combining it with equations (4.5) and (4.7) gives:

$$F_V = \beta \frac{d}{dt}\left(\frac{1}{F_V}\right) \quad [4.8]$$

where:

$$\beta = \frac{2Ks\varepsilon A^2}{re} \quad [4.9]$$

The solution to this is:

$$F_V = \left(\frac{\beta}{2}\right)^{1/2} t^{-1/2} \quad [4.10]$$

Substituting into equation (4.3):

$$a = \left(\frac{\beta}{2}\right)^{1/2} \frac{1}{A} = \left(\frac{Ks\varepsilon}{re}\right)^{1/2} \quad [4.11]$$

and $n = 1/2$.
Thus:

$$F_V = A\left(\frac{Ks\varepsilon}{re}\right)^{1/2} t^{-1/2} \quad [4.12]$$

The absorption ISA_{10} is F_V/A when $t = 600$ s.

4.3.3 Modelling the CAT test

For the CAT test (see Section 3.4.1) the area across which the water is flowing is approximately cylindrical (i.e. it is assumed that the observed section in Fig. 4.5 has parallel sides). If the wetting front is a distance x from the centre of the drilled hole and the depth of the hole is L the area will be:

$$A = 2\pi xL \quad [4.13]$$

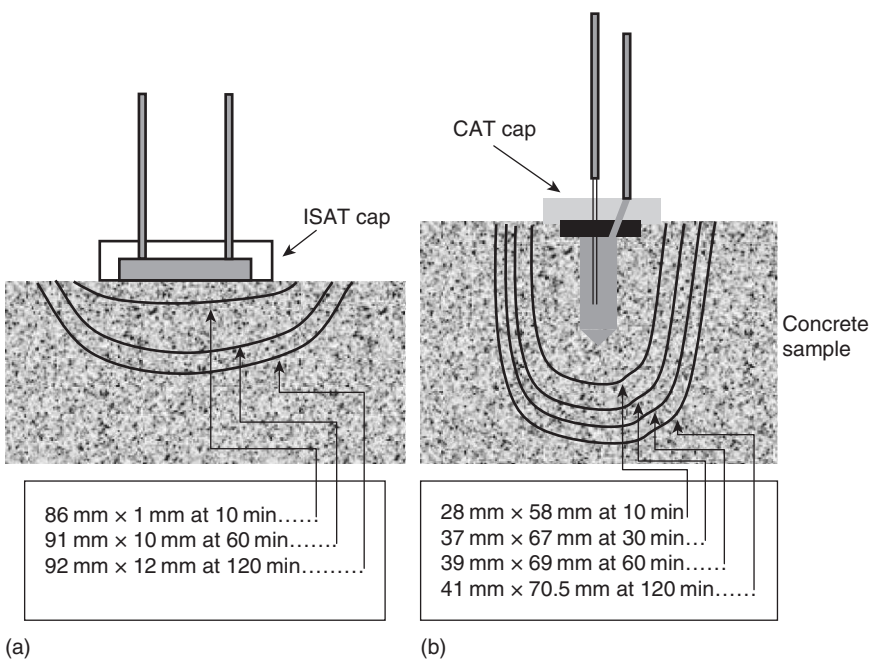

4.5 Typical wetting front profiles during ISAT (a) and CAT (b) runs for grade 35 water-cured concrete.

Substituting into equation (1.9) and integrating with respect to x:

$$\mathrm{Log}(x) - \mathrm{Log}(x_0) = \frac{2\pi LKP}{F_V e} \quad [4.14]$$

where:

x_0 is the radius of the drilled hole.

Combining with equation (1.34) and differentiating with respect to time:

$$\frac{\mathrm{d}(x^2)}{\mathrm{d}t} = x_0^2 \frac{\mathrm{d}}{\mathrm{d}t} \mathrm{e}^{\delta/F_V} \quad [4.15]$$

where:

$$\delta = \frac{8\pi LKs}{re} \quad [4.16]$$

The volume of concrete inside the wetting front will be:

$$V = \pi x^2 L - V_0 \quad [4.17]$$

where V_0 is the volume of the drilled hole.

Combining with equations (4.5) and (4.15) this gives:

$$F_V = \frac{\mathrm{d}}{\mathrm{d}t} \gamma \mathrm{e}^{\delta/F_V} \quad [4.18]$$

where:

$$\gamma = \varepsilon \pi L x_0^2 \quad [4.19]$$

The solution to this is:

$$t = \frac{\gamma}{\delta} \mathrm{e}^{\delta/F_V} \left(\frac{\delta}{F_V} - 1 \right) + \frac{\gamma}{\delta} \quad [4.20]$$

For an approximate solution, the exponential may be expanded as the initial terms of a power series:

$$\mathrm{e}^{\delta/F} \approx 1 + \frac{\delta}{F_V} + \frac{\delta^2}{2F_V^2} \quad [4.21]$$

Substituting and rearranging gives:

$$t = \frac{\gamma\delta}{2F_V^2} + \frac{\gamma\delta^2}{2F_V^3} \quad [4.22]$$

During the initial part of a test when t is small δ/F will be ≈ 0 and the last term may be omitted. This solution may be seen to be the same as the

one-dimensional solution in equation (4.10) with an area of $2\pi x_0 L$ (the area of the curved surface of the drilled hole).

4.4 Experimental testing for absorption

4.4.1 Preparation of test samples

To provide experimental confirmation of this analysis two concrete types, namely, Portland cement control (PC) and low water concrete (LWC), both of grade 35, were tested (Table 4.1). The test specimens (dimensions are detailed in each test procedure) were cast and kept under wet hessian for 1 day before demoulding. Two curing conditions were used: water curing at 20 °C (CC1) and air curing at 20 °C, 55 % RH (CC2), until testing at 28 days. The tests were carried out on duplicate specimens.

4.4.2 Test procedures

- Measurements of ISAT were carried out using samples (100 mm cubes) preconditioned in the oven at 105 °C until constant weight. To simulate a unidirectional flow, ISAT specimens were 100 mm cubes and the surface portion, not under the ISAT cap, was coated with grease. The initial surface absorption (ISA) was recorded at 10, 30, 60 and 120 min.
- CAT results were obtained in the same way as ISAT using 100 mm cubes conditioned in the oven exactly as for the ISAT samples.
- Measurements of water sorptivity were carried out as described in Section 4.2.1 on samples which had also been oven dried in the same way as the ISAT samples.
- A series of tests were carried out on concrete cubes in order to assess the shape of the wetting front after ISAT and CAT applications. This was done by splitting the test specimens at different intervals of time

Table 4.1 Concrete mix proportions for grade 35 concretes

Concrete type	Constituent materials (kg/m^3)					w/c	Admixture – Superplasticiser (% by weight of cement)
	PC	Water	Aggregates				
			20 mm	10 mm	Sand		
PC	290	190	800	400	715	0.66	–
LWC	240	160	840	410	745	0.66	2.6

(e.g. 10, 30, 60 and 120 min) to observe the depth and width of water penetration.
- The permeability was measured at high pressure as described in Section 4.2.

4.4.3 Experimental results

The relationships between ISA, CAT and time followed equation (4.3) with a high correlation coefficient ($r = 0.99$). In order to compare the results from the different experiments, it was necessary to express the absorption results in differential form. If the flow rate is assumed to be of the same form as equation (4.3), this may be integrated to give the measured weight gain (equation 4.4).

The absorption results showed a high correlation with this equation and results for a and n were obtained. The results for a and n from each of the three tests are given in Table 4.2. It may be seen that there is excellent agreement between the absorption results and the ISAT results and higher flow rates for the CAT.

The type and curing of concrete has a significant influence on the depth of water penetration. Typical wetting front shapes for ISAT and CAT applications for water-cured concrete of grade 35 are shown in Fig. 4.5. It may be seen that the wetting front shape is parabolic with a wide base on the concrete surface. This is attributed to the fact that the skin layer is more porous (due to bleeding channels, entrapped air, aggregate settlement, etc.). The wetting front for the ISAT is assumed to be flat in the analysis and for the CAT it is assumed to be cylindrical, but these are shown by the results to be quite good approximations.

4.4.4 Results for the model

The solutions given in equations (4.12) and (4.20) have been compared with the experimental results in Table 4.2 plotted from equation (4.3). The results

Table 4.2 Experimental results

Mix	Curing	ISAT		Sorption		CAT		Permeability
		$a \times 10^{-6}$	n	$a \times 10^{-6}$	n	$a \times 10^{-6}$	n	($m^2 \times 10^{-17}$)
PC	CC1	6.11	0.38	6.98	0.40	4.64	0.22	2.7
PC	CC2	13.95	0.40	14.26	0.40	8.53	0.24	33
LWC	CC1	5.40	0.39	4.83	0.38	4.43	0.24	0.4
LWC	CC2	9.28	0.40	7.96	0.38	6.79	0.27	2.0

are in Figs 4.6–4.9 which show flow per unit area plotted against time. For the CAT results, this area is the area of the curved surface of the drilled hole. These figures were obtained with the following fixed parameters:

- At 20 °C the viscosity of water $e = 10^{-3}$ Pa s and
- the surface tension of water $s = 0.073$ N/m.
- The area under the ISAT cap $A = 5.8 \times 10^{-3}$ m.
- The depth of the drilled hole for CAT, $L = 0.05$ m and the radius, x_0 was 6.5×10^{-3} m.

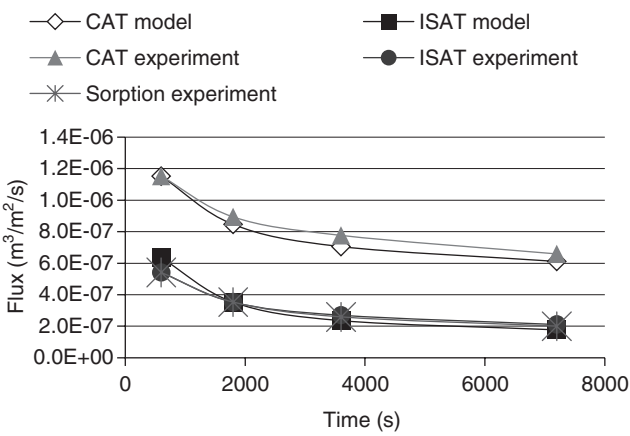

4.6 Water flow for PC mix with CC1 (water curing). The traces for the ISAT and sorption experiments are coincident.

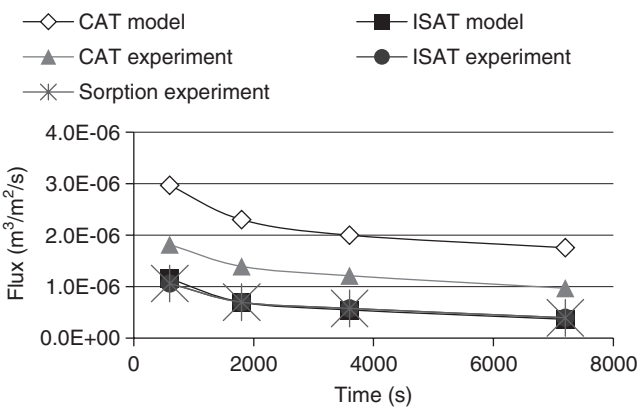

4.7 Water flow for PC mix with CC2 (air curing). The traces for the ISAT model, the ISAT experiment and the sorption experiment are coincident.

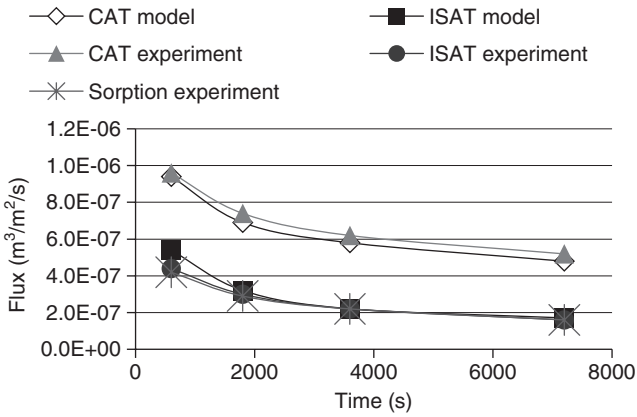

4.8 Water flow for LWC mix with CC1 (water curing). The traces for the ISAT and sorption experiments are coincident.

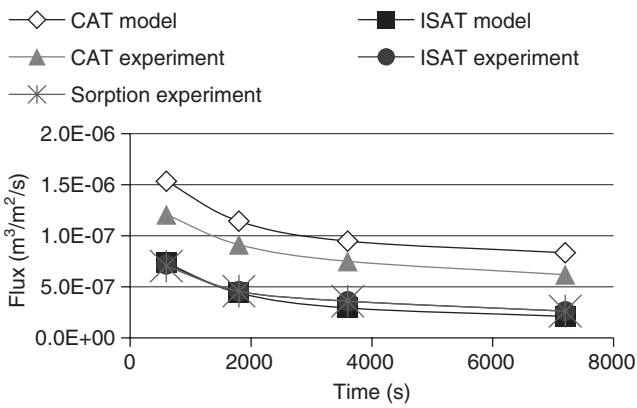

4.9 Water flow for LWC mix with CC2 (air curing). The traces for the ISAT and sorption experiments are coincident.

The other variables are the pore radius and the porosity. The values used for these are given in Table 4.3. The flow rate depends on the ratio of the two and neither was measured so a constant porosity of 7 % has been assumed which is typical for concrete. The different values for pore radius were set to give agreement with the model for the ISAT test. The pore radii obtained in this way are at the upper end of the range of pore sizes found in concrete. This is consistent with the assumptions of the model because, if the radius of a pore varies along its length, the capillary suction pressure to draw water along it will correspond to the largest radius. It may be seen that the model gives a lower pore radius for the LWC and for the better curing condition (CC1).

Table 4.3 Parameters for the model

Mix	Curing	Porosity ε	Pore radius r
		(%)	(μm)
PC	CC1	7	0.6
PC	CC2	7	2
LWC	CC1	7	0.12
LWC	CC2	7	0.3

It may be seen that the model gives a far more accurate prediction of the difference between ISAT and CAT for the water-cured samples. The reason for this is not known, but it is unlikely that different fundamental processes are responsible because all of the samples were dried before testing.

4.5 Tests using a vacuum to measure air flow

4.5.1 Approximations

The main approximations used for modelling the tests are an assumption of steady state for the gas flow and simplifications of the geometry. The steady state assumption is that, at any time, the mass of gas flowing into the section of the sample which is being tested is equal to the amount of gas flowing out of it. This is justified on the basis that the rate of change of pressure is relatively slow (the duration of the test is measured in minutes) and the volume through which the gas is flowing is relatively small. This assumption has been used extensively in the literature (e.g. Bamforth, 1987). The geometrical assumptions are that the flow to the surface tests is one-dimensional (towards the surface) and the flow to the drilled hole tests is radial towards the hole. These assumptions have been made in the context of the use to which the models have been put (evaluating sensitivity to concrete properties).

4.5.2 General model for the vacuum tests

In these tests, the permeating fluid is compressible and the observed flux F_V in m^3/s will therefore change with pressure. The flow is therefore best expressed as molecular flow where J is the total flux in $mol/m^2/s$ and dn/dt is the flow rate of the gas (mol/s). Both J and dn/dt are approximately constant across the sample (assuming a steady state within it). Thus the flow dn/dt is given by equation (1.11).

The change of pressure in the vacuum chamber will be given by

$$\frac{dP}{dt} = \frac{dn}{dt}\frac{RT}{V} \quad [4.23]$$

where:

V is the evacuated volume and
P is the pressure in it.

In order to apply these equations, it is now assumed that the gas is flowing into the vacuum from a region a distance X metres away where there is a large reservoir of gas at atmospheric pressure. Tests to measure X are presented in Chapter 5.

4.5.3 The APNS test

In this test (see Section 3.4.2), the flow is approximately one-dimensional out of the concrete towards the vacuum. The area A is therefore approximately constant. Integrating equation (1.9) across the sample gives:

$$\frac{dn}{dt} = \frac{KA(P_{atm}^2 - P^2)}{2XeRT} \quad [4.24]$$

Combining this with equation (4.23) gives:

$$V\frac{dP}{dt} = \frac{KA(P_{atm}^2 - P^2)}{2Xe} \quad [4.25]$$

The integral of this expression gives:

$$\frac{(P + P_{atm})(P_i - P_{atm})}{(P - P_{atm})(P_i + P_{atm})} = \exp\left[\frac{KAP_{atm}t}{eXV}\right] \quad [4.26]$$

where:

P_i is the initial vacuum and
P_{atm} is atmospheric pressure.

The APNS index is the value of t when P reaches 90 kPa from an initial $P_i = 1$ kPa.

4.5.4 Modelling the Figg test

The Figg test (see Section 3.3) has an approximately cylindrical geometry. Thus:

$$A = 2\pi xL \quad [4.27]$$

and

$$V = \pi x_0^2 L \qquad [4.28]$$

where:

x is the radius at which the flow is being considered
L is the length of the evacuated volume in m and
x_0 is its radius.

Following through the integration as for the APNS test gives:

$$\frac{(P + P_{atm})(P_i - P_{atm})}{(P - P_{atm})(P_i + P_{atm})} = \exp\left[\frac{2KP_{atm}t}{ex_0^2 \ln(X/x_0)}\right] \qquad [4.29]$$

A further analysis of this is given in Chapter 5 in which the accuracy is improved by including a second integral of a spherical region at the base of the hole. The Figg permeation index is the value of t when P reaches 55 kPa from an initial $P_i = 45$ kPa.

4.6 The choice of test for practical applications

When deciding which surface test to use on a given structure (selecting from the four in Table 3.1), the most important consideration may be the existence of local knowledge or standards; this is not considered here. The damage to the structure caused by the tests is on a similar scale for all four tests since the two which do not involve drilling a hole result in an unsightly grease deposit on the surface which is difficult to remove. The amount of work involved in carrying out each of the tests is also similar. The following discussion therefore only considers the ability of the tests to determine the potential durability.

While all of the tests measure permeability, it may be seen that two measure this for gas and two for water. Bamforth (1987) has published a very comprehensive discussion of the effect of gas slippage and gives a graph to correct for it at different pressures. In Table 4.4 two different concretes, A and B, are considered with water permeabilities of 10^{-17} and 10^{-18} m^2. These permeabilities are typical for grade 35 and 60 concretes (Bamforth, 1987). The corresponding gas permeabilities, the calculated results for the four tests for each concrete using the equations derived in this chapter and the average measured coefficient of variation for the tests on the concretes reported in Chapter 3 (using vacuum drying) are also given in the table. The variation for the ISAT was obtained from the tests described in Section 3.5.

Table 4.4 Comparison of test methods

Material	Water permeability K (m^2)	$ISAT_{10}$ min reading ISA_{10} 10^{-2} ml/m^2/s	CAT_{10} min reading CAT_{10} 10^{-2} ml/m^2/s	Gas permeability at 0.5 atmospheres absolute K (m^2)	APNS permeation index (s)	Figg permeation index (s)
Concrete A	10^{-17}	37	59	2×10^{-16}	7300	120
Concrete B	10^{-18}	12	14	10^{-16}	14600	240
Ratio A/B		3.1	4.2		0.5	0.5
Average V% (vacuum-dried)		15.7	14.1		–	19.1

The values used for the calculations in Table 4.4 were:

R	gas constant	8.31 J/mol/K
T	temperature	293 K
e	viscosity of water	10^{-3} Pa s
s	surface tension of water	0.073 N/m
A	area under ISAT test cap	5.8×10^{-3} m^2
V	volume under ISAT test cap	2.9×10^{-5} m^3
L	depth of drilled hole	50 mm
x_0	radius of drilled hole	6.5 mm
P_{atm}	atmospheric pressure	100 kPa
P_i	initial vacuum	45 kPa for Figg test and 1 kPa for APNS test
P	final pressure	55 kPa for Figg test and 90 kPa for APNS test
α	porosity	7 %
r	radius of largest pores	0.6 μm (see Table 4.3)

The unknown constant is X, the distance over which the pressure drop occurs in the gas tests. If no value of X is used, K/X may be used as a measure of permeability rather than K. This approach cannot be used for the Figg test because the cylindrical geometry gives a logarithmic relationship in equation (4.26). For the present discussion, the value is not important and a realistic estimate of 10 mm has been used. An extensive investigation which used computer modelling to avoid the necessity to use a simplified 'permeation block' of finite thickness is presented in Chapter 6, and it is concluded that for low porosity concretes, such as those used in the work reported here, the effect of the approximation is not substantial. In Chapter 5 a new method is presented to measure the value of X directly.

Table 4.4 shows that the derived equations give realistic values for the different test results. The conclusion from the table is that the water

tests, in particular the CAT test, should give better distinction between different concrete qualities because of the higher proportional change in the measured value for a given change in concrete permeability. The coefficient of variation may also be seen to be lower for the water tests (data is not currently available for the APNS test). It must be observed, however, that the tests measure different properties in that the water tests measure capillary suction as well as permeability. If possible, a site test programme should therefore use both tests. These results do not indicate a very clear preference for either surface or drilled hole tests. It may be argued that the drilled hole tests will be less affected by surface effects or contamination, but the surface tests measure the ingress of fluids into a structure more realistically.

4.7 Conclusions

- Analytical solutions have been presented for the main surface permeability tests and these gave realistic values for permeability.
- It was found that a full solution to the vacuum tests was not possible because the distance over which the vacuum decays is not known. This problem is addressed in Chapter 5.
- An analysis of the different tests concluded that the water tests would give more consistent results.

4.8 References

Bamforth P B (1987) The relationship between permeability coefficients for concrete using liquid and gas, *Magazine of Concrete Research*, **39** (138), pp. 3–11.

Levitt M (1970) The ISAT – A non-destructive test for the durability of concrete, *British Journal of Non-destructive Testing*, **13**, pp. 106–112.

5

Surface tests to determine transport properties of concrete – III: measuring gas permeability

DOI: 10.1533/9781782423195.60

Abstract: It was noted in Chapter 4 that it was not possible to determine the permeability from the gas tests because the distance over which the pressure drop occurs is not known. The development of a new non-destructive test capable of measuring the air permeability of *in situ* concrete is described. The new method measures the movement of gas between different holes drilled into the concrete and gives results for the permeability of the concrete and the distance over which the pressure drop occurs and, from this, the effective volume of concrete that is being tested.

Key words: permeability, Figg test, coefficient of permeability, test volume.

5.1 Introduction

The new test is shown in Fig. 5.1. It is basically similar to a Figg test (see Section 3.3) but additional holes in the concrete at either side are used to monitor the pressure drop.

5.2 Theoretical analysis

The volume of concrete that is being tested is measured by the distance X at which the pressure returns to atmospheric. To calculate this, the steady state is considered in which a constant vacuum is applied to the centre hole. The gas is compressible so equation (1.11) is used.

Considering the radial flow into the curved surface of the drilled hole, the area $A = 2\pi xL$ where L is the length of the evacuated volume (m). Equation (1.11) therefore becomes:

$$\frac{1}{2\pi L}\int \frac{\mathrm{d}n}{\mathrm{d}t}\frac{\mathrm{d}x}{x} = \frac{K}{RTe}\int P\mathrm{d}P \qquad [5.1]$$

This flow passes through the region in which the side holes are located.

Integrating from $X \rightarrow x_1$ where X = the distance from the centre of the main hole to a point where the pressure is atmospheric (m) and

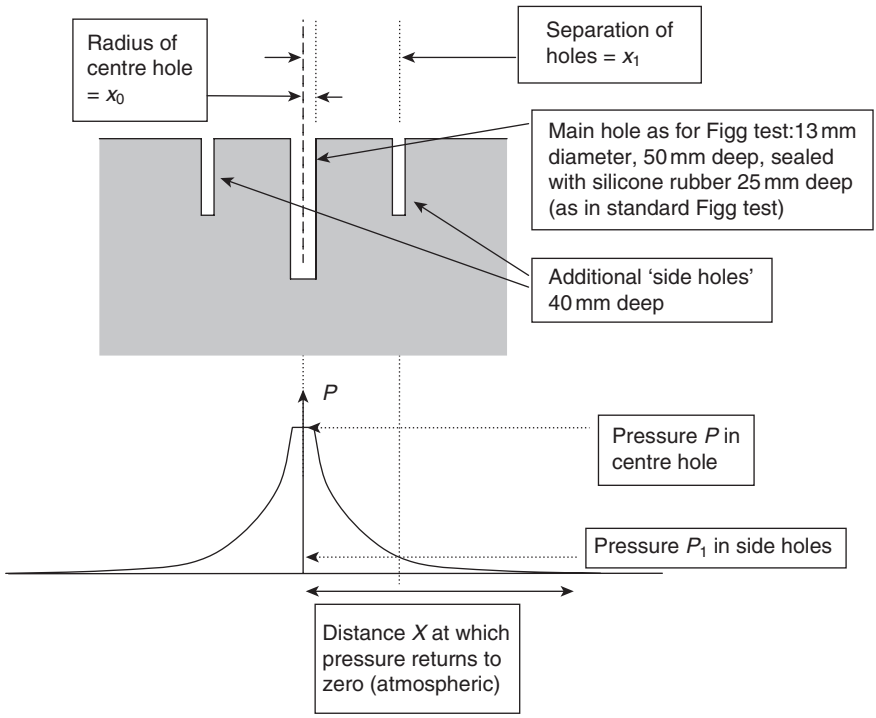

5.1 The three-hole test.

x_1 = the distance from the centre of the main hole to the centre of the side hole (m),

$$\frac{dn}{dt} \cdot \ln\left(\frac{X}{x_1}\right) = \frac{K}{RTe}\left(P_{atm}^2 - P_1^2\right) \qquad [5.2]$$

where:

P_{atm} is atmospheric pressure (Pa) and
P_1 is the pressure at the side hole (Pa).

Integrating from $x_1 \rightarrow x_0$ where x_0 = the radius of the main hole (m),

$$\frac{dn}{dt} \cdot \ln\left(\frac{x_1}{x_0}\right) = \frac{K}{RTe}\left(P_1^2 - P^2\right) \qquad [5.3]$$

where P is the pressure at the main hole (Pa).

Dividing equation (5.2) by equation (5.3) gives:

$$\frac{\ln(X/x_1)}{\ln(x_1/x_0)} = \frac{\left(P_{atm}^2 - P_1^2\right)}{\left(P_1^2 - P^2\right)} \qquad [5.4]$$

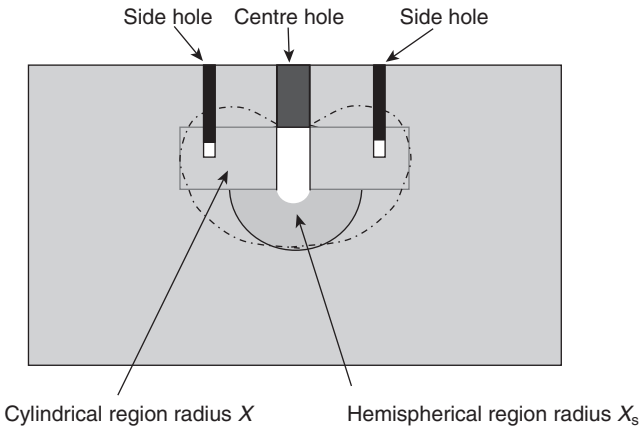

5.2 The developed model for the vacuum decay test. The solid lines show the pressure fronts used in the idealisation for the model. The dashed lines show possible location of the actual pressure front.

Equation (5.4) may be used to calculate X from experimental observations of P_1. The intrinsic permeability is obtained from an analysis of the decay transient when the Figg test is applied in the normal way using equation (4.29).

When analysing the transient, however, the total flow into the centre hole must be considered. The above analysis takes no account of the flow into the base of the drilled hole. To improve the approximation, a second region has been added to the model to include flow into the base of the hole as shown in Fig. 5.2. The drill bit used produced an approximately hemispherical inner surface to this region.

By including the hemispherical area and following through the integration equation (4.29) becomes:

$$\frac{(P+P_{\text{atm}})}{(P-P_{\text{atm}})}\frac{(P_{\text{i}}-P_{\text{atm}})}{(P_{\text{i}}+P_{\text{atm}})}=\exp\left\{\left[\frac{2KP_{\text{atm}}t}{ex_0^2}\right]\times\left[\frac{1}{\ln\left(\dfrac{X}{X_0}\right)}-\frac{1}{L\left(\dfrac{1}{X_{\text{s}}}-\dfrac{1}{x_0}\right)}\right]\right\} \quad [5.5]$$

where:

X_s is the radius of the hemispherical region below the base of the hole and L is the length of the evacuated volume.

In order to estimate X_s, the author suggests that it is best to assume that the flow rate per unit area at the boundaries of the two regions is the same. Equating the two flow rates and solving the equations gives:

$$-X\ln\left(\frac{X}{x_0}\right) = X_S - \frac{X_S^2}{x_0} \quad [5.6]$$

Equation (5.6) may be used to calculate values of X_s from measured values of X (from equation (5.4)) and these may then be used in equation (5.5) to calculate the permeability. Trial calculations using these equations have indicated that X_s is approximately $0.5X$ and approximately 30 % of the flow into the hole comes from the hemispherical region.

5.3 Investigation of methods for sealing the drilled holes

5.3.1 The different methods

The new test requires the measurement of pressure in the 'side holes'. These holes are different from the centre hole in that they are only used for measuring pressure (not applying it) and their diameter is as small as possible to prevent disturbance of the pressure decay. Tests were therefore carried out to see if the method of preparing the holes should be different from the normal method for the Figg test which was used on the centre hole. The four methods for preparing the holes are given in Table 5.1.

5.3.2 Mortar mixes

Mortar mixes were made by using a linear horizontal pan type mixer of 0.04 m^3 capacity. The mix design is shown in Table 5.2. All the samples were

Table 5.1 The methods for preparing the side hole

Method number	Method	Comments
1	6 mm plastic pipes cast in wet concrete. Metal rods inside the pipes to keep them clear.	Cannot be used on existing structures.
2	Hole drilled in set concrete and filled with epoxy. Plastic pipe inserted into wet epoxy. Hole drilled through to the concrete when the epoxy had set.	
3	Hole drilled in set concrete. Plastic pipe set into hole with liquid silicon rubber. Sponge to keep silicon out of pipe.	Difficult to inject the silicon to full depth.
4	Silicon rubber placed in hole to 25 mm depth. Hypodermic needle inserted through set silicon.	This is the standard Figg method. This method selected for the investigation.

Table 5.2 Mortar mix design

Constituent materials (kg/m^3)			
PC	Water	Sand	w/c
350	245	1400	0.7

cured in water at 20 °C for 7 days and then oven dried at 105 °C to constant weight and kept in the laboratory until tested.

5.3.3 Experimental procedure

Pressure measurements were made using piezoresistive pressure transducers and a data logger. The pressure transducers were of a type manufactured for use in intruder alarms in cars and were found to have a good linear response and to be easy to fit directly to the end of the hypodermic needle. The different methods were tested by applying a vacuum to the centre hole and then sealing it and letting the vacuum decay. 100 mm mortar cubes were used with a standard centre hole (13 mm diameter by 50 mm deep). The side holes were 6 mm diameter and 30 mm deep with a 5 mm deep void space. This diameter would be insufficient for measurement of flow rates because a significant proportion of the surface of the void could be obstructed by a single aggregate particle. These holes are, however, only used for observation of pressure, and the risk of the entire surface of the void being sealed by an uncracked aggregate particle is not seen as significant. A larger hole could cause significant disturbance to the air flow.

5.3.4 Selection of experimental method

The graph of pressure against time for each preparation technique is presented in Figs 5.3–5.6.

Comparison of the graphs of the four preparation techniques reveals that all the pressure decay curves for the different techniques were almost the same. This gives considerable confidence in all of the methods used and indicates that a selection may be made based on practical considerations.

Method 4 is ideal for use on site because method 1 cannot be used on site and method 2 is much more time-consuming than method 4. In method 3 it is difficult to inject the liquid silicon where the flexible tube limits the remaining space. This action also limits the diameter of the side hole in this technique. For these reasons, the selected technique is method 4, i.e. drill a hole, fill it with silicon and insert the hypodermic needle as in the Figg test.

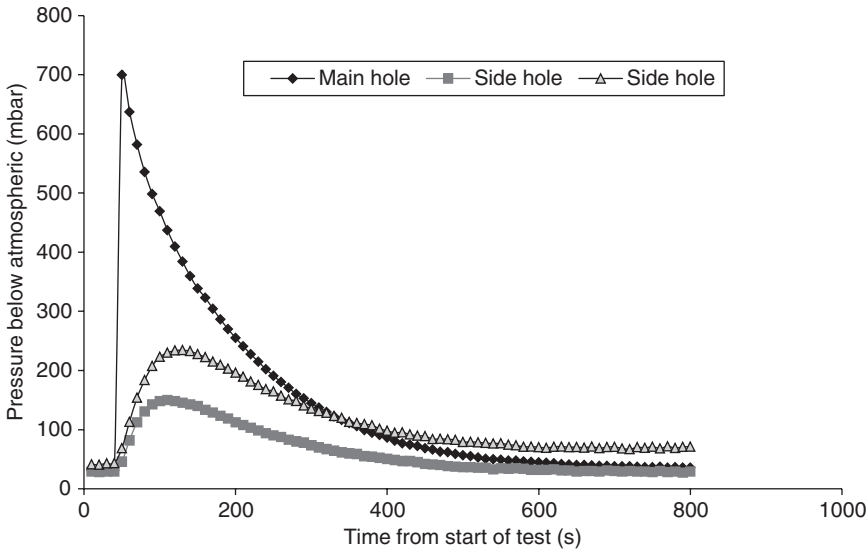

5.3 Pressure decay curves for method 1 (pipe cast into concrete).

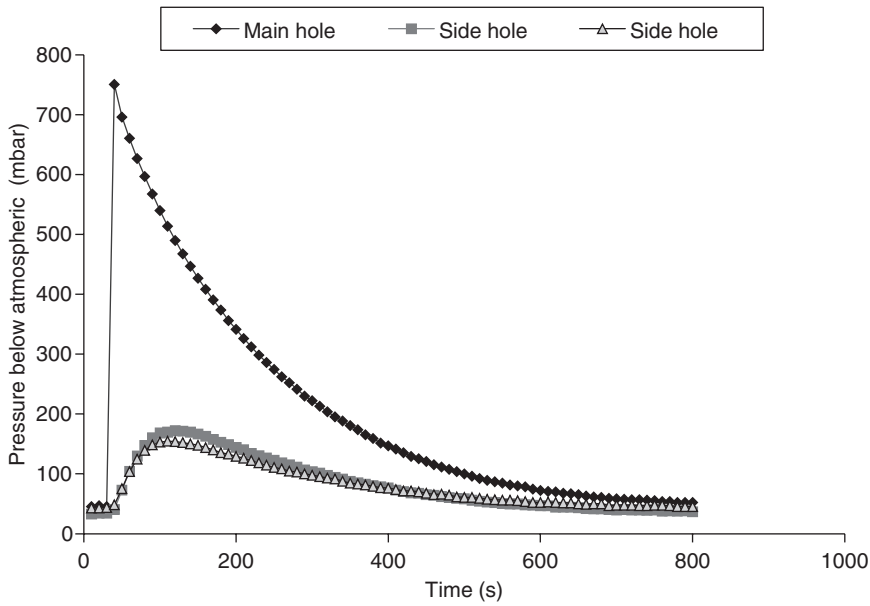

5.4 Pressure decay curves for method 2 (epoxy seal).

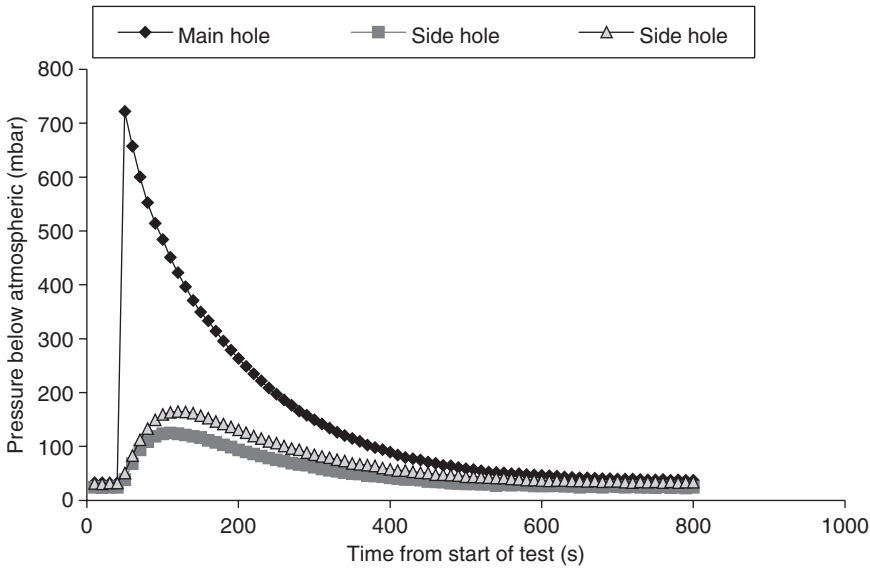

5.5 Pressure decay curves for method 3 (silicon rubber seal around pipe).

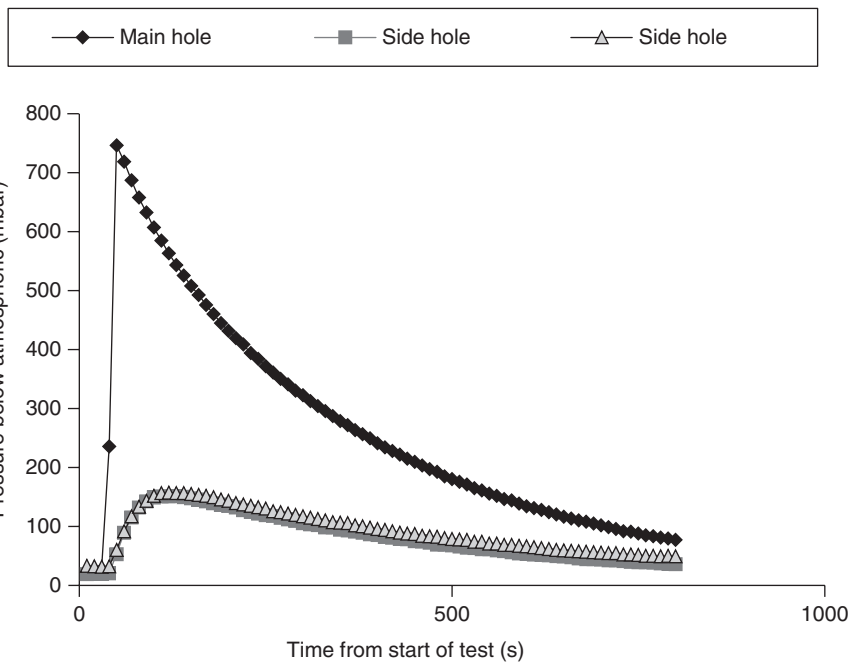

5.6 Pressure decay curves for method 4 (hypodermic through silicon rubber).

5.4 Determination of pressure decay profile

5.4.1 Experimental procedure

The distance X at which the pressure returns to atmospheric was determined by applying a constant pressure to the centre hole and measuring the pressure in the side hole. It was found that the piezoresistive pressure transducers could be conveniently assembled directly onto the hypodermic needles, thus minimising 'dead volume' which would have affected the readings. 4 mm diameter side holes were used. In order to minimise the effect of the 20 mm aggregate, these were drilled to 40 mm deep with a 20 mm deep void space. Before applying the vacuum, three pressure readings were taken at 10 s intervals in order to zero the pressure sensors.

5.4.2 Concrete mixes

Three different concrete mixes were designed and made as shown in Table 5.3. Three different specimen sizes (100 mm cube, 150 mm cube and 400 × 400 × 100 mm prism) were cast for each concrete mix. All the specimens were air cured at laboratory temperature for 28 days until tested.

5.4.3 Results

For each concrete mix, the pressure values were measured for all the three holes. A typical graph of vacuum pressure against time is shown in Fig. 5.7. The distance X was derived by substituting the value of the applied constant vacuum pressure and the resulting vacuum pressure in the side holes in equation (5.4).

The distance X for each concrete studied is shown in Table 5.4 and plotted in Figs 5.8–5.11 with regression lines to the data (where there are only two values of the dependent variable, this becomes a line through the average values of X).

Table 5.3 Concrete mix design

Mix number	Cement (kg/m^3)	Water (kg/m^3)	Coarse aggregate 20 mm (kg/m^3)	Sand (kg/m^3)	w/c
1	395	225	800	980	0.57
2	520	240	1050	590	0.46
3	410	250	1100	625	0.61

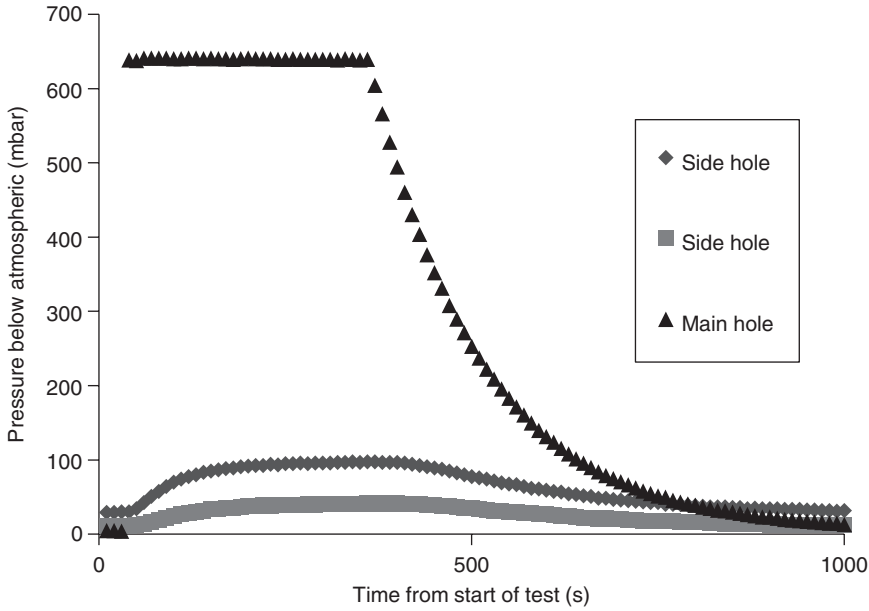

5.7 Pressure curves for a concrete specimen using the new method.

Table 5.4 Results for distance across permeation block obtained from the three-hole test

Mix no.	Sample size mm	x_1	P	P_1	X (mm)	P	P_1	X (mm)
1	100 × 100	30	742	57	38.7	633	56	38.9
	100 × 100	40	742	33	47.2	633	32	47.3
	150 × 150	30	770	117	54.6	656	110	53
	150 × 150	40	770	31	46.8	656	30	46.7
	400 × 400	30	755	158	73.9	640	149	70.9
	400 × 400	40	755	32	46.9	640	31	46.9
2	100 × 100	30	760	85	44.9	652	83	44.9
	100 × 100	40	760	31	46.7	652	30	46.7
	150 × 150	30	760	92	46.8	646	90	46.9
	150 × 150	40	760	53	52.9	646	52	52.9
	400 × 400	30	736	110	52.2	650	100	49.8
	400 × 400	40	736	81	62.9	650	55	53.9
3	100 × 100	30	749	129	59.2	636	120	57.2
	100 × 100	40	749	34	47.5	636	15	43.1
	150 × 150	30	745	127	58.4	633	116	55.6
	150 × 150	40	745	55	53.5	633	51	52.7
	400 × 400	30	756	104	50.2	640	98	49.3
	400 × 400	40	756	45	50.5	640	42	49.9

x_1 = separation of drilled holes (mm)
P = pressure at centre hole (mmHg)
P_1 = pressure at side hole (mmHg)
X = distance across permeation block (mm)

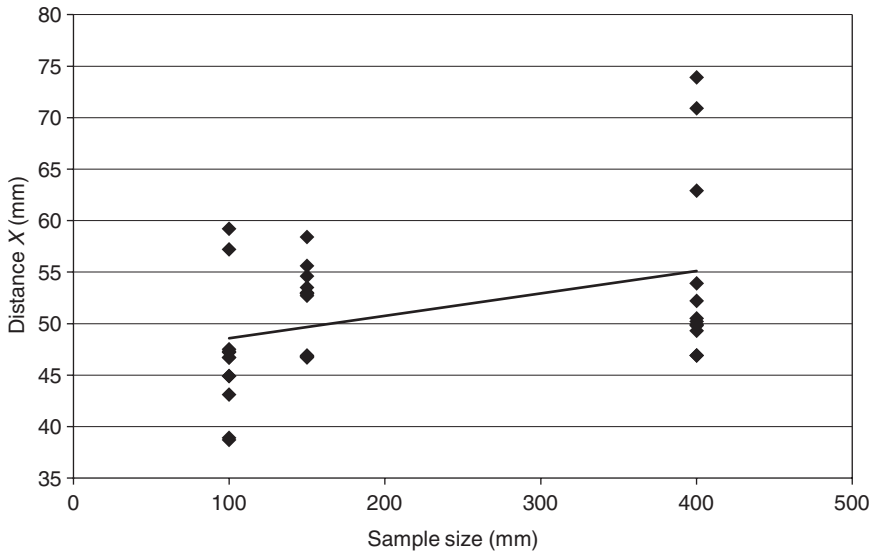

5.8 Effect of sample size on distance *X*.

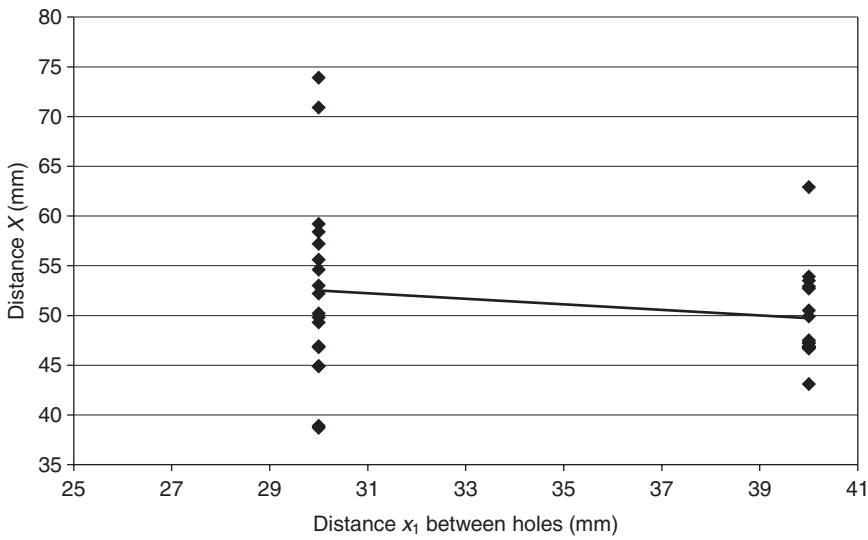

5.9 Effect of distance between holes on distance *X*.

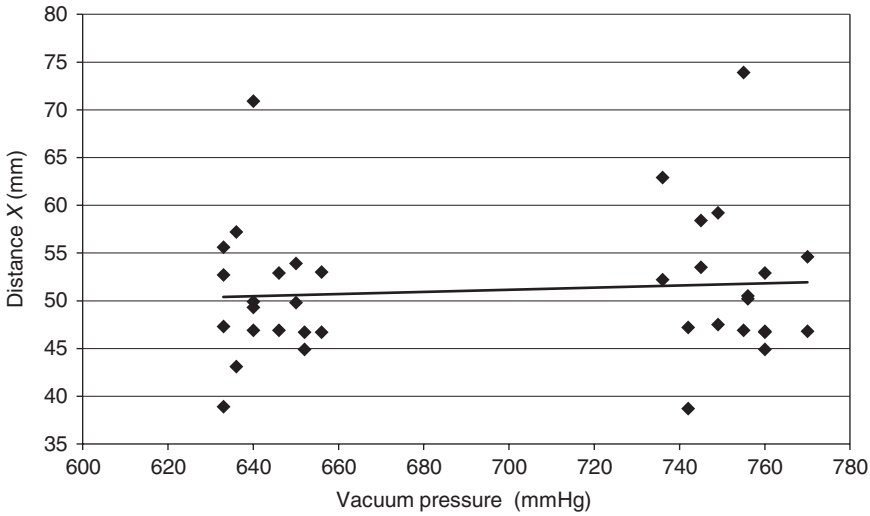

5.10 Effect of vacuum pressure on distance *X*.

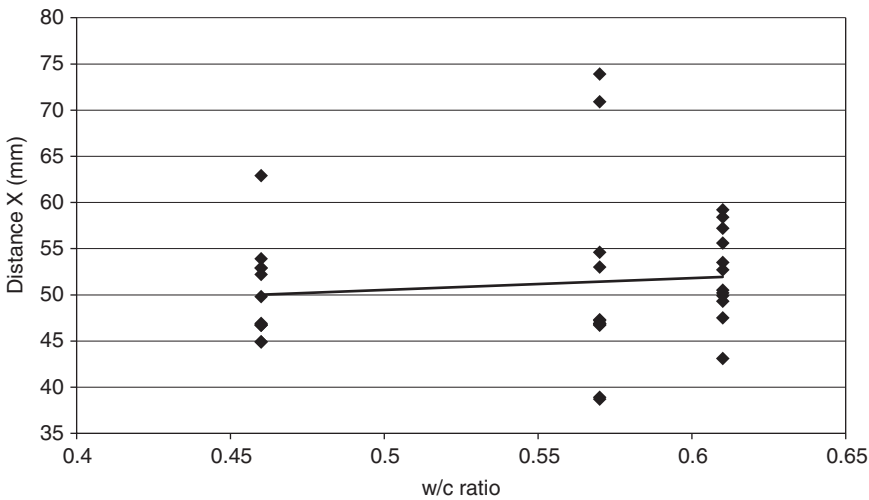

5.11 Effect of w/c ratio on distance *X*.

5.4.4 Discussion

It may be seen that this technique gives realistic values for the distance X. From Table 5.4 and Fig. 5.8, it may be seen that the distances lie within the specimen width, except a 100 mm cube specimen for mix number 3. The increase in specimen size shows a minor increase in X which was expected from the closeness of the radius X to the edge of the 100 mm cubes. The averages from the 150 mm and 400 mm samples are similar. The use of these larger samples gives confidence that the observed values of approximately 50 mm were not a product of edge effects. From Fig. 5.9 and 5.10, it may be seen that increasing the separation of the holes or the vacuum pressure only had a very minor effect on X, giving confidence in the modelling method. Figure 5.11 shows that there was very little change in X with water to cement (w/c) ratio. This does not indicate that the permeability did not change because a more permeable sample will have a higher rate of extraction of air from the side hole, but it will also have a higher rate of replenishment.

The following method is proposed for testing concrete:

1. Prepare for the Figg test using the standard method but with an additional hole 4 mm diameter, 40 mm deep at a distance of 30 mm from the centre hole.
2. Set up a data logger to take pressure readings in both holes at 10 s intervals.
3. Apply a constant vacuum to the centre hole until a stable pressure is recorded in the side hole and then seal the input and let the vacuum decay.
4. Calculate the distance X from equation (5.4) and then calculate the permeability by fitting equation (5.5) to the vacuum decay transient. This may be done by applying the equation at two different times and subtracting.

It may be seen that, in this study, the distance X was typically 50 mm. In order to calculate the permeability without drilling the second hole, this value might be used, but all of the samples tested in this study had low moisture contents and a higher moisture content could reduce X. If vacuum preconditioning (see Chapter 3) is used to standardise the moisture content, this would be unlikely to have any effect at less than 0.5 atmospheres of vacuum, i.e. more than approximately 20 mm radius.

This method has been applied to a range of different samples, and the permeability has been calculated. Figure 5.12 shows the results in which the permeability is plotted against the Figg permeability index which is obtained directly from the transient. These show that this new method demonstrates the great changes in permeability indicated by small changes in Figg index time at short times.

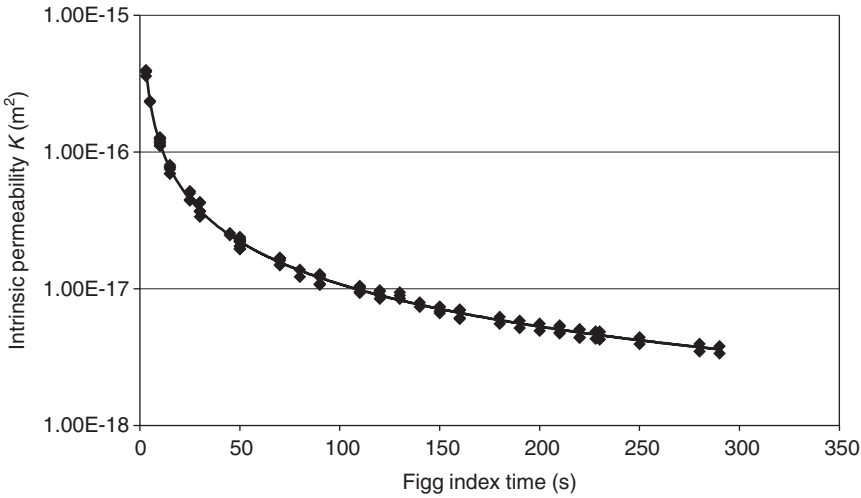

5.12 Relationship between permeability and Figg index.

5.5 Comparison of *in situ* test methods

5.5.1 Test methods

Having developed the necessary test methods and analysis in Chapters 3 and 4 and in preceding sections of this chapter, it is now possible to calculate the permeability from measurements of the initial surface absorption test (ISAT) and Figg test and compare them with direct measurements from the high pressure apparatus.

Vacuum preconditioning was used as described in Chapter 3 and the ISAT test was used with the analysis method described in Chapter 4 with the three-hole tests described in Section 5.1. The high pressure permeability apparatus described in Chapter 4 was also used.

5.5.2 Theoretical relationship between water permeability and gas permeability

The Klinkenberg equation (1.12) has a significant effect at low pressures. Values of b in the equation were calculated by Bamforth (1987) for concrete from the average values of water and gas permeability as follows:

$$b = 1.635 * 10^{-8} K_1^{-0.5227} \qquad [5.7]$$

Substituting the value of b in equation (5.7), a relationship between water permeability and gas permeability is derived. Bamforth reported that the

Table 5.5 Mix designs

Mix number	Cement (kg/m^3)	Water (kg/m^3)	Coarse aggregate 5–20 mm (kg/m^3)	Sand (kg/m^3)	w/c
1	400	230	810	990	0.58
2	400	190	810	990	0.47
3	400	230	–	1800	0.58

gas permeability values may be one or two orders of magnitude higher and the largest difference would occur when testing using a partial vacuum. It is therefore important to consider the effect of slippage when interpreting results obtained from gas measurement as a means of assessing concrete quality.

5.5.3 Experimental programme

Two different concrete mixes and one mortar were designed and made as shown in Table 5.5. The cement was Portland class 32.5R from Rugby Cement and the aggregates were quartzitic uncrushed from a quarry in Nottinghamshire, UK.

Mortar mixes were made by using a linear horizontal pan type mixer of 0.04 m^3 capacity. The concrete was mixed in the same mixer. The aggregates were first mixed with half the mixing water for 2 min and permitted to stand for 8 min. The cement and remaining water was then added and mixed for a further 3 min. Three different mould sizes, i.e. 100 mm cube, 150 mm cube and a prism of 400 × 400 × 100 mm, were cast for each mix.

Three curing regimes were followed:

1. air curing for 28 days in the laboratory at approximately 20 °C and 50 % relative humidity (RH);
2. water curing in tanks at 20 °C for 7 days then air cured to 28 days age;
3. 28 day water curing in tanks.

The programme of tests is shown in Table 5.6.

5.5.4 Results

Results from the three-hole gas test

For each sample, the pressure values were measured for all the three holes. A typical graph of vacuum pressure against distance is shown in Fig. 5.1. The distance X (the distance at which the applied vacuum pressure effect

Table 5.6 Programme for each test

	Three-hole test	ISAT	High pressure water test (see Section 4.2)
Air curing	3 × 100 mm cubes 3 × 150 mm cubes 2 × 400 mm prisms	2 × 100 mm cubes 2 × 150 mm cubes	2 × cores
7 day water curing	3 × 100 mm cubes 3 × 150 mm cubes	2 × 100 mm cubes 2 × 150 mm cubes	2 × cores
28 day water curing	3 × 100 mm cubes 3 × 150 mm cubes	2 × 100 mm cubes 2 × 150 mm cubes	2 × cores

reaches atmospheric from the main hole) was derived by substituting the values of the applied constant vacuum pressure and the resulting constant vacuum pressure into equation (5.4). Average values of the distance X for replicate samples are shown in Fig. 5.13.

The intrinsic permeability was obtained from equation (5.5) using the time Δt for the pressure in the centre hole to rise from 45 kPa to 55 kPa. By applying the equation at both pressures and subtracting, equation (5.8) was obtained:

$$K = \frac{e x_0^2}{2 P_{\text{atm}} \Delta t \left(\dfrac{1}{\ln\left(\dfrac{X}{x_0}\right)} - \dfrac{1}{L\left(\dfrac{1}{X_S} - \dfrac{1}{x_0}\right)} \right)} \ln\left(\frac{\left(55 \times 10^3 + P_{\text{atm}}\right)\left(45 \times 10^3 - P_{\text{atm}}\right)}{\left(55 \times 10^3 - P_{\text{atm}}\right)\left(45 \times 10^3 + P_{\text{atm}}\right)} \right) \quad [5.8]$$

The value used for the viscosity of air e was 1.8×10^{-5} Pa s. The resulting values for the permeability K are shown in Fig. 5.14.

Results from initial surface absorption test

The initial analysis of the results was carried out by assuming a relationship of the form of equation (4.3):

$$F_v = a t^{-n} \quad [5.9]$$

where a and n are constants. From equation (4.12) it may be seen that:

$$a = A \left(\frac{K s \alpha}{r e} \right)^{0.5} \quad [5.10]$$

The constant a was obtained from the intercept of the relationship of the logarithm of the flow rate against the logarithm of time, and the permeability

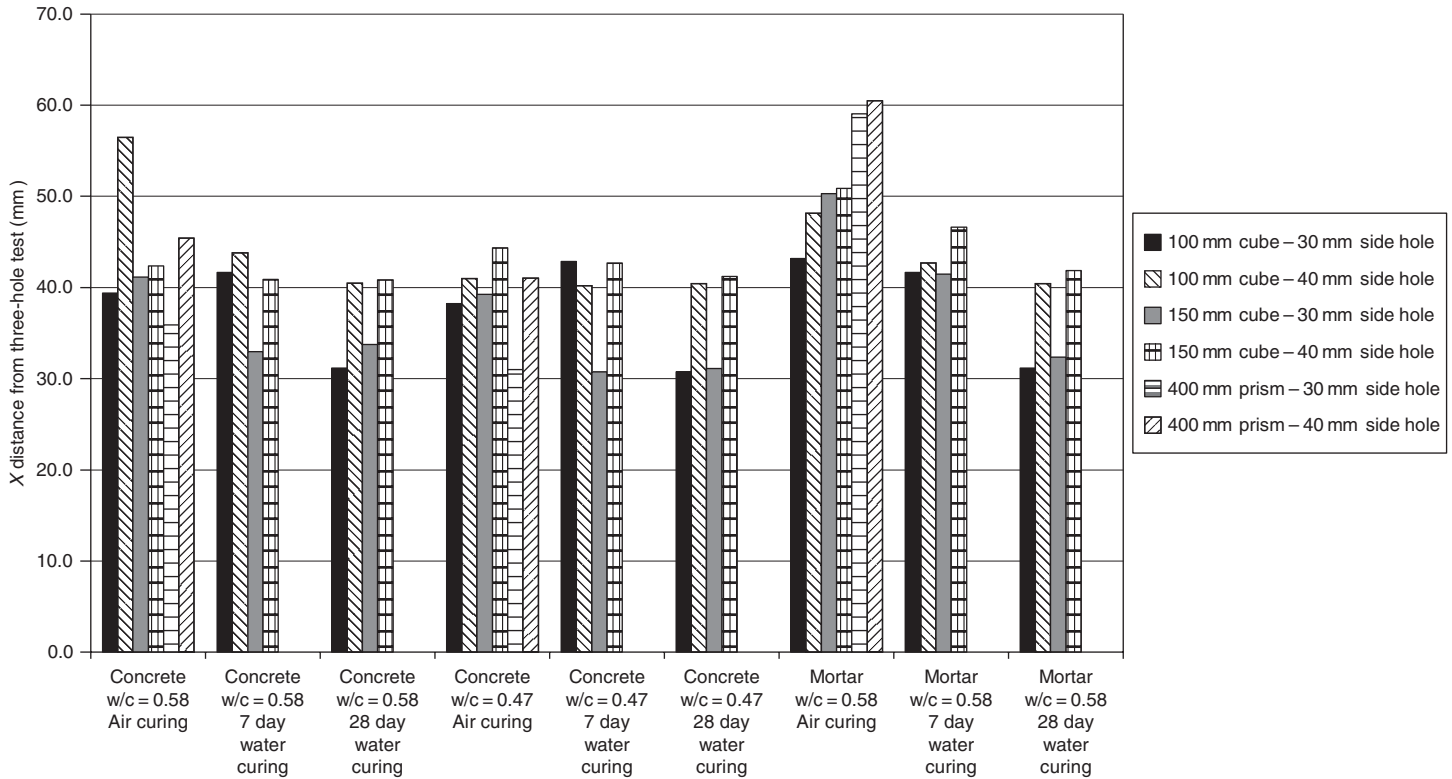

5.13 Distance *X* over which the vacuum decays in three-hole test.

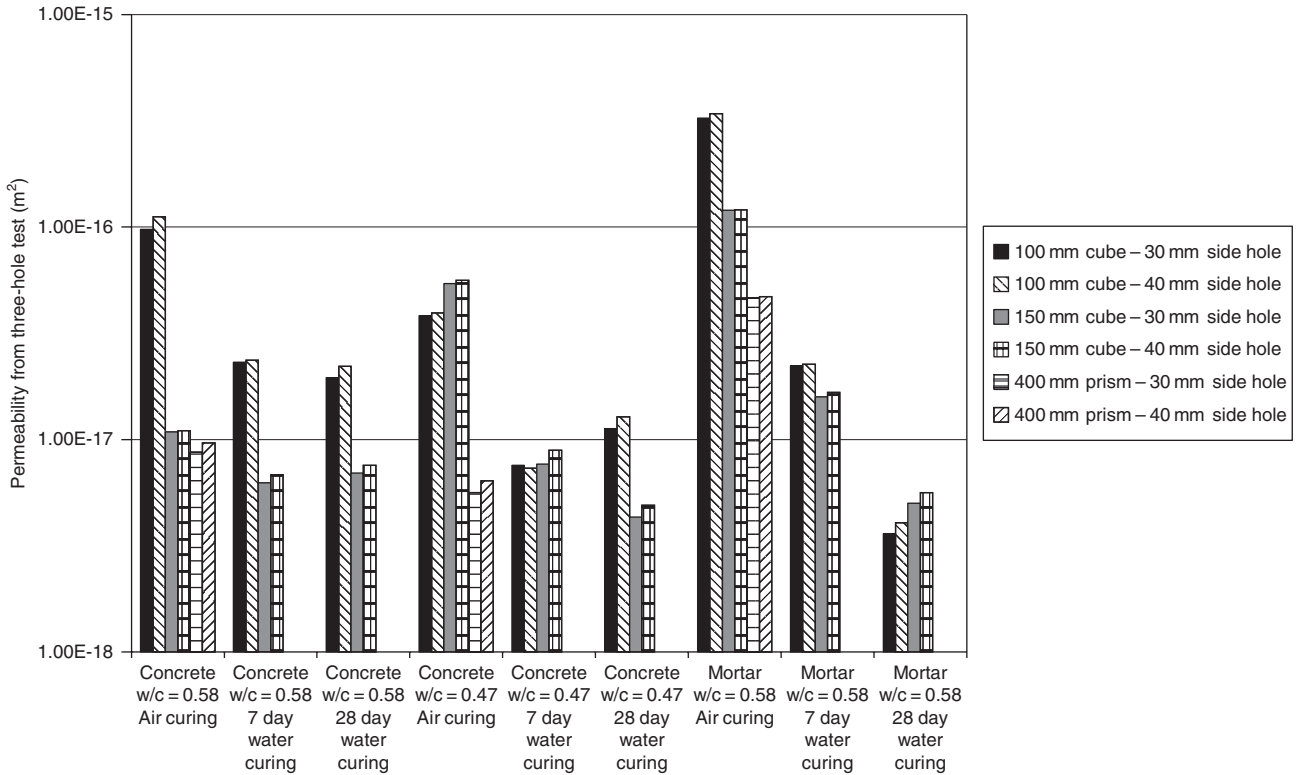

5.14 Intrinsic permeability calculated from the three-hole test.

K was obtained from it. This analysis has been used previously (e.g. Dhir *et al*., 1993), but it gave widely varying results. The reason for this was found to be that it does not assume any value for the constant n which may be seen from equation (4.12) to have a value of 0.5.

A simpler analysis was therefore carried out by applying equation (4.12) directly to the individual data points and obtaining an average result. The porosity of the concrete was assumed to be 10 % and 7 % for mixes 1 and 2, respectively, and the mortar 18 %. The radius of the largest pores was assumed to be 0.6 μm. These are typical values for mixes of this type. The values for surface tension and viscosity of water were 0.073 N/m and 10^{-3} Pa s, respectively. Figure 5.15 shows the average values and also the separate values for 100 mm and 150 mm cubes from which the averages were obtained.

Results from the high pressure permeability test

The time required to collect 10 ml of water was recorded and the flow velocity was computed. The values were substituted in equation (4.2) to obtain the intrinsic permeability. The results are shown in Fig. 5.16.

5.5.5 Discussion

Results for the individual tests

The results from the three-hole test confirm the observations from the data presented in Section 5.5 that the method gives realistic results but should not be used on small samples or near an open edge if used *in situ*.

The ISAT results in Fig. 5.15 show good agreement between tests on the two different sample sizes and a clear effect of reducing permeability with improved curing.

The results from the high pressure water test in Fig. 5.16 show an unexpected increase in permeability for the mortar samples when cured in water. The pressures used in this test are high (typically 60–100 atm) and it is suggested that some pathways through the pore structure were created.

Comparison of permeability values

Figure 5.17 shows the comparison between the three different experiments. The calculated relationship between gas and water permeability taking account of gas slippage (equation 1.12) is shown on the graph and the line of equality is also shown. It may be seen that the ISAT values show a good correlation (R^2 = 0.97) with the results of the three-hole test and all lie between the two lines, i.e. the ISAT values are above those predicted by the gas slippage theory but below the line of equality.

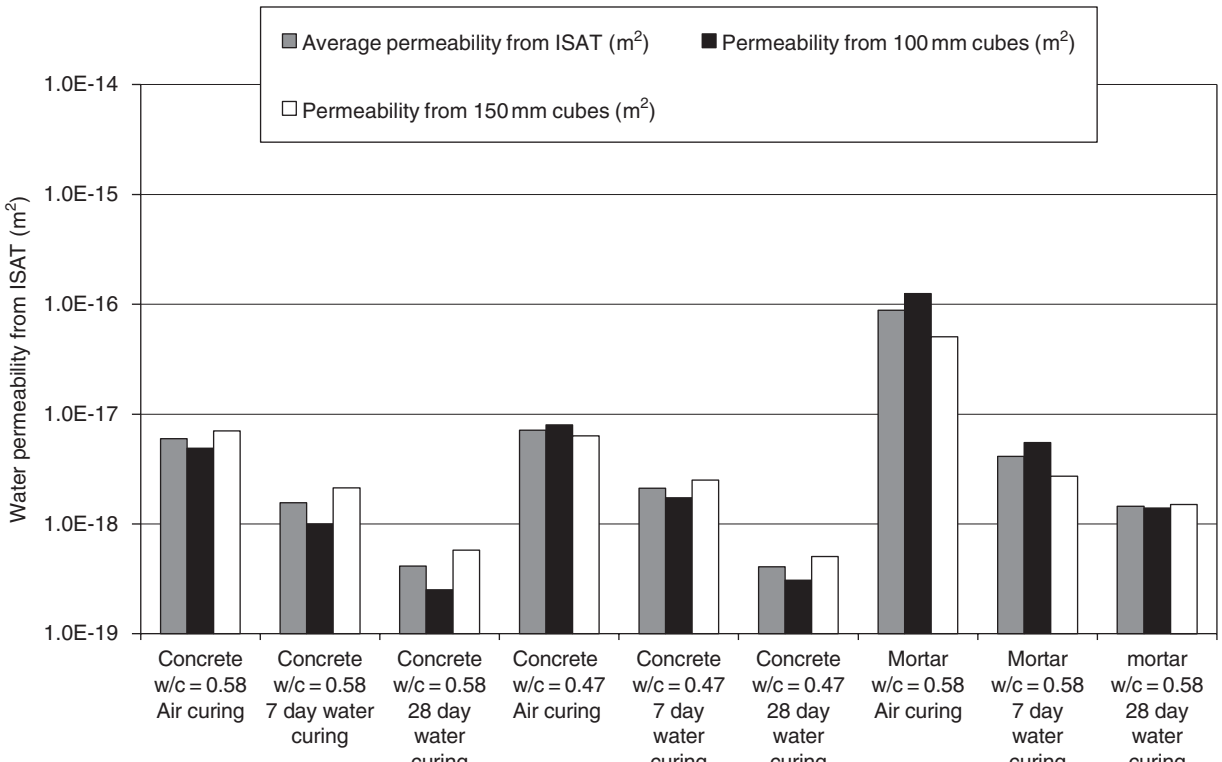

5.15 Intrinsic permeability calculated from ISAT.

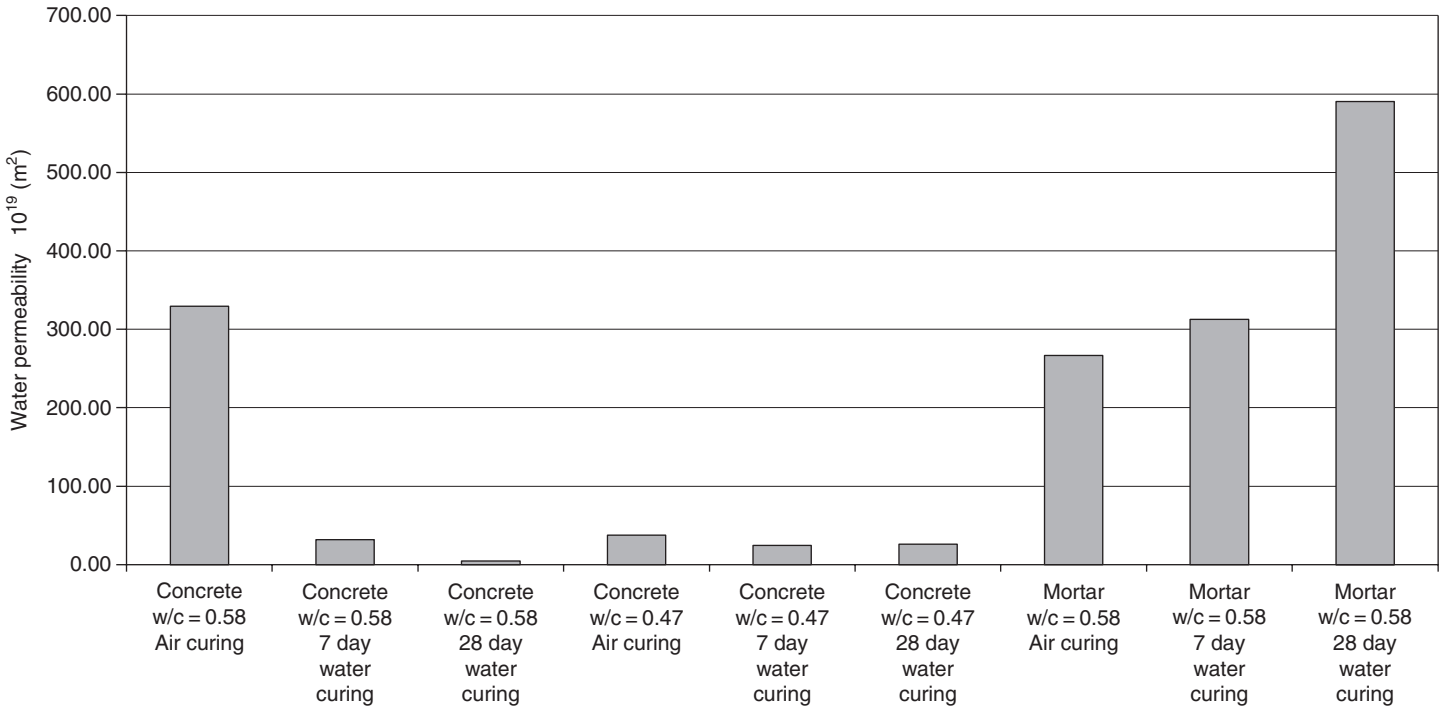

5.16 Water permeability from high pressure test (m^2).

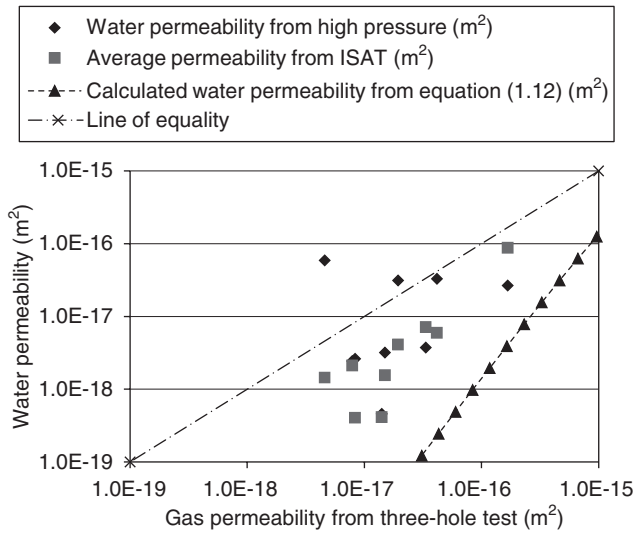

5.17 Comparison of permeabilities.

The only two points for the high pressure test which do not lie between the two lines are the two results for wet cured mortar which are noted above as outliers. These two points lie on and above the line of equality. With these exceptions, the high pressure test results lie in the same region as the ISAT results and show a correlation coefficient $R^2 = 0.59$ with the results of the three-hole test confirming the validity of the analyses for the non-destructive tests.

Some change in permeability measured from the ISAT might be expected because it is a surface measurement and the other two tests measure bulk properties. At the surface, poorer curing and a higher paste content could increase the permeability, but carbonation might reduce it. The present results do not indicate any systematic effect.

It is also of note that the intrinsic permeability should be an absolute property of the material and should not depend on the fluid used to derive it. The existence of the discrepancies quantified in equation (1.12) highlights the limitations of the Darcy equation (1.3). By replacing the analytical solutions presented in this work with numerical simulations containing corrections for gas slippage and other factors, it should ultimately be possible to derive permeability values which are the same for all fluids.

5.6 Conclusions

- The three-hole test is derived from the Figg test with additional holes drilled into the concrete. This new method reveals the volume of concrete

that is being tested and permits calculation of the permeability in absolute units.

- The volume of concrete tested in the Figg test on a dry sample has a radius of approximately 50 mm. The test should therefore be reliable in concrete with 20 mm aggregate.
- The three-hole test gives a good correlation with the ISAT test and direct measurements of permeability and gives confidence in the methods used in the context of the known variability of all measurements of concrete permeability discussed in Section 1.1.

5.7 References

Bamforth P B (1987)The relationship between permeability coefficients for concrete using liquid and gas, *Magazine of Concrete Research*, **39** (138), pp. 3–11.

Dhir R K, Shaaban I G, Claisse P A and Byars E A (1993) Preconditioning *in situ* concrete for permeation testing. Part 1: Initial Surface Absorption, *Magazine of Concrete Research*, **45** (163), pp. 113–118.

6

Measurements of gas migration in concrete

DOI: 10.1533/9781782423195.82

Abstract: This chapter describes a major programme to measure the gas permeability of concrete. The work was carried out by the author at the then Atomic Energy Research Establishment at Harwell for the application described in Chapter 14: to determine the effect of gas pressure on a nuclear waste repository. Because of the significant level of resources available in this programme, it was possible to determine the effect of different gases, moisture, reinforcement and construction joints to a significant level of accuracy.

Key words: gas permeability, moisture content, reinforcement, construction joints, Knudsen flow.

6.1 Introduction

When gas is flowing through concrete, the flow rate may be significantly affected by moisture in the pores and by reinforcement and construction joints. These effects are difficult to measure. In particular, if the effect of moisture is to be measured, the gas which is used must be at the same humidity as the sample. The work described here was carried out by the author at the then Atomic Energy Research Establishment at Harwell for the application described in Chapter 14: to determine the effect of gas pressure on a nuclear waste repository. Because of the significant level of resources available in this programme, it was possible to determine the effect of different gases, moisture, reinforcement and construction joints to a significant level of accuracy.

6.2 Experimental method

6.2.1 Production of samples

The experimental materials used in this study were prepared at either Sir Robert McAlpine Ltd or by Taywood Engineering Ltd. The ratios of water to hydraulic binder (w/b) and aggregate to binder and the total binder contents for the concretes are given in Table 6.1. The ground granulated blast furnace slag (GGBS)/Portland cement (PC) grout had a GGBS:PC ratio of 9:1. Commercial considerations meant that the compositions of the backfill grouts could not be given. The materials were mixed in pan or shear

Table 6.1 Water–binder (w/b) and aggregate–binder ratios and total binder content used in the manufacture of the experimental materials. Data for backfill grouts are unavailable. All ratios are by weight

Material	w/b	Aggregate/binder	Total binder (kg/m^3)
SRC-concrete	0.45	4	413
PFA/PC-concrete	0.475	4.55	400
GGBS/PC-grout	0.4	0	1350

Table 6.2 Physical properties of the experimental materials. Average pore radius values obtained using mercury intrusion porosimetry (MIP), but the measurements were not performed on the SRC-concrete

Material	Strength (MPa)	Density (kg/m^3)	Porosity (%)		Average pore radius (μm)
			Wt loss	MIP	
SRC-concrete	64	2478	13	–	–
PFA/PC-concrete	61	2430	12	11	0.011
GGBS/PC-grout	32	1890	40	29	0.011
Preliminary grout	0.9	1460	66	56	0.7
Reference grout	6	1755	54	44	0.45

mixers as appropriate and vibrated into moulds. The sulphate resisting cement (SRC) and pulverised fuel ash (PFA)/PC-concretes and the GGBS/PC-grout were cured for 24 h at 20 °C prior to demoulding then cured underwater at ambient temperature for 28 days. All materials were subsequently stored underwater at ambient temperature until required for use. The resulting compressive strengths and densities of all the experimental materials are given in Table 6.2.

The pore structures of all materials except the SRC-concrete were investigated using mercury intrusion porosimetry (MIP) using a Carlo Erba Strumentazione Porosimeter 2000 with a maximum operating pressure of 200 MPa (this technique is described in more detail in Section 8.3.2). The PFA/PC-concrete sample was prepared by taking a number of 10 mm cores from a larger specimen and breaking these up and mixing to ensure a representative sample was achieved. Simple cores were used for the remaining materials. The porosity and the average pore radius were obtained from the MIP, and this data is given in Table 6.2. In addition, the porosity was calculated from the weight loss on drying, given in Table 6.3, using the measured density of water-saturated material from Table 6.2. The discrepancies between the two methods of obtaining the porosity may be

Table 6.3 Fractional porosities obtained from the weight loss for each material during conditioning in the given relative humidity atmosphere (Wt) and from the measurement of gas accessible volumes (GAV). The negative value is due to inaccuracy in the measurement

Material	Dry		75% RH		100% RH	
	Wt	GAV	Wt	GAV	Wt	GAV
PFA/PC-concrete	14.3	2.9	1.2	–2.3	0	6.9
GGBS/PC-concrete	44.4	23.1	2.0	3.8	0	3.7
Preliminary grout	66.3	67.2	56.0	–	35.9	42.6
Reference grout	55.1	54.9	25.1	33.4	11.4	12.7

due either to the MIP failing to intrude fine pores or the drying causing the loss of some water of hydration. It is likely that the MIP data is the more accurate.

The MIP results revealed that the PFA/PC-concrete and the GGBS/PC-grout have relatively narrow and symmetrical pore size distributions in the range 5–50 nm. In contrast, the preliminary and reference backfill grouts have broad pore size distributions ranging from 5 nm to greater than 1 μm. These distributions are quite strongly biased towards the larger pore sizes as shown by the average radii given in Table 6.2.

6.2.2 Specimen preparation

Specimen conditioning

The specimens were conditioned prior to use in a controlled humidity atmosphere to establish a known water content. Three different humidities were selected: zero, 75% and 100% relative humidity (RH). The SRC-concrete was used in the dry condition only. The zero RH, dry specimens were dried for 24 h at 100 °C then stored in a sealed container containing silica gel desiccant. The remaining specimens were placed directly into sealed containers. The 75% and 100% RH were achieved by placing a quantity of saturated sodium chloride solution or demineralised water, respectively, into the containers.

Measurement of water saturation

The degree of water saturation was determined by monitoring weight loss during conditioning. The fractional weight losses incurred by conditioning, compared to the initial weight in a surface dry condition, are given in Table 6.3. The data in Table 6.3 confirms that that the grouts have substantial

porosity and shows that both the preliminary and reference grouts lost water even during conditioning at 100 % RH.

Measurement of gas accessible volume (GAV)

Analysis of the experimental data from the gas transport experiments was carried out using a numerical model of the gas migration process, as described below, and required the measurement of the 'gas accessible' volume (GAV) for each type of material and condition. This was measured by placing appropriate specimens into a sealed chamber at a known pressure and subsequently venting the gas into an additional, known volume. The resulting pressure drop, combined with the volumes of the system and the specimen, can be used to calculate the volume of porosity accessible by gas. This method has the advantage that the specimens are used in an intact, conditioned state and the measured porosity is directly associated with gas migration. The measured porosities obtained using this technique are given in Table 6.3.

The gas accessible porosity values for the backfill grouts are not significantly different from those obtained from weight loss measurements, as given in Table 6.3. The gas accessible porosity values were subject to some inaccuracy due to limitations in the measurements of the volumes. However, it appears from the comparison of the data in Table 6.3 that the PFA/PC-concrete and GGBS/PC-grout have significantly lower gas accessible porosities than is indicated by other measurement techniques.

6.2.3 Specimens containing interfaces

The influence of artefacts introduced by the construction process was assessed using specimens containing reinforcement bars and construction joints. The effect of interfaces on gas migration was investigated using specimens conditioned at both zero and 100 % RH.

Specimens of the PFA/PC-concrete were cast into moulds containing a section of reinforcing mesh oriented vertically in a cylindrical mould. The mix design and curing conditions utilised were identical to those discussed above. The mesh consisted of 4 mm diameter bars spaced at 50 mm centres. The cylinders were sectioned between the horizontal members of the mesh to produce specimens containing two bars perpendicular to the flat faces of the slices. The arrangement of the reinforcement bars in the cylinder is illustrated in Fig. 6.1. The interface between the reinforcement and the concrete was thus parallel to the direction of gas migration.

Construction joints were produced in specimens of the preliminary backfill grout. Previously cast cylinders, cured identically to those described previously, were split approximately in half in the direction perpendicular

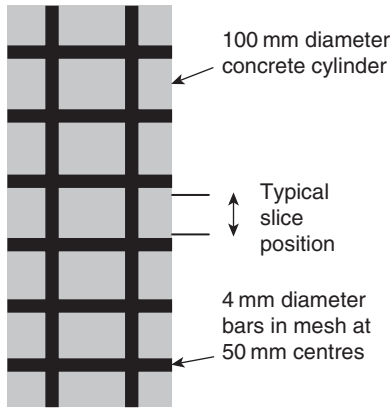

6.1 Illustration of the arrangement of reinforcement bars in PFA/PC-concrete cylinder used to produce specimens for the assessment of the effect of interfaces on gas migration.

to the flat faces and replaced in moulds prior to casting additional material of the same mix design as the original specimens. A further monolithic specimen was prepared from the additional material to act as a control. The specimens were subsequently cured at ambient temperature for at least 28 days. Sectioning produced specimens with the construction joint oriented parallel to the direction of gas migration.

6.2.4 Experimental apparatus

The flow of gas under an imposed pressure gradient was measured by monitoring the decay of a pressure difference across a membrane of the material with elapsed time. Experimental measurements were carried out using a variety of gases. The permeability of the dry SRC-concrete was measured using hydrogen and argon whilst that of the GGBS/PC and backfilling grouts and the flawed specimens was measured using helium and argon. The influence of gas type on gas migration was more fully investigated for the PFA/PC-concrete using five different gases: hydrogen, helium, methane, argon and carbon dioxide.

Measurement cells were constructed for operation at both low (0–200 kPa) and high (0–10 MPa) applied pressures.

Low pressure measurements

The general form of the low pressure apparatus is illustrated schematically in Fig. 6.2. The apparatus allowed the sampling of a fixed volume of the gas from one side of the cell. Specimens were in the form of 100 mm discs

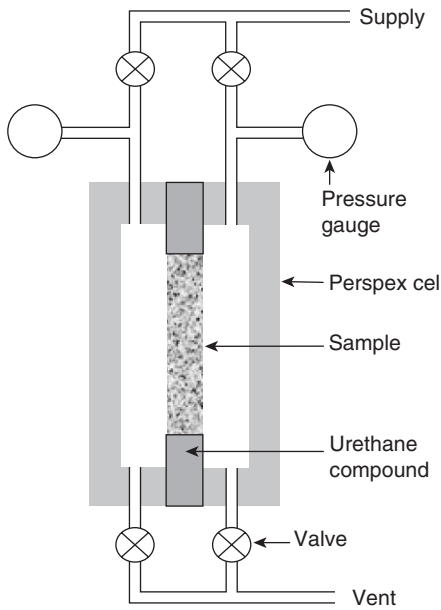

6.2 Schematic diagram of the experimental apparatus for the measurement of gas migration.

approximately 20 mm in thickness mounted into a perspex holder using a cold-setting urethane compound.

The apparatus was designed to allow the maintenance of a constant humidity atmosphere adjacent to the specimen during an experiment. This was achieved by placing either desiccant, salt solution or pure water into the cell along with the specimen.

The construction of the cells gave a reduction in the area of specimen exposed in the lower pressure reservoir compared to that exposed in the high pressure reservoir. Where necessary, a correction by a factor of 1.13 has been applied to the data to allow for this effect.

High pressure apparatus

The higher pressure experiments were performed either with or without triaxial confinement of the specimens using a cell similar to that described in Section 4.2. (However, this cell had a thinner and thus more readily punctured sleeve around the sample; the cell described in Section 4.2 was developed from it and is recommended for all work.) In particular, it was found that triaxial stressing of the high porosity preliminary backfill grout caused a substantial permanent reduction in the volume of the specimens and some experimental error may have occurred.

It is of note that the high pressure apparatus was far more difficult and time-consuming to use than the low pressure.

Specimen thickness

The specimen thickness was dependent on the measurement cell used. In the case of the triaxial cell, specimens approximately 100 mm thick were used whilst in the low pressure cells the specimen thickness was approximately 20 mm.

Types of experiment

Two variations on the basic experiment were performed. In the first, both reservoirs shown in Fig. 6.2 were isolated and the pressures allowed to relax to an equilibrium level. Such experiments allowed measurements to be made at an approximately constant average pressure. In contrast, measurements were also performed with a continuously varying average pressure by holding one reservoir at a constant applied pressure. In both cases, the range of average pressure values was determined by the initial conditions and the volumes of the two reservoirs.

Pressures used

The permeability measurements were made at a range of different average pressures. Constant average pressures of 100 kPa and 1.5, 7, 15, 22 and 72 MPa were used in the measurements on the PFA/PC-concrete whilst experiments on the grouts were constrained to a maximum average pressure of about 2 MPa to avoid specimen damage. The varying average pressure experiments were performed in two pressure ranges; 0–200 kPa and 0–3 MPa, denoted low and high pressure ranges, respectively.

Replicate samples

Between one and ten measurements were carried out for each set of conditions. The data generally exhibited very little variability between different runs on an individual specimen. It was considered that a measured intrinsic permeability represented the sum of the intrinsic permeability of the material and any additional contribution from short-circuit pathways such as cracks or incomplete sealing between specimen and container. Hence, it was not possible to obtain a measured intrinsic permeability below the true intrinsic permeability for the material. The best value of the intrinsic permeability for a material was taken to be the lowest value obtained.

Duration of experiments

The elapsed times required for the completion of a particular experiment were determined by the material being studied. These varied from about 10 s, in the case of dry preliminary backfill grout, to greater than a month for some of the materials in the 100 % relative humidity condition. The limit of accuracy of the experiments was ultimately controlled by the quality of the seals achieved in the measurement cells, both between the two reservoirs and to atmosphere. The effective lower and upper limits of resolution of the experimental apparatus were estimated as 10^{-21} and 10^{-14} m^2, respectively. Since the intrinsic permeability values are based on calculations of the rate of change of pressure, any experimental errors, such leaks between reservoirs or to atmosphere, will result in an over-estimate of the intrinsic permeability. The presence of leaks to atmosphere could be detected in the closed system mode by checking for conservation of the total mass of gas as it flowed from one reservoir to the other. Achieving an adequate seal to contain helium for more than a month required a considerable amount of work over a period of many months to select and assemble appropriate materials and fittings. In particular, several types of pipe and fittings such as PTFE were found to be permeable to this gas.

6.3 Analysis of experimental data

6.3.1 Analytical solution

The flow of a single gas between the two reservoirs in the apparatus will be such that the pressure difference is reduced and eventually eliminated. The flow of a fluid in a homogeneous porous medium under a pressure gradient is governed by the Darcy equation (1.6). The volumetric flow rate can be related to the molecular flow rate using the ideal gas approximation and the resulting version of the equation integrated across the whole specimen to give an expression for the molecular flow rate in terms of the applied pressures on either side of the membrane. The variation in pressure in one reservoir, in this instance that at the lower pressure, can be determined from this expression by the further application of the ideal gas approximation by integrating equation (1.9) as in equation (4.25):

$$\frac{\mathrm{d}P_1}{\mathrm{d}t} = \frac{KA}{2eLV}(P_2^2 - P_1^2) \qquad [6.1]$$

where:

$\mathrm{d}P_1/\mathrm{d}t$ is the rate of pressure change in the low pressure reservoir
V_1 is the volume of that reservoir and
P_1 and P_2 are the pressures in the low and high pressure reservoirs, respectively.

In a closed experiment, the change in pressure in the high pressure reservoir can be calculated from that measured in the lower pressure reservoir and hence P_2 obtained from P_1. Substituting for P_2 and integrating with respect to pressure and time gives an expression for the variation of pressure in the low pressure reservoir with time:

$$\frac{[(V'^2-1)p_1-(V'+1)(P_{20}+V'P_{10})][(P_{20}-P_{10})V'+P_{10}-P_{20}]}{[(V'^2-1)p_1-(V'-1)(P_{20}+V'P_{10})][(P_{20}+P_{10})V'+P_{10}+P_{20}]} = \exp\left[\frac{KA}{eLV_1}(P_{20}+V'P_{10})t\right] \quad [6.2]$$

where:

V' is the ratio of the reservoir volumes (V_1/V_2) and
P_{10} and P_{20} are the initial low and high pressures, respectively.

Equation (6.2) may be compared with equation (4.26) which was obtained from it and is a special case of it.

If the higher pressure is held constant, the effective value of V_2 is infinite and the ratio V' is zero. Applying this constraint to the equation above allows the determination of intrinsic permeability from the experiments with variable average pressure. The variation in the pressure in the higher pressure reservoir can be obtained using an analogous method. This derivation predicts the exponential relaxation of an applied pressure difference with time.

6.3.2 Numerical solution

The analytical solution for gas pressure variation given above assumes that steady state flow has been established, i.e. that the quantity of gas exiting the specimen into the lower pressure reservoir is equal to that entering the specimen from the higher pressure reservoir. For a compressible fluid in a medium with finite porosity, this is not strictly true. Hence, the analytical solution is only applicable to materials where the error caused by the assumption of zero porosity is not significant. The errors become large in specimens of high porosity subject to a large pressure difference. In order that the all the experimental data could be analysed, a numerical model of the variation in pressure with time was developed using a finite difference method similar to the model described in Chapter 2. The intrinsic permeability value obtained from the analytical solution was input as a starting value for the numerical calculation. Subsequently, the numerical model was run to produce a simulated data set of pressure versus time from which a new intrinsic permeability value was calculated using the analytical solution. This process was repeated until the simulated data set achieved a

satisfactory match to the experimental data. In Chapter 11, the use of artificial neural networks is discussed for the solution of a similar problem.

The intrinsic permeability values were obtained using this numerical method to extract them from both constant and varying average pressure experiments. The analytical solution alone was used to calculate the infinite pressure intrinsic permeability values and Klinkenberg constants from the varying average pressure experiments. This data will not be as accurate as that derived from the numerical solution.

6.3.3 Pressure at the completion of a test

The completion of an experiment was indicated by the achievement of a uniform pressure throughout the experimental apparatus. For materials with a low porosity, this pressure is equal to a volume-weighted average of the initial pressures in the two reservoirs. However, if the porosity is high, there is significant gas volume contained in the specimen and the final average pressure must include a contribution from the gas in the pore volume. If the flow is in steady state, the mean pressure P_m in the pore volume is not the linear average of the two initial pressures, due to the compressibility of the gas, but may be found from equation (6.2) as:

$$P_m = \frac{2}{3}\left[\frac{P_{10}^3 - P_{20}^3}{P_{10}^2 - P_{20}^2}\right] \qquad [6.3]$$

The overall average pressure can then be calculated using this value for the pressure in the pore structure and weighting according to the volume of the porosity. In some experiments, the volume of the porosity can be as much as half of the total volume. The assumption that the average pressure in the porosity is a linear average can lead in such circumstances to underestimation of the expected final pressure by over 10 %.

6.4 Results for gas permeability of concrete

6.4.1 Gas migration at constant average pressure

A typical pressure difference relaxation curve for a specimen of the PFA/PC-concrete is shown in Fig. 6.3. The final average pressure was as predicted by equation (6.3). Figure 6.4 shows a comparison of the gas intrinsic permeability values for the PFA/PC-concrete obtained using hydrogen, helium, methane, argon and carbon dioxide as the migrating gases. Measurements were made on material conditioned at 0, 75 % and 100 % RH. All experiments were performed at an average pressure of 100 kPa. Data for the 100 % RH conditioned specimen are only available for helium and argon.

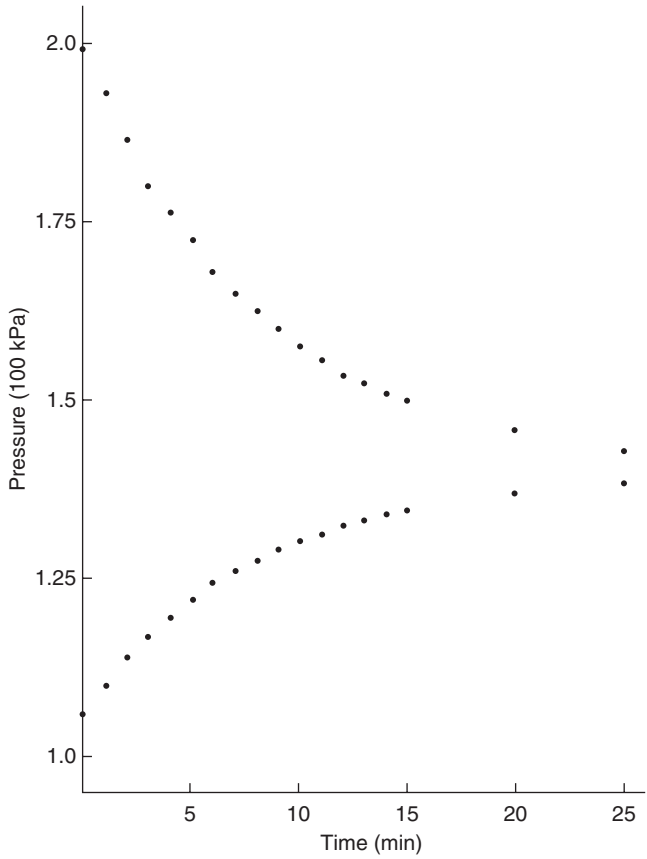

6.3 Typical variation in pressure observed during the measurement of the intrinsic permeability of PFA/PC-concrete. The migrating gas was argon. The two traces were recorded in the cells at each side of the sample.

At low pressures, Knudsen flow will be significant as discussed in Section 1.2.1. If the Klinkenberg relationship is applicable to this data, the measured permeabilities at constant pressure will depend on the mean free path for each gas. The mean free path of a gas molecule λ can be calculated in a number of ways. The equation used here is:

$$\lambda = \frac{2.02e}{\sqrt{\rho P}} \qquad [6.4]$$

where:

e is the viscosity,
P is the pressure and
ρ is the density.

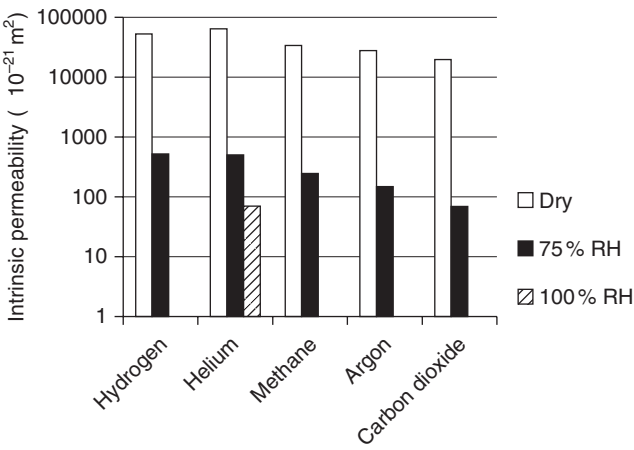

6.4 Summary of the intrinsic permeability values measured for PFA/PC-concrete conditioned under dry, 75% RH and 100% RH conditions. All measurements were performed using a constant average pressure of 100 kPa. At 100% RH the intrinsic permeability for argon was 10^{-21}. This was the only gas apart from helium to give a reading.

The mean free paths for the gases used at a pressure of 100 kPa and a temperature of 25 °C are given in Table 6.4. The variation in the intrinsic permeability with the type of gas for both the dry and the 75 % RH conditioned specimens at 100 kPa, given in Fig. 6.4, was correlated with the mean free path of the gas given in Table 6.4. Linear regression on the two data sets gave correlations of $r^2 = 0.92$ and 0.75 for the dry and 75 % RH conditioned specimens, respectively. The intercept as the mean free path tends to zero determined by linear regression gives the value of the infinite pressure permeability which equates with that in the Klinkenberg equation, since a mean free path of zero corresponds to a value of the Klinkenberg constant of zero. The infinite pressure intrinsic permeability values K_∞ derived in this way are 1.3×10^{-17} m^2 for dry material and 2×10^{-20} m^2 for that conditioned at 75 % RH.

6.4.2 Variation in gas permeability with pressure

The values of the intrinsic permeability of the SRC-concrete in the dry condition for hydrogen and argon migration at a range of approximately constant average pressures between 0 and 150 kPa are shown in Fig. 6.5. The data has been corrected by a factor of 1.13 to allow for the differing areas of the specimen exposed in the high and low pressure reservoirs as a result of the seal geometry. It is clear that the intrinsic permeability is

Table 6.4 Results of the measurements of gas flow in dry PFA/PC-concrete using varying average pressures. Data given are the means of best-fit values for the Klinkenberg equation. Low pressure data obtained for average pressures in the range 0–200 kPa. High pressure data obtained for average pressures in the range 0–7.5 MPa. Quoted errors are standard errors

Gas	Mean free path at 100 kPa (μm)	K_∞ (10^{-17} m^2)	b (×100 kPa)	
			Low pressure	High pressure
Hydrogen	0.194	4.9 ± 1.1	1.9 ± 1.1	–
Helium	0.305	5.2 ± 0.9	1.9 ± 0.8	0.9 ± 1.0
Methane	0.086	4.6 ± 1.6	0.3 ± 0.3	–
Argon	0.110	2.4 ± 0.3	1.6 ± 0.3	2.6 ± 3.7
Carbon dioxide	0.070	1.9 ± 0.2	0.5 ± 0.2	5.6 ± 3.4

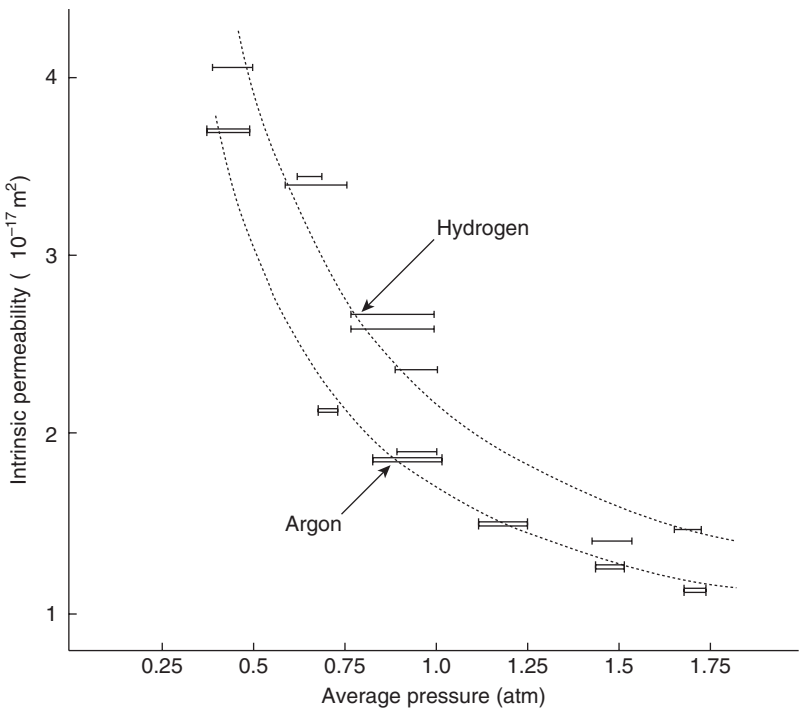

6.5 Variation in the intrinsic permeability values for hydrogen and argon in dry SRC-concrete with average pressure. The curves demonstrate the fit of the Klinkenberg equation to the data. The values are expressed as $K \times 10^{-17}$ m^2. Error bars illustrate the slight variation in average pressure which occurred during individual experiments.

inversely dependent on average pressure. The intrinsic permeability for hydrogen exceeds that for argon in the pressure range investigated. This is consistent with the observations made above and can be attributed to the increasing effect of Knudsen flow at lower pressures and the longer mean free path of hydrogen for a given pressure.

The Klinkenberg equation can be fitted to the data, as illustrated in Fig. 6.5. The infinite pressure intrinsic permeability values thus determined are 3.6×10^{-18} and $4.0 \times 10^{-18}\,m^2$ from the hydrogen and argon data, respectively. These values are close enough to be considered equal, within experimental error. The calculated values of the Klinkenberg constant are 6.6×10^5 Pa for hydrogen and 4.2×10^5 Pa for argon.

The dependence of the gas permeability for argon migration in the PFA/PC-concrete (conditioned at zero RH) on the average pressure is shown in Fig. 6.6. Data is included for experiments performed at both constant and varying average pressures. The range of data obtained at each pressure is illustrated. It is apparent that the intrinsic permeability decreases as the average pressure is increased. Plotting the best estimate intrinsic permeability for the set of experiments performed at, approximately, a particular value of the average pressure against the reciprocal of average pressure indicated that the Klinkenberg relationship is probably applicable, although the correlation obtained was not strong ($r^2 = 0.78$). Linear regression gave the infinite pressure permeability as $2.0 \times 10^{-17}\,m^2$ and the Klinkenberg constant as 190 kPa.

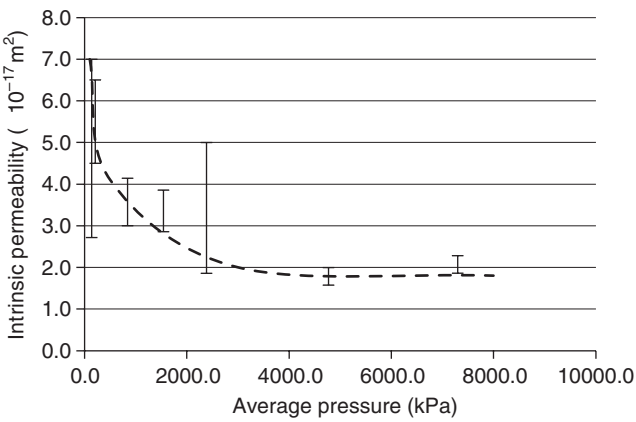

6.6 Variation in the intrinsic permeability for argon in dry PFA/PC-concrete with average pressure. Each point is the mean of several experiments carried out at the same average pressure. The intrinsic permeability values are expressed as $K \times 10^{-17}\,m^2$.

The change in permeability with average pressure shown in Fig. 6.6 is most significant at low average pressures. The results of a series of measurements performed with the average pressure varying between 0 and 200 kPa in PFA/PC-concrete conditioned at zero RH, using each of the five different gases, are given in Table 6.4. There is a possible correlation between the Klinkenberg constant and the mean free path for each gas, calculated using equation (6.4), at a pressure of 100 kPa and a temperature of 25 °C ($r^2 = 0.60$).

The infinite pressure intrinsic permeability should be a constant value, independent of the type of gas. The variation in the infinite pressure intrinsic permeability with gas type is not strongly correlated with the mean free path ($r^2 = 0.50$) and it is assumed that the differences between the values shown in Table 6.4 are due to experimental error. The mean value of the infinite pressure intrinsic permeability is $(3.7 \pm 0.6) \times 10^{-17}\,m^2$. This value is reasonably consistent with the values of 1.3×10^{-17} and $2.0 \times 10^{-17}\,m^2$ determined above.

The results of the measurements carried out with a varying average pressure of argon on the PFA/PC-concrete conditioned at 100 % RH implied an infinite pressure permeability of $(7.6 \pm 2.3) \times 10^{-17}\,m^2$. Comparison of this value with those given in Fig. 6.4 indicates that the former must be subject to error as the permeability is apparently three orders of magnitude greater when measured in the varying average pressure experiment. The varying average pressure experiments were performed using higher pressure differences, up to 3 MPa. It is postulated that the high applied pressures gave rise to mechanical failure in the specimens when used in the non-triaxial high pressure cell. Consequently, the data for PFA/PC-concrete in the 100 % RH condition has been omitted from Table 6.6 where they are quoted for comparison.

6.5 Comparison with gas permeability of grouts

6.5.1 Gas migration at constant average pressure

Table 6.5 details the measured intrinsic permeability values for the migration of helium and argon at an average pressure of 100 kPa in all of the experimental materials in both the dry and 100 % RH conditioned states. The data for the PFA/PC-concrete is included for comparison. In some of the materials in the dry state, in particular the two types of backfill grout, the gas migration was so rapid that only variable average pressure experiments could be performed. In these cases, the intrinsic permeability values for a constant average pressure of 100 kPa were calculated from the available data for varying average pressure, discussed below, using the Klinkenberg equation.

Table 6.5 Measured intrinsic permeability values for a constant average pressure of 100 kPa in the experimental materials. All data are expressed as K (m^2)

Material	Dry		100% RH	
	Helium	Argon	Helium	Argon
SRC-concrete	–	2×10^{-17}	–	–
PFA-concrete	6×10^{-17}	3×10^{-17}	7×10^{-20}	10^{-21}
GGBS-grout	5×10^{-16}	4×10^{-16}	4×10^{-19}	10^{-21}
Preliminary grout	2×10^{-14}	10^{-14}	2×10^{-16}	4×10^{-17}
Reference grout	3×10^{-15}	2×10^{-15}	7×10^{-17}	4×10^{-17}

Table 6.6 Measured values of the infinite pressure intrinsic permeability. Data for the dry conditioned specimens obtained for pressures in the range 0–200 kPa only. Quoted errors are standard errors. All data are expressed as K (m^2)

Material	Dry	100% RH
SRC-concrete	$(3.8 \pm 0.1) \times 10^{-18}$	–
PFA/PC-concrete	$(3.7 \pm 0.6) \times 10^{-17}$	–
GGBS/PC-concrete	$(5.3 \pm 1.0) \times 10^{-16}$	$(5.9 \pm 0.4) \times 10^{-18}$
Preliminary grout	$(4.4 \pm 1.1) \times 10^{-14}$	$(4.4 \pm 0.8) \times 10^{-16}$
Reference grout	$(4.4 \pm 1.1) \times 10^{-16}$	$(4.6 \pm 5.0) \times 10^{-16}$

6.5.2 Variation in gas permeability with average pressure

The infinite pressure permeabilities for all of the experimental materials are shown in Table 6.6 for migration at low pressure in materials conditioned at 0 and 100 % RH, with the exception of the value for the PFA/PC-concrete in the 100 % RH condition. It has been assumed that the infinite pressure permeability is a constant for all gases and hence the infinite pressure intrinsic permeability values given are the average of the data for all gases studied in each material. Figure 6.7 illustrates the fit of the Klinkenberg equation to the variation in the measured intrinsic permeability for the GGBS/PC-grout for average pressures in the range 0–100 kPa.

Table 6.7 gives the measured values of the Klinkenberg constant for all the experimental materials in the dry condition for both low and high average pressures. Where the table shows that the Klinkenberg constant is within experimental error of zero or negative, the change in permeability with pressure over the pressure range investigated was very small. A negative value may be the result of a systematic error in the data analysis

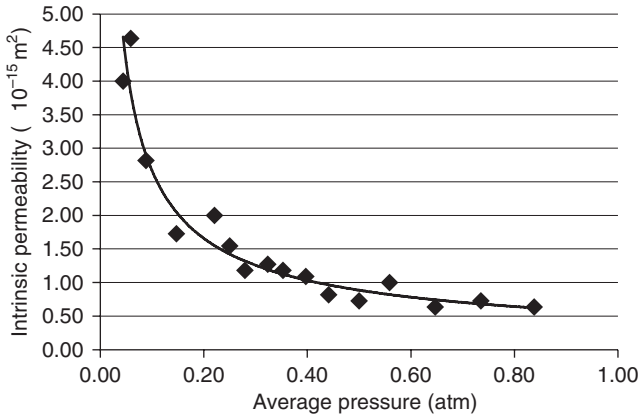

6.7 Variation in intrinsic permeability with average pressure in the GGBS/PC-grout during a single varying average pressure experiment. Measured values of the infinite pressure intrinsic permeability and Klinkenberg constant were 3.64×10^{-16} m^2 and 7.31×10^4 Pa, respectively.

Table 6.7 Measured values of the Klinkenberg constant b (from equation 1.12) for materials in the dry condition obtained using varying average pressure experiments. Where quoted, errors are standard errors. All data are expressed as $b \times 10^5$ Pa

Material	Low pressure (100 kPa)		High pressure (>100 kPa)	
	Helium	Argon	Helium	Argon
PFA/PC-concrete	1.9 ± 0.8	1.6 ± 0.3	0.9 ± 1.0	2.6 ± 3.7
GGBS/PC-grout	0.5 ± 0.3	–(0.3 ± 0.1)	1.2 ± 0.6	–(1.8 ± 3.7)
Preliminary grout	–(0.4 ± 0.2)	–(0.8 ± 0.2)	2.3 ± 0.3	1.1 ± 0.2
Reference grout	20.6 ± 9.5	6.0 ± 1.9	2.2 ± 0.7	–(3.7 ± 1.9)

when the change in intrinsic permeability is small. In such circumstances, it must be assumed that the intrinsic permeability is constant with average pressure and equal to the infinite pressure intrinsic permeability.

The Klinkenberg constants for the materials in the 100 % RH conditioned state were not measured for all materials and pressure ranges. When the values were measured, using high average pressures, in the range 0–3 MPa, the Klinkenberg constants were found to be negative or not significantly different from zero for all materials. The data are considered to indicate that there was little or no change in the infinite permeability for average pressures in the high pressure range.

6.6 The effect of interfaces on gas permeability

6.6.1 Influence of reinforcement on gas migration

The intrinsic permeability values for a constant average pressure of 100 kPa and the infinite pressure intrinsic permeability values for both the dry and 100 % RH conditioned specimens are given in Table 6.8. This data can be directly compared with the data for unreinforced, PFA/PC-concrete given in Tables 6.5 and 6.6.

The presence of the reinforcing bars appeared to increase the intrinsic permeability of dry material (measured at a constant average pressure of 100 kPa) by a factor of between three and four. There was no significant difference between unreinforced and reinforced material for the 100 % RH condition at a constant average pressure of 100 kPa. However, at a constant average pressure of about 1.6 MPa, the intrinsic permeability values for helium and argon were increased to 2×10^{-19} and 1×10^{-19} m^2, respectively. This represents an increase by about an order of magnitude compared to the data obtained at 100 kPa. This increase in permeability with average pressure is not observed for the unreinforced material and must be attributed to the influence of the reinforcement.

6.6.2 Influence of construction joints on gas migration

The experimental results obtained for the preliminary backfill grout containing a construction joint are given in Table 6.8. No data was obtained at constant average pressure in dry material as the extremely high permeability made experiments too rapid. The control specimen gave a 100 kPa argon intrinsic permeability of 6.3×10^{-16} m^2 for material in the 100 % RH condition. The infinite pressure intrinsic permeability values for

Table 6.8 Measured values of intrinsic permeability for the flawed specimens. The constant average pressure data were obtained from experiments at an average pressure of 100 kPa. Where quoted, errors are standard errors. All data are expressed as K (m^2)

		Rebar in concrete	Joint in backfill
K measured at 100 kPa			
Dry	Helium	2×10^{-16}	–
	Argon	10^{-16}	4×10^{-14}
100 % RH	Helium	5×10^{-21}	3×10^{-15}
	Argon	6×10^{-21}	2×10^{-15}
Infinite pressure permeability			
Dry		$(2.0 \pm 0.7) \times 10^{-16}$	2.19×10^{-13}
100 % RH		1.08×10^{-19}	$(4.4 \pm 1.9) \times 10^{-15}$

the control specimen were 2.3×10^{-13} and 4.6×10^{-16} m^2 for the dry and 100 % RH conditions, respectively. This data is significantly greater than that obtained for the normal specimens of the grout, given in Tables 6.5 and 6.6. It is apparent that the batch of grout used in the preparation of the construction joints is not consistent with the other specimens of this material.

The construction joint increased the 100 kPa permeability of 100 % RH conditioned material by a factor of three compared to the control specimen and a factor of 70 compared to the pristine material. The infinite pressure permeability was equal to that of the control specimen for the dry condition and was approximately an order of magnitude greater for the 100 % RH condition.

6.6.3 Variability in the measurements

The contribution to experimental error arising from inter-specimen variability is mainly due to the variation in the number of short-circuit pathways in different specimens of the same material. In addition, some irreproducibility may occur between individual experimental runs on the same specimen and from differences in the intrinsic permeability values of individual specimens of the same material. The total variability in the measurements of the intrinsic permeability for a particular material under a fixed set of conditions can be quantified by the coefficient of variability of the data. This is equal to the ratio of the standard deviation to the mean for the data, usually expressed as a percentage.

The intrinsic permeability measurements made at a constant average pressure of 100 kPa, summarised in Fig. 6.4 and Table 6.5, generally exhibited overall coefficients of variability of between 10 and 40 %. The reproducibility of repeated measurements on an individual specimen was generally of the order of a few per cent. Hence, the measurement of gas permeability using this experimental technique seems to be inherently reproducible.

In contrast, the measured infinite pressure intrinsic permeability values, given in Table 6.6, had coefficients of variability of between about 30 and 200 %. The large variability in the infinite pressure intrinsic permeability is due to the error produced when the Klinkenberg equation is fitted to data which exhibit a very small change in permeability over the pressure range investigated. This is particularly true of the backfill grouts.

6.7 Discussion

6.7.1 Bulk gas flow in dry material

The experimental data shown in Fig. 6.4 demonstrates that the intrinsic permeability for the PFA/PC-concrete measured at a constant average

pressure of 100 kPa is dependent on the mean free path of the gas. Experiments conducted with a varying average pressure show that the intrinsic permeability for a particular gas in both the SRC and PFA/PC-concretes decreases with increasing average pressure, as shown by the data in Table 6.4 and Fig. 6.5. This variation is also demonstrated by the compilation of the data for argon migration in dry PFA/PC-concrete shown in Fig. 6.7.

The data for the SRC-concrete, shown in Fig. 6.5, demonstrates that this material exhibits a significantly lower permeability than the PFA/PC-concrete. This is at variance with the general expectation that the mass transport characteristics of a PFA-modified material will be lower than those of an unmodified cement due to hydration products from the pozzolanic reaction filling the pores. The infinite pressure intrinsic permeability given in Table 6.6 for the SRC-concrete is an order of magnitude lower than that given for the PFA/PC-concrete. The measured fractional porosities of the two materials, given in Table 6.2, are similar. The observed difference in performance may be the result of differing degrees of damage to the pore structures of the two materials during drying.

A Knudsen number (see Section 1.2.1) significantly greater than unity indicates that Knudsen flow will be important. The mean free path is dependent on the nature of migrating gas, as shown above. Consequently, the contribution from Knudsen flow at a given pressure will depend on the gas flowing, as shown by the data in Fig. 6.4. The average pore radius for the PFA/PC-concrete, given in Table 6.2, is 0.011 μm whilst the mean free path at 100 kPa and 25 °C varies between 0.070 and 0.305 μm for the gases used in these experiments. Hence, the Knudsen numbers are in the range 6–28 and a significant contribution from Knudsen flow at 100 kPa would be expected.

The data shown in Fig. 6.7 demonstrates that the change in the argon intrinsic permeability of the PFA/PC-concrete for an increase in the average pressure from 100 kPa to 7.5 MPa is a decrease by about a factor of 2.5. Comparison of the infinite pressure intrinsic permeability values for dry material given in Table 6.4 for the different gases with the intrinsic permeability values obtained at a constant average pressure of 100 kPa given in Fig. 6.4 also indicates that the permeability decreases by at most a factor of two as the pressure is increased over this range. The majority of this decrease occurs in the 0–1 MPa pressure range, as shown in Fig. 6.6.

6.7.2 Bulk gas flow in water-saturated material

The behaviour of the PFA/PC-concrete in the partially or fully water saturated condition is qualitatively similar to that in a dry condition. Figures 6.3 and 6.4 demonstrate that the intrinsic permeability is dependent on the type of gas for concrete conditioned at 75 % RH, although the measured

intrinsic permeability values are significantly lower than those of dry material.

The reduction in the measured intrinsic permeability for material conditioned at high relative humidities must be due to the effective blocking of pores which remained filled with water after conditioning. The relationship between the radius of the largest filled pore and relative humidity *RH* is given by the Kelvin equation (3.1).

RH of 75 % gives a maximum filled pore radius of about 4 nm whilst at a RH of 100 % all pores should be filled with water. Hence, at 75 % relative humidity the majority of the porosity should be available for gas migration. The reduction in the intrinsic permeability for 75 % RH conditioned materials apparent in the experimental results hence indicates that gas migration is significantly influenced by the finer porosity and that much of the pore volume may not form interconnected networks with constrictions larger than 4 nm.

The material conditioned at 100 % RH demonstrated a further decrease in the intrinsic permeability. The Kelvin equation predicts that all porosity is water-filled for this condition and hence a reduction is expected. However, the only mechanism available for gas migration in material that is fully water saturated will be solution-diffusion, where dissolved gas molecules diffuse in the pore solution. Using a solubility of 9×10^{-4} M and a diffusion coefficient of $2 \times 10^{-12}\,m^2\,s^{-1}$ (Harris and Nickerson, 1989), an equivalent intrinsic permeability of about $10^{-23}\,m^2$ is obtained. This value is significantly less than that obtained for helium migration in the PFA/PC-concrete, $7 \times 10^{-20}\,m^2$, and it must be concluded that either there was leak across the specimen or that some interconnected porosity remains open in the specimens conditioned at 100 % RH, or water was expelled from the pores as discussed in Section 6.7.5 below.

6.7.3 Gas migration in grouts

Table 6.5 shows that the intrinsic permeability values at 100 kPa for the three different grouts in the dry condition are of similar magnitude and are an order of magnitude or more greater than those measured for the PFA/PC-concrete. The intrinsic permeability values for the grouts are decreased by two or three orders of magnitude for the 100 % RH conditioned specimens compared to the dry materials. The intrinsic permeability values for the GGBS/PC-grout in the 100 % RH conditioned state is substantially lower than those of the other grouts and is comparable in magnitude to that of the structural concrete.

Comparison of the data obtained using helium and argon as the migrating gases in dry materials shows that there is no significant dependence on gas type for the preliminary backfill grout. Hence, there is apparently little or no

Knudsen flow occurring at 100 kPa. Some dependence on gas type is exhibited by the GGBS/PC and reference backfill grouts. The observed variation in behaviour must be due to the differences in pore sizes between the grouts.

Comparison of the intrinsic permeability values extrapolated to infinite pressure, given in Table 6.6, with those obtained at 100 kPa average pressure (Table 6.5) indicates that there is no consistent relationship between the two. This demonstrates that the intrinsic permeability values of these materials are not strongly dependent on average pressure at pressures of 100 kPa and above. The values of the Klinkenberg constants for these materials were extracted from the data. However, the results were found to be extremely variable and some values were negative, indicating an increase in the intrinsic permeability with increasing average pressure. Hence, the intrinsic permeability values for the high porosity grouts can be considered to be approximately constant over the range of average pressures studied here.

6.7.4 Comparison with water intrinsic permeability values

Since the viscous flow of fluids is governed by the Darcy equation (1.6), the intrinsic permeability should be equal for all fluids. The flow of gases is complicated by the Klinkenberg effect and compressibility, but the infinite pressure intrinsic permeability values for dry material should be equal to those for liquids such as water, as discussed in Chapter 1. The data for material conditioned at 100 % RH cannot be directly compared to that for water flow.

The water intrinsic permeability values for both the SRC- and PFA/PC-concretes have been shown to be less than about $10^{-21}\,m^2$. Table 6.5 indicates that the infinite pressure intrinsic permeability values for the concretes are more than four orders of magnitude greater than this. Although the water permeability measurements were complicated by the continued hydration of the materials, it is unlikely that the difference can be explained by this effect.

The water intrinsic permeability of the preliminary backfill grout has been measured as about $4 \times 10^{-16}\,m^2$. This value is approximately two orders of magnitude lower than the infinite pressure intrinsic permeability of the dry grout given in Table 6.6. In contrast, the water permeability of the reference backfill grout, at $2 \times 10^{-16}\,m^2$, is close to the infinite pressure intrinsic permeability. No water permeability data is available for the GGBS/PC-grout.

The data discussed above demonstrates completely different relationships between water and gas intrinsic permeability. Only the reference backfill grout shows the close agreement between the two data expected initially. The reasons for these differences in the behaviour of the materials are uncertain, and may reflect differences in pore structure under dry and

wet conditions, that is the presence of water not only fills pore space but changes its characteristics.

6.7.5 Interaction between gas and water in cementitious materials

Comparison of the intrinsic permeability values obtained for the experimental materials in the dry and 100 % RH conditioned states demonstrates that the influence of water within the pore structure of cementitious materials is crucial in determining gas migration rates. The comparison between the effective intrinsic permeability for the solution-diffusion migration mechanism and the measured intrinsic permeability values demonstrates that none of the experimental materials can be considered to be fully water saturated under any of the experimental conditions in this study (see Section 6.7.2).

As discussed above, the only mechanism available for gas migration in fully water-saturated material is solution-diffusion. The equivalent intrinsic permeability for solution-diffusion, about 10^{-23} m^2, is significantly lower than the lowest intrinsic permeability values measured for any of the 100 % RH conditioned materials. Hence it appears that the gas migration observed in this study may differ significantly from that expected for the truly water-saturated condition.

The application of a pressure difference to a water-saturated porous material will result in the expulsion of water from pores which exceed a particular size. The expulsion of a fluid from a capillary requires the application of an excess pressure denoted the capillary pressure. The capillary pressure p for a pore of radius r, assuming an angle of contact between the fluid and the capillary wall of 90°, is given by equation (1.34).

The approximate capillary pressures for the average pore radius of both the PFA/PC-concrete and the GGBS/PC-grout are 13 MPa whilst those for preliminary and reference backfill grouts are 210 and 320 kPa, respectively.

In the low pressure experiments, the maximum applied pressure was 200 kPa. This pressure can expel water from pores of the order of 0.7 μm. The MIP results for the two backfill grouts show that both materials exhibit a significant volume of porosity with pore radii above this value. Hence, water expulsion may occur in the 100 % RH conditioned specimens even in the low pressure experiments. Measurements made on the backfill grouts using higher applied pressures may exhibit significant water expulsion effects. This would result in measured intrinsic permeability values in excess of that expected for fully-saturated material based on the solution-diffusion model of gas migration. In addition, the increased expulsion of water at higher pressures may give an increase in permeability with applied pressure.

The above discussion assumes that the average pore radius obtained from the MIP measurements is the maximum pore size available. This is unlikely to be true and, although the pore size distributions of the high porosity grouts are substantially skewed towards the larger pore sizes, there will be significant porosity with radii in excess of the average values. The experimental results appear to demonstrate that the migration of gas is significantly affected by the presence of these larger pores.

Similar effects would be expected for the PFA/PC-concrete and the GGBS/PC-grout. However, the finer pore structure would mitigate the effect and hence the measured intrinsic permeability values for 100 % RH conditioned material should be closer to the value predicted by the solution-diffusion model. This is demonstrated by the comparison between the measured intrinsic permeability values for these materials and those measured for the backfill grouts.

The weight losses measured during conditioning at 100 % RH for both the preliminary and reference backfill grouts indicate that full water saturation may not have been achieved prior to the commencement of the experiments. It is possible that the water within the larger pores in these materials was draining under the influence of gravity. Thus, the data obtained for 100 % RH conditioned specimens may not be representative of the behaviour of fully water-saturated material.

The retention of water within a capillary is governed by the balance between the capillary pressure and the gravitational force exerted by the weight of the water. Consequently, water will only be retained in pores of a given radius if the pore length does not exceed a particular value. This length can be calculated by equating the capillary pressure to the hydrostatic pressure of a column of water in equation (1.35).

The maximum pore heights calculated from this equation are 21 and 32 m for the preliminary and reference backfill grout average pore radii, respectively. Since the specimen thicknesses are only a few centimetres, it is apparent that the weight loss cannot be explained by gravitational draining.

If the movement of water under the influence of gravity is occurring, despite the argument above, it may provide an additional means whereby the migration of gas within a repository could occur. In particular, the movement of water may allow a consequent migration of gas as a 'bubble' which migrates upwards as the water flows down around it. This is considered as a possible mechanism for the escape of gas from a nuclear waste repository as discussed in Chapter 14.

6.8 Conclusions

- The gas intrinsic permeability values for generic repository construction materials have been determined for specimens in dry and in both

partially and fully water-saturated conditions. It has been shown that the permeability of the structural PFA/PC-concrete is dependent on both gas type and average pressure under all conditions. The intrinsic permeability is approximately independent of average pressure at pressures above about 1 MPa. These effects are attributable to an additional component of gas flow caused by significant Knudsen flow at lower average pressures. The intrinsic permeability is significantly reduced for water-saturated conditions due to a reduction in the volume of porosity available for gas flow.

- Gas flow in the two high porosity backfill materials is not significantly dependent on the average pressure in the range 100 kPa to 3 MPa. Some differences are observed for measurements carried out using helium and argon. The contribution of Knudsen flow to gas migration in these materials is small at the average pressures studied due to the generally larger pore size when compared with the structural concrete. The intrinsic permeability is significantly reduced when the materials are water saturated, but it remains several orders of magnitude greater than that observed in the PFA/PC-concrete. The GGBS/PC-grout, typical of the encapsulation materials placed within waste packages, has a similar intrinsic permeability value to those measured for the backfill grouts when dry but exhibits a significantly lower permeability, close to that of the concrete, when water saturated. Some dependence on average pressure is observed. The properties of this material may be affected by damage during drying.
- The presence of interfaces within the cementitious materials, such as construction joints, results in an increase in the permeability of the materials when water is present. No significant increase was observed in dry materials.
- The observed intrinsic permeability values for water-saturated materials are all significantly greater than the intrinsic permeability predicted by the solution-diffusion mechanism of gas migration. This may be due to the movement or displacement of the water within the pore structure or, in particular, expulsion of water from the pores by the applied gas pressure. Such an effect would result in an increase in the intrinsic permeability at higher applied pressures.

6.9 Reference

Harris A W and Nickerson A K (1989) *Diffusion under water-saturated conditions in preliminary design backfilling grout (lime grout)*, Nirex Safety Study Report NSS-R189, UK Nirex Ltd, Harwell.

7

Water vapour and liquid permeability measurements in concrete

DOI: 10.1533/9781782423195.107

Abstract: This chapter shows how water permeability may be calculated from measurements of drying under a vacuum. The results obtained are for water vapour transport at low pressures, and gas slippage theory is then used to compare them with liquid water permeability measurements on samples of the same mixes. The experimental work includes the drying procedure and also the ISAT and the high pressure test for direct permeability measurements. The results from all of these tests are compared and additional gas and liquid permeability data from Chapter 5 are included for comparison. It is concluded that, with appropriate analysis, all of the procedures give comparable values for intrinsic permeability.

Key words: mortar drying, permeability, absorption test, ISAT, vapour permeability

7.1 Introduction

The processes which take place when concrete is dried are substantially controlled by the transport properties and thus observations of drying may be used to calculate values for the transport parameters. It is possible to consider the movement of water vapour from the drying front in terms of either vapour diffusion or pressure-driven flow. Following from the discussion in Section 1.2.2, it is apparent that the two approaches lead to the same equations so either approach may be used. In this chapter, the permeability is used and thus a number of other tests for permeability have been used to compare with results for the drying test on the same mixes.

7.2 Experimental methods

7.2.1 Sample preparation

Four mortar mixes were used and the mixture proportions and strengths are shown in Table 7.1. The test specimens (dimensions are detailed in each test procedure) were cast and kept under wet hessian for one day before demoulding. All samples were then cured in water at 20 °C until testing at 28 days. All testing was carried out at 20 ± 2 °C.

Table 7.1 Mortar mix proportions

Mix	Design 28 day cube strength (MPa)	PC (kg/m^3)	Sand (kg/m^3)	w/c
A	20	449	1411	0.79
B	35	544	1342	0.65
C	50	679	1235	0.53
D	60	943	108	0.38

7.2.2 The drying test

Samples were cast in cylindrical moulds 30 mm diameter by 50 mm long. The moulds were laid on their sides for setting in order to keep their ends under identical conditions. After curing, PVC adhesive tape was wound round the curved surfaces of the cylinders to prevent moisture evaporation except from the top and bottom ends. The cylinders were then placed in a glass desiccator connected to a vacuum pump with a 0–25 mbar (0–2.5 kPa) pressure gauge on it. The vacuum pump was run until the air in the desiccator became dry, as indicated by the colour change of silica gel in the desiccator (this took up to 30 h). The colour changes at water content of 8 % by mass which occurs at a humidity of 15 % at atmospheric pressure, i.e. a partial vapour pressure of 0.3 kPa.

The vacuum pressure was monitored during the drying process. At different times, samples were taken out of the desiccator and weighed and then split down the axis and the depth of drying at each end was measured visually. No precautions were taken to prevent carbonation of the samples but, since the experiments only lasted for a few days, the weight gain from this process was not considered to be significant.

7.2.3 Oven drying

Specimens were dried in an oven for 3 days at 105 °C to calculate porosity.

7.2.4 Water permeability

The water permeability was measured in a modified Hoek cell as described in Section 4.2.2. Due to the high pressures used, the flow through the samples became constant only approximately 1 h after the start of the test for most of the samples. The flow rate was determined by measuring the rate of water flowing from the upper surface using a graduated measuring cylinder.

7.2.5 The ISAT test

The initial surface absorption test (ISAT) was carried out as described in Section 3.2.

7.2.6 Water absorption (sorptivity) test

Cubes from mix C (100 mm) were oven dried at 105 °C and then immersed in water to a depth of 20 mm and the mass gain was recorded at intervals up to 2 h. The test is described in Section 4.2.1.

7.2.7 Test programme

The programme of testing is shown in Table 7.2.

7.3 Methods of analysis of results

7.3.1 Transport processes

For the analysis of the results, it is necessary to determine which processes are transporting the water during the tests. The main process that is considered in this chapter is pressure-driven flow measured by permeability as described in equations (1.4) and (1.7)

It should also be noted that equation (1.4) can only be applied to a steady state in which the pressure is constant. For all of the work in this chapter, equation (1.7) was integrated with respect to time and the condition of constant pressure through the time step is therefore met as the time step approaches zero.

7.3.2 The drying test

The rate of loss of moisture from the specimens will be governed by the movement of vapour from the drying front to the surface. There are two

Table 7.2 Testing programme

Test	Mixes tested	Number of replicates	Properties measured
Drying	A, B, C, D	3 (6 of mix C)	Dry depth, mass loss and pressure
High pressure permeability	A, B, C, D	2	Flow rates in steady state
ISAT	C	2	Flow rates at 10, 20, 30, 60 and 120 min
Adsorption	C	2	Mass at 0, 5, 15, 30, 60 and 120 min

possible transport processes to consider for this test: pressure-driven flow and moisture diffusion. It is noted in Section 1.2.2 that for a gas or vapour where the concentration is proportional to the pressure the equations for the two mechanisms give the same result as shown in equation (1.19).

The pressure at any point in the system will be made up of contributions from several different gases and vapour. The effect of them will be additive and any pressure measurement will record the total. A change in one partial pressure will not affect the others. At the drying front, the pressure of water vapour will depend on the equilibrium with the adjacent liquid and will be determined by the temperature and surface tension. The pressure outside the sample will be determined by the vacuum pumping and will be substantially lower. Thus there is a pressure drop and the flow caused by it will be controlled by the permeability.

Diffusion is driven by a chemical concentration gradient and would typically be relevant to a liquid with a higher concentration of salt at one position than another. It is also used to measure the movement of one gas through another and could be the main mechanism to transport vapour through air from a drying surface. In this experiment, however, there is virtually no air present with the pressure in the desiccator reduced to 0.1 kPa (0.001 atm) and the diffusion coefficient for vapour through air cannot therefore be relevant. The transport is therefore controlled by permeability and is described by the Darcy equation (1.4) which may be expressed as:

$$V_F = \frac{K_v}{e}\frac{P}{x} \qquad [7.1]$$

where:

V_F is the Darcy velocity for the water vapour (m/s)
K_v is the intrinsic permeability for the vapour (m^2)
P is the vapour pressure difference (Pa) and
x is the distance from the drying front to the surface of the sample (m).

The Darcy velocity may be related to the movement of the drying front by equating the water volumes as follows:

$$V_F = \varepsilon \frac{dx}{dt} W_F \qquad [7.2]$$

where:

ε is the porosity
t is time (s) and
W_F is the ratio of the water vapour volume to the volume of the same mass of water as a liquid.

Combining equations (7.1) and (7.2) and integrating gives:

$$K_v = \frac{eW_F \varepsilon x^2}{2Pt} \quad [7.3]$$

The drying depth is related to the mass loss by the relationship:

$$x = \frac{M}{\varepsilon A \rho} \quad [7.4]$$

where:

M is the cumulative mass loss (kg)
ρ is the density of liquid water (kg/m^3) and
A is the cross-sectional area through which the transport is taking place (m^2).

Equation (7.3) may be seen to have a similar form to the equation presented by Vuorinen and Valenta (cited by Neville (2011)) for water intruding into concrete under pressure:

$$k = \frac{\varepsilon x^2}{2ht} \quad [7.5]$$

where k is, in this case, the coefficient of permeability or hydraulic conductivity (m/s) and h is the head of water.

The partial pressure of water vapour above a liquid surface at 20 °C is 2 kPa. This pressure is correct for pure water but will have been affected by the presence of the dissolved ions in the water. This would be expected to lower the vapour pressure and lead to a slight reduction in the flow.

The measured pressure in the desiccator was initially 0.6 kPa but fell to 0.1 kPa during the test. Of the pressure in the desiccator, the partial pressure due to vapour will initially have been approximately 1 % of the total (which would be the case in a room at a humidity of 50 %). Thus the vapour pressure in the desiccator was below 1 % of 0.6 kPa and the drop in pressure from the drying front to the concrete surface was close to 2 kPa.

Not all of the pores will dry at exactly the same pressure. It has been shown (Vuorinen, 1970 and Section 6.7.5) by measuring gas permeabilities at different humidities that the Kelvin equation (3.1) gives a good indication of the pore sizes in concrete that will sustain a meniscus. This shows, however, that the smallest capillary pores (0.01 μm) will not sustain a meniscus below 90 % relative humidity (RH). Thus all the pores will empty of liquid within 10 % of the distance over which the pressure drops.

Using standard gas constants for a molecular mass of 18, the constant W_F was calculated to be 1.25×10^3 by assuming the vapour was an ideal gas. The viscosity of water vapour $e = 2 \times 10^{-5}$ Pa s.

7.3.3 Calculation of porosity from weight loss during oven drying

The porosity of the PC samples was calculated from the weight loss using the Powers model (Powers, 1960). For this calculation, the water and cement which combine to form hydrated cement are assumed to do so in a fixed ratio. Neville (2011) uses a w/c ratio of 0.23:1, but in this work a ratio of 0.25:1 has been used because it gave a better agreement with other measurements of porosity as discussed in Chapter 8.

The weight of the samples when cast M_{wet} was obtained by subtracting the weight of the container from the initial weight. The weight of water M_w in the wet sample was then calculated from the mix proportions. The dry weight M_{dry} was measured. Thus the mass of absorbed water is given by:

$$M_{aw} = M_w - (M_{wet} - M_{dry}) \quad [7.6]$$

and from the assumption of the ratio of combination of 4:1, cement:water (i.e. w/c = 0.25), the mass of hydrated cement is given by:

$$M_{hc} = 5 \times M_{aw} \quad [7.7]$$

The mass of each component of the hydrated sample was therefore known and the specific gravity of the sample was calculated from equation (7.8):

$$\frac{M}{SG} = \sum \frac{M_i}{SG_i} \quad [7.8]$$

where the specific gravity (SG) is the mass divided by the net (skeletal) volume, and M_i and SG_i are, respectively, the mass and specific gravity of component i.

The sum is across all of the components of the dry mix, i.e. cement, hydrated cement, aggregate (if present) and the solids in the admixtures. The specific gravity of each component was measured experimentally except for the hydrated cement for which a value of 2.15 g/cc was used (Neville, 2011). The dry density (DD) was obtained by dividing the dry mass by the volume obtained by weighing wet and dry and the porosity was then obtained from equation (7.9):

$$\text{Porosity} = 100\left(1 - \frac{SG}{DD}\right) \quad [7.9]$$

This is the standard equation for calculating the porosity of hydrated samples by measuring the dry and saturated densities.

7.3.4 The absorption and ISAT

For the ISAT, the transport process will be pressure-driven flow but, in this case, the pressure driving it will arise from the capillary suction at the wetting front. The flux is given in equation (4.12).

The terms for pore size and surface tension arise from the inclusion of capillary suction in the analysis. For the analysis of the ISAT results, it is only necessary to equate the Darcy velocity to the flux divided by the surface area and equation (4.12) may be used directly. The experiment gives a flow rate of water in a capillary tube and, if this is reduced in proportion to the ratio of the area of the capillary to the wetted concrete surface, the Darcy velocity is obtained.

For the analysis of the absorption results the flux is related to mass gain:

$$F_V = \frac{1}{\rho}\frac{dM}{dt} \qquad [7.10]$$

and equations (4.12) and (7.10) are integrated to give:

$$K = \frac{reM^2}{4s\varepsilon tA^2\rho^2} \qquad [7.11]$$

where M is the cumulative mass gain.

7.3.5 The high pressure test

The high pressure test clearly measures the permeability and this was calculated from the observed flow rate by direct application of Darcy's law (equation 4.2).

7.4 Results and discussion

Oven drying of the samples causes micro-cracking and will have contributed to the spread of data. The results are shown in Figs 7.1–7.6.

Figure 7.1 shows the average values for water permeability. It may be seen that the methods of analysis give consistent results from the different experiments and also the expected increase of permeability with w/c ratio.

7.4.1 Comparison of permeabilities from mass loss with those from drying depth

Figure 7.2 shows all of the permeability results for mix C. The first three series (adsorption, ISAT and high pressure) are very close. The vapour permeability would be expected to be substantially higher, but the results from the measured drying depths may be seen to fall over a very wide range.

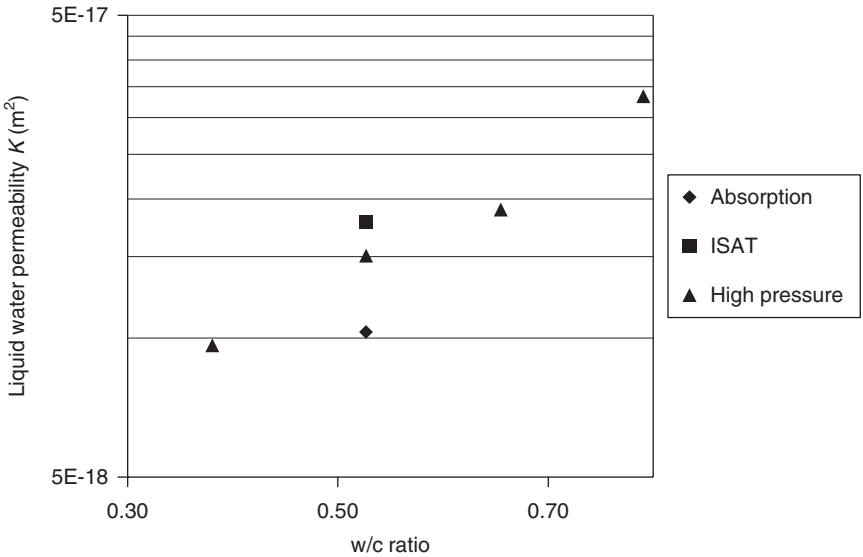

7.1 Results for liquid water permeability.

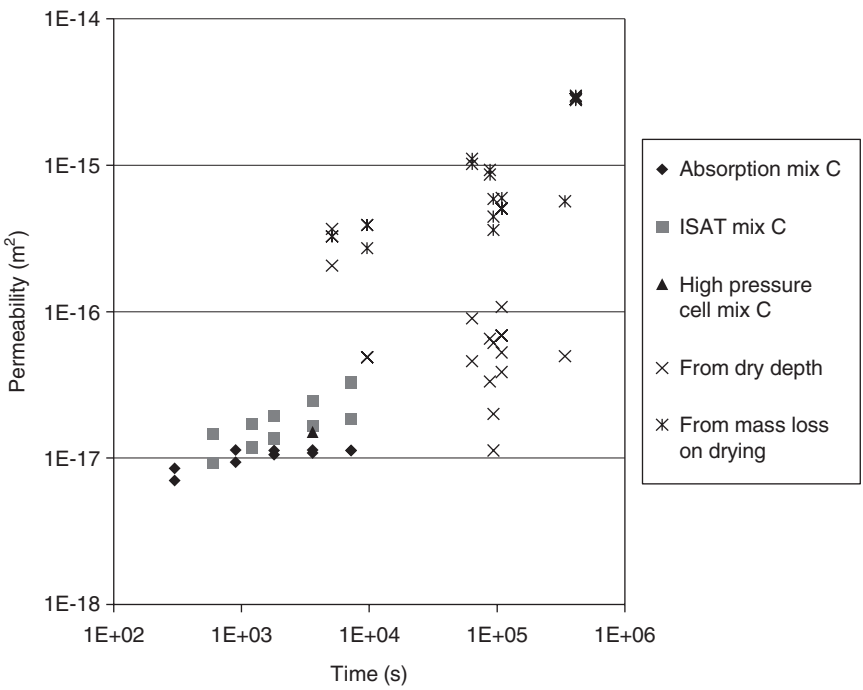

7.2 All permeability results vs time for mix C.

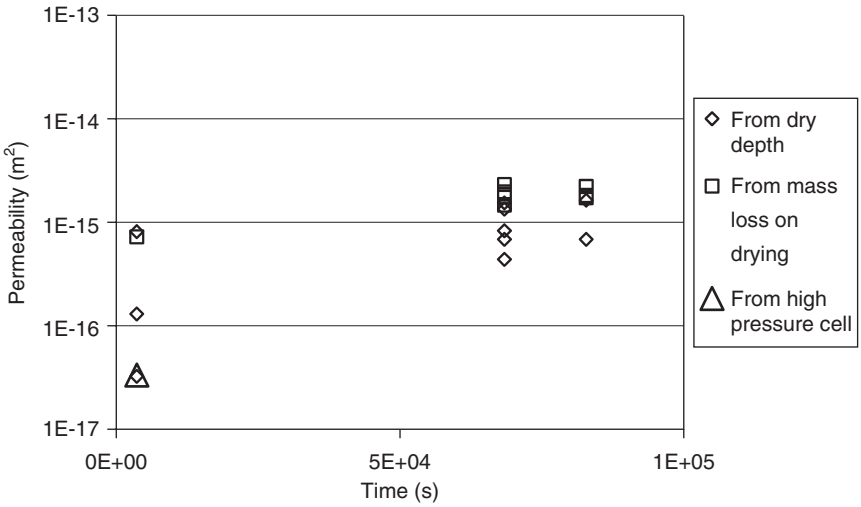

7.3 Permeability vs time for mix A.

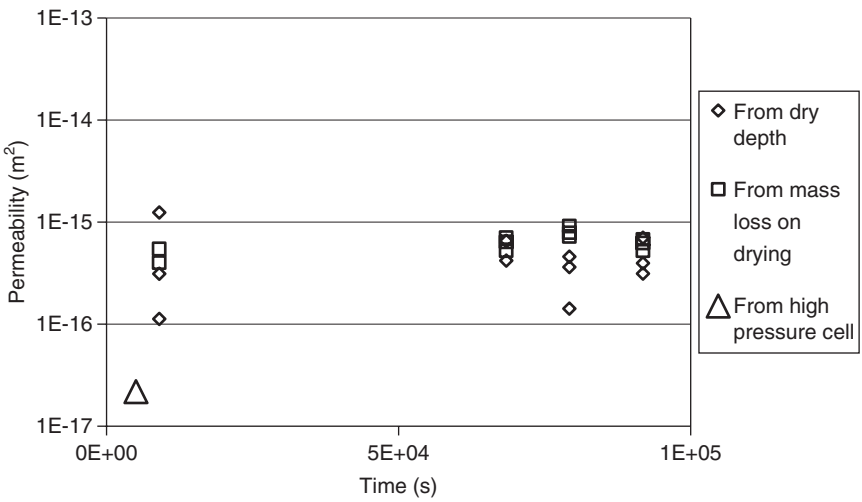

7.4 Permeability vs time for mix B.

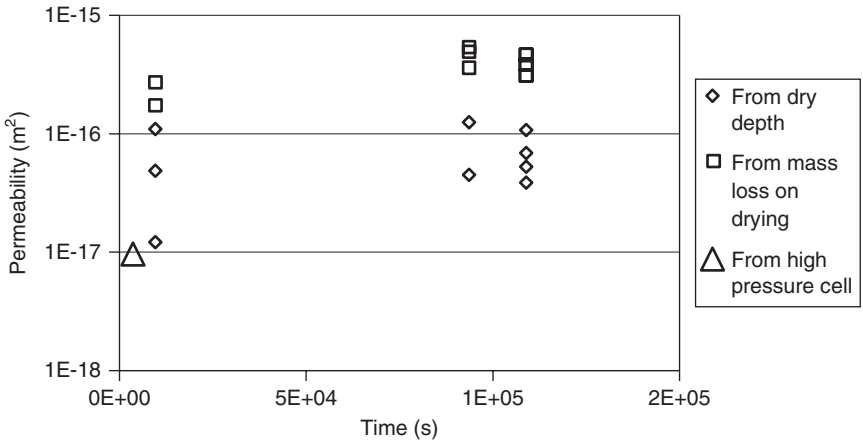

7.5 Permeability vs time for mix D.

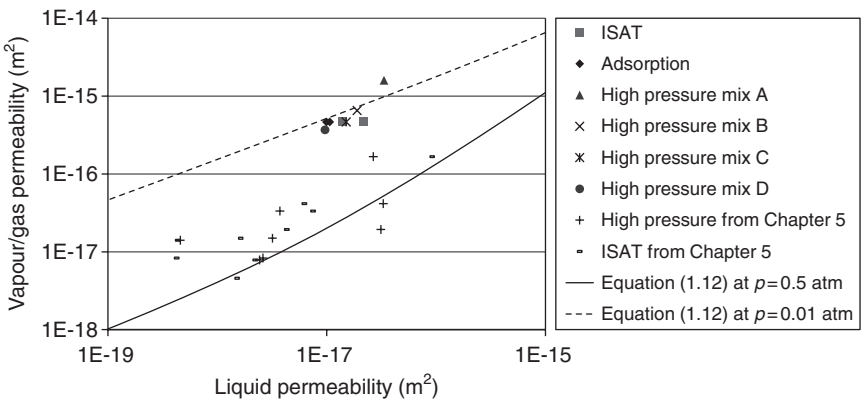

7.6 Vapour permeability vs liquid permeability for all results.

The results from mass loss are, however, grouped in an expected range and are therefore indicated to be far more reliable than the results from drying depth. The results from the drying depth measurements are generally lower than those for mass loss, indicating that significant drying may have occurred from regions which still appeared to be wet when the samples were inspected. Since the larger pores would dry first, this implies that the visible moisture was in the smaller ones (possibly below 0.1 μm).

The reduction in permeability which is normally observed during testing with water may be caused by sedimentation causing blocking of pores and would thus not be expected to occur during vapour transport.

Figures 7.3, 7.4 and 7.5 show the permeability vs time for mixes A, B and D for the high pressure cell and drying experiment data. These support the observation that the mass loss data was far more consistent than the observations of drying depth. They all also show the drying depth data giving lower results. The drying front was readily visible on the tested samples, but a further disadvantage of this method would be that on some samples (e.g. white cement) it could be very difficult to see. The mass loss was observed to be the more reliable test in these laboratory trials, but this conclusion might not be valid in other circumstances such as site testing.

The high pressure cell data which is for liquid rather than vapour is consistently lowest and the reasons for this are discussed below.

7.4.2 Relationship between liquid and vapour permeabilities

The Klinkenberg equation is discussed in Section 1.2.1. Values of b were calculated by Bamforth (1987) for concrete from the average values of water and gas permeability as follows:

$$b = \beta_1 K_1^{\beta_2} \qquad [7.12]$$

in which β_1 and β_2 are constants and Bamforth proposed the values:

$$\beta_1 = 1.635 \times 10^{-8}$$

and

$$\beta_2 = -0.5227$$

Substituting the value of b in equation (1.12), a relationship between water permeability and gas permeability is derived. Bamforth reported that the gas permeability values may be one or two orders of magnitude higher and the largest difference would occur when testing using a partial vacuum. It is therefore important to consider the effect of slippage when interpreting results obtained from gas measurement as a means of assessing concrete quality.

It was found in Chapter 5 that Bamforth's constants gave a lower bound for the water permeability. The results from this work are included in Fig. 7.6 and the line through the data has been derived from equations (7.10) and (7.11) and using

$$\beta_1 = 3.5 \times 10^{-9}$$

and

$$\beta_2 = -0.48$$

which may be seen to fit the data. For the results from Chapter 5 which are shown on the graph, the average gas pressure was 0.5 atm.

Figure 7.6 also shows a second line from the same equations using the same constants but with the average pressure at 0.01 atm (1 kPa) which is applicable to the work reported here. The graph shows the results for the different tests on liquid water plotted against the vapour permeabilities derived from mass loss and these may be seen to lie close to the line.

7.5 Conclusions

- A simple laboratory procedure in which mass loss is measured may be used to yield results for the permeability of concrete to water vapour which are consistent with the results from other tests.
- This work indicates that, when measurements are made on samples dried under vacuum, the depth of drying observed by breaking the samples open does not give the best results. The mass loss is far more reliable.
- Gas slippage theory must be used when calculating the intrinsic permeability from the transport of water vapour in concrete.
- These results therefore indicate that this method of analysis gives agreement between the permeability values calculated from observations from the different experiments and that they may be used to confirm the results from individual tests and identify testing methods that are giving inconsistent results.

7.6 References

Bamforth P B (1987)The relationship between permeability coefficients for concrete using liquid and gas, *Magazine of Concrete Research*, **39** (138), pp. 3–11.

Neville A M (2011) *Properties of Concrete* (5th edn), Pearson, Harlow.

Powers T C (1960) Physical properties of cement paste and concrete, *Proceedings of the 4th International Symposium on the Chemistry of Concrete*, Vol. 2, US Department of Commerce, Washington DC, pp. 577–613.

Vuorinen J (1970) On use of dilation factor and degree of saturation in testing concrete for frost resistance, *Nordisk Betong*, **14** (1), pp. 37–64.

8

Measurement of porosity as a predictor of the transport properties of concrete

DOI: 10.1533/9781782423195.119

Abstract: Fluid transport through concrete takes place almost entirely through the pores. The porosity is a measure of the total pore volume and does not take account of the connectivity or tortuosity of the pores, but it would still be expected to be a good predictor of transport. This chapter introduces different methods for measuring porosity and transport. The precise mechanism involved in a 'vapour transport' experiment is then discussed and relationships between porosity and transport are presented.

Key words: porosity, helium intrusion, mercury intrusion, oxygen permeability, vapour transport.

8.1 Introduction

It is often easier and more reliable to measure the porosity of concrete and use it to predict the transport rather than to measure the transport properties directly. Fluid transport through concrete takes place almost entirely through the pores. This porosity can be measured directly with helium or mercury intrusion and calculated from weight loss on drying. These three measurements will give different results, and it is important to compare them before using them as predictors. A range of transport measurements are compared with porosities measured using these three methods. Chloride transport is considered in detail in Chapters 10–13, but a simple method is presented here to compare with porosity. Carbonation is controlled by the transport of atmospheric carbon dioxide into concrete and is thus an indirect measure of transport. Electrical resistivity is a measure of electromigration. A method for measuring oxygen transport is presented in detail. Finally, a method intended to measure water vapour transport is presented, but it is concluded that the samples were actually saturated during the test, indicating that the drying test presented in Chapter 7 would be preferred for this measurement.

Table 8.1 Mix designs

Mix	A	B	C	D
SF/(PC + SF)	0.20	0	0.20	0
Water/(PC + SF)	0.30	0.30	0.46	0.46
Superplasticiser/(PC + SF)	0.014	0.014	0.019	0.019
Fine aggregate/(PC + SF)	1.5	1.5	2.3	2.3
Coarse aggregate (5–20 mm)/(PC + SF)	3	3	4	4
PC (kg/m^3)	344	430	252	315
SF (kg/m^3)	86	0	63	0

8.2 Sample preparation and testing programme

8.2.1 Sample preparation

The mix designs are shown in Table 8.1. The silica fume (SF) was supplied by Elkem Chemicals from their works in Norway. The superplasticiser was a salt of napthalene formaldehyde condensate supplied by FEB (UK). The fine aggregate came from North Nottinghamshire and was a natural sand. The percentages given for superplasticiser were calculated from the quantities of solids which form 40 % of the solution as supplied. Mortar samples were made with the same proportions but without the coarse aggregate. Paste samples were made with the same proportions but without the coarse or fine aggregates.

The mortar samples were mixed in a Hobart mixer. The superplasticiser was mixed with the water and added to the sand and cement when they had already been mixed in a dry condition. Mixing continued for 2 min after a uniform consistency was observed. The highest speed of the mixer was used for the mixes with lower workability but, for those with highest workability, this caused them to be ejected from the mixer and a lower speed was used. The samples were cast in the appropriate moulds, kept covered in the laboratory for 24 h and then placed in the following curing conditions.

After casting, the samples were covered and kept at 20 °C for 24 h until they were struck. They were then cured using the three different curing conditions given in Table 8.2. The samples were tested at 3, 28 and 90 days. All combinations of the four mixes, three curing conditions and three test ages were used for the tests, giving a total of 36 'sample conditions' which reflect a wide range of possible conditions for site concrete when first exposed to an aggressive environment.

Different types of sample were used for the different tests as described below. No study was made of the surface properties of concrete, so for all samples used to measure transport properties samples were cut from the

Table 8.2 Curing conditions

Curing condition 1 (CC1)	99% RH, 20°C
Curing condition 2 (CC2)	Treated with curing membrane and then stored at 70% RH, 20°C for 6 days and then in water at 6°C
Curing condition 3 (CC3)	In water at 6°C

Table 8.3 Summary of test programme

Test	Material
Porosity measurements	
Mercury intrusion	Paste
Helium intrusion	Paste/mortar/concrete
Weight loss	Paste/mortar/concrete
Transport property measurements	
Chloride transport	Concrete
Carbonation	Mortar
Oxygen transport	Mortar
Water vapour transport	Paste
Initial resistivity	Concrete
28 day resistivity	Concrete
Other properties	
Compressive strength	Concrete

centres of the specimens and the outer surfaces were not tested. The temperature of 6°C was chosen as being the lowest at which mixes of this type should be placed on a well managed site.

8.2.2 Sample testing programme

The tests that were carried out are summarised in Table 8.3. Compressive strength was measured because this is the property that is most often known for concrete mixes. The compressive strength was measured on 100 mm concrete cubes.

8.3 Tests for porosity

8.3.1 Helium intrusion

The net volume of samples was measured by helium intrusion using a Micromeritics Autopycnometer 1320. This machine measures the volume of helium that a sample displaces (i.e. the net volume). The sample is positioned

in one of two chambers which initially have equal volumes. After evacuation, an equal volume of helium is introduced into each chamber and the pressures are measured. The machine then calculated a volume change to the empty chamber to make the two volumes equal, i.e. to compensate for the presence of the sample. The volume change is effected with a piston and the helium is introduced again. The cycle repeats until equal pressures are found in both chambers at which time the volume of the sample is known from the position of the piston.

The samples were ground to pass a 1.18 mm sieve before testing to ensure full penetration into the pore structure. The samples were then weighed before testing and the specific gravity was calculated as the mass divided by the net volume. The dry density (DD, the mass divided by the bulk volume) was obtained from the weight loss measurements. The porosity was then obtained from equation (7.9).

The results are presented in Fig. 8.1. The consistent trends which may be observed in this figure indicate that the resolution of the measurements was adequate to differentiate the samples.

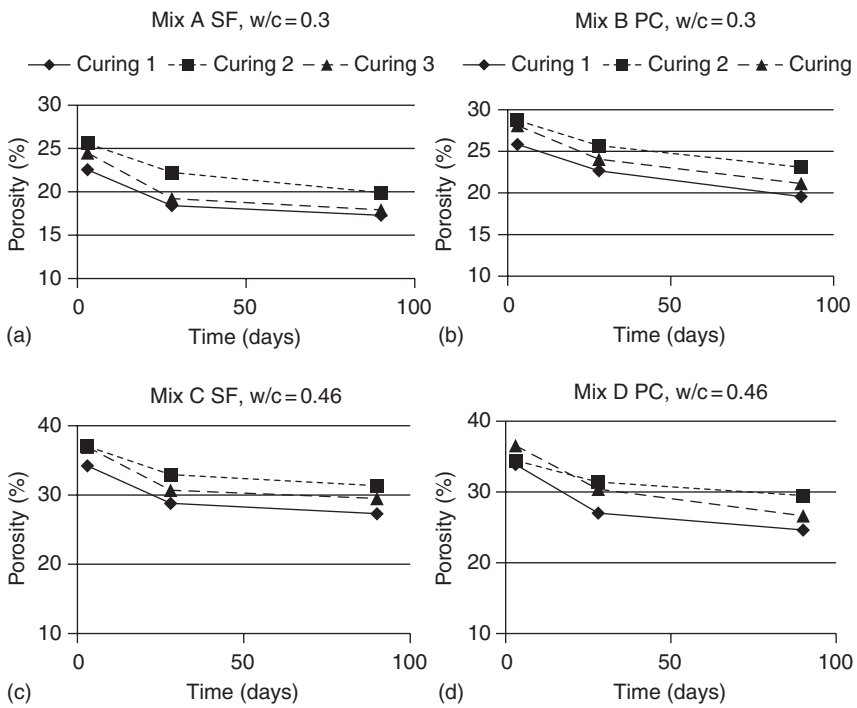

8.1 Porosity results for paste samples measured as percentages (obtained by helium intrusion). (a) Mix A SF, w/c = 0.3; (b) mix B PC, w/c = 0.3; (c) mix C SF, w/c = 0.46; (d) mix D PC, w/c = 0.46.

8.3.2 Mercury intrusion

Cylindrical samples of paste with a diameter of 25 mm and a length of approximately 15 mm were intruded using a Micromeritics Auto-Pore 9200 intrusion machine. In this technique, a small mortar sample is immersed in mercury in a glass container connected to a capillary tube with a conductive metallic coating. The entire container is then immersed in oil which is pressurised. As the pressure increases, the mercury is forced down the capillary tube and into the pores of the mortar. The volume entering the pores is measured as a change of electrical capacitance of the capillary tube. Mercury is used, despite its health risks, because of its high surface tension.

The machine had a maximum operating pressure of 414 MPa. The diameter of the pores was obtained using equation (8.1):

$$r = \frac{-2\gamma \cos\varphi}{P} \qquad [8.1]$$

where:

r is the radius of the smallest pore that the mercury can enter
γ is the surface tension of the mercury
φ is the contact angle of the mercury with the pore surface and
P is the pressure.

The values used for the contact angle and the surface tension of the mercury were 130° and 0.484 N/m which give a minimum pore diameter of 0.003 μm at the highest pressure. Figure 8.2 shows a typical output from the mercury intrusion. In order to characterise the salient features of the intrusion curves for further analysis, the total intruded volumes in the pore size ranges in Table 8.4 were obtained from the experimental data. The recovery volume is the volume of mercury which came out of the samples when the pressure was released.

These ranges are presented in Fig. 8.2 which shows the cumulative and differential intrusion volumes for two replicate samples with the size ranges marked with the vertical gridlines. For each range, the porosity was calculated as a percentage of the bulk volume of the samples.

8.3.3 Weight loss

For this purpose, samples were cast in disposable plastic cups. This method was used because the cups were convenient and did not require mould oil which would have affected the weight. The following weights were recorded:

1. wet weight when cast;
2. wet (submerged) and surface dry weights after curing to give the density;
3. dry weights after drying to constant weight in a ventilated oven at 110 °C.

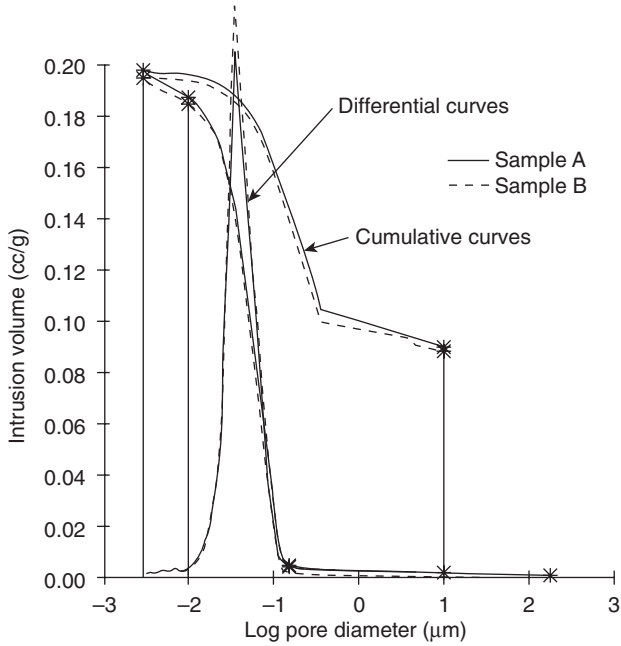

8.2 Typical cumulative and differential mercury intrusion curves for two replicate samples. The vertical lines show the ranges that were used for analysis.

Table 8.4 Porosity in pore size ranges

Range	Typical porosity
10–170 μm	0.5%
0.15–10 μm	0.7%
0.01–0.15 μm	16%
0.003–0.01 μm	7%
0.003–10 μm (recovery)	10%

The Powers model was used to obtain the porosity as described in Section 7.3.3. These equations do not work for samples containing additional components such as SF. Attempts were made to extend the model using data from thermogravimetric analysis to determine the proportions of hydration products in the hydrated SF samples, but the porosities obtained were not consistent with other observations and are not reported here.

8.4 Tests for properties controlled by transport

8.4.1 Carbonation

Mortar samples measuring 25 mm by 25 mm by 200 mm long were exposed to an atmosphere of 90 % CO_2 at a pressure of 1 bar at 21 °C and 70% relative humidity (RH). The apparatus for this experiment was complicated by the need to extract moisture arising from the reaction. The shrinkage was measured at 18 days after exposure with a comparator using a linear voltage displacement transducer (LVDT). The recorded strain was a total arising both from the carbonation and from drying shrinkage while in the carbonation chamber.

8.4.2 Resistivity

Concrete samples 75 mm diameter by 220 mm long were cast with a 12 mm diameter steel bar 225 mm long positioned centrally and projecting 50 mm from one end and thus having 45 mm cover at the other end. The samples were cast upside down by locating the steel bar in a wooden block in the base of a cylinder mould. They were then immersed in salt-saturated water to a depth of 190 mm (i.e. with 30 mm of concrete clear of the solution). A circuit was then formed between the steel bar and a mild steel secondary electrode in the salt solution. The chloride was driven into the concrete by electromigration by applying a negative voltage to the secondary electrode at 100 mV relative to a saturated calomel reference electrode in the solution for up to 28 days using a potentiostat.

To measure resistivity, the potentiostat was disconnected and an alternating voltage of 100 mV at 50 Hz was applied to the circuit and the current was measured. These samples were also used for corrosion tests reported in Chapter 13 but, by using alternating current, the readings of resistivity were not affected by corrosion of the bar.

8.4.3 Chloride transport

Concrete beams were cast measuring 500 mm long by 100 mm square. A rebate 20 mm deep by 40 mm wide by 300 mm long was formed in the top of each beam and, after curing, four 32 mm diameter holes were drilled to a depth of approximately 10 mm in the bottom of the rebate using a heavy rotary hammer drill. The rebate was then filled with saturated salt solution and the samples kept at approximately 20 °C. After 28 days, samples were drilled from the bottom of the holes and tested for acid soluble chloride by titration. The procedure was:

1. remove salt solution and wash off remaining salt;
2. permit to dry at room temperature;

3. drill for 10 s and discard dust;
4. drill for 5 s and retain dust as sample 1 (approx. 5 mm depth);
5. drill for 5 s and discard dust;
6. drill for 5 s and retain dust as sample 2 (approx. 10 mm depth).

The depth of the sampling was calculated by weighing the samples and checked by measurement with a caliper. The results were obtained by fitting an exponential decay function to the two readings and integrating.

The transport in this test will have been substantially affected by ion–ion interactions as discussed in Chapter 10 so no attempt was made to obtain diffusion coefficients using Fick's law.

8.5 Oxygen transport

8.5.1 Apparatus

Sections (20 mm long) of 25 mm mortar cores were tested for oxygen transport under an applied pressure difference of 1 and 2 bar. The rate of flow was measured with a bubble flow meter. The apparatus is shown in Fig. 8.3. The seal is formed by first coating the curved surface of the sample with silicone rubber and then compressing it into a surround of synthetic rubber.

8.3 Leeds gas permeameter.

8.5.2 Preparation of the samples

Mortar samples were cast as 100 mm cubes. When they were struck, the 25 mm cores were cut from them and 20 mm long samples were cut from the central portion of the cores. At the test age, the samples were dried for 24 h and at 105 °C and placed in a desiccator. When they had cooled, a thin film of silicone rubber was applied to the curved surfaces and allowed to set for 24 h before testing.

Before testing the CC2 samples, any remaining curing agent on the end surfaces was removed using no. 40 grit sandpaper. Penetration of this material into the pores could, however, have reduced the flow rates, but inspection of the samples indicated that this would not have been significant.

8.5.3 Testing procedure

The samples were tested at applied oxygen pressures of 1 and 2 atm above ambient. Two samples were tested for each condition. Before testing, the samples were allowed a minimum of 30 min to equilibrate and to purge the air from the system and, for samples with very low flow rates, this was increased to several hours. Two readings were taken on each sample at each pressure and the average of these two readings was used. Different diameter bubble flow meters were used, ranging from 1.7 mm for very low flows to 10 mm for high flows.

Leakage was checked using some spare samples; these were spread with silicone rubber over the flat surfaces as well as the curved surface and checked for gas flow. No flow was observed. If there had been any substantial leakage, the range of the data would have been increased.

8.5.4 Calculation of the coefficient of permeability

The general equations for pressure-driven flow from Section 1.2.1 are used and the analysis is similar to that in Section 4.5. If Q is the volume per second passing through the sample measured at the low pressure P_1 (assuming an ideal gas):

$$Q = V_F A \frac{P}{P_1} \qquad [8.2]$$

where:

A is the cross-sectional area of the sample and
P_1 is the low pressure (i.e. the pressure on the outlet side of the sample, this is atmospheric pressure in this work).

Thus:

$$\frac{Q}{A}\frac{P_1}{P} = \frac{K}{e}\frac{\mathrm{d}P}{\mathrm{d}x} \quad [8.3]$$

and:

$$\frac{\mathrm{d}x}{\mathrm{d}P} = \frac{A.K}{Q.e.P_1}P \quad [8.4]$$

Integrating across the sample:

$$X = \frac{AK(P_2^2 - P_1^2)}{2QeP_1} \quad [8.5]$$

where:

P_2 is the high pressure (i.e. the pressure on the input side of the sample) and
X is the sample thickness.

Thus:

$$K = \frac{2XQeP_1}{A(P_2^2 - P_1^2)} \quad [8.6]$$

The viscosity of oxygen gas $e = 2.02 \times 10^{-5}\,\mathrm{Ns/m^2}$ and $P_1 = 1\,\mathrm{atm} = 0.101\,\mathrm{MPa}$.

8.5.5 Relationship between readings at different pressures

The relationship between the readings at the two pressures is shown in Fig. 8.4 which is plotted logarithmically to spread the readings. It may be seen that the data lie very accurately on the line of equality, indicating that the use of Darcy's equation was justified and Knudsen flow was not significant. The average of the two readings was calculated and is plotted in Fig. 8.5.

8.6 Vapour transport

8.6.1 Preparation of the samples

Paste samples for measurement of water vapour transport were cast as 100 mm cubes, and 25 mm diameter cores were cut from them before curing. At the test age, thin discs were cut from the central portion of the cores. The thickness of each disc was measured with a micrometer. The thickness of all the discs fell in the range 3.5–4.7 mm. The discs were permitted to dry at room temperature for approximately 2 h and then set in epoxy resin in holes formed in the lids of 125 cc sample bottles. The bottles were then part filled with de-ionised water and the lids put on them and sealed as shown

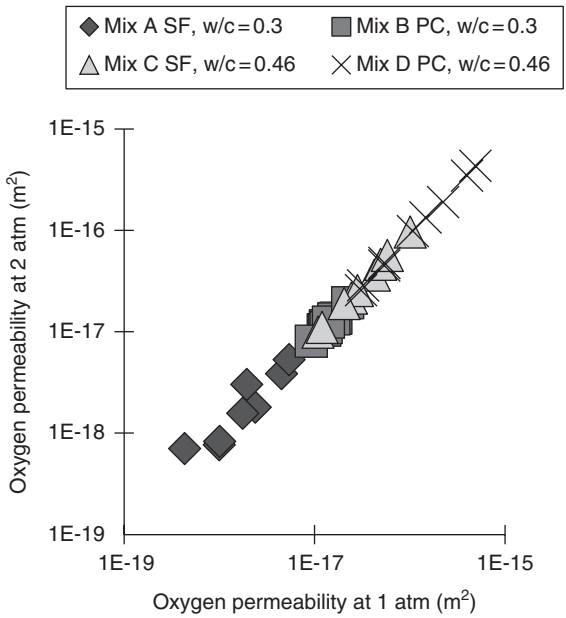

8.4 Relationship between measurements of the oxygen permeability *K* made at 1 atm pressure drop and those at 2 atm.

in Fig. 8.6. The effectiveness of the seals was checked by briefly inverting the bottles. the bottles were then placed in trays in large storage containers. Details of the environmental conditions in the containers were:

Container 1: Open to the atmosphere in a room controlled at 70 % RH.
Container 2: Sealed with a quantity of sodium dichromate in the bottom to give an RH of 55.2 %.
Container 3: Sealed with a quantity of lithium chloride to give an RH of 12.4 %.

All of the containers were kept at 21 °C. The RH was checked periodically using an electronic probe. The water transmission rate was measured by weighing the bottles. Two samples were tested for each of the four mixes, three curing conditions, three test ages and three containers to give a total of 216 bottles.

8.6.2 Blank tests

In addition to the sets of cementitious samples, a number of blank samples (coins) were tested. No measurable weight loss occurred, and this confirmed that the bottles and seals were impermeable and the only transmission path was through the samples.

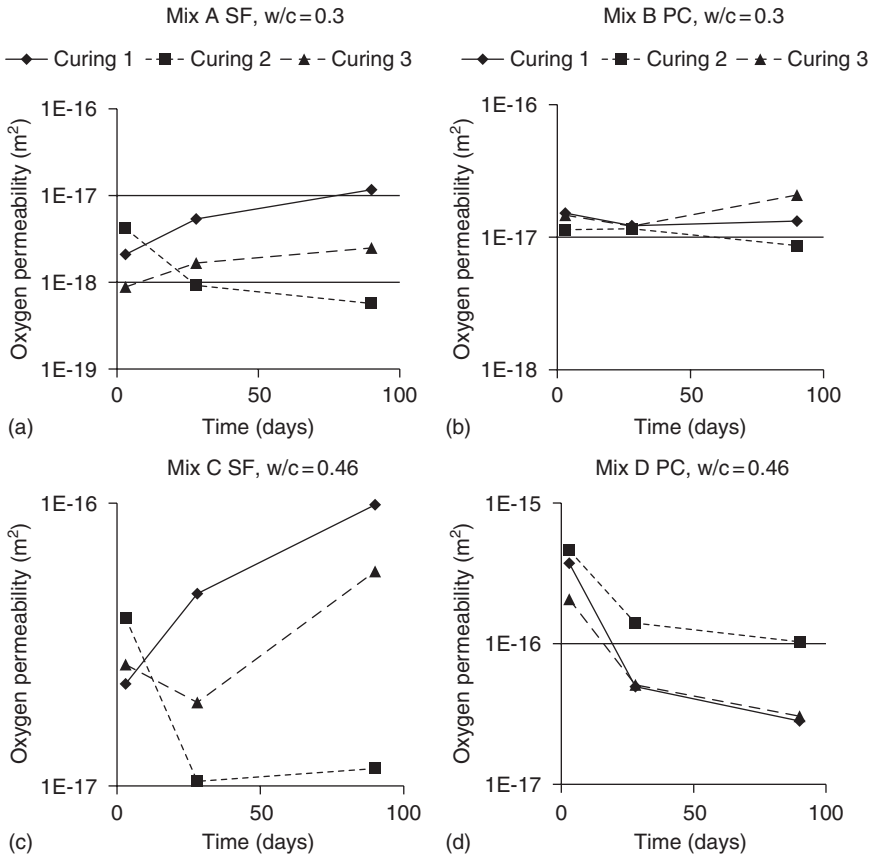

8.5 Oxygen permeability K in m^2 calculated from an average of the readings at 1 and 2 atm. (a) Mix A SF, w/c = 0.3; (b) mix B PC, w/c = 0.3; (c) mix C SF, w/c = 0.46; (d) mix D PC, w/c = 0.46.

8.6.3 Analysis of the data

Initial preparation

The weights of the bottles were initially plotted against time. A typical plot showing results of six samples is shown in Fig. 8.7. These plots were used to identify bottles where obvious leakage was causing a wrong result. Out of the total of 216 bottles, there were three of this type and the results from them were not used.

Interpretation of the data

It may be seen from Fig. 8.6 that the initial mass loss rate is higher than the steady state. The following two processes are believed to contribute to this effect.

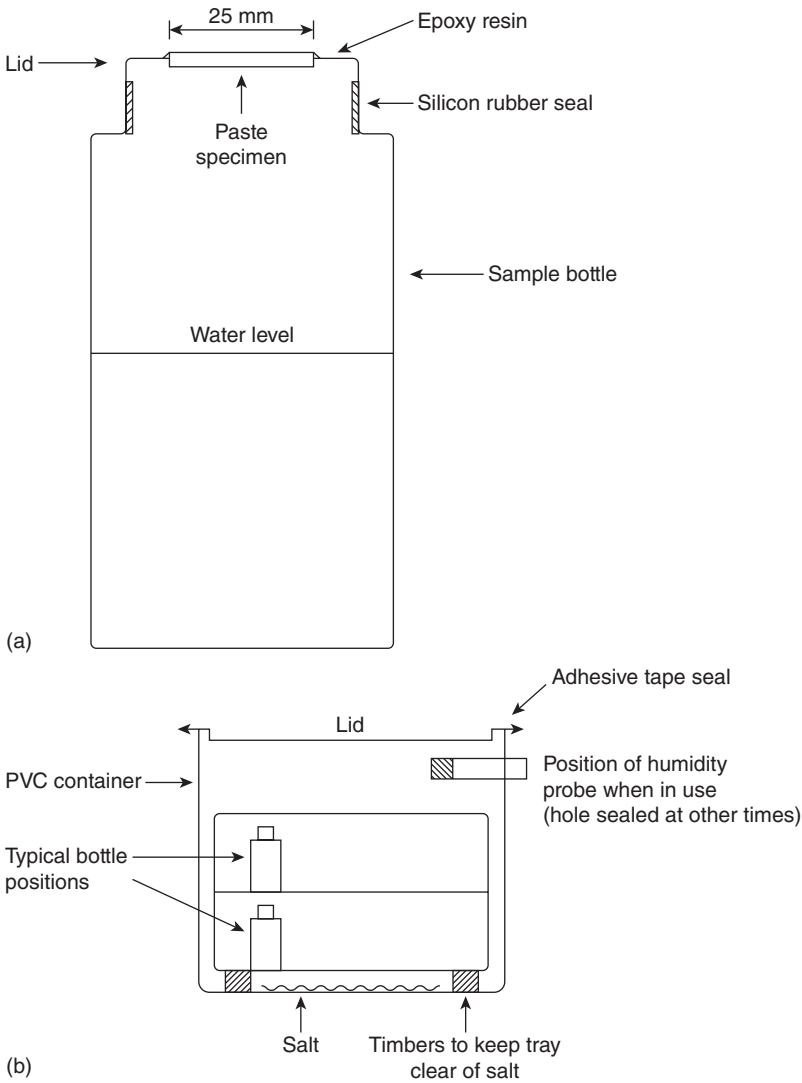

8.6 Diagrams showing (a) detail of bottle for vapour transmission measurement and (b) details of container.

1. When the samples were first installed they had a relatively constant moisture content throughout. Whatever the final distribution, it was certainly not constant across the thickness. An increase in moisture content on the wet side would not affect the measured weight, but a loss from the dry side would cause a loss of weight. The factors controlling the exact rate of moisture loss are complex because the rate of migration of water will depend on the local humidity gradient, and the total amount to be lost from any given depth will depend on the final

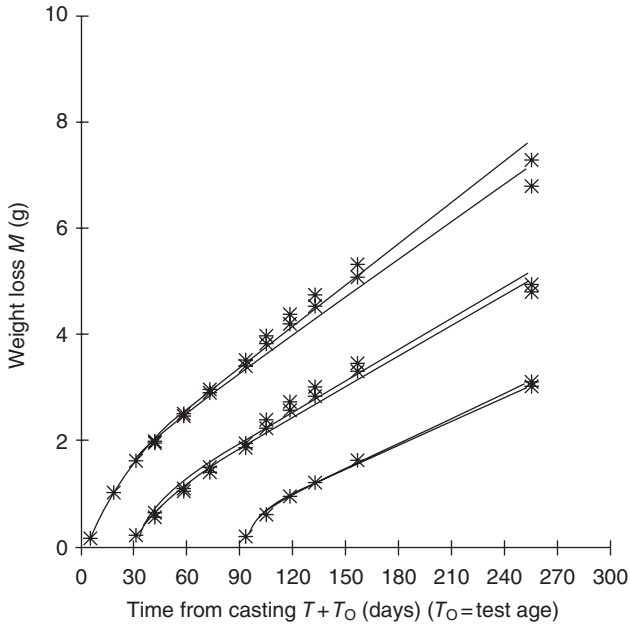

8.7 Typical outputs for vapour transmission mix C, container 1, CC.

distribution. As a rough approximation it is, however, reasonable to assume an exponential decay, i.e. the rate of loss will be proportional to the amount remaining to be lost.

2. When the samples were installed they were not fully hydrated. Due to the presence of moisture, the hydration will have continued and the hydration products will have formed in previously open pores. The factors controlling the transmission rate are again complex because the rate of hydration will depend on the availability of water. An exponential decay may be very approximately justified by assuming that the rate of hydration depends on the quantity of cement remaining to hydrate, and the rate of transmission decreases linearly with the quantity of hydration products present. Thus the rate of hydration will decay exponentially and the rate of transmission will follow it.

If the two processes are assumed to proceed at approximately the same speed they may be represented by a single term to describe the initial additional losses, i.e. $M_0 e^{-Kt}$ where K is a rate constant to represent the effect of both processes. Thus:

$$M = M_0 - M_0 e^{-Kt} + Ct \qquad [8.7]$$

Table 8.5 Values of the constants of equation (8.7)

Test age (days)	Sample no.	Constants		
		C	M_0	K
3	1	0.026	1.186	0.056
3	2	0.024	1.240	0.055
28	1	0.019	0.784	0.067
28	2	0.019	0.689	0.061
90	1	0.016	0.545	0.131
90	2	0.015	0.547	0.155

where:

M is the cumulative mass loss to current time t and
$M_0 + Ct$ is the linear long term mass loss.

This equation was fitted to each set of results and thus, for each sample, the constant C represents the steady state loss and the constants M_0 and K show the extent and duration of the initial additional losses. These values are shown in Table 8.5 for the experimental results shown in Fig. 8.7.

Effect of sample thickness

The dependence on thickness in the data was checked by considering each similar pair of samples. For each pair, the percentage difference in thickness and the percentage difference in the constants C, M and K were calculated. No correlation was found between any of the constants and the thickness, and it was thus concluded that the rate is independent of thickness.

Effect of relative humidity (vapour pressure difference)

The dependence of the measured weight losses on RH was investigated by plotting the relationship between the results from the samples exposed to different environments (Fig. 8.8). It may be seen that there are clear linear relationships between the results from the different environments, i.e. different relative humidities.

The target RH for container 1 was 70 % and for container 2 it was 55.2 %, and thus a linear dependence of rate on RH would give a ratio of (100 – 55.2)/100 – 70) = 1.49. If Darcy's law is applied, equation (8.6) shows that each of the terms is squared and this gives a ratio of 1.36. The other ratios are in Table 8.6.

The data indicates that the losses from container 1 were higher than expected because of increased air circulation (container 1 was open, but

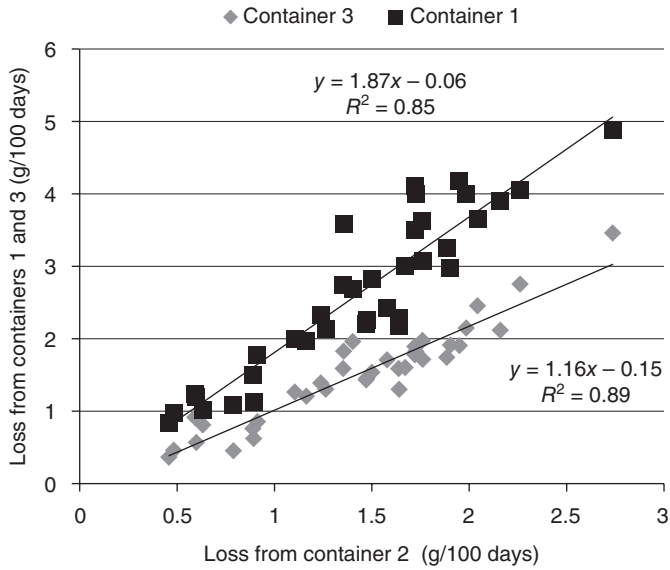

8.8 Relationship between the weight losses of equivalent samples in the different containers.

Table 8.6 Effect of relative humidity on weight loss

Container	Ratio of RH drop	Darcy ratio	Observed *C* ratio
2/1	1.49	1.36	0.95 (0.88)
3/2	1.95	1.41	1.83 (0.85)

Note: figures in brackets after the ratios are the values of R^2 for the relationship.

containers 2 and 3 were closed). The relationship between containers 2 and 3 shows a direct dependence on RH more than a Darcy relationship.

An average of the results for the three containers was obtained after multiplying the results from containers 1 and 3 by a constant factor to give each set the same mean value in order to give equal weighting. The average is plotted in Fig. 8.9.

8.7 Results and discussion

Two readings were obtained for each sample condition for each experiment. The average of each pair of readings was used for the analysis reported here.

The relationships between all of the different variables studied (data columns) were calculated as the correlation coefficient R^2. The value of this

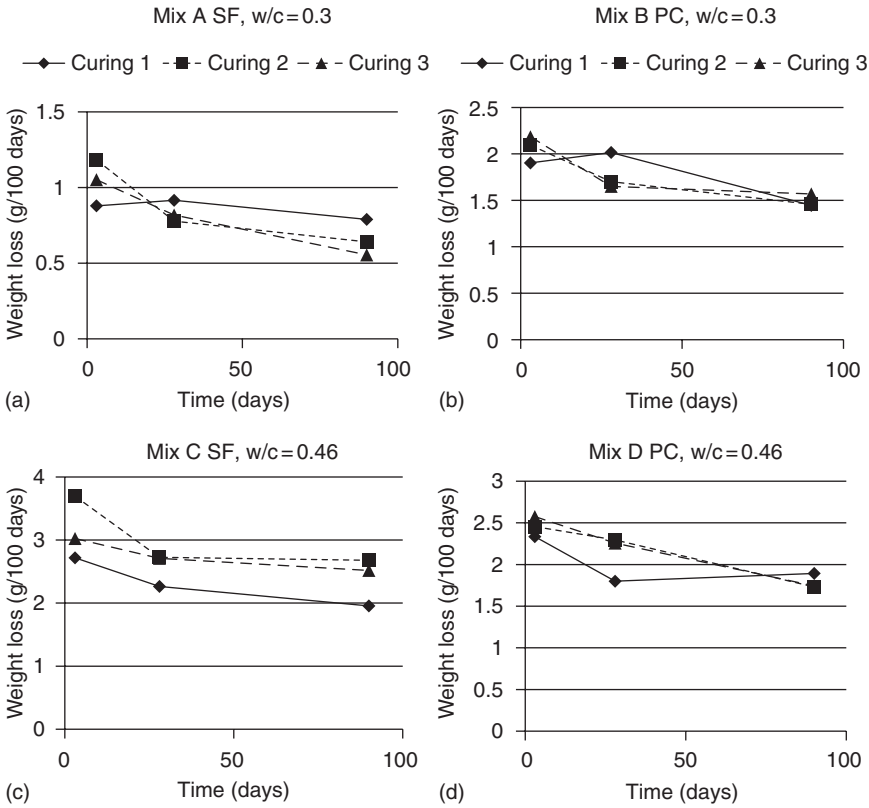

8.9 Average weight loss from the three containers in g/100 days all normalised to the same average as container 2. (a) Mix A SF, w/c = 0.3; (b) mix B PC, w/c = 0.3; (c) mix C SF, w/c = 0.46; (d) mix D PC, w/c = 0.46.

for 1 % significance is 0.17 for the Portland cement (PC) and SF samples together (a complete column of 36 values) and 0.31 for the PC or the SF samples individually (half a column – 18 values) (see for example Tables 8.7 and 8.8).

8.7.1 The mechanisms of oxygen and vapour transport

The experiments indicate that the transmission of oxygen is adequately described by the Darcy equation. The mechanism of transmission of water vapour is clearly different. This difference is shown very clearly in Fig. 8.10 where the results of oxygen transmission are plotted against vapour transmission and the log of the oxygen permeability has similar range to the water transmission measurements. The observation that the water transmission rate is independent of the sample thickness severely limits the

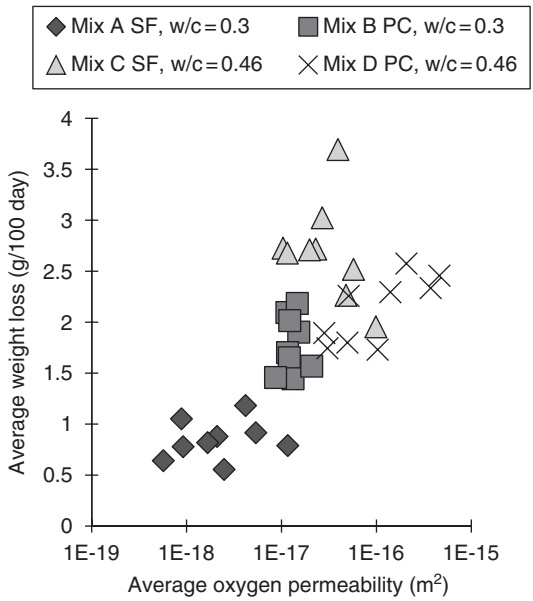

8.10 Relationship between the permeabilities to oxygen and water.

choice of possible mechanisms. The possibility of a continuously changing moisture content across the thickness consistent with a Darcy relationship is ruled out. Typical values of mean free path are given in Table 6.4 and are in the range of 0.1 μm; however, Table 8.4 shows typical pore diameters of 0.01 μm or below. The mean free path of a molecule of water vapour at room temperature is many times greater than the size of continuous pores in concrete and the Kelvin equation (3.1) shows that at 96 % RH pores with diameters below 35 μm will sustain a meniscus. It may therefore be concluded that, with the exception of an outer surface layer, the pores are all either full of water or vapour at near 100 % RH. This model would indicate that keeping one side at 100 % RH would make the transmission rate independent of thickness.

Further support for the theory that this is not a vapour diffusion process is gained from the observation of water droplets on the underside of the samples. These droplets will clearly prevent the ingress of any gas or vapour into the sample. Rose (1965) discussed the various degrees of saturation possible in a porous body. He suggests two mechanisms of transmission without full saturation, but without a vapour pressure gradient. One takes place when just the necks of the pores are filled with water, where vapour condenses on one side of the neck and evaporates from the other. The other mechanism is surface creep of a fine film of water coating the pore surfaces.

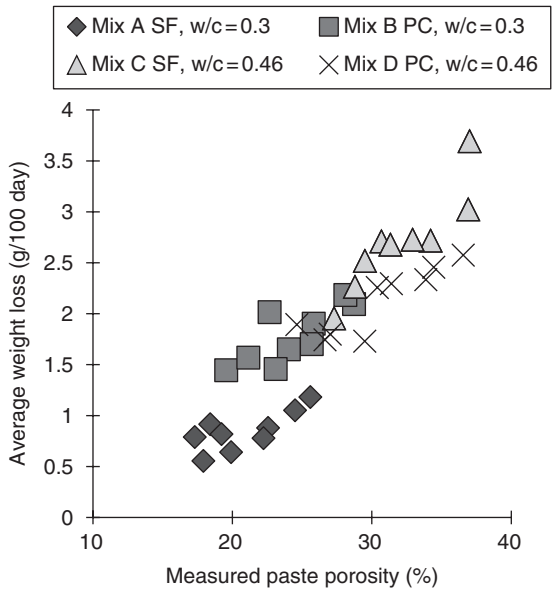

8.11 Correlation between water permeability and porosity.

Powers (1960) proposed a mechanism for the loss of water from the dry side. He observed that if it was necessary for water to evaporate from surfaces in the necks of the outer pores as in the 'ink bottle' analogy, virtually no water would be lost. He therefore proposed a mechanism where the process is controlled by the formation of vapour bubbles in those pores at the surface which are of adequate size. The total areas which will be intersected by a cut through a sample will form the same fraction of the cut surface area as the fraction of the sample volume occupied by the pores, i.e. the porosity. This would indicate that the rate would be linearly dependent on porosity which may be seen to be a measure of a surface as well as bulk property. The relationship is shown in Fig. 8.11, and it can be seen that the line is an excellent fit ($R^2 = 0.81$), but it does not pass through the origin (for the steady state, 90 day porosity values were used). The data indicates that at porosity 11 %, the pores become either discontinuous or too small for bubble formation and the transmission stops.

8.7.2 The effect of test age

It may be seen from Figs 8.1 and 8.9 that the vapour transport and porosity decrease with increasing maturity as expected. Figure 8.5, however, shows the oxygen permeability increasing with time for the SF samples from CC1 (moist cure at 20 °C). It is possible that this could have been caused by open

porosity caused by the depletion of lime during the progress of the pozzolanic reaction, but the absence of this effect in the dry cure samples (CC2) indicates that it was caused by cracking as a result of the drying procedure on the SF samples. It is therefore indicated that the conditions most likely to produce samples which are virtually impermeable to oxygen in normal environments are prolonged moist curing of SF samples with low water to cement (w/c) ratios.

8.7.3 The relative importance of the measurements of oxygen and vapour permeability

The results from the vapour transmission experiment have been presented in units of weight loss because the permeability model used for the oxygen results was not correct for the physical process. If the equations are used, however, to obtain an estimate of the relative effect of the two processes, the permeability coefficients in m^2 are equal to 7×10^{-16} times the weight loss in g/100 day. This calculation assumes that the transmission of water is by pure vapour permeation and should therefore be treated with considerable caution. A value of 10^{-5} has been used for the viscosity of water vapour. Using this factor, the measured water permeabilities lie in the range of 2×10^{-15}–4×10^{-16} while the oxygen permeabilities lie in the range of 10^{-15}–10^{-21}. These results imply that the transport rates of water and oxygen in the control mixes are similar, but the use of the SF with a low w/c ratio (mix A) could cause the permeability to oxygen to become significantly lower than that for water. The major increase in the sensitivity to different curing regimes shown in Figure 8.5 is, however, a cause for concern if this property is to be used. In particular, the increase in permeability with curing time for both SF mixes in CC1 (20 °C) is of interest.

The observed sensitivity of the water vapour transport rates to the different curing conditions will have been reduced by the effect of continuing hydration during the experiments.

8.7.4 The effect of water vapour on the oxygen permeability

All of the samples tested for oxygen permeability in this work were dried before testing. Measuring gas permeabilities at other humidities is difficult because both the samples and the gas to be permeated through them must be equilibrated to the required humidity at the start of the test and the entire system must be sealed from the atmosphere during the test to prevent drying. Results from experiments of this type are presented in Chapter 6 and show the permeability of a grout falling from 3×10^{-16} when dry to 3×10^{-18} at 75 % RH and to below 10^{-21} at close to 100 % RH. If a similar

effect was observed with samples of mix A where the permeability is already low, the effect would create an almost impermeable barrier to oxygen.

8.7.5 Comparison between different measurements of paste porosity

Comparison between the different test methods

The relationship between the different measurements is shown in Figs 8.12 and 8.13. Comparisons could only be made for paste because these were the only type used for mercury intrusion. From Fig. 8.12 it may be seen that mercury intrusion yields a lower value than helium intrusion. This would be expected because the samples were ground for helium intrusion and the low molecular size and viscosity of the helium. The calculations of porosity were only used for the PC samples, but Fig. 8.13 shows that these samples correlate well, with the helium results giving generally slightly lower values.

Porosities for different pore size ranges

The porosity from mercury intrusion was, as described above, subdivided into porosities for different pore size ranges. These porosities in the different pore size ranges were correlated with the total porosities also obtained from mercury intrusion. No correlation was observed in the size range for the largest pores.

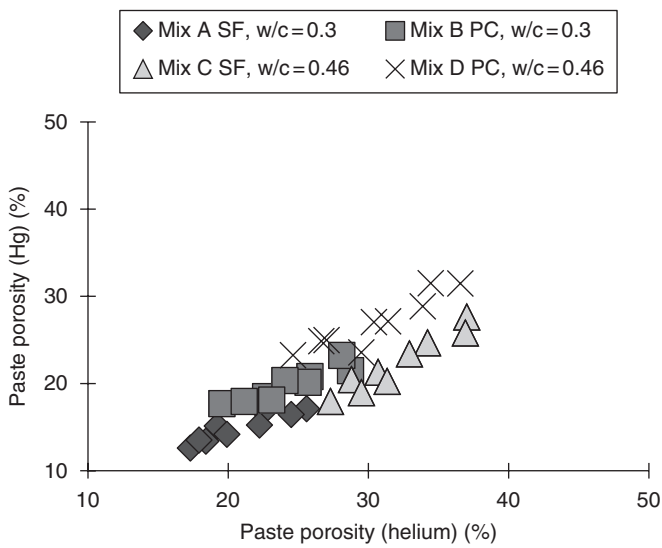

8.12 Comparison of paste porosities from helium and mercury intrusion.

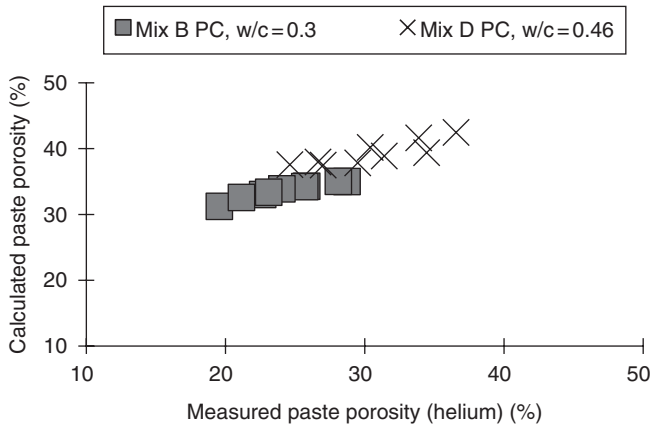

8.13 Comparison of calculated paste porosity with measured porosity from helium intrusion.

The correlation between porosities in the 0.15–10 μm range and total porosity was negative (Fig. 8.14). Significance values of R^2 of 0.314 for the SF samples and 0.340 for all of the samples were obtained. The negative correlation indicates that the porosity in this range, which increases with a decrease in total porosity, is unlikely to be significant in predictive models for properties which generally correlate with porosity.

The bulk of the pores lie in the 0.01–0.15 μm range and a good correlation with the total porosity was expected. Figure 8.15 shows, however, that the SF samples had significantly lower porosity in this range and the relationship with total porosity was therefore different from that for the PC mixes.

Figure 8.16 for the 0.003–0.01 μm range shows the extent of the refinement of the pore structure caused by the SF. The correlations with total porosity are not significant, but the effect of the SF is very clear. This refinement of the pore structure has the effect of reducing the recovery volumes for the SF samples. This may be seen in Fig. 8.17.

8.7.6 Measurements from concrete, mortar or paste

For the helium intrusion and the weight loss measurements, tests were carried out on concrete, mortar and paste samples. When considering which of these to use as predictors for concrete properties, there are two conflicting factors: measurements on concrete are theoretically the most realistic, but concrete porosities are lower than those for mortar and paste so the accuracy of measurement will be lower. It is obviously possible to calculate one porosity from another with a knowledge of the proportions and porosity (if any) of the aggregate. Table 8.7 shows some of the correlations of porosities with properties that were measured.

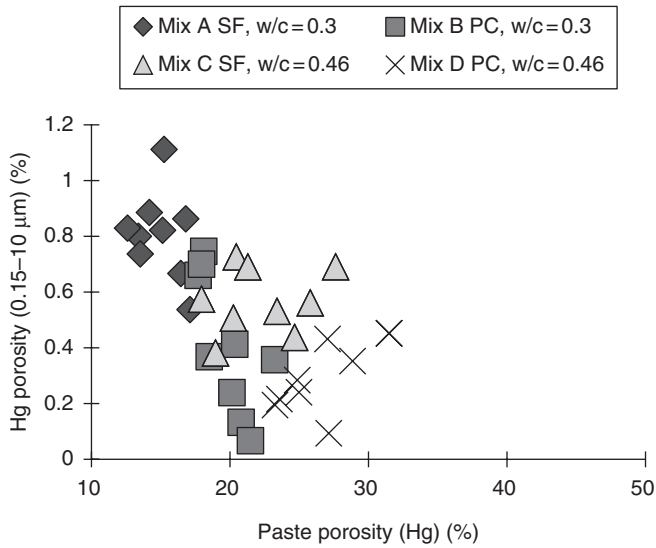

8.14 Mercury intrusion porosity in the 0.15–10 μm pore size range vs total mercury intrusion porosity.

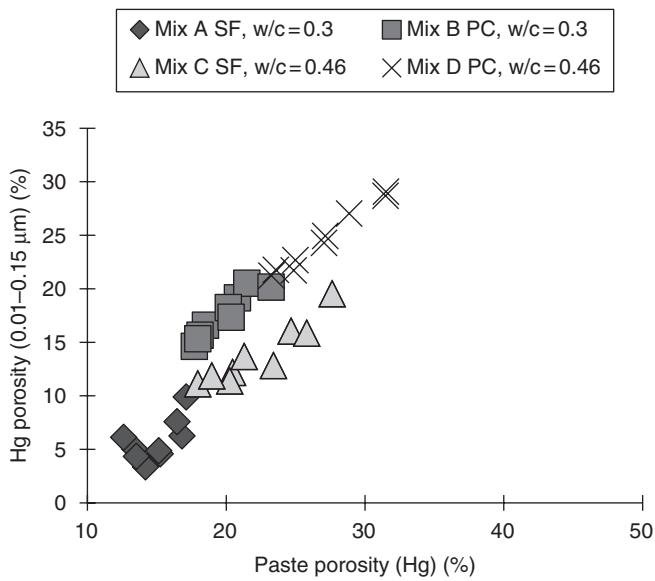

8.15 Mercury intrusion porosity in the 0.01–0.15 μm pore size range vs total mercury intrusion porosity.

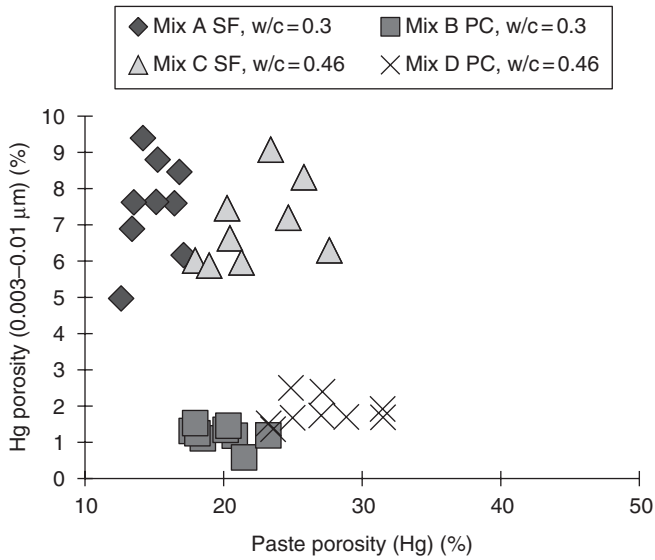

8.16 Mercury intrusion porosity in the 0.003–0.01 μm pore size range vs total mercury intrusion porosity.

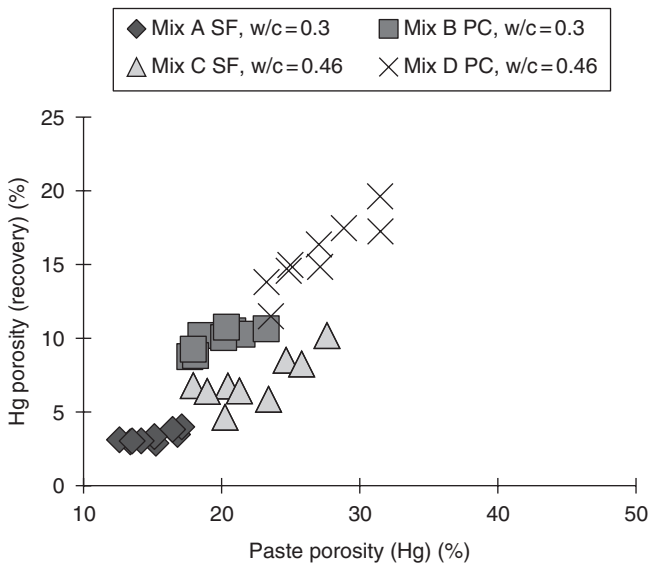

8.17 Mercury intrusion recovery porosity vs total mercury intrusion porosity.

Table 8.7 Comparison of correlations (values of R^2) for paste, mortar and concrete for chloride transport and strength

Predictor	Type of sample	Property	
		Chloride transport	Strength
Measurements of porosity from helium intrusion (all samples)	Paste	0.537	0.671
	Mortar	0.376	0.295
	Concrete	0.593	0.450
Calculations of porosity from weight loss (PC samples only)	Paste	0.756	0.944
	Mortar	0.045	0.006
	Concrete	0.646	0.884

It may be seen that the mortar results generally gave poorer correlations, but neither the concrete or the paste was found to be universally better. The correlations for paste and concrete porosity for all of the measured properties are shown in Table 8.8 and are discussed in subsequent sections.

8.7.7 Pore size ranges in mercury intrusion

For the main transport properties, attempts were made to develop multiple regression models based on the porosities from different pore size ranges obtained from mercury intrusion. It was hoped that the different characteristics of the pore size distributions would combine in linear combinations to form a predictive model. It was found, however, that in each case a single predictor model based on the total porosity could not be improved by including any of the individual pore size ranges. This might be expected from the negative correlation between total porosity and some of the porosities in size ranges.

8.7.8 Chloride transport

The relationship between chloride concentration and paste porosity measured by mercury intrusion is shown in Fig. 8.18. The measured chloride concentration will be proportional to the chloride transport to the point of measurement. It may be seen that the porosity measurement works as an excellent predictor and the correlation coefficient is 0.77. If the porosity from helium intrusion is used (Fig. 8.19), it may be seen that the transport would be over-estimated for mix C, which is the SF mix with the higher w/c ratio. Looking at the relationship between the mercury and helium porosities (Fig. 8.12), it may be seen that mix C has a higher than expected porosity from the helium intrusion. It is concluded from these observations that mix C has a substantial closed porosity which was not accessed by the mercury

Table 8.8 Correlations – values of R^2

Property	Predictor	All	PC	SF
Chloride concentration	Paste porosity (helium)	0.537	0.730	0.661
	Concrete porosity (helium)	0.593	0.702	0.257
	Paste porosity (mercury)	0.771	0.808	0.716
	Calculated paste porosity		0.756	
	Calculated concrete porosity		0.646	
Carbonation strain microstrain	Paste porosity (helium)	0.652	0.717	0.717
	Concrete porosity (helium)	0.458	0.719	0.617
	Paste porosity (mercury)	0.625	0.788	0.698
	Calculated paste porosity		0.615	
	Calculated concrete porosity		0.700	
Log of oxygen permeability ($m^2 \times 10^{-18}$)	Paste porosity (helium)	0.448	0.700	0.424
	Concrete porosity (helium)	0.645	0.743	0.428
	Paste porosity (mercury)	0.634	0.807	0.374
	Calculated paste porosity		0.741	
	Calculated concrete porosity		0.743	
Water vapour transport	Paste porosity (helium)	0.807	0.765	0.922
	Concrete porosity (helium)	0.334	0.613	0.703
	Paste porosity (mercury)	0.600	0.699	0.903
	Calculated paste porosity		0.574	
	Calculated concrete porosity		0.516	
Inverse of cube strength (N/mm^2)	Paste porosity (helium)	0.671	0.861	0.602
	Concrete porosity (helium)	0.450	0.901	0.157
	Paste porosity (mercury)	0.780	0.941	0.683
	Calculated paste porosity		0.944	
	Calculated concrete porosity		0.884	
Log of initial resistance (Ω)	Paste porosity (helium)	0.208	0.741	0.294
	Concrete porosity (helium)	0.232	0.726	0.228
	Paste porosity (mercury)	0.279	0.769	0.301
	Calculated paste porosity		0.813	
	Calculated concrete porosity		0.613	
Log of 28 day resistance (Ω)	Paste porosity (helium)	0.276	0.701	0.808
	Concrete porosity (helium)	0.589	0.763	0.669
	Paste porosity (mercury)	0.532	0.801	0.753
	Calculated paste porosity		0.850	
	Calculated concrete porosity		0.632	

because the samples were not ground before the mercury test and because of the higher viscosity of the mercury. This closed porosity would not contribute to the chloride transport.

For the PC samples alone, all three different methods of measuring porosity gave high correlations of porosity with chloride concentration in the range 0.65–0.8.

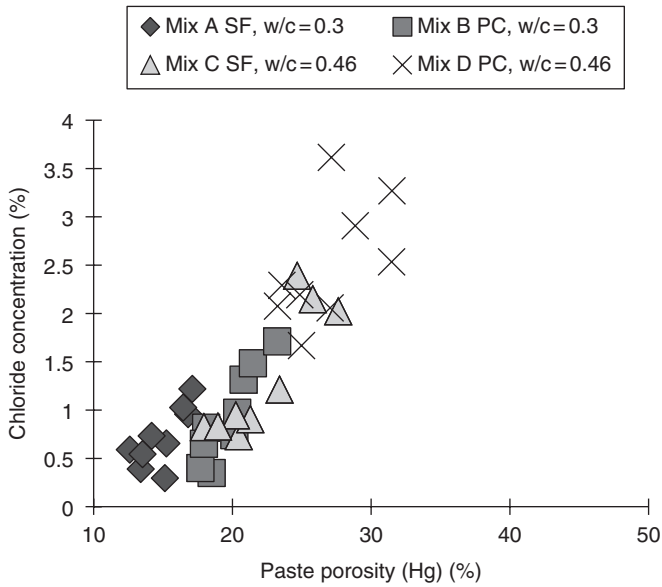

8.18 Chloride concentration from diffusion test vs mercury intrusion porosity.

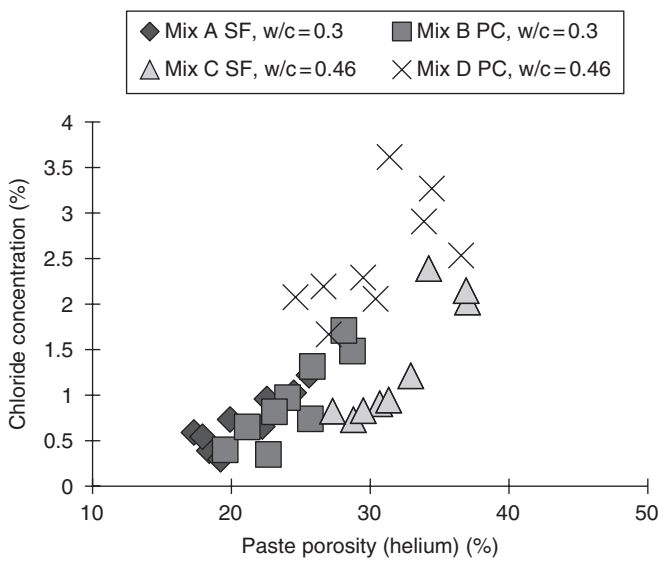

8.19 Chloride concentration from diffusion test vs helium intrusion porosity.

8.7.9 Carbonation

The relationships between carbonation strain and helium and mercury porosity are similar (Figs 8.20 and 8.21). The helium porosity shows a slightly higher correlation (see Table 8.8), but both measurements may be taken as equally good predictors of carbonation.

8.7.10 Oxygen transport

The observed values of oxygen permeability had a range of several orders of magnitude, and none of the measured porosities were good predictors for them. It was found, however, that the log of the oxygen permeability could be predicted with porosity. For the PC samples, all of the measurements of porosity gave R^2 in the range 0.7–0.8. For the SF, the correlations are far lower, and the reason for this may be seen from Fig. 8.22 which shows the relationship with the porosity from mercury intrusion. It may be seen that there are some SF samples which had low porosity but high permeability giving an apparent decrease in permeability with increasing porosity for the lower porosity samples of mixes A and C. This might have been caused by the creation of a connected pore system when the calcium hydroxide is depleted by the pozzolanic reaction, but there is no other evidence to support this explanation and micro-cracking of the higher strength samples during drying is probably more likely.

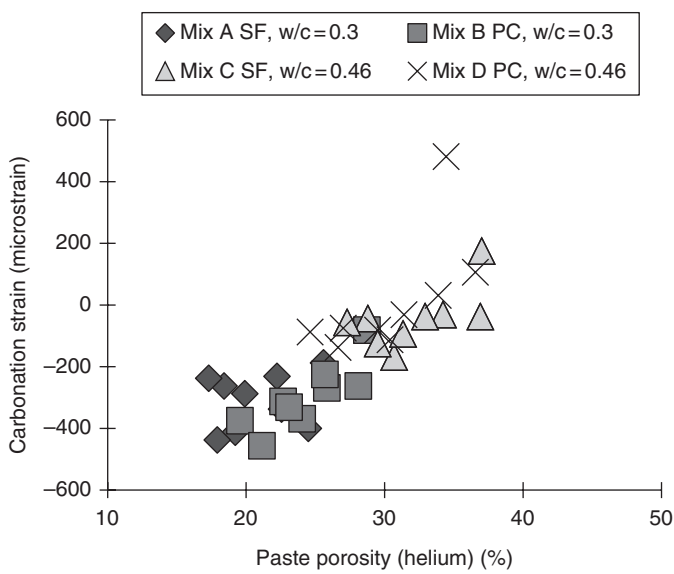

8.20 Carbonation strain vs helium intrusion porosity.

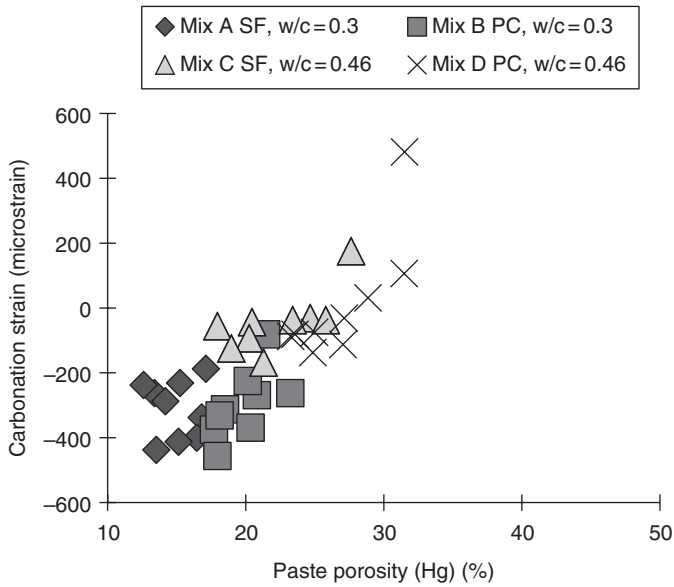

8.21 Carbonation strain vs mercury intrusion porosity.

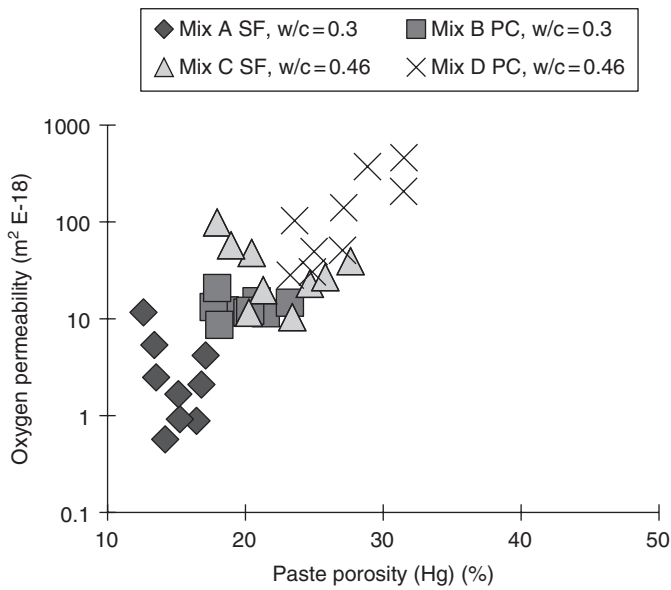

8.22 Oxygen permeability vs mercury intrusion porosity.

8.7.11 Water vapour transport

It was shown in Section 8.12.1 that, in the experiments that were carried out, the water vapour transport rate was controlled by the rate of evaporation from the low humidity side of the sample. This rate of evaporation will depend on the surface area of the pores exposed on the surface and this area will, in turn, depend on the total porosity. It may be seen that, as expected from this, the correlation is highest with the helium intrusion. Looking at the relationships in Figs 8.23 and 8.24, it is apparent that mix D is the cause of the poorer relationship with mercury intrusion results. This will be because all of the other mixes have a higher proportion of closed porosity.

8.7.12 Cube strength

In order to obtain a good predictive model, the inverse of the cube strength was used. The relationship with the calculated paste porosity was excellent (for PC samples only). In this case, the strength is likely to be used as the predictor for porosity, and the relationship with mercury porosity may be seen in Fig. 8.25.

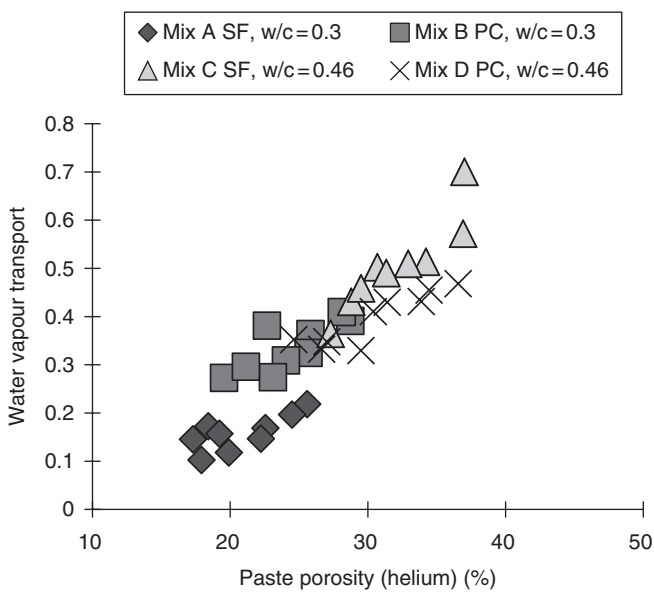

8.23 Water vapour transport (relative units) vs helium intrusion porosity.

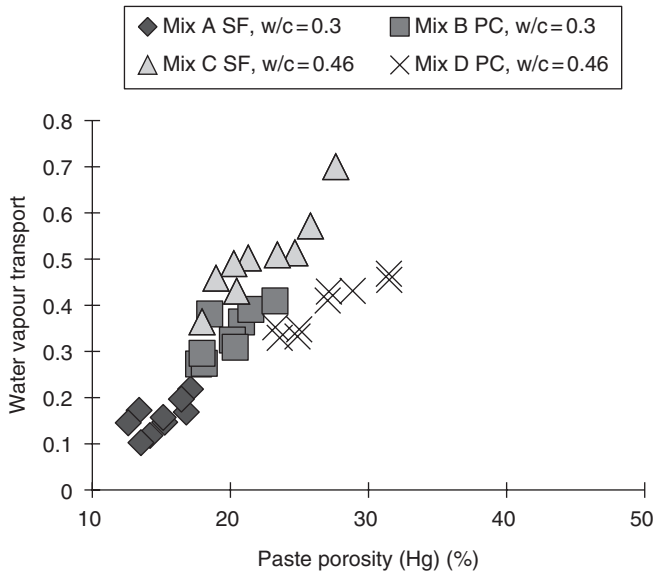

8.24 Water vapour transport (relative units) vs mercury intrusion porosity.

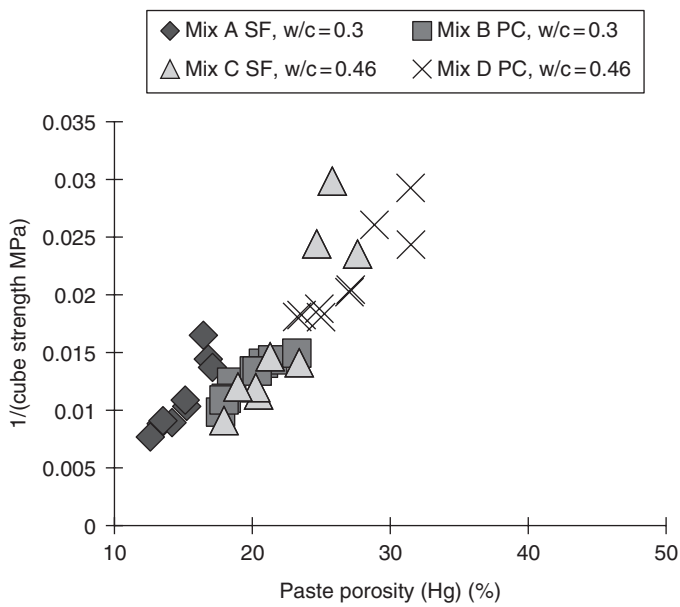

8.25 Inverse of cube strength vs mercury intrusion porosity.

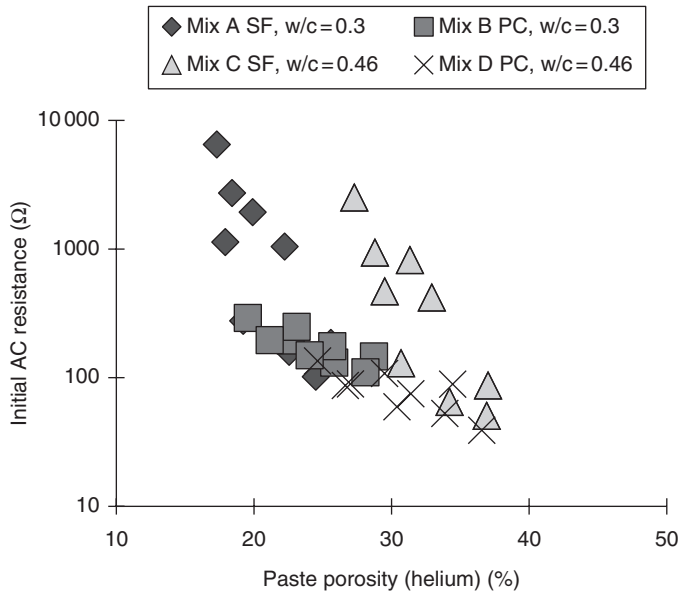

8.26 Electrical resistance at start of corrosion test vs helium intrusion porosity.

8.7.13 Resistivity

In order to obtain better predictions, the log of the resistance values was used in all cases. The relationship between porosity and initial resistance is clearest in fig. 8.26, giving the results from helium intrusion. The PC results and the SF results from tests at age 3 days all lie on a clear line, and the 28 day results from cold curing (CC3) also lie on this line. The other SF samples lie above the line. This increase in resistance has been caused by the depletion of lime by the pozzolanic reaction and is independent of porosity (Cabrera and Claisse, 1991). After 28 days of anodic polarisation, all of the SF samples have high resistivity due to lime depletion and lie on a separate clear line (Fig. 8.27). Because all of the resistance samples were the same size, the resistivity values for the materials will be proportional to the measured resistances.

8.8 Conclusions

- Transport of oxygen through dry cementitious samples is accurately described by the Darcy equation, and the measured permeabilities vary over a substantial range of values.

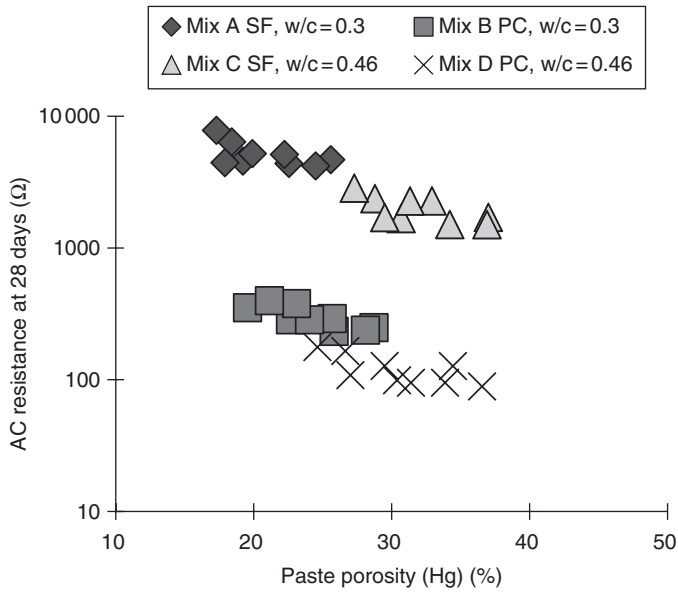

8.27 Electrical resistance after 28 days of test vs mercury intrusion porosity.

- The rate of transport of water vapour was not found to vary greatly for the different samples and was proportional to the porosities of the samples.
- The results indicate that under the correct conditions SF could be used to make a material which is almost impermeable to oxygen.
- When using measurements of porosity as predictors for bulk concrete properties, it was equally valid to use measurements on paste or concrete samples.
- The models using total porosity to predict the performance of the concrete could not be improved by including data for the individual pore size ranges from mercury intrusion.
- Mercury intrusion was the best predictor of chloride transport because the mercury does not penetrate closed porosity and this closed porosity does not contribute to the transport.
- Helium intrusion was the best predictor of water vapour transport if it is controlled by evaporation because it will depend on the total porosity.
- The resistivity of concrete was predicted well by porosity models but, for mixes containing SF, the effect of lime depletion by the pozzolanic reaction is more significant.

8.9 References

Cabrera J G and Claisse P A (1991) The effect of curing conditions on the properties of silica fume concrete, in Swamy R N (ed.), *Blended Cements in Construction*, Elsevier, London.

Powers T C (1960) Physical properties of cement paste and concrete, *Proceedings of the 4th International Symposium on the Chemistry of Concrete*, Vol. 2, US Department of Commerce, Washington DC, pp. 577–613.

Rose D A (1965) Water movement in unsaturated porous material, *Rilem Bulletin*, No. 29, pp. 119–124.

9

Factors affecting the measurement of the permeability of concrete

DOI: 10.1533/9781782423195.153

Abstract: In this chapter, it is shown that the interpretation of even fundamental tests for permeability such as the high pressure test described in Chapter 4 is not as simple as it would appear. It was observed that, depending on the strength of the sample, the permeability either increased or decreased during the testing process. Also the results were affected by sample size. This makes the measurements difficult to interpret due to experimental effects of sample size and changes of flow with time. However, the results did not change significantly with pressure, and results obtained for tests with water were not significantly different when synthetic leachate was tested.

Key words: permeability, sample size, effect of pressure, siltation, high pressure test.

9.1 Introduction

The high pressure test described in Chapter 4 is the simplest test for permeability. No assumptions are made in the very simple analysis of the results. It is also unaffected by Knudsen flow and the ideal gas approximation described in Chapter 1 which affect the gas tests. It would therefore be assumed that this test would give reliable and unchanging results for permeability. However, a series of experiments described here show that this is not the case. At high pressures, the permeability of low strength samples increased during the test and it decreased for high strength samples. It is assumed that this would have been caused by fluid breaking through the pore walls in low strength samples and siltation at high strength. An effect of sample size was also observed, but the mechanism for this is not apparent.

9.2 Experimental programme

The objectives of the experiments were to establish the permeability of the different concretes and mortars in order to provide data which could be used in calculations of the performance of waste containment barriers for the application described in Chapter 15. In order to do this, an investigation has been carried out into the evolution of bulk permeability with increased

sample volume and different pore pressure and specimen size. In all tests, the confining to pore pressure ratio was kept constant.

The specific objectives were to measure the following:

1. the permeability of the specimens to water;
2. the change in permeability in the presence of leachate;
3. the relationship between numbers of sample volumes passing and changes in permeability;
4. the effect of different residence times in the sample by running the test at different pressures and/or sample thicknesses – this determines the sensitivity of the observed permeability to changes in pressure;
5. the effect of sample size and boundary effects by testing samples in a larger cell.

9.2.1 Eluted liquids

Both deionised water and a synthetic (acetogenic) leachate have been eluted through the materials to examine their effects on permeability evolution of the mixes. The composition of the synthetic leachate used in this work was obtained by comparing the composition of various natural and synthetic leachates and is given in Table 9.1. This solution was chosen as it represents a leachate from the early (acetogenic) phase of a landfill and is therefore the most aggressive solution to which a cementitious barrier would be likely to be exposed. The evolution of leachate chemistry during the service life of a landfill, normally shows a decrease both in acidity and ionic strength as the landfill matures, so experiments using this solution are thought to be conservative.

9.2.2 Mix designs

The mixes were designed with consideration for requirements for strength, permeability, chemical conditioning capacity ('through pH') and cost–benefit analysis. The results of a screening programme on a large number

Table 9.1 Composition in grams of synthetic leachate, per litre of solution (pH = 5.1)

2.043	Concentrated sulphuric acid
4.48	Acetic acid
1.897	Potassium chloride
7.755	Calcium acetate
1.186	Ammonium chloride
0.91	Sodium chloride
2.588	Sodium hydroxide

Table 9.2 Mix proportions and strength of the mortar mixes used for hydraulic conductivity study

Mortar mix	Cementitious material	% by mass	Pozzolanic ash	% by mass	Fine aggregate (<5 mm)	% by mass	w/c ratio	28 days strength (MPa)
Cement/quartz	PC	11.8	–	–	Quartz	88.2	0.92	15
Cement/quartz	PC	16.7	–	–	Quartz	83.3	0.75	20
Typical site trial mix	CKD	20.7	Lagoon ash	13.6	Ferro-silicate slag	65.9	0.39	5

CKD = cement kiln dust.

of mixes led to the selection of three candidate mixes which satisfied the criteria. Two samples from each selected mix design were tested with leachate and two more were tested with water.

The designs of the three mixes are given in Table 9.2. Two of these mixes were Portland cement (PC) mortar mixes with different strengths and permeability coefficients and one other mix was one of the several cell mixes used for site trials. For one of the mixes, a low strength of about 5 MPa was deliberately engineered to find the effect of applied pore pressure and number of sample volumes eluted on the coefficient of permeability.

9.2.3 High pressure test

This is described in Section 4.2.2. Measurements were normally made after one sample volume (SV) of liquid had passed through the mortar specimens. Assuming an average permeability of 10^{-9} and a maximum leachate head of 1 m above the liner described in Chapter 15, this corresponds to 16 years of exposure in service. The specimens were cylindrical with either 54 mm diameter and about 30 mm thickness or 100 mm diameter and 55 mm thickness and were cured for 1 month before testing.

9.3 Results

The effect of eluted volume on the coefficient of permeability at different pore solution pressures is shown in Figs 9.1–9.3. The effect of permeating a volume of liquid equal to seven times the sample volumes are shown in these figures. One sample volume shown on the graph represents a volume of fluid passing through the sample equal to the total overall volume of the

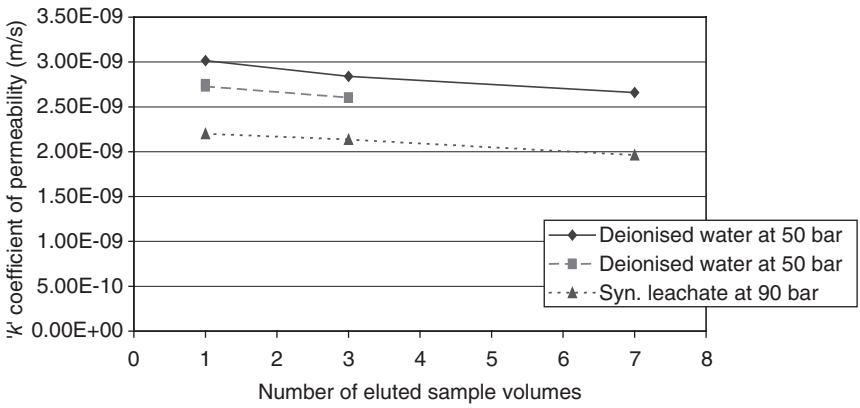

9.1 Permeability vs eluted sample volume for 5 MPa cement mortar mix.

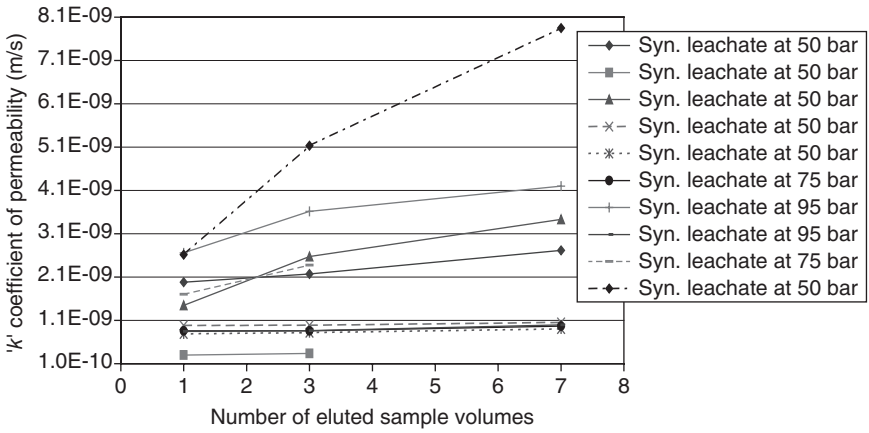

9.2 Permeability vs eluted sample volume for 15 MPa cement mortar mix.

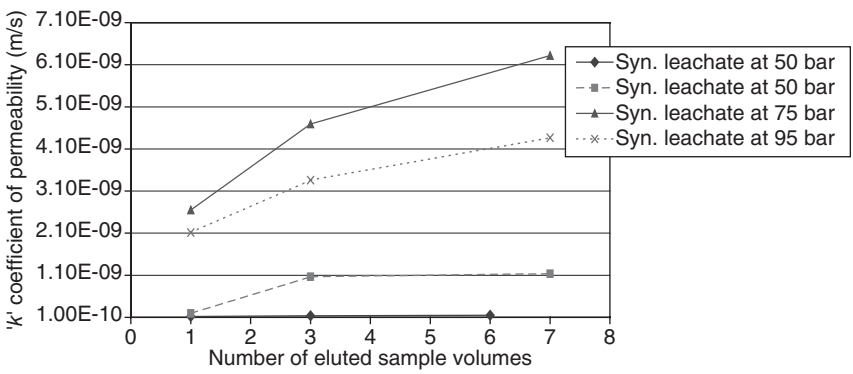

9.3 Permeability vs eluted sample volume for 20 MPa cement mortar mix.

sample itself, not just its porosity. For low strength materials, such as materials being used in the novel liner mixes, i.e. compressive strength of up to 5 MPa, increased eluted sample volumes slightly decrease the coefficient of permeability, but this is in contrast to higher strength materials in which the permeability increases. The author suggests that the reason for this is that high strength materials are rigid whereas low strength materials are compliant and weak bonding fine particles cause blockage of the pore routes in these types of materials by 'silting'. In previous work by the author, Claisse and Unsworth (1996) found a slight decrease in intrinsic permeability coefficient after permeating 30 times the sample volumes for higher strength PC mixes. This may have been due to using concrete which contained coarse aggregate; however, the permeabilities for intermediate number of sample volumes passing were not determined so a more detailed comparison cannot be made. In the investigation reported here the results clearly indicated a decrease in hydraulic conductivity for lower strength mixes and a slight increase in permeability coefficient for the higher strength mixes with increasing number of permeating sample volumes.

The effect of specimen size on the coefficient of permeability at different pore solution pressures is shown in Figs 9.4–9.6. Increasing the specimen size slightly increases the coefficient of permeability in lower strength mixes and decreases the coefficient in higher strength mixes. This trend is in agreement with findings from Figs 9.1–9.3 and, as high strength materials are rigid, larger volumes would reduce the permeability. From Figs 9.1–9.6, it can also be seen that the permeability coefficient does not change significantly with pore solution pressure.

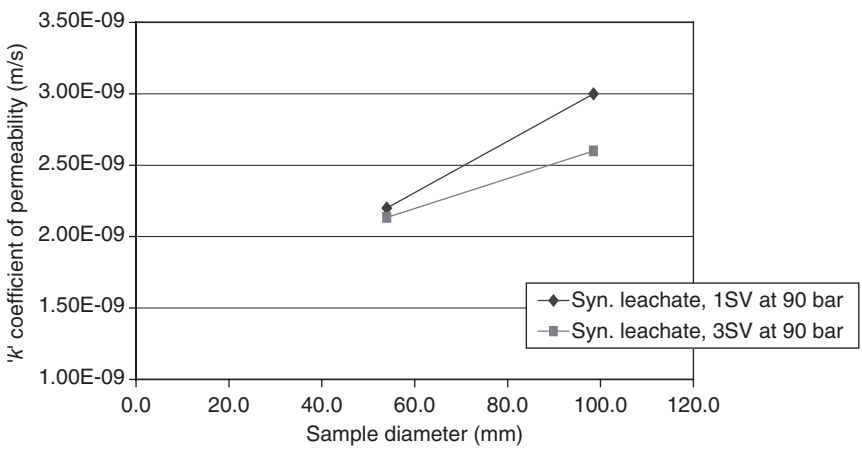

9.4 Coefficient of permeability vs sample size for 5 MPa cement mortar mix.

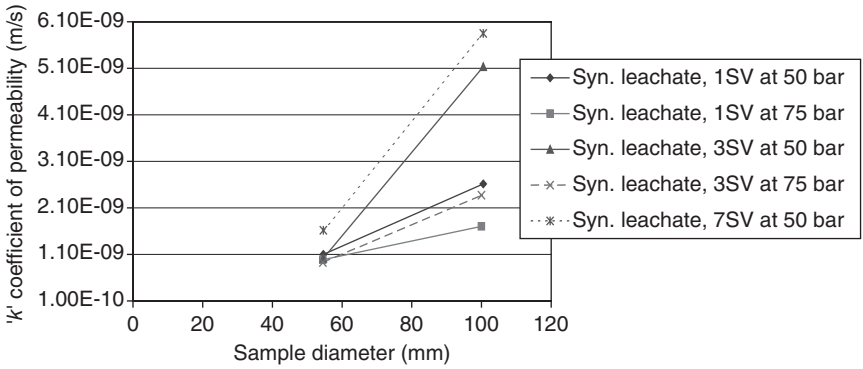

9.5 Coefficient of permeability vs sample size for 15 MPa cement mortar mix.

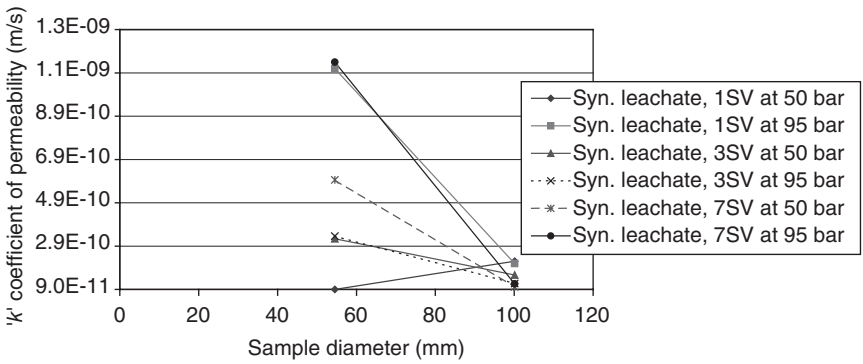

9.6 Coefficient of permeability vs sample size for 20 MPa cement mortar mix.

9.4 Discussion

The following differences between the test conditions and site conditions may make the test results conservative:

- The samples were tested at early ages (normally 28 day). It is well known (Neville, 2011) that the permeability of concrete reduces substantially with age as the hydration progresses.
- The simulated leachate used for the experiments was free of all particulate matter. A typical leachate on site contains a large fraction of material with the potential for siltation in pores.

The following may make the conclusions unsafe:

- The results are to be used in a system with a leachate head up to 10 m. The applied pressure of up to 10 MPa in the testing represents a head

of up to 1000 m. The calculations using the Darcy equation automatically assume that the flow will reduce linearly with pressure (i.e. the permeability will not change). While the present results do not prove that it will not change, they do not indicate any trend to show that it would.

- The area of a typical disposal cell is 1–2 ha while the experimental samples are six orders of magnitude smaller. The possibility of defects (which are a main consideration when modelling high density polyethylene – HDPE) must therefore be considered. The main defect in a concrete liner will be a crack, and this problem is addressed with the use of a clay layer which will extrude into and seal the cracks (trials of this method are reported in Section 15.6). The reason why larger laboratory samples appeared more permeable is not clear, but it is not indicated that this trend would be likely to continue up to site scale samples.

And the following appear to be well represented in the experiments:

- Each sample volume of fluid passing through the liner corresponds to at least 16 years of operation. The tests have been run for up to seven sample volumes, i.e. the equivalent of just over 100 years. Nuclear repositories are designed for very much longer periods, but for normal landfill design this is currently typical. Most current designs are based on a HDPE membrane with a design life no greater than this. The membrane is used with a mineral barrier (e.g. bentonite enhanced sand), but most modelling relies substantially on the membrane itself.
- The temperature of the trial cells has been monitored and did not deviate by more than a few degrees from typical room temperatures which were measured during laboratory testing.

9.5 Conclusions

- Depending on the strength, the cementitious mortar mixes behave differently with permeating number of sample volumes at the same pore pressure and age. For low strength materials such as controlled low strength materials, which are increasingly being used, increased eluted sample volumes slightly decrease the coefficient of permeability but this is in contrast to higher strength materials in which the coefficient of permeability increases.
- Increasing the testing specimen volume slightly increases the coefficient of permeability in lower strength mixes and decreases the coefficient in higher strength mixes.

- Variation in pore solution pressure during high pressure permeability test does not significantly affect the permeability coefficients in low strength cementitious mixes.
- Large site trials are a necessary step in establishing the performance of concrete barriers.

9.6 References

Claisse P A and Unsworth H P (1996) The engineering of a cementitious barrier, in Bentley S P (ed.), *Engineering Geology of Waste Disposal*, Engineering Geology Special Publication No.11, The Geological Society, London, pp. 267–272.

Neville A M (2011) *Properties of Concrete* (5thedn), Pearson, Harlow.

10

Electrical tests to analyse the transport properties of concrete – I: modelling diffusion and electromigration

DOI: 10.1533/9781782423195.161

Abstract: In this chapter, a measurement of electromigration is analysed. The 'rapid chloride permeability test' (RCPT) is described in ASTM standard C1202. The aim of the analysis is to obtain the fundamental properties of the concrete (diffusion coefficient and capacity factor) from the test. A computer model is described. The model represents the key processes of diffusion and electromigration using standard equations but then maintains charge neutrality by modelling changes to the voltage distribution. Results are presented to show that the measurement of the non-linearity of the voltage distribution can be used to detect cement replacements such as pulverised fuel ash (PFA) and ground granulated blast furnace slag (GGBS) in concrete.

Key words: rapid chloride permeability test (RCPT), rapid chloride, ASTM C1202, ion–ion interactions, Kirchoff's law.

10.1 Introduction

The ASTM C1202 'rapid chloride permeability test' (RCPT) (ASTM, 2012) is used extensively in many countries to measure the potential durability of concrete structures. However, it emerges that this test is highly complex because several different types of ions are moving and they interact. This is the first of three chapters describing the analysis of this and related tests, and their relevance to durability assessment is discussed in Chapter 13. The fundamental problem that emerges is that the current which is measured in the test is not primarily carried by chloride ions. The main charge carriers are hydroxyl, sodium and potassium ions and the concentrations of these (and thus the current) can be substantially reduced by the addition of pozzolans such as silica fume. Methods to overcome this problem are presented in subsequent chapters.

In this chapter, the processes which occur are described initially at a macroscopic level and then at a microscopic level. Equations are developed to represent the processes, but these cannot be used to give a full solution.

The methods described in Chapter 2 are therefore used to develop a computer model. The model represents the key processes of diffusion and electromigration using standard equations but then maintains charge

neutrality by modelling changes to the voltage distribution. This method enables the model to predict current–time transients similar to those recorded in experiments and it can then be used to obtain basic parameters such as diffusion coefficients for tested samples by optimising to the observed data.

Experimental data showing a non-linear voltage distribution is presented together with model results which show that the non-linearity has a significant effect on the current. Other predictions from the model are compared with published data and shown to give good agreement.

10.2 The ASTM C1202 test and the salt bridge

The RCPT was developed by Whiting (1981) and has been standardised as ASTM C1202-12 (ASTM, 2012). The apparatus is shown in Figs 10.1 and 10.2. A steady external electrical potential of 60 V DC is applied to a sample of concrete 50 mm thick and 100 mm diameter for 6 h and the total charge passing is measured as the integral of the current–time transient. The anode and cathode are filled with 0.30 N sodium hydroxide and 3.0 % sodium chloride solutions, respectively. The samples are prepared for the test by vacuum saturation.

In the work presented here, in addition to the standard test, a salt bridge was added in the middle of the sample to check the voltage distribution (Figs 10.1 and 10.2). A hole of 4 mm diameter and 5–8 mm deep was drilled

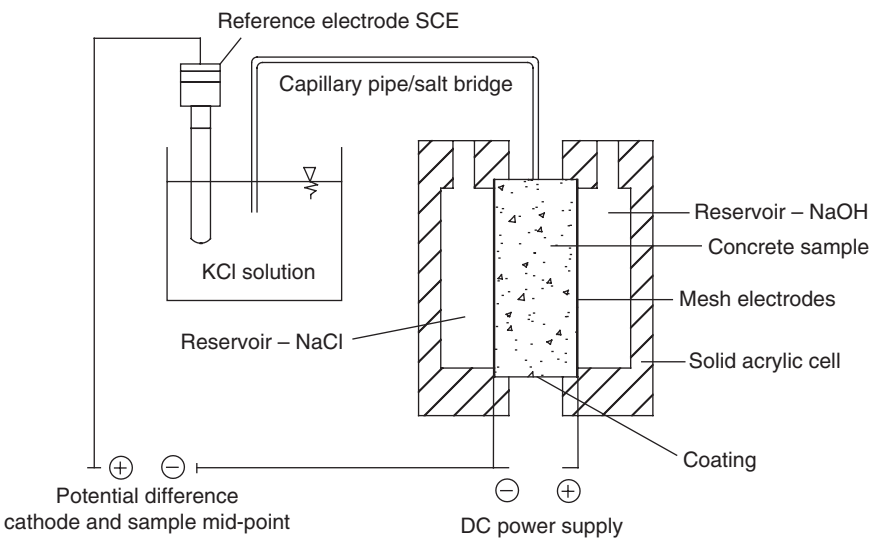

10.1 Schematic arrangement of the ASTM C1202 test with salt bridge.

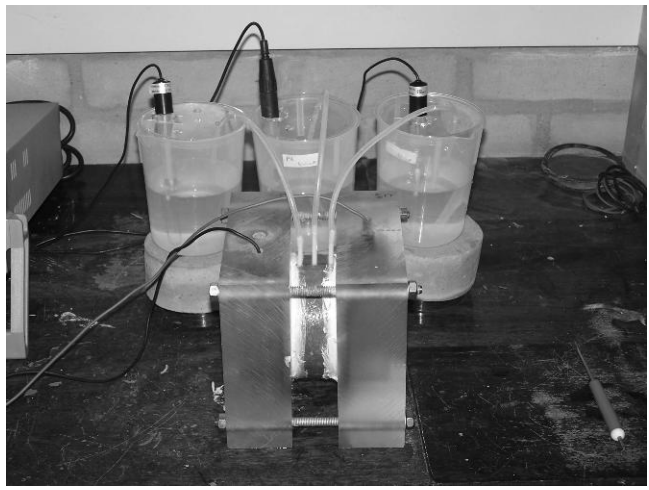

10.2 An ASTM C1202 with three salt bridges at different locations.

at the mid-point. The salt bridge used was a solution of 0.1 M potassium chloride which was found to avoid any junction potential at the interface of the salt solution and the pore solution because both ions in it have similar mobility. The salt bridge pipes were 4.5 mm diameter. and were inserted into the hole. The voltage was measured using a saturated calomel electrode (SCE) relative to the cathode cell. The current through the concrete and the voltage at the mid-point were measured continuously every 10 s with a data logger. The membrane potential was calculated by subtracting the value of the voltage measured from the initial value measured at the start of the test.

In previous research, Zhang and Buenfeld (1997) measured the membrane potential across Portland cement (PC) mortar specimens during a diffusion test using reference electrodes and salt bridges in external cells. They found that for different simulated pore solutions, the total junction potentials formed between the measurement devices and the simulated pore solution were in the range of –0.8 and –6 mV. Those values were relatively low compared with the membrane potential measured during the migration tests; therefore, the liquid junction potential formed between the salt bridge and the pore solution concrete sample was not included in the calculations reported here.

The tests were carried out in a temperature controlled room at 21 ± 2 °C. During the tests the temperature was measured continuously in the anodic reservoir. A 3 A, 70 V programmable DC power supply was used although, as noted below, it was often necessary to deviate from the standard and run at voltages below 60 V to avoid over-heating.

The data logger had 16 analogue inputs with 12-bit resolution. A very high input impedance was required in order to ensure that the measuring process did not change the voltage readings. The internal resistance of the data logger had to be significantly greater than the resistance of the concrete during the test, because when measuring voltages the resistance of the equipment itself has an effect on the voltage of the circuit. To achieve the required analogue input performance of the data logger, it had a high resistance voltage divider followed by an operational amplifier configured as a voltage follower.

10.3 The physical processes

10.3.1 The transport processes

The significant transport processes which take place during the test are diffusion and electromigration. These are discussed in Chapter 1. The combined effect of the two processes is given by the Nernst–Planck equation (1.26). Analytical solutions to this equation are available and they are given in Section 10.4. However, they assume that the chloride ion is the only charged particle in the system. The effect of interaction with other ions may be considered on a macroscopic or a microscopic level, and these are discussed in Sections 10.3.2–10.3.3.

10.3.2 Kirchoff's law

Macroscopically, the procedure to maintain the charge balance is, according to Kirchoff's law: '… *the current density (i) into any point will equal the current out of it*'. If the sample is considered (as in a numerical model) as a sequence of cells, this means that for any time the total current in cell i is equal to the current in cell $i + 1$ (equation 10.1):

$$\sum_k I_{i,k} = \sum_k I_{i+1,k} \qquad [10.1]$$

The effect of Fick's law is shown in Fig. 10.3. When a chloride ion enters the sample it cannot just stop because this would violate the law. Something must carry the charge away.

In a diffusion or migration test, the charge build-up generated by differences of mobility of ions in the pore solution is dissipated by the distortion of the electrical field. Only a multi-species system can be physically possible because, if there is only one ion, charge neutrality is never reached.

10.3.3 Ion–ion interactions

The flux F in equation (1.26) has a term in it for the electric field $E = d\phi/dx$. This will arise both from the applied voltage and the distribution of charged ions in the sample.

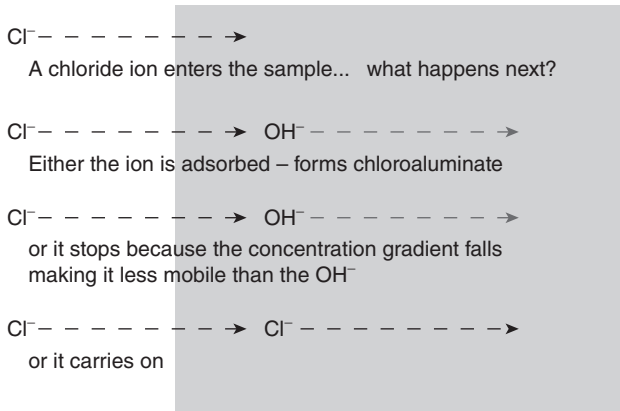

10.3 Schematic representation of the progress of a chloride ion.

The field caused by the applied voltage will be uniform across the sample. At the start of the experiment, all of the ions will be in pairs with no net charge but as soon as, for example, a chloride ion migrates into the sample without its sodium pair it will create a field E which will cause a potential difference given by equation (10.2)

$$\phi = \int E \, \mathrm{d}x \qquad \mathrm{V} \tag{10.2}$$

This will distort the uniform voltage drop caused by the applied potential. The effect of the field will be to inhibit further migration of ions causing any more build-up of charge. In this way, Kirchoff's law will take effect and the current into any point within the sample will equal the current out of it. In the solutions at either end of the sample, neutrality will be maintained by ion generation and removal at the electrodes.

The change in voltage will be a direct effect of different ionic concentrations in the sample. Soon after the start of the test, there will be chloride ions in one side of the sample and sodium in the other side. The regions with these ions in them will have different resistivities due to the different mobilities of the different ions; thus the system is equivalent to three different resistances in series. The voltage drop will depend on the size of each resistance and will not be uniform across the sample. This is shown schematically in Fig. 10.4.

At the start of the test there is assumed to be virtually no chloride in the sample. When the voltage is applied, the chloride ions will start moving into it. If they are to be responsible for the measured current they will be moving without the sodium anions. The rate at which they can flow in will be determined by the number of charge carriers (primarily hydroxyl ions)

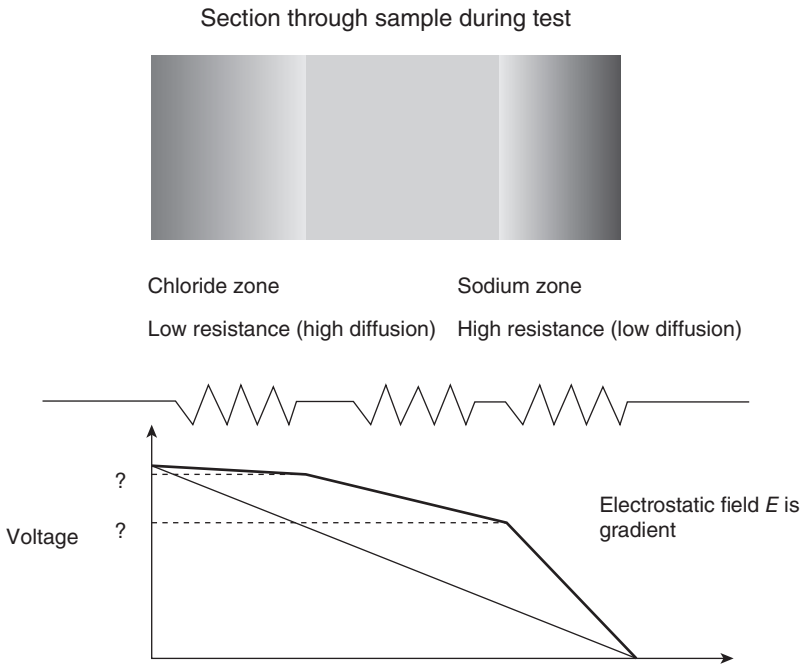

10.4 Schematic diagram of the effect of changes in resistivity.

already available in the sample to carry the current forward to the anode. This concentration of existing charge carriers may be measured as the resistivity of the sample as discussed above. Clearly, if there are no existing charge carriers in the sample (i.e. it is an insulator) no current will flow and chloride will only penetrate by diffusion.

In order to calculate what happens next, it is necessary to consider the physical situation in the sample. Charged ions can only move if charge neutrality is preserved. Thus, for example, a negative chloride ion can only move to a region of the sample if either its sodium counter-ion moves with it or a different negative ion such as a hydroxyl ion is displaced ahead of it. If charge neutrality is not preserved, electric fields build up to prevent the movement. Thus the ability of the chloride ion to move through the region of the sample is determined by the concentration and mobility of other ions in the region. Referring to the Nernst–Einstein equation (1.25), this may be represented as a change in conductivity (or resistivity) of the region. One effect of this is shown in Fig. 10.4. The different resistivities in different regions of the sample make the voltage drop across it non-linear. The difference between the measured voltages and the linear change is known as the membrane potential.

Yu *et al*. (1993) have carried out experimental measurements of ionic diffusion at an interface between chloride-free and chloride-containing cementitious materials. They observed that the chloride ions obeyed Fick's law, but the hydroxyl ions distributed themselves to preserve charge balance. This movement would have been caused by an electric field established by the chloride ions and is the mechanism proposed in the present work.

10.3.4 Microscopic considerations

Whenever different ions with different mobilities at different concentrations in the concrete pore solution start to move, there is a tendency for the segregation of charge and the breakdown of the law of electro-neutrality. As a result, several complex and not completely well understood interactions happen in the pore solution, such as the interaction of ions with the solvent or the electrical ion–ion interactions. In order to quantify ion–ion interactions, an electrochemical theory was proposed by Debye and Hückel (1923).

From a 'simplistic' microscopic point of view, the Debye and Hückel (ion-cloud) theory can be used to calculate the electrostatic potential contributed by the surrounding ions to the total electric potential at one reference ion. Once a reference ion is selected, the solvent molecules are replaced by a dielectric continuum medium with permittivity ε and the other ions involved are replaced by an excess of charge density (Fig. 10.5). Assuming that the excess charge distribution is spherically symmetrical around the reference ion, the relationship between excess charge density ρ_r and electrostatic potential ϕ_r at a specific radial distance r can be given through Poisson's equation (10.3) (Bockris and Reddy, 1998):

$$\frac{1}{r^2}\frac{\mathrm{d}}{\mathrm{d}r}\left(r^2\frac{\mathrm{d}\phi_r}{\mathrm{d}r}\right) = -\frac{4\pi}{\varepsilon}\rho_r \qquad [10.3]$$

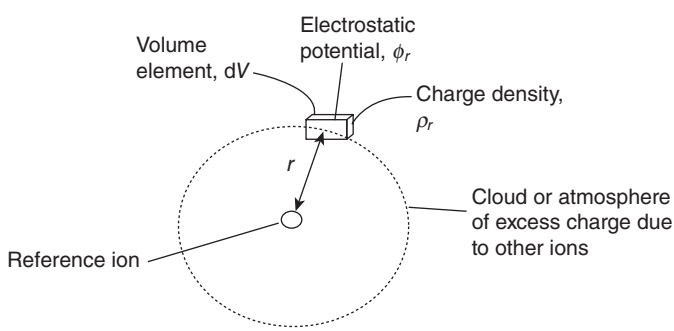

10.5 Ionic cloud of an electrically charged element.

The excess charge density in the volume element dV is obtained in the Debye–Hückel theory through the linearisation of the Boltzmann equation (equation 10.4):

$$\rho_r = -\sum_i \frac{n_i^0 z_i^2 e_0^2}{K_B T} \phi_r \qquad [10.4]$$

where:

z_i is the valence of ion i
e_0 is the electronic charge
n_i is the total number of ions i per unit volume
K_B is the Boltzmann constant
T is the temperature (K) and
the Σ symbol refers to all the species i.

Similarly, the maximum value of charge in a spherical cloud is given through the Debye–Hückel length κ^{-1}, which gives an indication of the thickness of the ionic atmosphere from equation (10.5):

$$\kappa^2 = \frac{4\pi}{\varepsilon K_B T} \sum_i n_i^0 z_i^2 e_0^2 \qquad [10.5]$$

The problem can be simplified and linearised and a general equation can be obtained (equation 10.6):

$$\frac{1}{r^2} \frac{\mathrm{d}}{\mathrm{d}r} \left(r^2 \frac{\mathrm{d}\phi_r}{\mathrm{d}r} \right) = K_B^2 \phi_r \qquad [10.6]$$

the solution of which is shown as equation (10.7):

$$\phi_r = \frac{z_i e_0}{\varepsilon} \frac{\mathrm{e}^{-K_B r}}{r} \qquad [10.7]$$

It can be seen from equation (10.7) that the microscopic treatment of the electrostatic potential for the ion–ion interaction is highly complex. Further discussion is given by Luping *et al.* (2012). It has been defined for the reference ion; however, it needs to be applied to the whole concrete system.

Going from a micro to a macro approach, a general model with a larger scale allows a similar, but simpler solution. The simple treatment of the concrete as a circuit in which physical laws must be valid seems to be more appropriate. In that way, the macroscopic electrical model introduced in this chapter permits the inclusion of the ion–ion effects coupling all the species involved to the charge neutrality. This is well suited to analysis with a computer model which is discussed in Section 10.5.

10.4 Analytical solutions

10.4.1 An analytical solution for a single ion

Luping and Nilsson (1992) presented an integrated solution to the Nernst–Planck equation (1.26) which gives the concentration of chloride ions at different times:

$$c_{\mathrm{cl}-} = \frac{c_0}{2}\left[e^{ax}\operatorname{erfc}\left(\frac{x+aDt}{2\sqrt{Dt}}\right)+\operatorname{erfc}\left(\frac{x-aDt}{2\sqrt{Dt}}\right)\right] \qquad [10.8]$$

where:

$$a = \frac{zF_{\mathrm{a}}E}{RT}$$

and c_0 is the concentration at the surface (in the reservoir).

This may be differentiated to give the current:

$$I = AF_{\mathrm{a}}D_{\mathrm{cl}}c_{\mathrm{s}}\left[\frac{1}{\sqrt{\pi D_{\mathrm{cl}}t}}\mathrm{e}^{\frac{(x-aD_{\mathrm{cl}}t)^2}{4D_{\mathrm{cl}}t}}+\frac{a}{2}\operatorname{erfc}\left(\frac{x-aD_{\mathrm{cl}}t}{2\sqrt{Dt}}\right)\right] \qquad [10.9]$$

This solution is accurate for a single ion. However, it contains a term for E, the electric field, and the only value that can be used is that for the applied electric field in the tests. It has been shown above (see Fig. 10.4) that E is not a constant across the sample.

10.4.2 Considering multiple ions

If a constant electric potential is applied, as in the ASTM C1202 test, the total flux J_i for each species in the system must be the sum of the migration flux $(J_{\mathrm{M}})_i$ and the diffusion flux $(J_{\mathrm{D}})_i$.

$$J_i = (J_{\mathrm{M}})_i + (J_{\mathrm{D}})_i \qquad [10.10]$$

Using this notation, equation (1.13) becomes:

$$(J_{\mathrm{D}})_i = -D_i\frac{\partial c_i}{\partial x} \qquad [10.11]$$

where:

J_i is the flux of species i (mol/m^2/s)
D_i *is* the diffusion coefficient of species i (m^2/s)
c_i is the ionic concentration of species i in the pore fluid (mol/m^3)
and x is the distance (m).

and the Nernst–Planck equation (1.26) becomes:

$$J_i = -D_i\frac{\partial c_i}{\partial x}-\frac{z_iF_{\mathrm{a}}}{RT}D_ic_i\frac{\partial \phi}{\partial x} \qquad [10.12]$$

If used in this form with E as the applied field, the Nernst–Planck equation supposes that the flux of each ion is independent of every other one; however, due to ion–ion interactions, there are ionic fields that affect the final flux. The drift of a species i is affected by the flows of other species present. The law of electroneutrality ensures that no excess of charge is introduced. Under a concrete migration test, the current density into any point will equal the current out of it (Kirchoff's law):

$$0 = F_a \sum_i z_i J_i \qquad [10.13]$$

Faraday's law states the equivalence of the current density i_i and the ionic flux:

$$i_i = -z_i F_a J_i \qquad [10.14]$$

In an electrolyte solution in which concentration gradients of the ionic species and an electrical field are present, the total current density (i_T) is equal to the sum of the current density produced by the diffusion and the migration conditions:

$$i_T = -\sum_i z_i F_a (J_D + J_M)_i \qquad [10.15]$$

The total current can be given from equation (10.12):

$$i_T = \sum_i z_i F_a R T u_i \frac{\partial c_i}{\partial x} + \sum_i z_i^2 F_a^2 u_i c_i \frac{\partial \phi}{\partial x} \qquad [10.16]$$

where u_i is the mobility of species i in the pore fluid ($m^2\ s^{-1}\ V^{-1}$).
The electric potential gradient is given by two terms: a linear or ohmic potential and a non-linear or membrane potential as in the Nernst–Planck equation:

$$\frac{\partial \phi}{\partial x} = \underbrace{\frac{i_T}{\sum_i z_i^2 F_a^2 u_i c}}_{\text{Ohmic potential}} - \underbrace{\frac{\sum_i z_i F_a R T u_i \frac{\partial c_i}{\partial x}}{\sum_i z_i^2 F^2 u_i c}}_{\text{Membrane potential}} \qquad [10.17]$$

The first term is related to the ohmic potential when an external voltage is applied and gives the charge transfer driven entirely by forces arising from that external voltage. The second term of equation (10.17) is that for the membrane potential gradient $\delta\phi_p/\delta x$, formed when various charged species have different mobility. In a concrete migration test, the non-linearity of the electric field is due to the membrane potential gradient and it is equivalent to the liquid junction potential (Lorente *et al.*, 2007):

$$\frac{\partial \phi_p}{\partial x} = -\frac{RT}{F_a} \frac{\sum_i z_i u_i \frac{\partial c_i}{\partial x}}{\sum_i z_i^2 u_i c_i} \quad [10.18]$$

The overall conductivity of concrete σ can be related to the partial conductivity of one species σ_i:

$$\sigma_i = t_i \sigma \quad [10.19]$$

where t_i is the transference number of species i, which is defined as:

$$t_i = \frac{Q_i}{Q} = \frac{i_i}{i} \quad [10.20]$$

where Q_i is the charge contribution of species i and
Q is the total charge passed through the sample.

Thus the electric field due to the diffusion potential can be expressed in terms of the transference number:

$$\frac{\partial \phi_p}{\partial x} = \frac{RT}{F_a} \sum_i \frac{t_i}{z_i} \frac{\partial \ln c_i}{\partial x} \quad [10.21]$$

10.5 The computer model

10.5.1 Key concepts

The model is similar to the one described in Chapter 2 except that it considers diffusion and electromigration rather than diffusion and advection. It works by repeated application of equations (1.13) and (1.20) through time and space.

However, in order to apply equation (1.20) it is necessary to know the electric fields. This changes and is extremely difficult to calculate (as shown in Section 10.4). The model therefore avoids this calculation by applying Kirchoff's law which states that the current must be the same at all points through the sample, i.e. charge neutrality must be maintained. In the computer code, the net charge is calculated for different values of electric field on an iterative basis until the correct value is obtained to achieve neutrality at each time step. The diffusion is calculated initially from equation (1.13). This is unaffected by the electric field. Repeated calculations of electromigration are then made to achieve charge neutrality. By using a process of back-calculation, this is normally achieved in just two or three iterations. This process is shown schematically in Fig. 10.6.

Voltage changes are thus applied within the model by distorting the voltage and checked by ensuring that charge neutrality is maintained

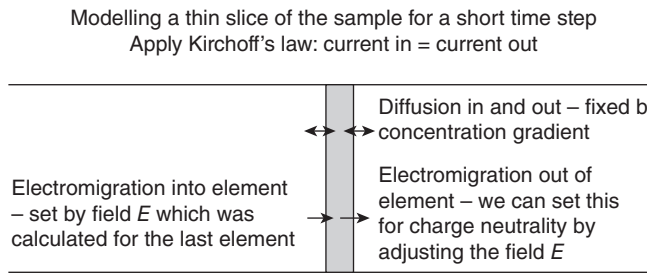

10.6 The basis of the voltage correction in the model.

throughout the sample at all times. This is clearly not possible if only one ion type is being considered and therefore all of the migrating ions are considered together. The initial concentrations in the sample must be equal for anions and cations and, if the data does not comply with this requirement, the model will not run.

Ion generation and removal at the electrodes is represented in the model by assuming that the ions being generated and removed are always hydroxyl ions. This assumption is probably most accurate at the cathode where hydroxyl ions are produced together with some hydrogen gas. At the anode, hydroxyl ions are removed and the resulting oxygen may be used in corrosion of the electrode, but checks on the sensitivity of the model have shown that this will not cause a significant error.

The sizes of the steps of time and space are set by continuously reducing them and checking that the calculated solution remains constant. In particular, the time step is reduced sufficiently to ensure that the concentration does not change by more than 10 % during any time step. In order to reduce the time required for calculation, the programme progressively increases the time step but, in the early stages of a run, they are kept small by this requirement for stability. The calculations are carried out for ions in solution and at the end of each time step they are redistributed between those adsorbed and those in solution using the capacity factor to calculate adsorption.

The model was proposed for four ions in the pore solution, but can be easily changed to any number of ions. The ions considered were potassium found in the initial pore solution of the sample, sodium and hydroxide found in the pore solution and in the external cells, and chloride found in the external cells.

The transport processes into the concrete were restricted by binding with linear isotherms. A linear isotherm defines a linear relationship between

free and the bound ions over a range of concentration at a given temperature, as described in Section 1.3.1. It would be relatively simple to include non-linear binding if data was available to define it. A conceptual diagram of the model is shown in Fig. 10.7.

10.5.2 Temperature

When the current flows, it will cause ohmic heating in the sample. This is regularly observed during the experiments. The heat will be lost at a rate which is approximately proportional to the temperature difference between the sample and room temperature. This effect has been included in the code with a constant of proportionality for the heat loss which was determined from experimental observations of the peak temperatures.

10.5.3 Initial checks

The model was checked against equation (10.9), but this was only possible after disabling the voltage correction, temperature change routines and changes to the concentrations in the reservoirs which are not included in the analytical solution. With these precautions, exact agreement was obtained.

10.6 Initial experimental validation

10.6.1 Methods used in the initial validation

The model described in Section 10.5 will calculate currents and concentrations at different times working from the properties of the ions: diffusion coefficients, capacity factors and initial concentrations. However, the main use of the model is to calculate these properties from results of the experiment, particularly the current–time transient. For this initial work, a simple linear optimisation system was used. In this method, different values for the properties were modelled and the results optimised to fit with the intial current, final current and total charge. The use of artificial neural networks, which is a far more powerful method, is presented in Chapter 11.

The migration of four ions was considered: chloride, hydroxyl, sodium and potassium. Each of these is defined by three variables: a diffusion coefficient, a capacity factor and an initial concentration in the sample. The programme which was used was capable of optimising three of the resulting 12 variables which define the system. In effect, nine variables had to be set and the remaining three are calculated. The hydroxyl and chloride diffusion and initial concentration of hydroxyl ions were calculated. Table 10.1 shows the initial values of the variables.

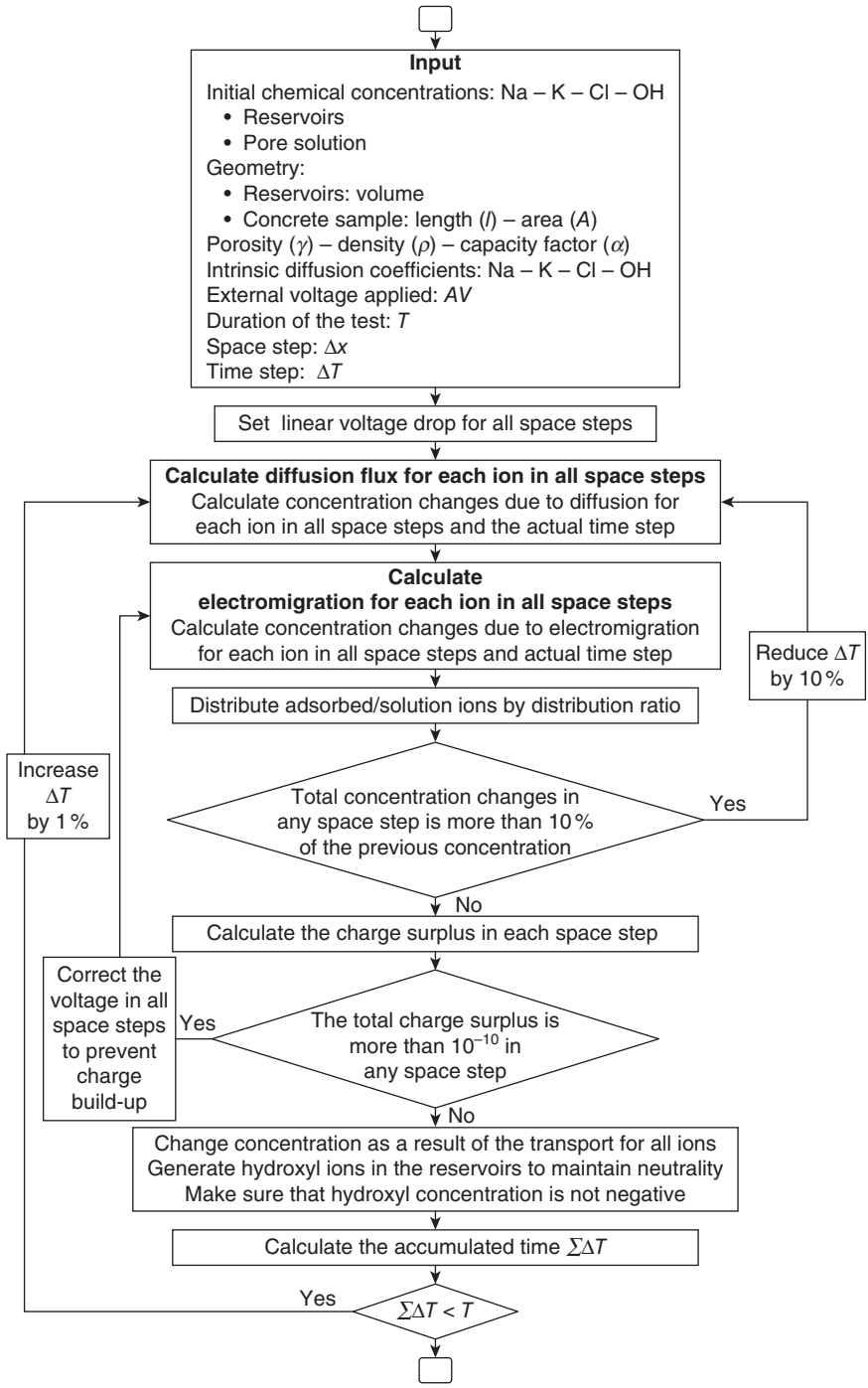

10.7 The computer model.

Table 10.1 Values for variables at start of run in base case prior to optimisation to fit experimental data

Ion	Valence z	Intrinsic diffusion coefficient D (m^2/s)	Concentration C (mol/m^3) (in liquid)			Capacity factor
			Negative reservoir	In sample	Positive reservoir	
Hydroxyl	–1	1.65E-10	0	275	300	0.2
Chloride	–1	6.00E-10	500	0	0	2
Sodium	1	4.00E-10	500	138	300	0.2
Potassium	1	9.00E-11	0	137	0	0.2
Anion	1	0	0	0	0	0.1

Table 10.2 Mixes used for experimental work

Mix	GGBS/ cement	Water/ cementitious	Sand/ cementitious	Superplasticiser/ cementitious
A	–	0.7	1.5	–
B	0.25	0.3	2.6	0.013

10.6.2 Mix designs

Mixes were cast to the proportions shown in Table 10.2 and cured in water for 28 days. The initial testing was carried out using apparatus which was similar to that described in Section 10.2 but with the following specific differences:

1. The end-volumes were larger at 0.8 l, compared with typical volumes of 0.2 l for the standard apparatus.
2. The experiment was run at 40 V.
3. The samples were run for 1000 min (17 h). These longer runs typically give far greater changes in current during the test than are normally observed during a 6 h test.
4. The cells were designed to give access to the top of the sample. For some samples, this was used to establish a salt bridge by drilling 4 mm diameter holes in the samples and installing a flexible plastic pipe containing 0.1 M potassium chloride. The other end of the pipe was placed in a beaker with a reference electrode.

These non-standard cells were developed for this initial work because it was thought that they would be easier to use. However, it was decided for subsequent work that the cells described in the standard (with the addition

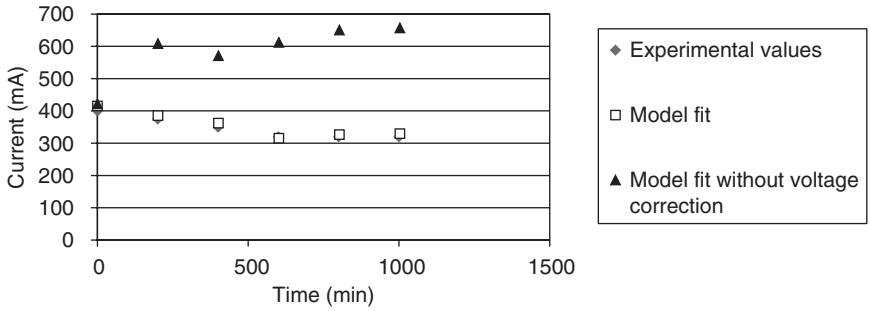

10.8 Example of model fit by optimisation for mix A.

of the salt bridge) would be used, and this is recommended for any future work.

10.6.3 Fitting the data

It was observed that optimising with three variables normally gave the model sufficient degrees of freedom to calculate a good theoretical fit to experimental data sets. Figure 10.8 shows the model fit to the data for mix A. This was obtained by optimising to the experimental results. The obtained intrinsic diffusion coefficients were 7.8×10^{-11} for hydroxyl and 2.9×10^{-10} for chloride, and the initial concentration of hydroxyl ions was 245 mol/m^3. It may be seen that the model was able to give a good fit to the shape of the curve. Figure 10.8 also shows the effect of modelling the system with a linear voltage drop (i.e. no voltage correction), and it may be seen that the effect is significant.

10.6.4 Effect of hydroxyl ion concentration

Figure 10.9 shows the predicted effect of the hydroxyl ion concentration on the initial, final and average results. Typically, this concentration would be most affected by the addition of pozzolanic materials which would deplete the free lime during hydration. Sugiyama *et al.* (2001) observed that the initial current is far more significantly affected by this concentration than the final current, and it may be seen that this observation is well predicted by the model.

10.6.5 Chloride profiles

Figure 10.10 shows chloride concentrations predicted by the model at different times and compares them with those found experimentally by different authors. For this modelling, the volume of the input reservoir was

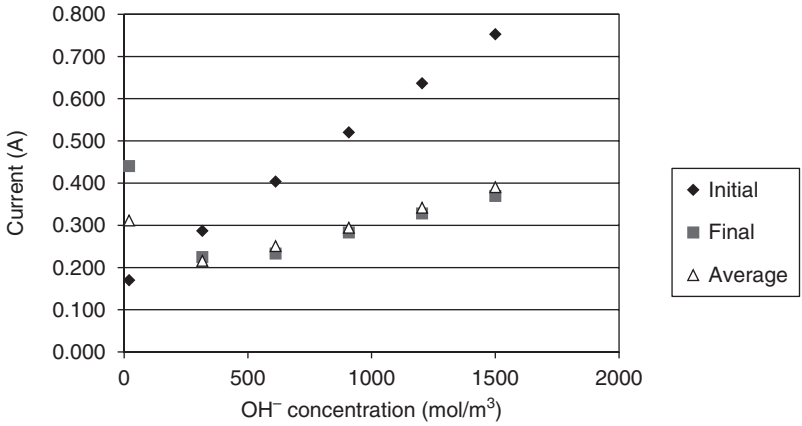

10.9 Predicted effect of hydroxyl ion concentration on current.

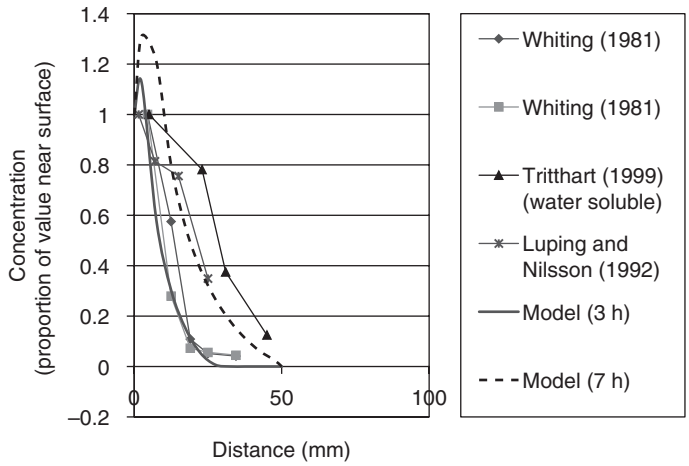

10.10 Comparison of model with reference data for chloride profiles.

increased to reduce predicted changes in concentration. It may be seen that the model predicts a small build-up of chlorides just below the surface that has not been observed, but the shape of the main part of the curve follows the observations.

10.6.6 Salt-bridge measurements

Figure 10.11 shows the current–time transient for a sample of mix B. The fit to this curve was obtained with intrinsic diffusion coefficients of 1.65×10^{-11} for hydroxyl and 4×10^{-11} for chloride, and the initial concentration of hydroxyl ions was 90 mol/m^3. Figure 10.12 shows the voltage distribution

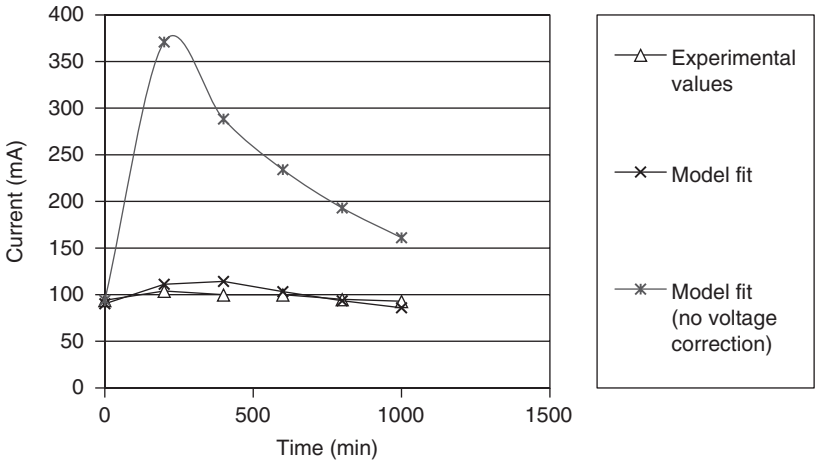

10.11 Model fit to current transient for mix B.

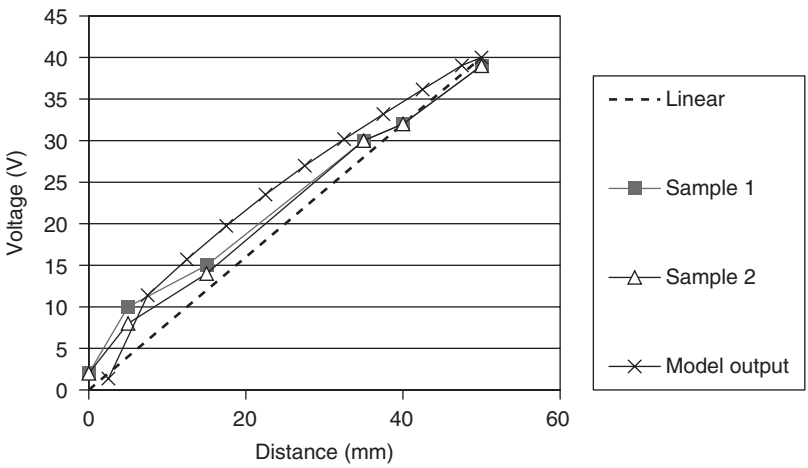

10.12 Experimental and theoretical voltage distribution for mix B.

across the sample after 6 h indicating the predicted values and two measurements made on replicate samples. It may be seen that the deviation from a linear voltage drop is small, but reference to Fig. 10.11 shows that it has a very significant effect on the current.

10.6.7 Effect of sample length

Figure 10.13 shows the predicted effect of changing the sample length. It may be seen that it is non-linear with a greater increase in charge passing at shorter lengths. This effect was observed by Abou-Zeid *et al*. (2003) for all of a number of series of samples tested.

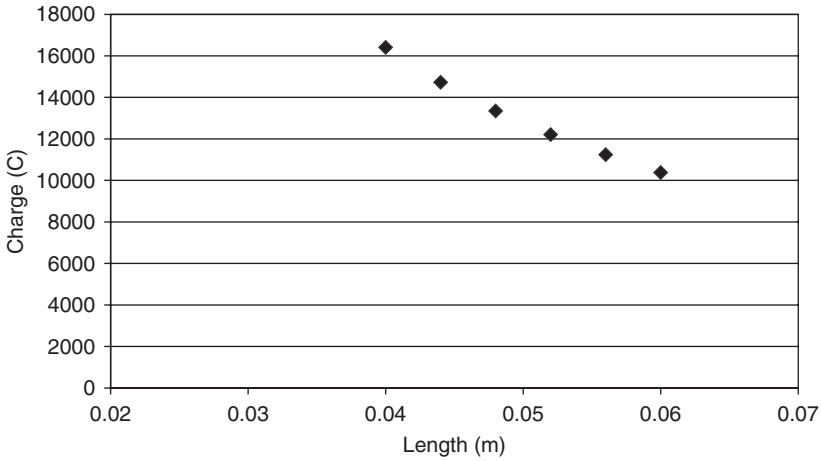

10.13 Predicted effect of sample length on charge passing.

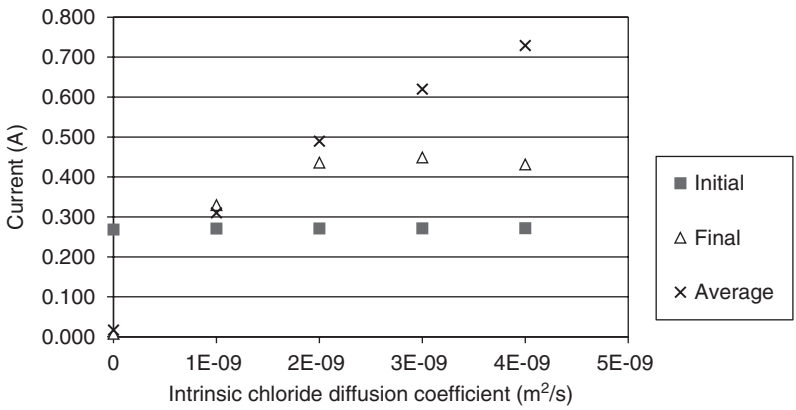

10.14 Predicted effect of chloride diffusion coefficient on current.

10.6.8 Discussion

Figures 10.14 and 10.15 show the predicted relationship between the measured charge passing and the diffusion coefficients for chloride and sodium. This basic relationship would be expected, and it has been observed by Yang (2004) and others. Comparing these with Fig. 10.9, it may be seen that it is indicated that a high initial current shows a high hydroxyl concentration, but a high average current (i.e. a current that increases and then falls) shows a high chloride diffusion and a more uniform trend shows high sodium diffusion.

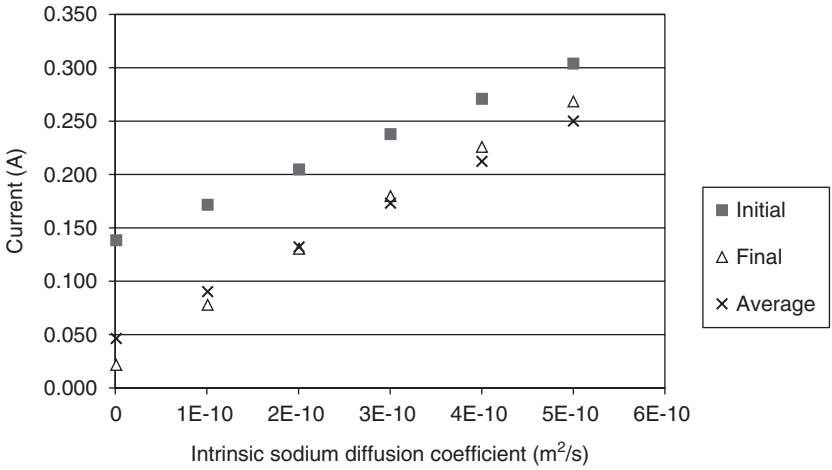

10.15 Predicted effect of sodium diffusion coefficient on current.

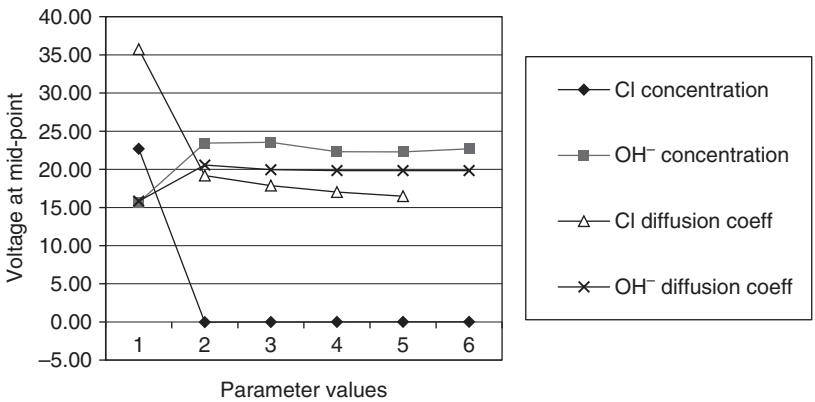

10.16 Predicted effect on mid-point voltage of varying different parameters.

Figure 10.16 shows the predicted voltage at the mid-point of the sample at the end of the test as the different variables are changed. This voltage would be 20V in a linear voltage distribution (i.e. half the applied voltage). It may be seen that measuring this would yield very useful data for the model to work with and could separate out different phenomena. Pre-saturating the sample with chlorides is predicted to have a very significant effect by reducing the resistivity across all of it except a small region near the anode where the ions are depleted. The hydroxyl ion concentration may be seen to have a significant effect on the mid-point voltage with a change from below 20V to above 20V as the concentration increases.

All of the results reported here were taken over a test period of 17 h. It is suggested that this increased time adds significantly to the value of the data. Permitting the reservoir concentrations to change (by limiting their volume) will also cause the current to change more during the test and give a clearer 'signature' to show the properties of the sample being tested.

10.7 Full model validation

This work was a far more comprehensive validation of the model carried out in a later programme using ASTM standard cells.

10.7.1 Sample preparation

Mixes of mortar with water to cement (w/c) ratio of 0.49 (mix 1) and 0.65 (mix 2) were cast. Ordinary Portland cement CEM I without mineral or chemical admixtures was used. The binder/sand ratio was 2.75 for all mixes. For each mix, five cylinders of 100 mm diameter and 200 mm height were made to be used both in the porosity and electromigration tests.

The specimens were cured under controlled humidity and temperature, and all the migration tests were made at ages between 28 and 38 days. The cylinders were cut to make samples 50 mm thick and 100 mm diameter. Two samples were taken of each cylinder, being taken from its central part. The test was run on two replicate samples and the reported result is the average of both results.

10.7.2 Porosity measurement

The open porosity accessible by water ε was measured using the simple method of water displacement. The central part of each cylinder (30 mm thickness) was vacuum saturated until constant weight and weighed in water and air. They were then dried in an oven at 105 °C until constant weight and weighed again. The porosity was found with equation (7.9). Three replicates were tested for each mix.

10.7.3 Strength measurement

Three 50 mm cubes for each mix were cast in order to measure the mortar strength. Concrete strengths were obtained from 100 mm cubes.

10.7.4 Electromigration test procedure

Standard cells were used as shown in Fig. 10.2. The anode and cathode reservoir cells were filled with a 0.30 N NaOH and a 3.0 % NaCl solution, respectively (as specified in ASTM C1202), and a DC voltage of 30 V was applied for 21 h. This voltage was lower than that specified in the ASTM

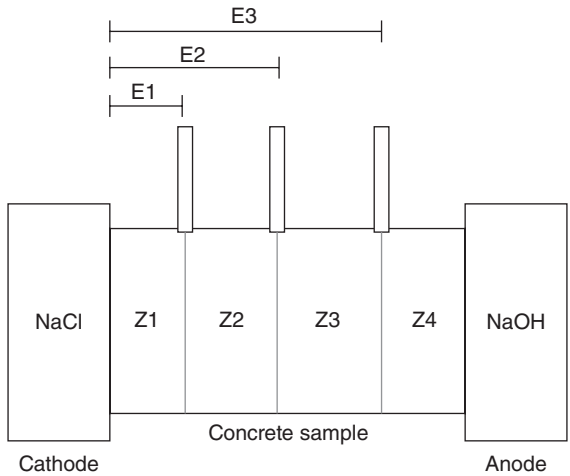

10.17 Target locations of the points where the voltage was measured.

standard because 60 V caused unacceptable heating. The current was monitored every 2 min as well as the potential difference between the salt bridges in the sample and the negative electrode of the system.

The test was run as described in Section 10.2. For both mixes, the voltages were measured at three different positions. The target location of those points was the mid-point and the quarters of each sample. The distance between the points where the potential was measured and the edge of the sample in contact with the negative electrode (cathode) is shown in Fig. 10.17. The locations of the salt bridges define four zones named as Z1, Z2, Z3 and Z4, and the electric potential difference across each one was measured.

10.7.5 Experimental results

As at the start of the test the electric field is linear across the sample, the gradient or difference between the measured voltage at any time and the linear condition can be calculated. This value corresponds to the membrane potential and was calculated by subtracting the value of the voltage measured from the initial value measured at the start of the test for each time and position:

$$\Delta V = V_{\mathrm{Ti}} - V_0 \qquad [10.22]$$

where:

ΔV corresponds to the membrane potential
V_{Ti} is the voltage measured at time t and
V_0 is the voltage at the start of the test.

Table 10.3 Results of compressive strength and porosity

Mix	w/b	Concrete strength (28 days) (MPa)	Open porosity (%)
1	0.49	36.59	18.5
2	0.65	31.48	25.4

In order to avoid the noise found experimentally during the logging of the tests, a commercial curve fitting software was used. It was found that this noise was substantially reduced by slightly increasing the depths of the drilled holes for the salt bridges. This observation indicates that the noise was caused by the random distribution of aggregate limiting the contact between the salt bridges and the pore volume.

The results of strength and porosity are shown in Table 10.3. Figure 10.18 shows the variation of the voltage across the sample in the mixes tested. Points E1, E2 and E3 are the points where the voltage was measured at the quarters and mid-point of the sample. Although there was noise in the voltage for all the samples, there is a good defined trend and the profile and the replicates in each mix were very similar. The voltage for each sample was not linear with respect to time and position during the test.

The behaviour of the membrane potential across the samples during the test is shown in Figs 10.19 and 10.20 as contour graphs, each graph represents the average of two samples. The value for the membrane potential at the edges of the sample was assumed as zero because those points correspond to the electrodes in the solutions. Both mixes showed a similar distribution of the membrane potential. There was an increase of voltage in the area that was near to the alkaline solution (positive electrode) and both mixes reached a maximum value of voltage with a subsequent reduction. In the area near to the cathode, the membrane potential either tended to be constant during the test or presented a smooth negative variation.

All the membrane potentials at any point throughout the duration of the test can be seen from the contour plots. However, tests of this type are expensive and not easy to complete. As alternative, it has been proposed to study just the behaviour of the mid-point as a source of additional information in a practical situation. It is expected that the mid-point voltage would provide sufficient information for most practical purposes.

10.7.6 Results from the computer model

In order to validate the numerical model, migration tests for both mixes were simulated. The test for mix 1 with water to binder ratio (w/b) = 0.49, was selected as initial comparison and in the simulation of mix 2

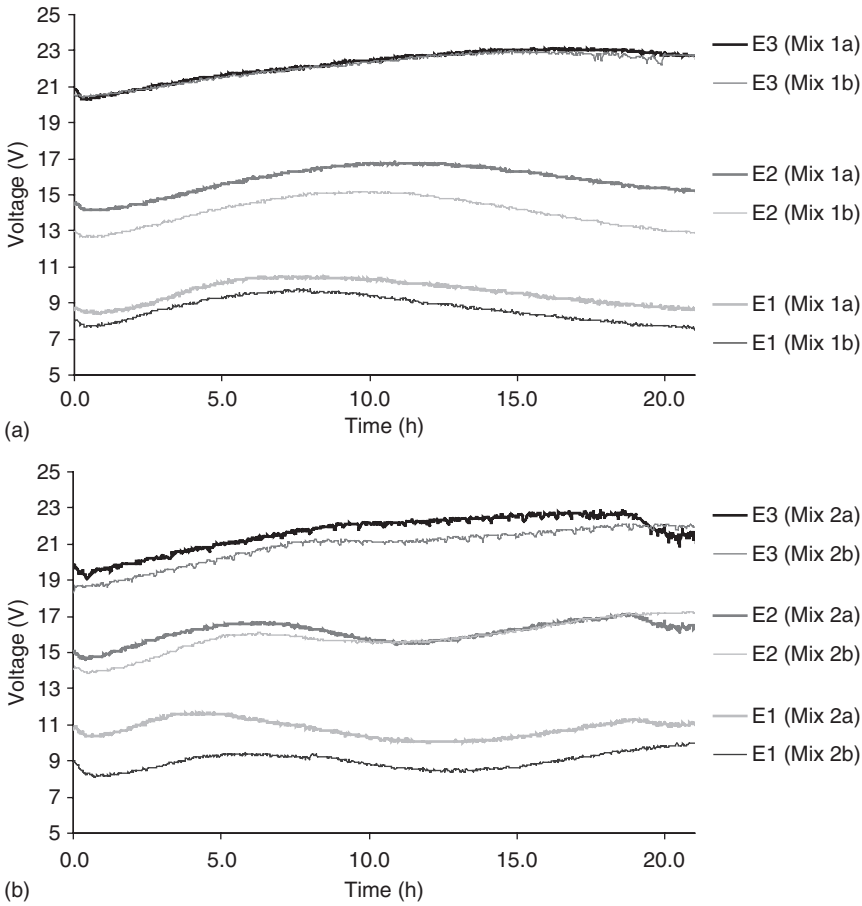

10.18 Difference of potential across the sample: (a) mix 1; (b) mix 2.

(w/b = 0.65) the value of the porosity was adjusted to obtain the value measured experimentally. The characteristics of the system sample/cells are shown in Table 10.4. For this particular simulation, the initial pore solution concentration was based on published results (Bertolini *et al.*, 2013). The intrinsic diffusion coefficients for all the ions were obtained applying an optimisation process for mix 1. The computer program was run enough times to find the best combination of coefficients to fit the experimental values of current and membrane potential in the mid-point of the sample.

The intrinsic diffusion coefficients for sodium and potassium found were significantly lower than the values for chlorides and hydroxides as observed previously by other researchers (Andrade, 1993; Zhang and Buenfeld, 1997). These results confirm that the mobility of cations in porous media

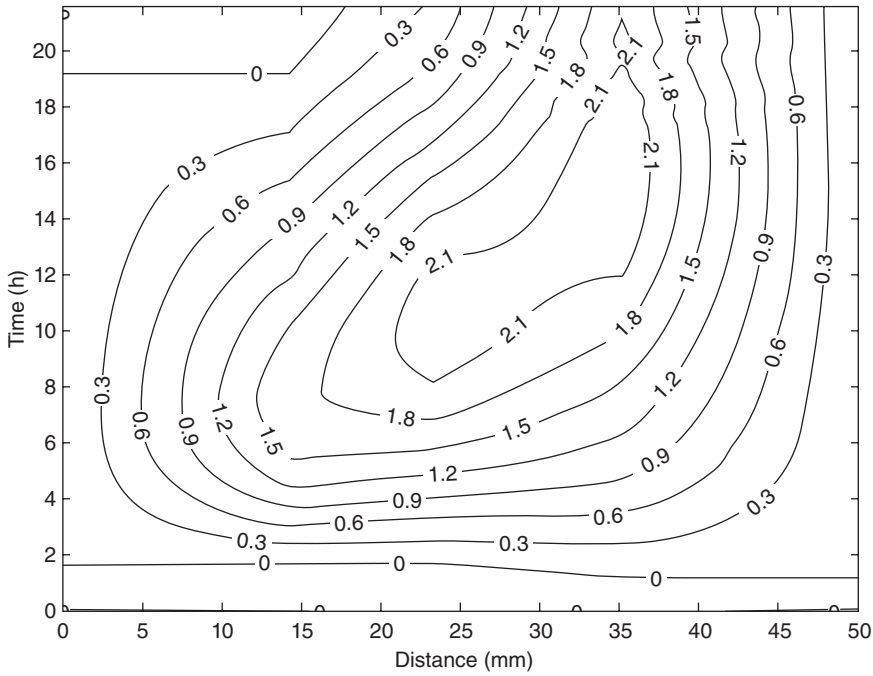

10.19 Average membrane potential mix 1 – w/b = 0.49.

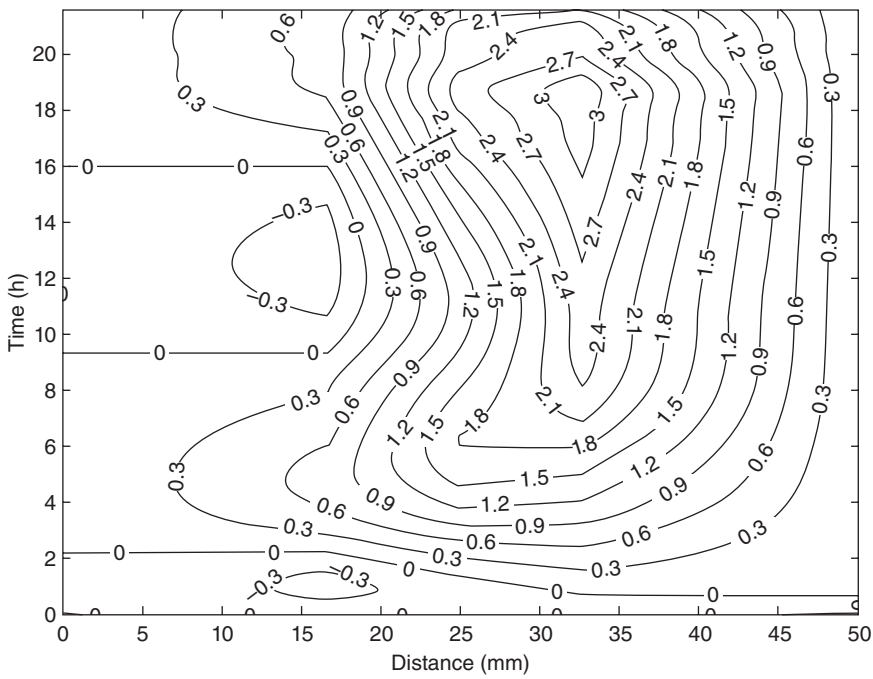

10.20 Average membrane potential mix 2 – w/b = 0.65.

Table 10.4 Input parameters at the start of the simulation

	Intrinsic diffusion D (m^2/s)	Concentration (mol/m^3) upstream (negative)	Concentration (mol/m^3) pore solution	Concentration (mol/m^3) downstream (positive)
Hydroxyl	1.60E-10	0	240	300
Chloride	3.00E-10	529	0.0	0
Sodium	4.00E-11	529	79	300
Potassium	9.00E-12	0	161	0

Sample length/radius (m): 0.05/0.05.
Run time (h): 21.
Ext. voltage (V): 30.
Porosity: 0.19.
Cell volume (m^3): 0.0002.
Cl capacity factor: 0.3.

differs from that observed if they diffuse in an ideal solution. In the same way, the observed intrinsic diffusion coefficients for chlorides and hydroxides show that both ions are responsible for most transport of charge; however, small changes in the diffusion of cations produce large changes in the mid-point membrane potential. Although the ratio of the intrinsic diffusion coefficients of chloride and hydroxide was greater than 1, it is apparent that the high mobility of chlorides is reduced in the computer model through the adsorption reactions between the ions and the hydration products of concrete which are modelled using a linear isotherm.

The total electrical current through the samples is shown in Fig. 10.21 where the experimental results are presented with the simulations for mixes one and two. For mix one the current modelled is presented both with the membrane potential and without any voltage correction. The experimental results and the simulation with the membrane potential were in good agreement, being better for initial times than for long times. The difference between them at the end of the tests was around 35 %. In contrast, the profile of the current without including the membrane potential was significantly different to the experimental results. Although the initial current was similar, there was a maximum current value three times greater than when the voltage was corrected. The current passed by mix 2 presented a similar profile for the experimental results and the simulations with the membrane potential corrections. As was expected, mix 2 showed higher values of current because of its higher w/c ratio.

The behaviour of the simulated membrane potential of mix 1 across the sample and during the test is shown in Fig. 10.22 as a contour graph. The numerical values were taken from the numerical program and plotted with

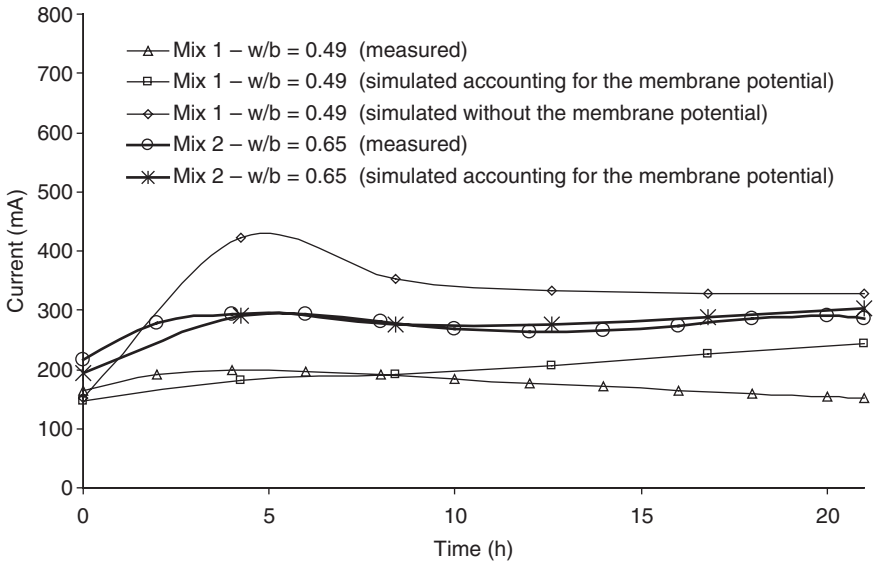

10.21 Current variations during the experiments.

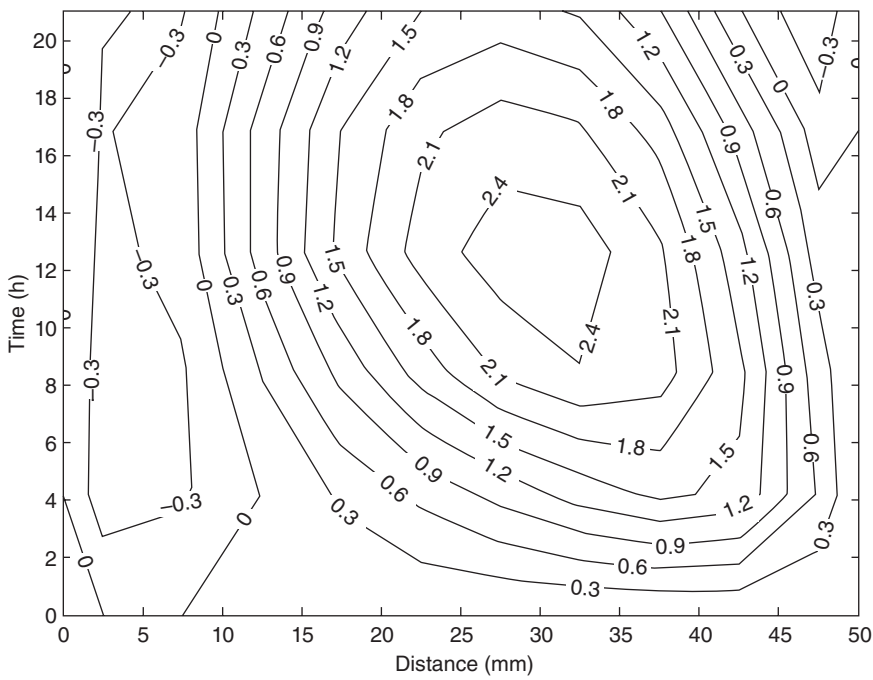

10.22 Simulated membrane potential (V) (mix 1 – w/b = 0.49).

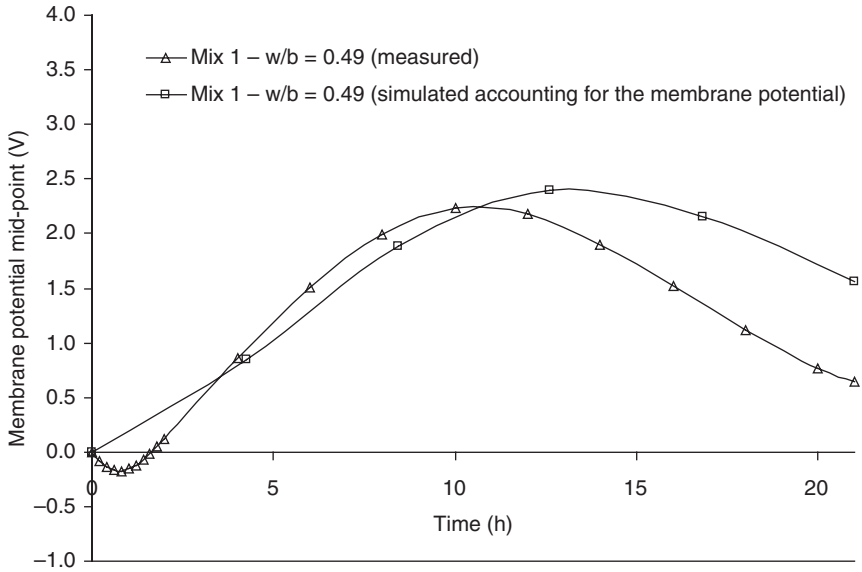

10.23 Simulated membrane potential mid-point (mix 1 – w/b = 0.49).

the contour function of Matlab®. The simulated membrane potential behaves in the same way as the corresponding experiment (Fig. 10.19). The voltage was negative in the first half of the sample throughout the experiment; in contrast, the second half of the sample had positive values of membrane potential. The simulated and measured mid-point membrane potential is showed in Fig. 10.23 for mix 1. Although the measured profile showed some initial negative values and reached a local maximum membrane potential voltage before the simulations, both graphs showed similar behaviour and have the same profile. From a macroscopic point of view, the local maximum or any feature of the mid-point membrane potential can be explained as a result of the variation of the conductivity of the pore solution due to the migrations of all ions involved. The transient conductivity is defined by the relationship between the transient voltage and the transient current at any point.

Although the principal aim of the computer model was to simulate the chloride penetration, the profile of the other ions was calculated as result of the interactions between them. The relationship between the transport properties of the chloride and hydroxide ions has been recognised for a long time, however, the transport of potassium and sodium in concrete is not extensively reported in the literature. Figure 10.24 shows the profiles of concentration for the four ions during the simulation of mix 1.

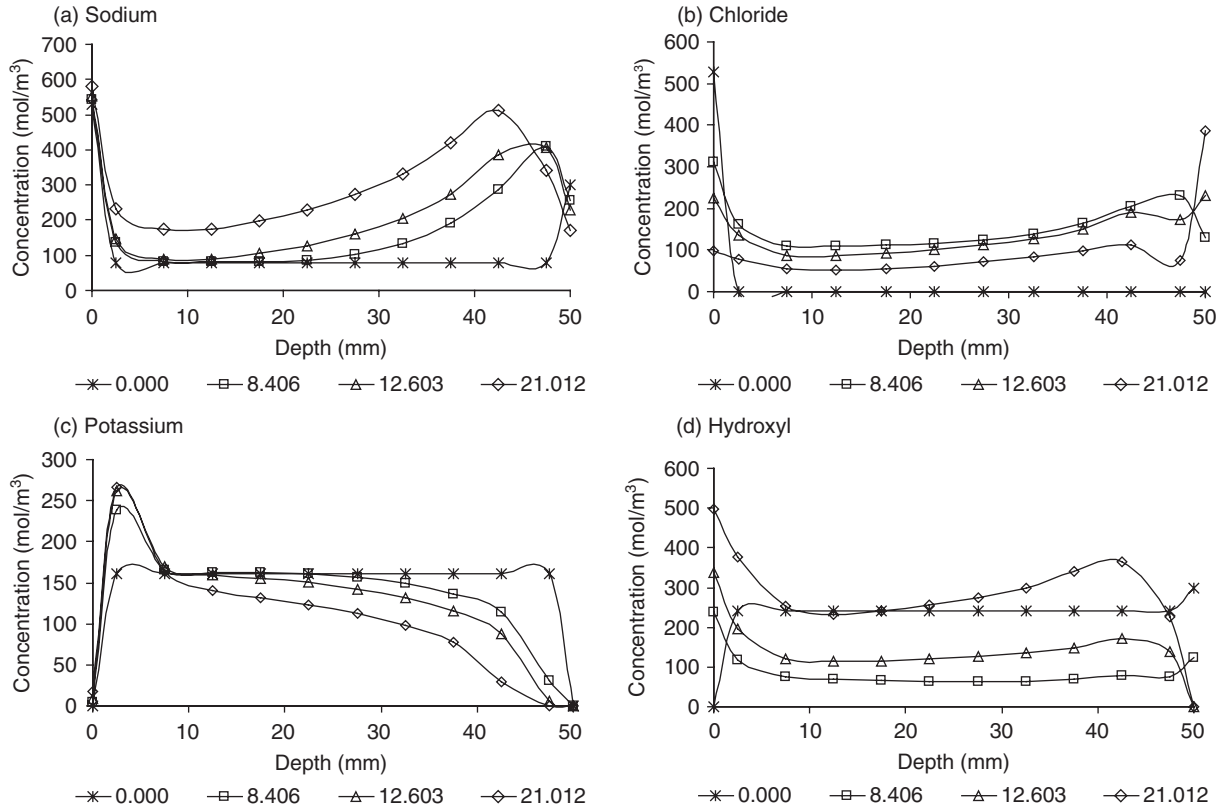

10.24 Concentration across the sample, distances (depth) from negative side in mm (on the horizontal axis) vs concentration in mol/m^3 (mix 1 – w/b = 0.49). The four curves in each graph are for different times in hours.

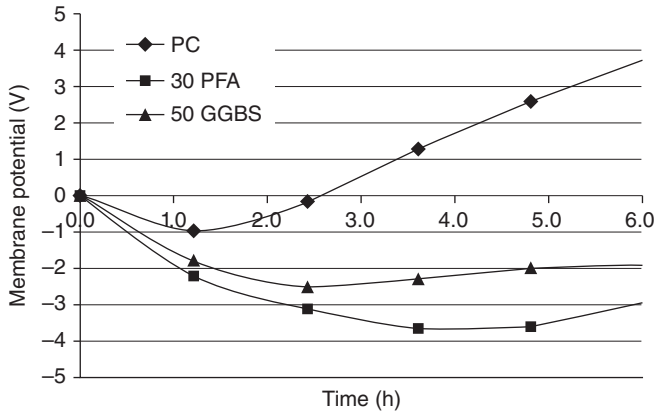

10.25 The membrane potential (i.e. the difference between the voltage and the linear voltage drop) for mid-point voltages in an ASTM C1202 test for PC (CEM1), 30% PFA (pulverised fuel ash) and 50% GGBS (ground granulated blast furnace slag).

10.7.7 Identifying different mixes

A further use for the measurement of the mid-point potential was identified during this research. Frequently, samples obtained from cores cut from existing structures are tested using the ASTM test and the composition is not known. Figure 10.25 shows the membrane potential at the mid-point voltages from samples containing the most common cement replacement (PFA and GGBS).

It may be seen from Fig. 10.25 that changing the cementitious components in a mix has a significant effect on ionic voltages. This is because they significantly change the ionic concentrations (e.g. pozzolans deplete hydroxyl ions). These signature traces mean that this test could be used to identify replacement materials.

It may be seen from Fig. 10.26 that the total charge passing is very different for the different mixes. This difference is caused by ion–ion interactions and does not necessarily indicate a change in the diffusion coefficient.

10.8 Conclusions

- It has been proved that the voltage drop in concrete samples during a migration test is not linear with respect to time and position. The application of the Nernst–Planck equation to the simulation of migration of any ionic species through a saturated porous medium accounting for

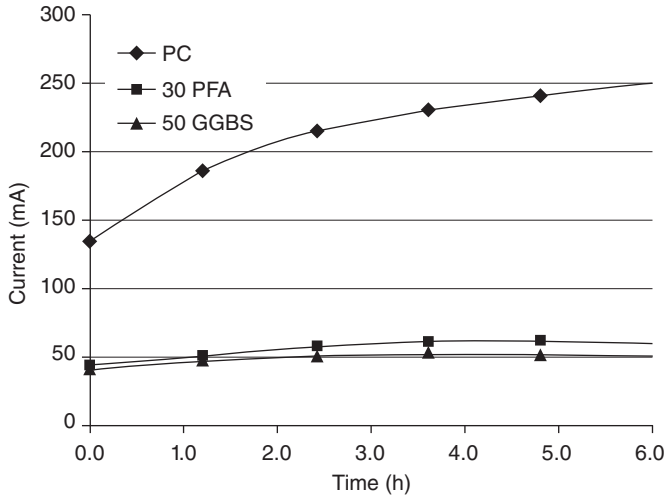

10.26 Current vs time data for GGBS and PFA mixes.

the non-linear voltage allows models to include all the microscopic interactions in a macroscopic way.

- All the ions (sodium, potassium, hydroxide and chlorides) present in a migration test, either in the pore solution or coming from the external cells, need to be included in the simulation in order to account for the non-linear effects caused by differences of mobility. The computer model proposed predicts the transient current and the membrane potential during the experiments.
- If a concrete sample is being tested and it gives a low Coulomb value, this could be caused by a low chloride diffusion coefficient, but it could also be caused by the use of a pozzolanic material to deplete the hydroxyl ions. Measuring the mid-point voltage could differentiate between these two effects and determine whether the sample was as good as the Coulomb value indicated. It is suggested that drilling a small hole and measuring this voltage on a spare channel in the data logger would not add significantly to the cost of these tests but could yield very useful data for analysing the results.

10.9 References

Abou-Zeid M N, Meggers D and McCabe S L (2003) Parameters affecting the rapid chloride permeability test, *Concrete International*, **25** (1), pp. 61–66.

Andrade C (1993) Calculation of chloride diffusion coefficients in concrete from ionic migration measurements, *Cement and Concrete Research*, **23** (3), pp. 724–742.

ASTM (2012) *ASTM C1202-912 Standard Test Method for Electrical Indication of Concrete's Ability to Resist Chloride Ion Penetration*, ASTM International, West Conshohocken PA, pp. 620–625.

Bertolini L, Elsener B, Pedeferri P, Redaelli E and Polder R B (2013) *Corrosion of Steel in Concrete: Prevention, Diagnosis, Repair* (2nd edn), Wiley-VCH, Weinheim.

Bockris J and Reddy A (1998) *Modern Electrochemistry 1: Ionics* (2nd edn), Plenum Press, New York.

Debye P and Hückel E (1923) The theory of electrolytes. I. Lowering of freezing point and related phenomena (PDF), *Physikalische Zeitschrift*, **24**, pp. 185–206.

Lorente S, Voinitchi D, Begue-Escaffit P and Bourbon X (2007) The single-valued diffusion coefficient for ionic diffusion through porous media, *Journal of Applied Physics*, **101** (2), p. 024907.

Luping T and Nilsson L-O (1992) Rapid determination of the chloride penetration diffusivity in concrete by applying an electrical field, *ACI Materials Journal*, **89** (1), pp. 49–53

Luping T, Nilsson L and Basheer P (2012) *Resistance of Concrete to Chloride Ingress*, Spon Press, London.

Sugiyama T, Tsuji Y and Bremner T W (2001) Relationship between coulomb migration coefficient of chloride ions for concrete in a steady-state chloride migration test, *Magazine of Concrete Research*, **53** (1), pp. 13–24.

Tritthart J (1999) Ion transport in cement paste during electrochemical cholride removal, *Advances in Cement Research*, **11** (4), pp. 149–160.

Whiting D (1981) *Rapid determination of the chloride permeability of concrete*, Report No. FHWA/RD-81/119, Federal Highway Administration, Washington DC.

Yang C-C (2004) Relationship between migration coefficient of chloride ions and charge passed in steady state, *ACI Materials Journal*, **101** (2), pp. 124–130.

Yu S W, Sergi G and Page C L (1993) Ion diffusion across an interface between chloride-free and chloride-containing cementitious materials, *Magazine of Concrete Research*, **45** (165), pp. 257–261.

Zhang J Z and Buenfeld N R (1997) Presence and possible implications of a membrane potential in concrete exposed to chloride solution, *Cement and Concrete Research*, **27** (6), pp. 853–859.

11

Electrical tests to analyse the transport properties of concrete – II: using a neural network model to derive diffusion coefficients

DOI: 10.1533/9781782423195.193

Abstract: In this chapter, the computer model of electromigration which was introduced in Chapter 10 is combined with an artificial neural network (ANN) model to enable values for diffusion coefficients to be determined from test results from the modified ASTM C1202 rapid chloride test. The ANN is necessary because the model in Chapter 10 requires values for the diffusion coefficients and capacity factors of the mobile ions and uses these to predict the test results for current and membrane potential. By using the ANN, it is possible to use the test results to calculate the diffusion coefficients and capacity factors from the test results.

Key words: artificial neural networks, optimisation, membrane potential, capacity factor, diffusion, electromigration.

11.1 Introduction

The methods presented in Chapter 10 can be used to predict the current–time transient and the mid-point voltage during a rapid chloride test. The calculations require input values of the diffusion coefficients and capacity factors of all the ions. However, the usual requirement in practical applications would be to obtain the coefficients from experimental results. Thus a prediction method was used. There are many possibilities for this. Section 6.3.2 describes how the output from a numerical model was optimised by repeatedly running it until the results were seen to be close to those observed. Section 15.3 refers to an optimisation routine that worked by progressively optimising each variable. This could only work for a small number of variables and was very slow. There are many other possibilities, including the response surface method. However, the fastest and most efficient method is to use an artificial neural network (ANN).

Table 11.1 Concrete mix design

Mix	w/c	PC (kg/m^3)	Fine agg. (kg/m^3)	Coarse agg. (kg/m^3)	Water (kg/m^3)
PC 4	0.4	400	705	1058	160
PC 5	0.5	400	664	995	200
PC 6	0.6	400	622	933	240

11.2 Experimental method

11.2.1 Concrete mixes

Samples of Portland cement (PC) with different water to cement (w/c) ratios were mixed. Table 11.1 shows the mix designs and the nomenclature used in this study. All the tests were made on samples around 6 months old which were kept in a controlled humidity and temperature room until each test was started. During the mixing, depending on the water content, the mixes had different flow properties. In order to avoid affecting the strength because of the differences in the mix compaction, all the mixes were compacted mechanically with a vibrating table. The moulds were filled with concrete in three layers and compacted to remove the air and reach the maximum density.

11.2.2 Current and membrane potential in the ASTM C1202 test

The ASTM C1202 test is described in Section 10.2. Each test was run twice and the result shown is the average of both results.

11.2.3 Porosity measurement

The porosity was measured by weight loss as in Section 7.3.3.

11.3 Neural network optimisation model

The computational model used two main techniques. The electro-diffusion numerical routine described in Section 10.5 was used. However, because in reality the physical transport properties are unknown, a neural network algorithm was trained to optimise those physical properties. As a result of combining both techniques, the transport properties of a concrete sample could be determined from experimental observations of mid-point membrane potential and current measured simultaneously during a migration test.

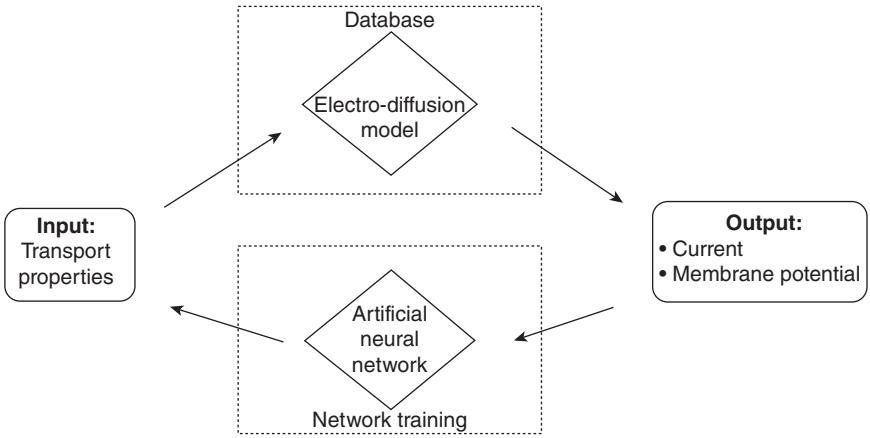

11.1 Conceptual diagram integrated model.

To train the network, the numerical electro-diffusional model was run many times in order to obtain a database of the input and the corresponding target vectors. During the training, the outputs of the model were used as inputs for the neural network. All the data was normalised between –1 and +1 in order to avoid the influence of the scale of the physical quantities. In the same way, the tangential transfer function was limited to be between –1 and +1. The Levenberg–Marquardt training algorithm was used. Figure 11.1 shows a conceptual diagram of the integrated model.

The optimisation model used a feed-forward back-propagation network with a multilayer architecture. Six neurons defined the input layer, corresponding to values of the current and the mid-point membrane potential at different times. A middle hidden layer had three neurons, and the output layer has seven neurons corresponding to the intrinsic diffusion coefficients of Cl^-, OH^-, Na^+ and K^+, the porosity, the hydroxide composition in the pore solution at the start of the test, and the binding capacity factor for chloride ions. The neural network model was constructed using the neural network tool box of Matlab®. Figure 11.2 shows the input, the hidden layer and the outputs of the network.

11.3.1 Integrated numerical and neural network model

Obtaining the related transport chloride properties of concrete from measurements of current has been reported (Yang *et al.*, 2007); however, long durations and steady state conditions are required. In the present research, with the simultaneous measurement of the current and the

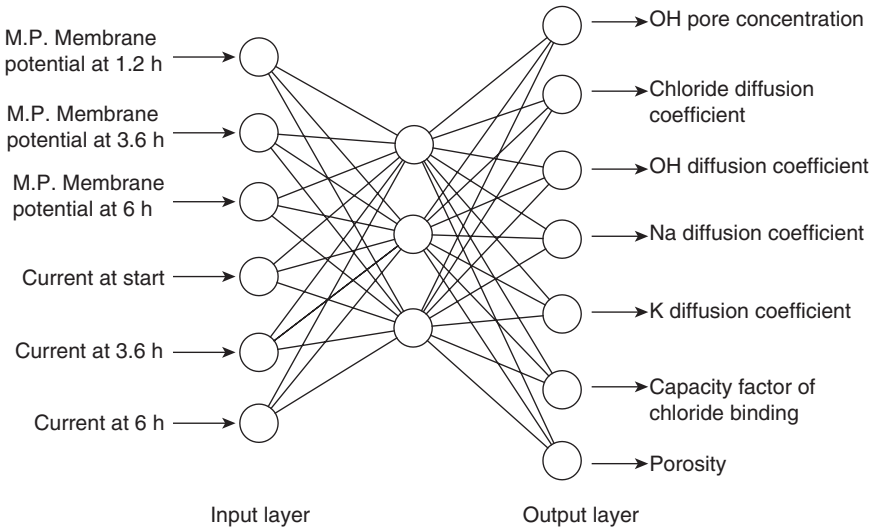

11.2 Multilayer neural architecture used.

mid-point membrane potential, it is possible to determine a unique combination of the transport properties by using a trained neural network. In order to simulate the transport properties of concrete and taking into account the complex variables related with the physical phenomenon, two assumptions were made:

1. The only ions that interact with the cement matrix products are chlorides, and that interaction is defined with a linear binding isotherm. Although it has been demonstrated experimentally (Delagrave *et al*., 1997) that non-linear isotherms reflect the absorption phenomena better, the model uses an average linear isotherm that represents in a good way the average adsorption of chlorides as described in Section 1.3.1.
2. At the start of the test, the chemical pore solution is composed of ions OH^-, K^+, and Na^+ and, in order to keep electroneutrality, it was assumed that the concentration of hydroxyl ions is equilibrated with a proportion of 33 % of sodium and 66 % of potassium. This assumption was based on published results (Bertolini *et al*., 2013).

11.4 Results and discussion

11.4.1 Experimental determination of the transient current, membrane potential and the diffusion coefficients

The average current measured for each mix in the migration test is shown in Fig. 11.3. As was expected, an increase in the w/c ratio gave an increase

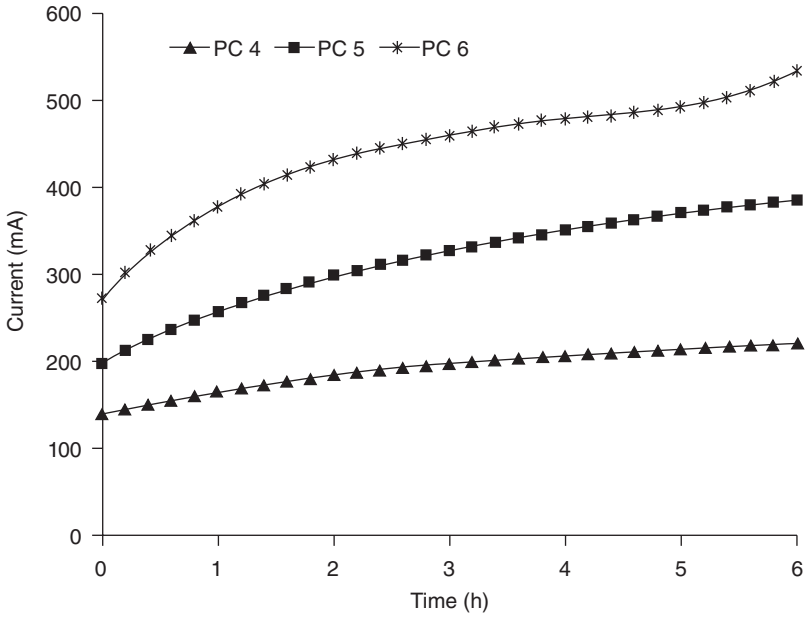

11.3 Current measured experimentally.

in the current passed, and a corresponding increase in the temperature of the sample. The measured maximum value of temperature in the anode solution was 63, 44, and 36 °C for samples of w/c ratio of 0.6, 0.5 and 0.4, respectively, and the values of charge calculated as the area under the graph of current versus time were 9580, 6863 and 4149 C for samples of w/c ratio of 0.6, 0.5 and 0.4, respectively.

The measured membrane potential is shown in Fig. 11.4a. There was noise in the results as noted in Chapter 10. They were filtered with commercial curve fitting software in order to find the best trend, and this can be seen in Fig. 11.4b. The average membrane potential for each mix is shown in Fig. 11.4c, it can be seen that for all mixes the membrane potential showed a rise from its initial value; however, mix PC-6 showed an initial decrease during the first 2 h.

11.4.2 Prediction of chloride related properties

The trained neural network was fed with the values for the current transient and the mid-point voltage from the migration test and, from this data, the chloride transport related properties were calculated. As a measure of the reliability of the network, the transport properties obtained were used to run the electro-diffusional model in order to obtain a simulated transient

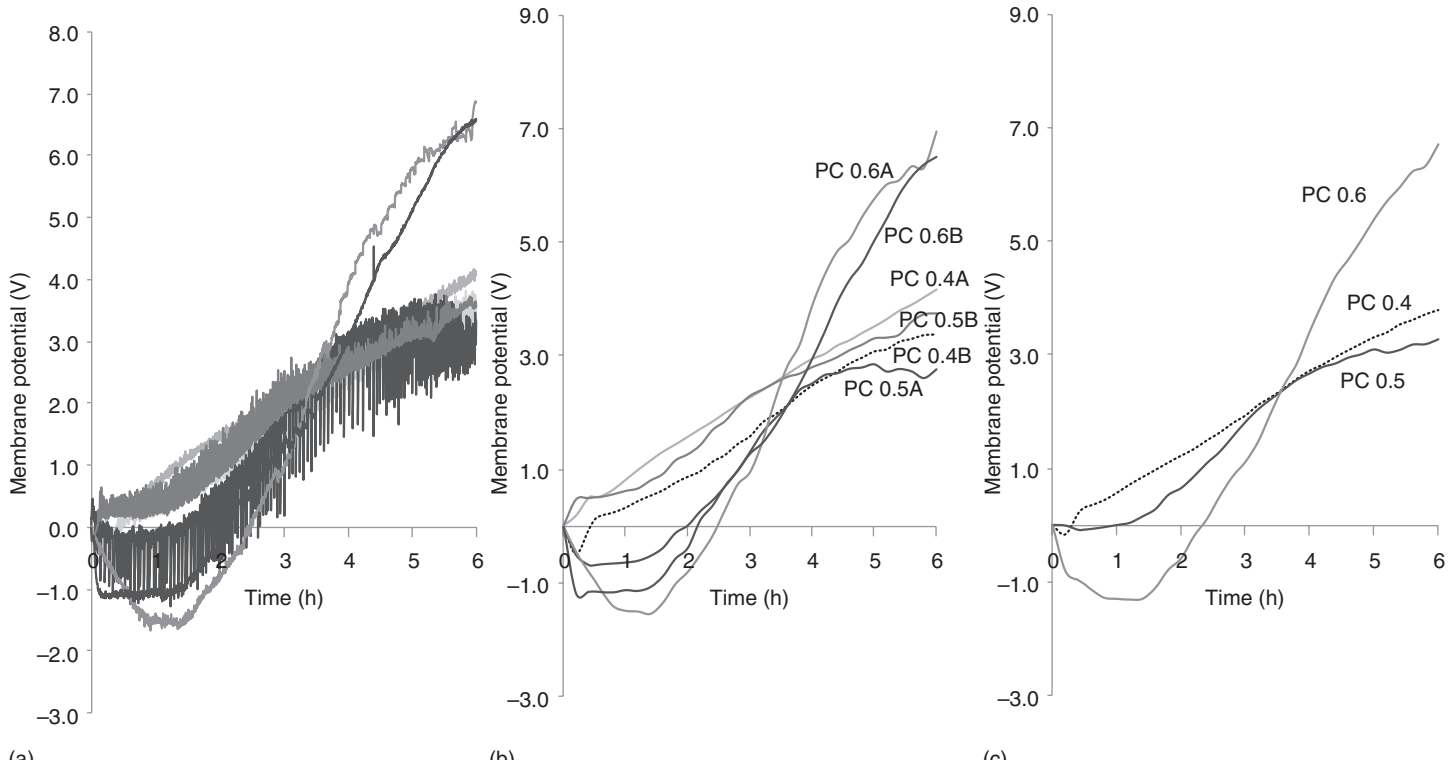

11.4 Measured membrane potential.

current and mid-point membrane potential. The comparison of these curves is shown in Fig. 11.5. It can be seen that, for the current, the simulations are in very good agreement with the experiments and, for the membrane potential, although there are some small differences, there is a well-defined trend.

The differences between the measured and simulated membrane potential can be explained by factors related to the accuracy of the measurement device used during the experiment, the heating of the material under an electrical field, or the variability of the test. However, it may be seen that the neural network is able to give a good fit to the profile of the membrane potential, given that the number of possible combinations of properties that yield a given current and membrane potential is almost infinite.

The transport properties calculated by modelling the test results include the porosity, the binding capacity factor and the initial hydroxide composition at the start of the test. As was expected, the porosity increases with an increase of the water to binder (w/b) ratio (Fig. 11.6a). It can be seen that the trend of the measured porosity is similar to that calculated; however, some differences arise from errors in either the numerical or experimental methods. The binding capacity factor decreases as the w/b ratio increases, presumably due to the refining of the hydration compounds enabling them to bind more free chloride ions (Fig. 11.6b). The calculated initial chemical content of the pore solution increases with an increase in the w/b ratio. This can be attributed to the increased amount of water, which can keep more alkalis in the pore solution.

The calculated intrinsic diffusion coefficients for all the species involved in the simulation (Cl^-, OH^-, Na^+, K^+) are shown in Fig. 11.7. As observed by other researchers (Andrade, 1993), the anions generally had lower diffusion coefficients than chlorides and hydroxides. The exception to this was mix 6, where hydroxide and sodium have a similar diffusivity. As was expected, the calculated numerical values of the intrinsic coefficients for all the species are, for all the cases, lower than the coefficients of diffusion in infinite diluted solutions in electrochemistry textbooks (Bockris and Reddy, 1998). The values obtained are physically possible and are in acceptable ranges.

11.5 Conclusions

The experimental–numerical procedure gave viable results for the fundamental properties of concrete. The initial hydroxide composition of the pore solution, the chloride binding capacity, the porosity and the diffusion coefficients for all the species involved were calculated and gave results which were comparable with those reported elsewhere.

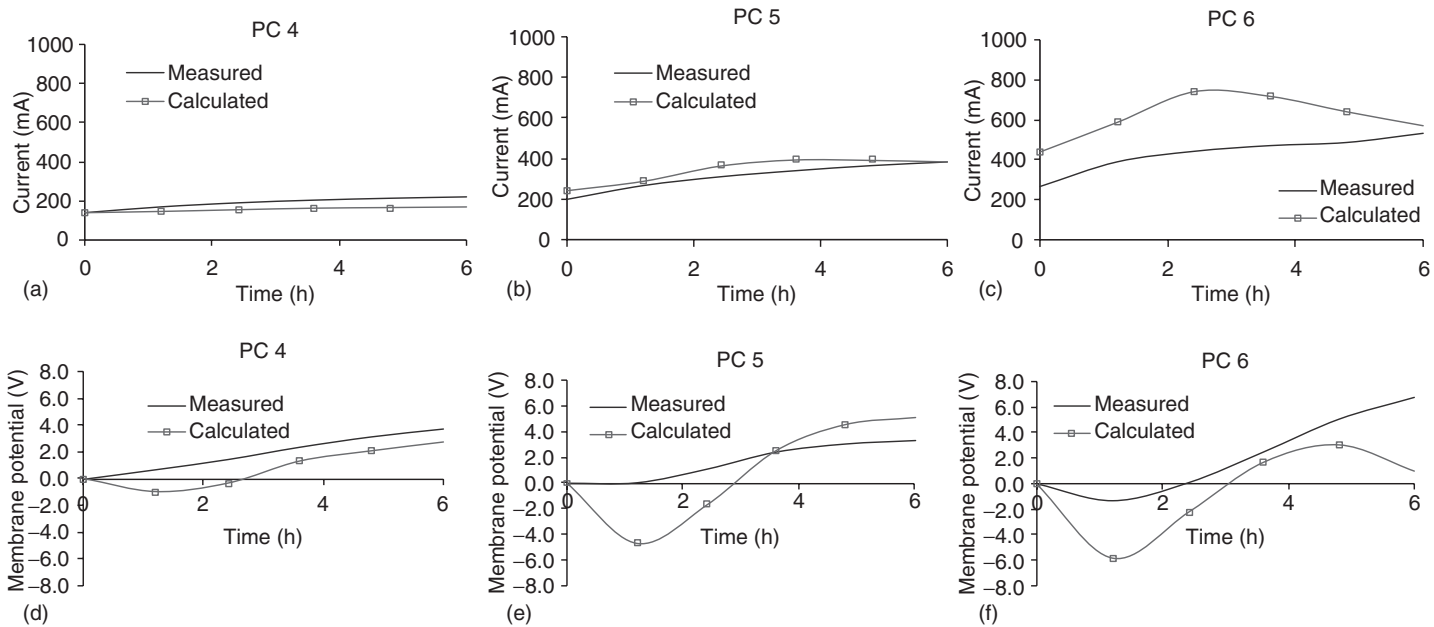

11.5 Transient current ((a)–(c)) and mid-point membrane potential ((d)–(f)), simulated and measured.

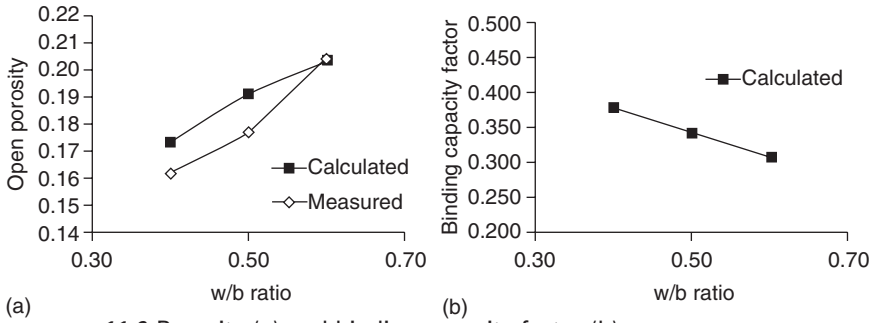

11.6 Porosity (a) and binding capacity factor (b).

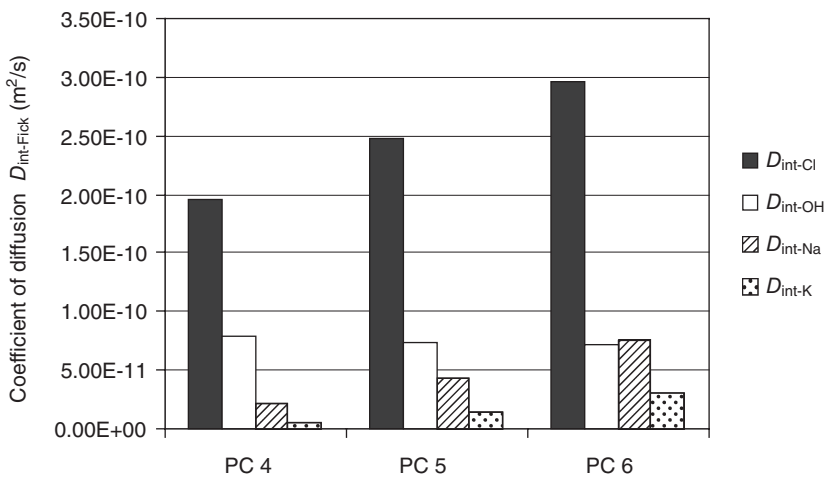

11.7 Intrinsic diffusion coefficients (D_{int}) calculated.

11.6 References

Andrade C (1993) Calculation of chloride diffusion coefficients in concrete from ionic migration measurements, *Cement and Concrete Research*, **23** (3), pp. 724–742.

Bertolini L, Elsener B, Pedeferri P, Redaelli E and Polder R B (2013) *Corrosion of Steel in Concrete: Prevention, Diagnosis, Repair* (2nd edn), Wiley-VCH, Weinheim.

Bockris J and Reddy A (1998) *Modern Electrochemistry 1: Ionics* (2nd edn), Plenum Press, New York.

Delagrave A, Bigas J, Ollivier J, Marchand J and Pigeon M (1997) Interface of the interfacial zone on the chloride diffusivity of mortars, *Advanced Cement Based Materials*, **5**, pp. 86–92.

Yang C, Chiang S and Wang L (2007) Estimation of the chloride diffusion from migration test using electrical current, *Construction and Building Materials*, **21** (7), pp. 1560–1567.

12

Electrical tests to analyse the fundamental transport properties of concrete – III: modelling tests without applied voltages

DOI: 10.1533/9781782423195.202

Abstract: In this chapter, the use of the models developed in Chapters 10 and 11 is extended to interpret the results from simple diffusion tests in which no voltage is applied. The general approach used was to solve the Nernst–Planck equation numerically for two physical ideal states that define the possible conditions under which chlorides will move through concrete. These conditions are named here as voltage control and current control. For each condition, experiments and simulations were carried out in order to establish the importance of electrical variables such as voltage and current in modelling chloride transport in concrete.

Key words: chloride diffusion, voltage control, current control, analytical solution, ion–ion interactions.

12.1 Introduction

The methods developed in Chapters 10 and 11 might appear to be completely irrelevant to a diffusion experiment where there is no applied voltage. However, experiments of this type will develop their own voltages, and the work reported in this chapter shows that this has a very significant effect. The computer model cannot, however, be applied in the form presented in Chapter 10 because there are two distinct boundary conditions which apply. These conditions are named here as voltage and current control. For each condition, simulations were carried out in order to establish the importance of electrical variables such as voltage and current. Voltage control applies to the standard test in which a voltage is applied (as in Chapters 10 and 11). Current control applies to a test with no applied voltage. A voltage may develop, but the current is controlled and it is zero.

12.2 Test methods

12.2.1 'Simple' chloride diffusion test

This test is commonly used for concrete testing. The chloride diffuses into the concrete with no applied voltage. It may be referred to as a 'gravity'

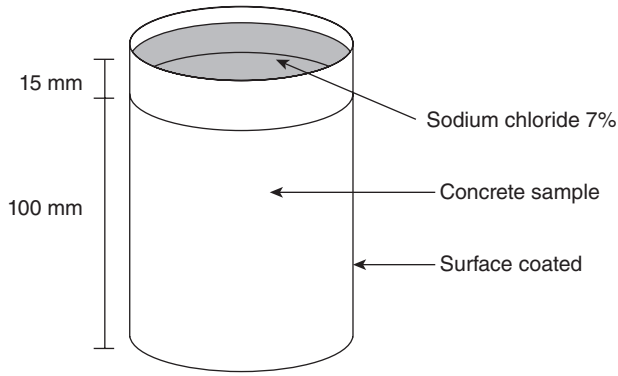

12.1 Simple diffusion test.

test due to the geometry, but the effect of gravity (i.e. pressure-driven flow controlled by permeability) is actually minimal, the diffusion being a far more significant transport process.

The sawn surfaces of 100 mm diameter and 100 mm high concrete cylinders were placed in contact with a solution of sodium chloride (Fig. 12.1). To prepare the samples, the curved surface of each cylinder was covered with a rubber coating in order to avoid moisture exchange and carbonation during the test. After the samples were coated, the surface that would be in contact with chlorides was placed in contact with a solution of 0.5 g/l of calcium hydroxide for 1 week to avoid any initial sorption effect when the chloride solution was introduced.

During the test, the external concentration of chloride was 7 % sodium chloride and it was renewed every 3 weeks. After 12 weeks of diffusion, the chloride penetration depth was measured using the colorimetric method (Meck and Sirivivatnanon, 2003). Each sample was split axially and sprayed with a solution of 0.1 M silver nitrate. After 15 min a white silver chloride precipitation on the split surface was visible and the penetration depth was measured. It was assumed that the free chloride concentration at which the colour changes is around 0.07 N for Portland cement (PC) concrete (NTBUILD-492, 1999).

This method may be compared with the 'drilled hole' tests described in Section 8.4.3. Each one has advantages. The test described here is more conventional for laboratory work, but it relies on an indicator to detect the chlorides rather than full titration of a dust sample. On the other hand, the drilling test, which more closely resembles site testing methods, has poorer measurement of depth.

12.2.2 ASTM C1202 high voltage test

Further work was carried out with the ASTM C1202 test as described in Section 10.1 using mortar samples.

12.3 The analytical solution

The solution of the Nernst–Planck equation presented in equation (1.26) for a single ion in isolation with zero external voltage gives equation (12.1) and corresponds to the solution of Fick's second law presented by Crank (1976):

$$c(x,t) - c_0 = (c_s - c_0)\left[\operatorname{erfc}\left(\frac{x}{\sqrt{4tD}}\right)\right] \qquad [12.1]$$

where:

c_0 is the initial concentration of chlorides in the sample and
c_s is the chloride concentration at the surface.

This may be seen to be the solution for equation (10.8) with no applied voltage.

It was assumed that at the start of the test the initial concentration of chlorides inside the sample was zero ($c_0 = 0$). The free chloride concentration, the depth of penetration, the chloride surface concentration c_s and the time of the diffusion test were known so the diffusion coefficient could be calculated using equation (12.1). However, this equation (although commonly used) takes no account of ion–ion interactions.

The limitations of this equation are shown in Fig. 12.2 which was obtained from the mixes reported in Chapter 11. The relationship between the chloride coefficients obtained from the diffusion test (using Fick's law) and the migration test (using the integrated model) is shown. The correlation coefficient R^2 was 0.99, indicating a strong relationship between the coefficients, but the values are quite different. The differences arise because of the physical equations used. Both coefficients are related but are defined in a different way. The first was obtained with Fick's law under conditions of pure diffusion and the second was obtained with the Nernst–Planck equation, including chloride adsorption and interaction among all the species involved. The differences were overcome by using the numerical model as described below.

12.4 Computer modelling – theoretical background

12.4.1 Voltage control

This was analysed as described in Chapter 10 and is applicable to the voltage-driven tests.

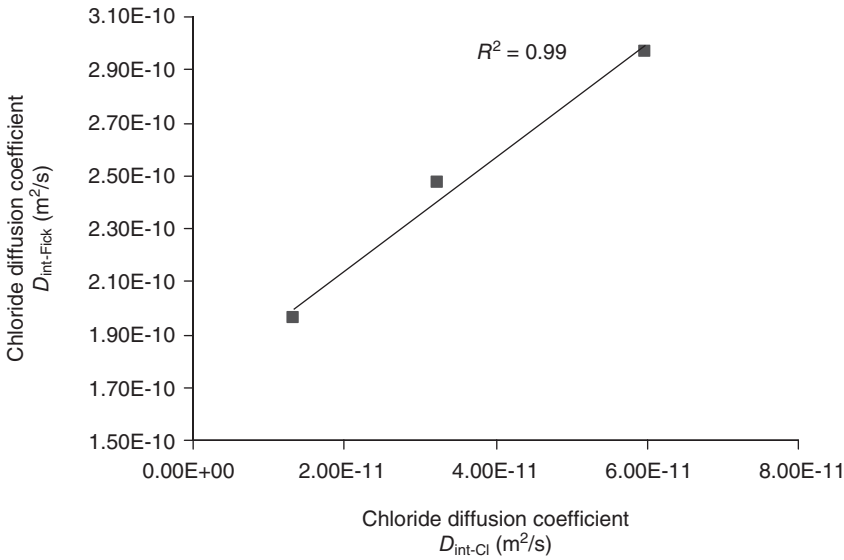

12.2 Relationship between the calculated chloride diffusion coefficients. $D_{int\text{-}Cl}$ was calculated using the methods in Chapter 11. $D_{int\text{-}Fick}$ was calculated using the traditional method from equation (12.1).

12.4.2 Current control

In the second condition called 'current control', the concrete between two electrodes is subject to a constant electrical current. For this condition, when the current is zero, the phenomenon of normal diffusion with no applied potential as in the simple diffusion test can be simulated. If the 'current control' condition is used with a non-zero current, the phenomena of either cathodic protection or electrochemical chloride removal can be modelled.

When chloride ions are just permitted to diffuse through concrete, the system acts like a dry-cell battery and a voltage is developed. Some previous authors have modelled chloride diffusion by simply integrating Fick's law as in equation (12.1) and using a diffusion coefficient for chloride ions. The true situation in normal diffusion is, however, far more complex because the voltage that is developed will inhibit further transport unless it is dissipated by further ionic transport. This further transport may be negative ions (such as OH^-) moving in the opposite direction to the Cl^- or positive ions (such as Na^+) moving with them and may be the determining factor for the rate of transport of the Cl^-. This should not be modelled with a voltage control algorithm set to zero applied voltage because this implies that the two ends of the sample are short-circuited.

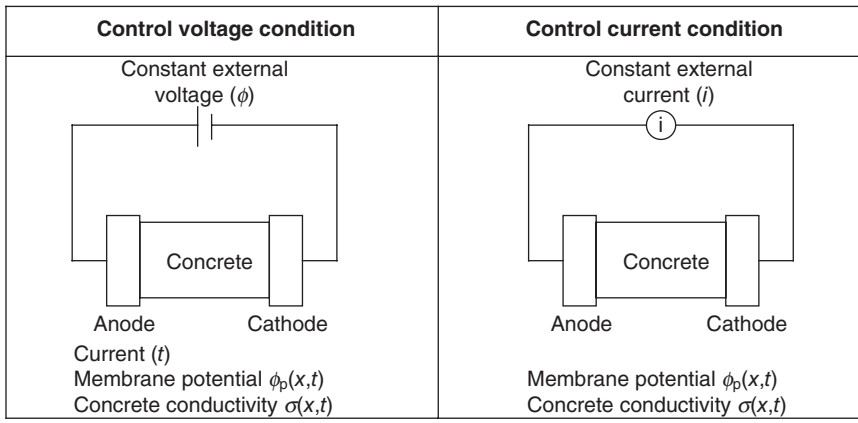

12.3 Electrical voltage and current approaches.

In the numerical algorithm used with a non-zero current control condition, the physical equations used to avoid the charge build-up are the same as used previously (voltage control); however, in this approach, in addition to keeping the charge neutrality throughout the sample at all times for all the ions together, it is necessary to keep the current density constant during whole duration of the test. Figure 12.3 shows a schematic representation of the electrical voltage and current conditions.

The computer model is described in Section 10.5 and was adapted so it can be set under two conditions; first, a migration test with an applied steady external voltage ($\phi \neq 0$) can be modelled under a condition called voltage control in this book. In this, for each time step, although the current density into any point is equal to the current out of it (Kirchoff's law), the total current is transient and changes with time (but not with position). The second condition, current control, allows the model to simulate a self-diffusion test under no external field applied. In this, in addition to the voltage correction necessary to prevent a charge surplus, the programme keeps the total current equal to a pre-set value (zero for this test). As outputs in both conditions, the model calculates the transient current caused by each ion, the concentrations, the voltage variation and the membrane potential at all times during the test and in each position.

12.5 Experimental programme

12.5.1 Materials

A single mortar mixture having a water to cement (w/c) ratio of 0.36 and a sand-to-binder ratio of 3 was cast for the ASTM C1202 tests. PC (CEM

I) without mineral or chemical admixtures was used. All the specimens were cured under lime water at 21 ± 2 °C prior to testing for 90 days. Because of the low w/c ratio, the mixture had a poor workability; it was compacted manually using prolonged tamping in order to reach its maximum density. Table 12.1 shows the proportions of the materials used.

12.5.2 Test methods

Table 12.2 is a summary of the principal transport properties and variables obtained following the methodology in Chapter 11. The heat loss factor is a property of the cell and was adjusted to give the observed temperature rise due to the modelled Joule heating in the sample.

Table 12.1 Mortar mixture proportions

w/b	PC (kg/m^3)	Sand (kg/m^3)	Water (kg/m^3)
0.36	650	1950	234

Table 12.2 Optimised and physical parameters used in the simulations

	Valence, *z*	Intrinsic diffusion coefficient *D* (m^2/s)	Concentration (in liquid) (mol/m^3)			Binding capacity factor
			Negative	In sample	Positive	
Hydroxyl ion	–1	7.877E-11	0	239.973	300	0.171
Chloride ion	–1	1.904E-10	530	0.00E+00	0	0.383
Sodium ion	1	2.061E-11	530	7.92E+01	300	0.171
Potassium ion	1	4.099E-12	0	1.61E+02	0	0.171

No of cells: 100.
Time step (s): 2.
Run time (h): 6.
Porosity: 0.171.
Applied voltage (V): 60.
Sample length (m): 0.05.
Sample radius (m): 0.05.
Room temperature (K): 295.
Cell volumes (m^3): 2.00E-04.
Heat loss factor (J/K): 0.30.

12.5.3 Computer simulations

Using the transport related properties of the optimised mortar (Table 12.2), the voltage control ASTM C1202 test was simulated. Additionally, using the same set-up and test conditions, current control tests were simulated under conditions of non-zero current (0.1 A – 6 h) and zero current (0 A – 12 days).

12.6 Results and discussion

12.6.1 Voltage control

The simulated membrane potential for the mortar mixture is shown in Fig. 12.4 as a contour map. It can be observed that the membrane potential is non-linear in time and position and only during the initial time step at the start of the test can the electrical field be considered linear. If the model is used without the voltage correction, (i.e. no charge neutrality and no interaction among species), the membrane potential would have a value of zero for each time and position.

Figures 12.5 and 12.6 show the ionic current carried for anions and cations. Although the total current at any point within the sample must be the same at any given time, the currents passed by individual ions do not

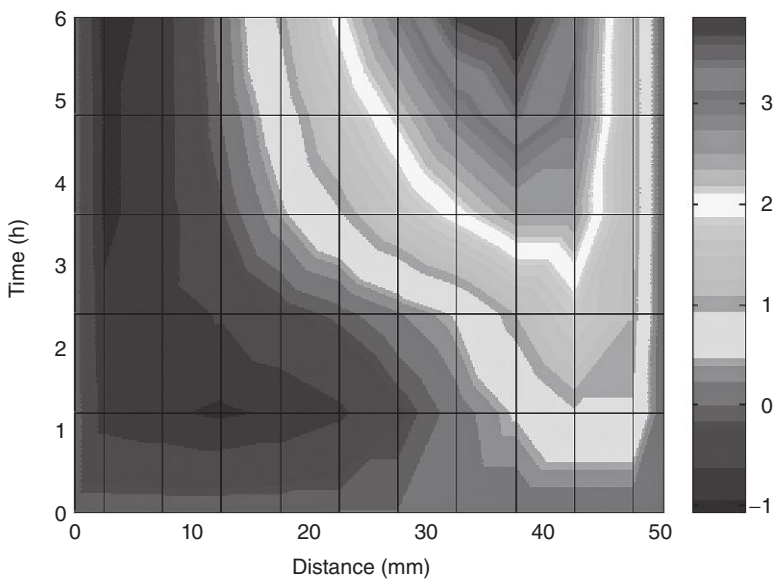

12.4 Membrane potential (V) for the mortar mixture. The negative voltages are near the sodium chloride cell (the cathode) at distance = 0 mm.

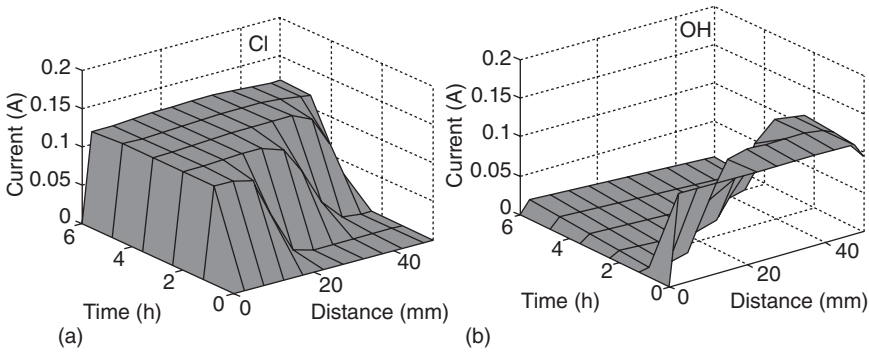

12.5 Ionic current during the ASTM C1202 test: (a) chloride ions; (b) hydroxyl ions.

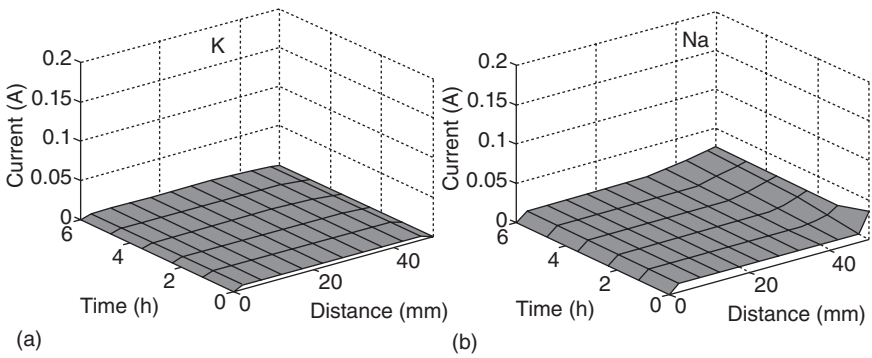

12.6 Ionic current during the ASTM C1202 test: (a) potassium; (b) sodium.

follow this rule and are typically different. From the figures, it can be observed that the hydroxide and chloride ions are responsible for most of the total current passed. At the beginning of the test, hydroxyl ions predominate; however, around 2 h later, chlorides, which are now penetrating massively into the sample, have begun to control the current. By the end of the test, the chloride ions were responsible for about 80 % of the total current. The role of cations is less important than that of anions; however, they are essential for establishing the necessary conditions of neutrality within the system. Although chloride and hydroxide are much more mobile species, without sodium and potassium the neutrality condition would never be successfully achieved.

Figure 12.7 shows the simulated current passed for each ion and the total current for three different times of the test. Figure 12.7a shows the condition

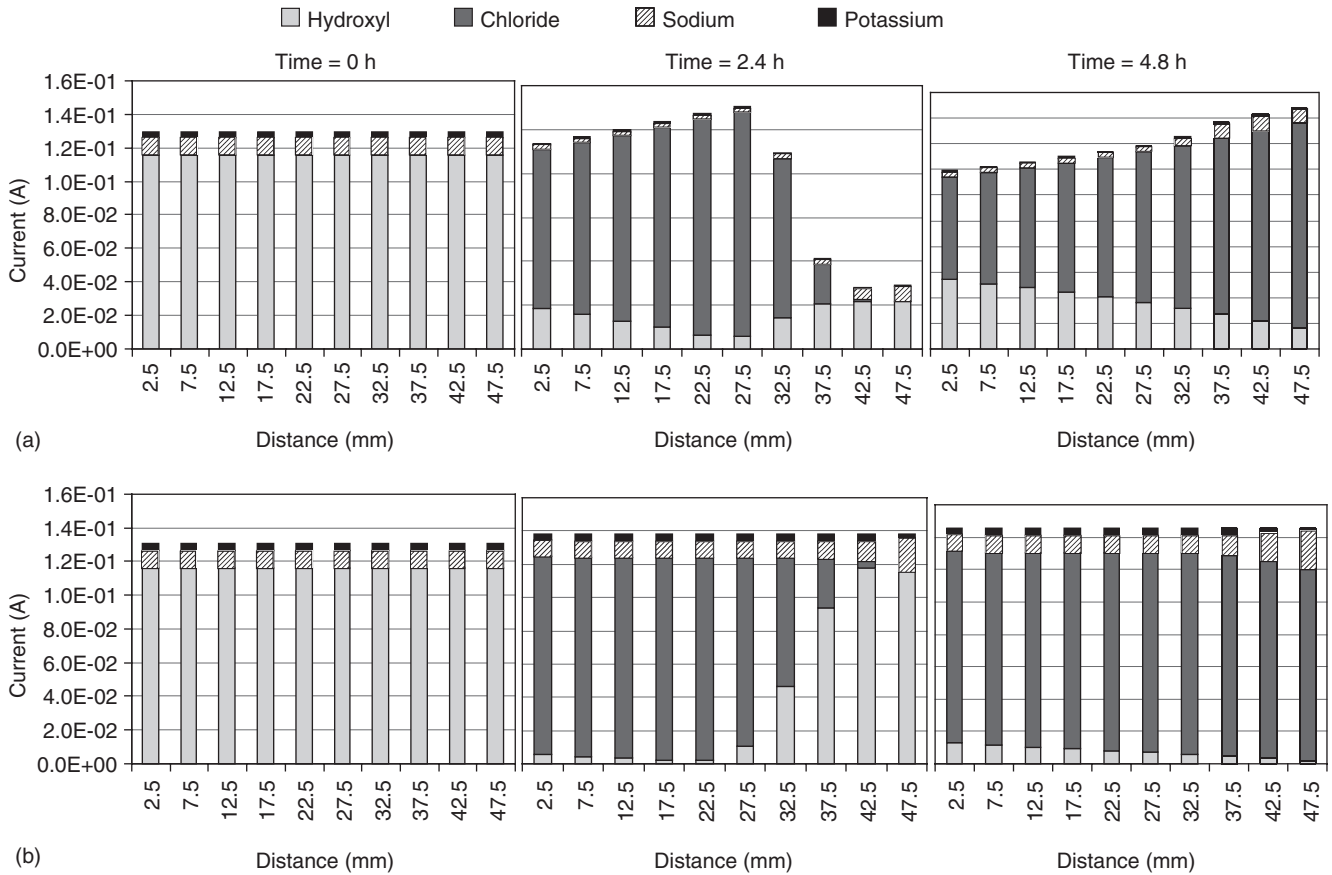

12.7 Ionic current in the ASTM C1202 test: (a) model results without voltage correction; (b) model results with voltage correction.

where no voltage correction is taken into account in the model, so the condition of charge neutrality is not satisfied (no membrane potential or no ionic coupling). Figure 12.7b shows similar results using the voltage correction included in the model, where it can be seen that, at any time, the total current in all the length of the sample is the same; however, the contribution of each ion is not necessarily the same.

The ionic concentrations of OH^-, Cl^-, Na^+ and K^+ are shown in Fig. 12.8 as contour maps. At the beginning of the test, chlorides were present only in the cathode external reservoir; however, as the test progressed, chlorides penetrated the specimen and reached the other external cell (anode). Also, from the results of concentrations, it can be seen that prior to the start of the test, the hydroxyl ions were uniformly distributed in the pore solution

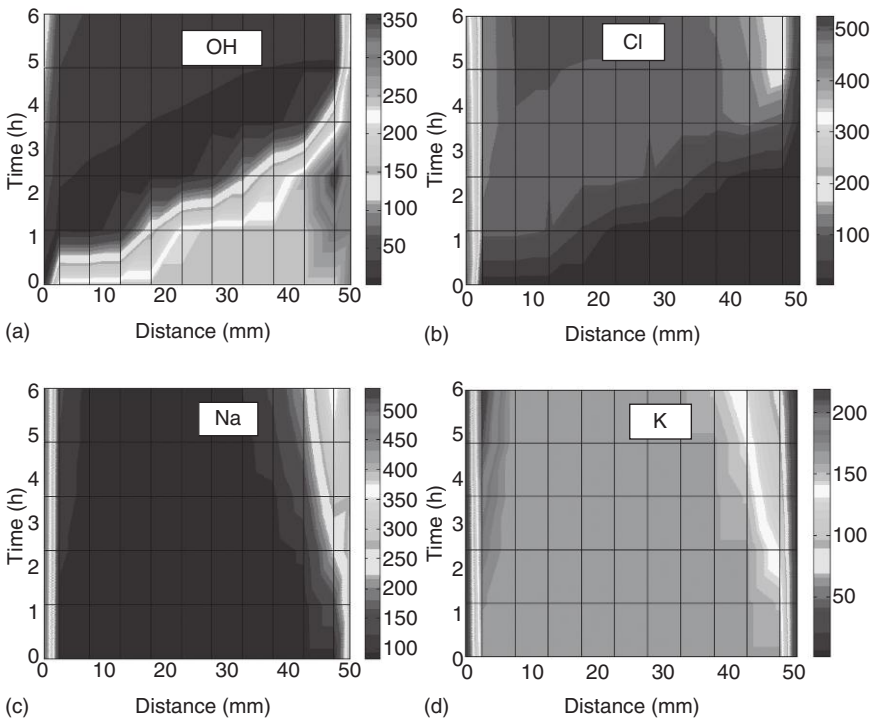

12.8 ASTM C1202 concentrations for hydroxyl, chloride, sodium and potassium (mol/m^3). (a) Hydroxyl: the high concentrations are near the sodium hydroxide cell (the anode at distance 50 mm) at time 2.5-h. (b) Chloride: the lowest concentrations are at early times near the anode (at distance = 50 mm). (c) Sodium: the highest concentrations are at later times near the anode (at distance = 50 mm). (d) Potassium: at later times the high concentrations are near the cathode (at distance = 0 mm) and the low concentrations are near the anode.

and in the anode external cell. However, the concentration of those ions increases in the cathode while decreasing in the anode. This behaviour is considered realistic because in an actual test the hydroxyl ions will migrate towards the anode where they are oxidised, releasing electrons. Simultaneously, at the cathode, hydroxyl ions and oxygen are released from water molecules, as a result of electrolysis. The results presented agree well with the findings of Prince *et al*. (1999).

12.6.2 Current control model (non-zero current)

Under a current control condition, the concrete sample subjected to a steady known electrical current requires an external voltage that does not remain constant over time. The simulated voltage required at different times, for a constant 100 mA, is shown in Fig. 12.9. At the beginning of the test, the voltage drop was linear through the sample; however, voltage deviations were necessary to keep the total current constant. Simulations of ionic current for each ion included here showed a similar behaviour to that obtained in Figs 12.5 and 12.6. Chloride and hydroxyl ions were

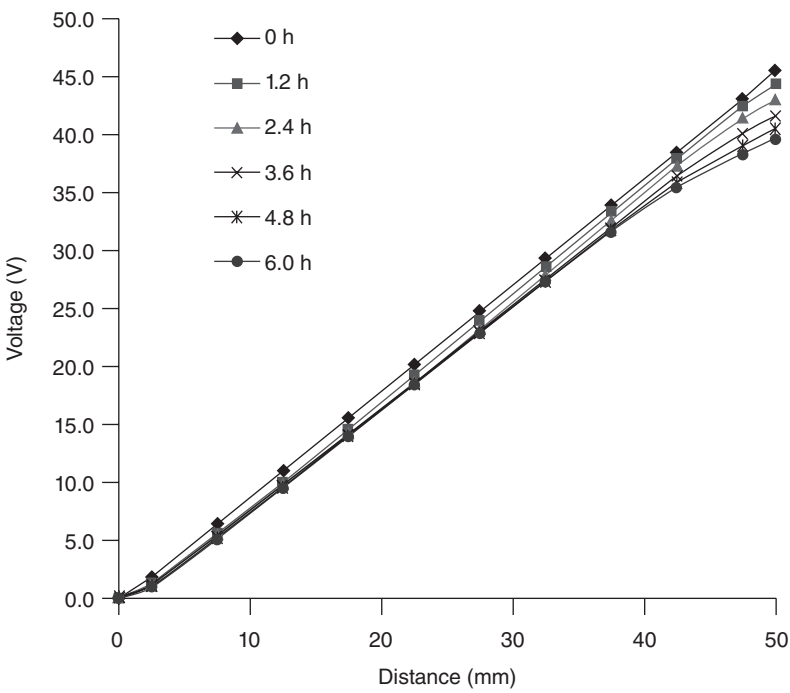

12.9 Voltage adjustments at different times to maintain a current of 100 mA in the current control condition.

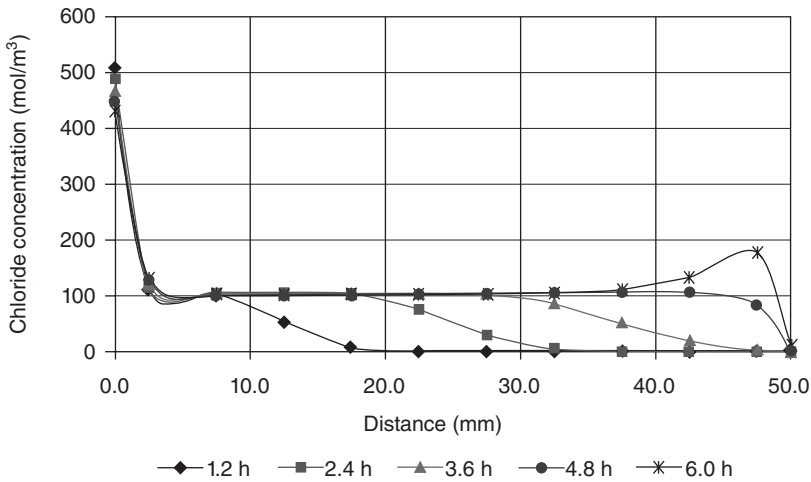

12.10 Chloride profile at different times with current control (100 mA).

responsible for the majority of the current carried, while sodium and potassium together carried only a minor amount of the overall current.

The free chloride concentration profile for the 100 mA current control test, simulated at different times, is shown in Fig. 12.10. This test is regarded as a non-steady condition, the source reservoir is depleting over time and the chloride ions are just beginning to reach the anode reservoir.

12.6.3 Current control model (zero current)

This condition could reflect a standard diffusion cell using the same cells and solutions stated in the standard ASTM C1202 test but with no applied voltage or the 'simple' chloride diffusion cell described in Section 12.2.1. Figure 12.11 shows the membrane potential results across the entire sample obtained from the numerical current and voltage control modes at the end of the test (12 days). In the voltage control model, the membrane potential across the whole sample, between anode and cathode (50 mm), was equal to zero. This was expected because the voltage control states an external voltage applied of 0 V (i.e. an electrical short circuit connecting the ends of the sample). In contrast, although the applied external current was zero, the current control model showed a potential of –0.03 V between anode and cathode.

Figure 12.12 shows the results of total current calculated at 12 days of diffusion for different modelling conditions. As was expected, using the current control model (CC), the total current simulated at different positions

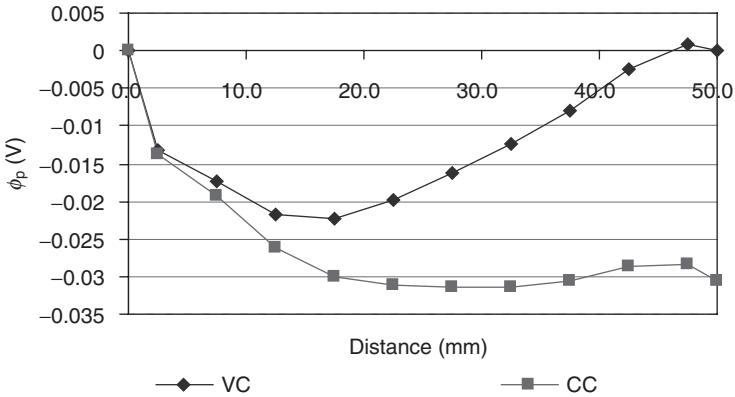

12.11 Membrane potential (with respect to the cathode) at the end of the test (288 h): CC, current control; VC, voltage control.

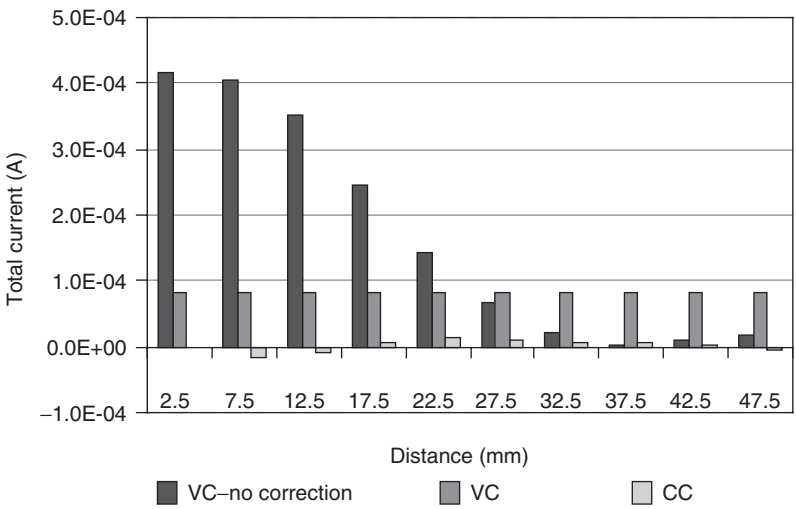

12.12 Total ionic current for different modelling assumptions: VC–no correction, no ionic interactions (charge build-up); VC, voltage control; CC, current control.

at the end of the test was always approximately equal to zero. In contrast, for the voltage control model (VC) with the applied voltage equal to zero, a small total current was developed (0.00008 A) showing the cell worked like a battery. It is important to notice that in both models, the charge neutrality condition was fulfilled, but in the current control condition it was forced to be equal to zero. In contrast, the simulations of the total current without coupling all the species involved (VC–no correction) give very high numerical values of current because the charge neutrality is not met in full.

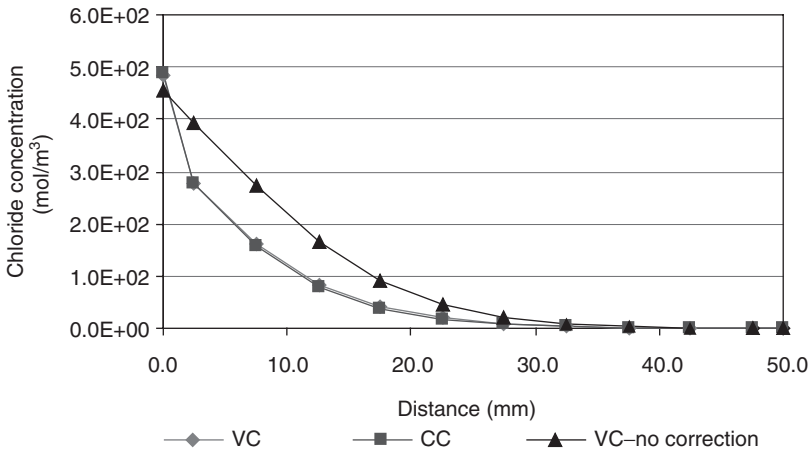

12.13 Chloride profiles obtained using different models. The lines for VC and CC are over-laid.

Under this last condition, the Nernst–Planck equation is solved independently for each ion and, as the external voltage is equal to zero, the model solves the Fick's equation for each ion.

The simulated chloride profile for the voltage and current control conditions at 12 days is shown in Fig. 12.13. Although the membrane potential and the current obtained from both models were different, important differences were not found between the chloride profiles – the concentrations for both models were very similar. In contrast, the profile obtained using the voltage control with no charge neutrality (i.e., Fick's law) is very different and is higher.

12.6.4 Modelling the simple (gravity) diffusion test

The gravity chloride diffusion test described in Section 12.2.1 was simulated using the computer model for mix PC4 (used in Chapter 11, see Table 11.1) to give the current and the chloride concentration for 36 days and experimental data for this mix was also obtained in the laboratory. Figure 12.14 shows the profile of the current which was simulated using three different approaches;

1. *The electrodiffusion current control model with zero current*. As was expected, the total current was equal to zero at any point of the sample. The current density generated by each ion was annulled by the current density generated by the remaining ions. When any species diffused through the sample, a charge surplus was avoided through the generation

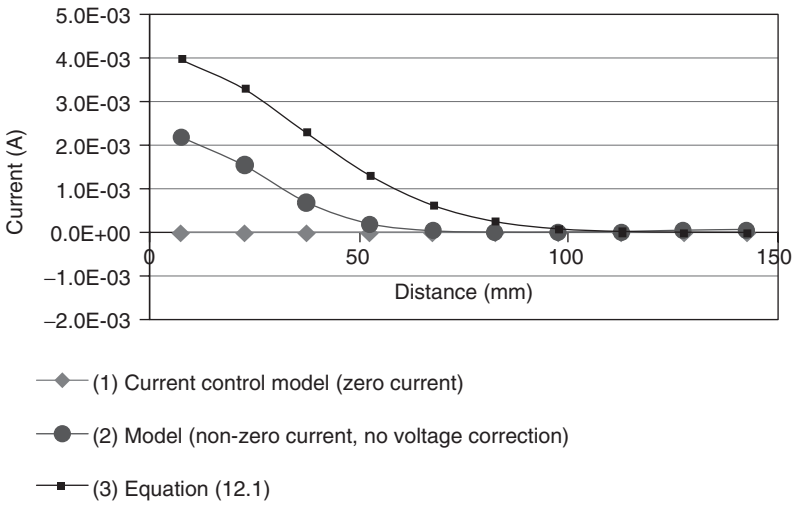

12.14 Total current at 864 h (36 days).

of a membrane potential. The authors suggest that this simulation best represents the physical situation in the sample.

2. *The electrodiffusion model with no voltage correction*. In this, in the solution of the Nernst–Planck equation there is no membrane potential generation. As a result, the Nernst–Planck equation was solved using Fick's first law for each ion. The total current had a value of 2.1 mA near the surface because at that point the flux of chloride and sodium was high. In the same way, far away from the surface the current decreased. The total current for any point is the result of the sum of the current for each ion, according to its charge and diffusion direction.
3. *The theoretical equation (12.1)*. In this, it is supposed that the only species involved are chlorides. The total current profile obtained was of a similar shape to condition (2), but the total current near to the surface was 4 mA.

The chloride concentration profile at different distances from the external NaCl solution is shown for 90 days in Fig. 12.15. This graph includes modelled and experimentally observed values. Five different modelling approaches were used for analysis of the the current:

- Approach 1. The electrodiffusion current control model with zero current using the transport related properties calculated from the experimental data from ASTM C1202 voltage-driven tests using the model and the neural network as described in Chapter 11.

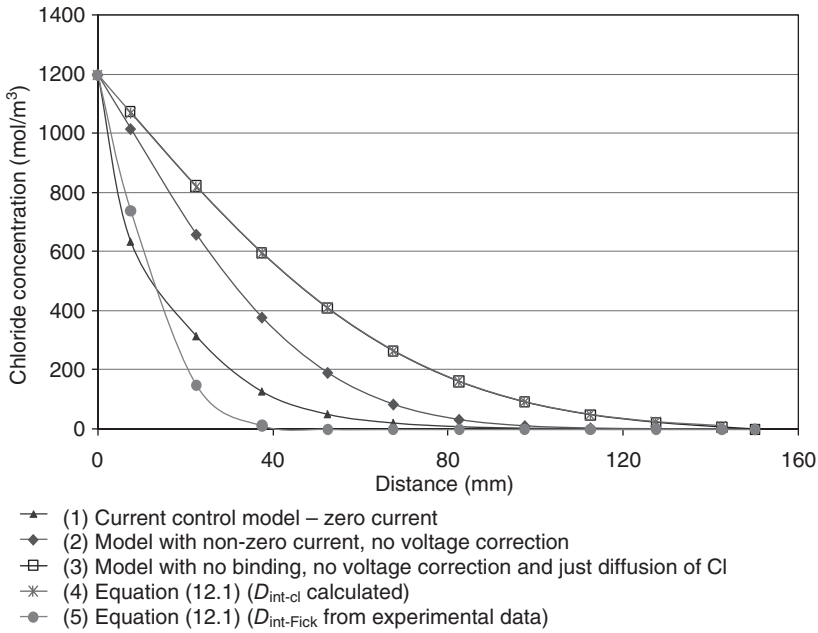

12.15 Chloride profile at 90 days.

- Approach 2. The electrodiffusion model with no voltage correction using the transport related properties as in approach 1.
- Approach 3. The electrodiffusion model, but with only chlorides present in the system so there was no pore solution or chloride binding. The transport properties for chlorides were used as in approach 1.
- Approach 4. Equation (12.1) (Fick's law), using the intrinsic chloride diffusion coefficient obtained from the neural network as in approach 1.
- Approach 5. Fick's law, but the concentration was obtained from experimental data using the chloride coefficient of diffusion obtained with the diffusion test D_{Fick}. This represents the profile of a function that passes through two points where the concentration was measured experimentally. However, some deviations can be expected because of the variability and uncertainty in the assumption that the change of colour in the colorimetric method is at 0.07 mol/l.

Approaches 3 and 4, as was expected, had the same profile; the chloride concentration was the same for both conditions. This provides a check that, for a simplified condition, the computer simulation gave the correct solution.

It can be seen from the graph that for approaches 3 and 4 that permit development of a net total current (which is not possible in reality because

there is no circuit) the chloride concentration is higher. The higher the total current developed, the higher the chloride profile simulated.

Approach 5 represents the real free chloride concentration (as measured in the diffusion test), and it can be seen that it has a similar trend to the one predicted with the current control model (approach 1).

12.7 Conclusions

The straightforward application of Fick's law to simulate chloride diffusion in concrete which has been used by many authors in the past can be significantly improved by using a numerical simulation which includes the effects of the other ions in the system.

12.8 References

Crank J (1976) *The Mathematics of Diffusion* (2nd edn), Oxford University Press, Oxford.

Meck E and Sirivivatnanon V (2003) Field indicator of chloride penetration depth, *Cement and Concrete Research*, **33**, pp. 1113–1117.

NTBUILD-492 (1999) *Concrete, mortar and cement-based repair materials: Chloride migration coefficient from non-steady-state migration experiments*, Nordtest, Espoo.

Prince W, Perami R and Espagne M (1999) Mechanisms involved in the accelerated test of chloride permeability, *Cement and Concrete Research*, **29** (5), pp. 687–694.

13

Applications using measured values of the transport properties of concrete I: predicting the durability of reinforced concrete

DOI: 10.1533/9781782423195.219

Abstract: The transport properties control the durability of concrete and, in particular, the corrosion of reinforcement. The mechanisms for this are discussed and experimental measurements of corrosion using linear polarisation are presented. These are then correlated with a number of transport related properties. The use of the Nordtest NT Build-492 and the ASTM C1202 electrical tests for predicting corrosion is then considered. It is shown that the Nordtest suffers from the same problems as the ASTM described in Chapters 10–12. However, it is concluded that durability models such as the NRMCE Life-365 model have similar problems so the data from the tests could possibly be suitable for them.

Key words: reinforced concrete, durability, corrosion of reinforcement, NT Build-492, durability models.

13.1 Introduction

By far the most common application for data on transport properties is the prediction of the durability of reinforced concrete. While there are some types of deterioration such as freeze–thaw or sulphate attack which affect the concrete itself, most damage occurs through corrosion of the reinforcement. This chapter considers the two main methods used to predict corrosion from transport properties. The first is simply to attempt to correlate corrosion with various transport measurements and the second is to develop predictive models, normally based on diffusion of chloride ions.

13.2 Controlling parameters for concrete durability

Having defined the transport processes in earlier chapters, the key questions are how they may be controlled and how they will affect the durability of a structure. In Fig. 13.1, the left hand column shows a number of factors which we may expect to affect the properties of concrete. They do not, however, directly affect the transport properties and the next column shows the actual internal properties which they are likely to affect. These include micro-cracks, the chemistry and also the 'formation factor' for the pores

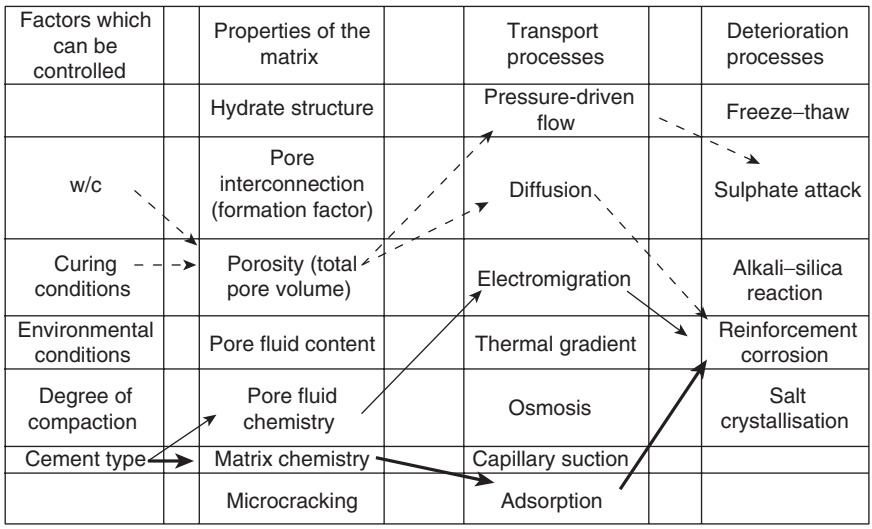

13.1 Factors affecting durability.

which is a measure of how many direct paths there are through the pore structure. The third column shows the transport properties and the final column shows the deterioration processes that we want to inhibit. Thus we change something in the left hand column in the hope that it will affect the next two columns and finally get a result in the last column. The complexity of this situation explains why it is so difficult to achieve durability in a structure. For structural analysis, the relationship between what we do and the results that we get is defined by quite precise equations. For durability, even moving from one column to the next in the figure is unfortunately only possible by using experimental data which is often difficult to interpret. There are, however, numerous significant relationships on the figure which may be exploited.

The dashed line arrows start from the water to cementitious (w/c) ratio and the curing conditions. If the water content is kept low, this will reduce the number of capillary pores that contain it and the overall porosity will be reduced. Similarly good water-retaining curing will promote full hydration and the resulting products will fill many of the pores and reduce the porosity. Following across the figure shows that this will reduce the pressure-driven flow and the diffusion. The pressure-driven flow then causes frost attack (in combination with capillary suction) and diffusion is a key mechanism in reinforcement corrosion by carbonation or chloride ingress.

The thin solid arrows show that the cement type will be the major factor determining pore fluid chemistry. In particular, the use of a pozzolanic

material such as pulverised fuel ash (PFA) or silica fume (SF) will reduce the amount of hydroxyl (lime) and alkali ions in solution. These are the main charge carriers and therefore the electromigration will be greatly reduced. The key effect of this is to reduce corrosion of reinforcement because this depends on the electromigration of these negatively charged ions from the cathode to the anode so they can combine with positive metal ions.

The thick solid arrows show that the cement type will also be the key factor in determining the chemistry of the cement matrix that forms the structure of the hydrated paste. In particular, if a sulphate resisting cement is used there will be few aluminates in it. This will, in turn, severely limit the ability of the matrix to adsorb chloride ions and they will thus remain free to cause corrosion.

There are very many other links in the figure; indeed, almost every factor in each column affects every factor in the next one to some extent and exploring each of them reveals methods that offer the potential to be exploited to improve durability.

It may be seen from the discussion above that reducing transport processes will normally improve durability. An exception to this is the deterioration of saturated concrete in fire. The Channel Tunnel linking England with France experienced a severe fire and photographs of the damage remarkably reveal apparently undamaged reinforcing steel with virtually no remaining concrete. In this incident, the exceptionally low permeability of the concrete prevented the escape of steam from the pores of the saturated lining segments and caused them to literally explode. This phenomenon may be demonstrated by placing very low permeability concrete in a microwave oven. The only solution to this that is known to the author is to mix the concrete with polypropylene fibres that melt at high temperatures and provide pathways to vent the steam.

When considering Fig. 13.1 it must also be observed that building structures with concrete with low transport properties is of no use at all if the depth of the cover layer is not maintained. If the reinforcement is just a few millimetres below the surface, nothing will protect it from the external environment.

13.3 Measuring corrosion of reinforcement

13.3.1 Theoretical analysis

The corrosion experiment is shown in Fig. 13.2. The secondary electrode was mild steel. The concrete samples were also used for resistivity measurements (see Section 8.4.2 for sample dimensions) by applying an alternating voltage between the steel bar in the sample and the secondary

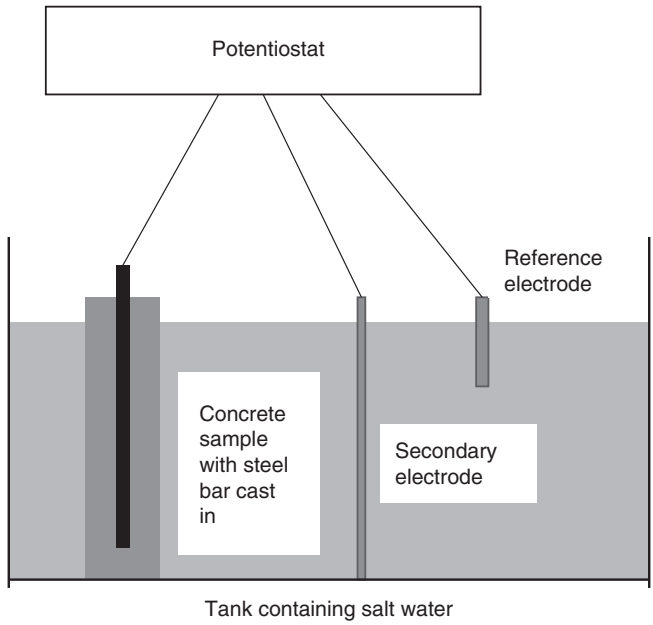

13.2 Diagram of corrosion experiment.

electrode. The potentiostat is basically a power supply, but a complex device is needed because the reference electrode can only be used for measuring voltages, not applying them. Thus the potentiostat applies voltages to the secondary electrode while controlling them with measurements from the reference electrode.

Figure 13.3 shows the equivalent circuit for a steel corrosion sample. The anode and cathode both occur at the surface of the steel inside the concrete. The concrete resistance occurs in the thickness of concrete between the steel bar and the salt solution in the tank. The external voltage is measured between the reference electrode and the top of the steel bar in the concrete. The external current I_x flows through the secondary electrode.

The electrochemical process at the anode involves the dissolution of Fe^{++} ions into the pore solution. The relationship between the voltage across it and the ionic current is assumed to be logarithmic as in equation (13.1):

$$\phi = \phi_{a0} - B_1 \mathrm{Log}\left(\frac{I_a}{I_{a0}}\right) \qquad [13.1]$$

where:

ϕ_{a0} is the exchange voltage which would occur across the anode if it was in isolation

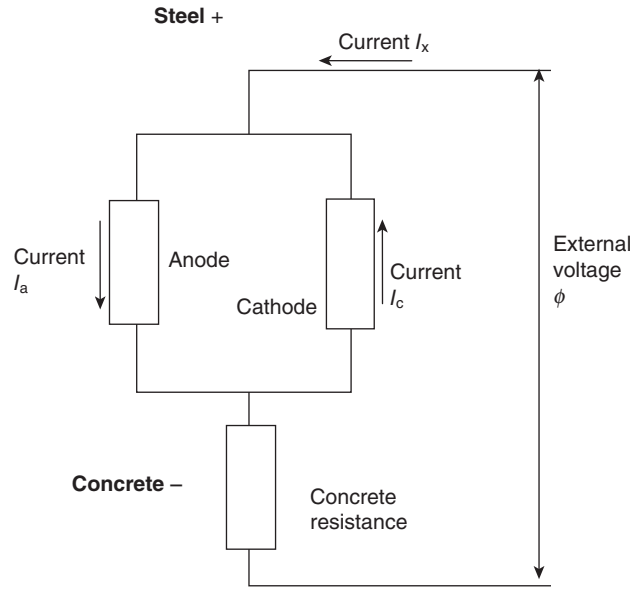

13.3 Equivalent circuit diagram of steel corrosion in concrete.

I_{a0} is the exchange current which would flow equally in and out of the bar in isolation and
B_1 is a constant known as the Tafel constant.

The electrochemical process at the cathode is the formation of hydroxyl ions from oxygen and water and will similarly be logarithmic as in equation (13.2):

$$\phi = \phi_{c0} - B_2 \mathrm{Log}\left(\frac{I_c}{I_{c0}}\right) \qquad [13.2]$$

where:

ϕ_{c0} and I_{c0} are the cathode exchange voltage and current and
B_2 is a second Tafel constant.

If there is no external applied voltage the voltage is known as the rest potential $E0$ and the current flowing round the 'loop' is the corrosion current I_{corr} which would occur in normal conditions in a structure. Thus:

$$E0 = \phi_{a0} + B_1 \mathrm{Log}\left(\frac{I_{corr}}{I_{a0}}\right) = \phi_{c0} - B_2 \mathrm{Log}\left(\frac{I_{corr}}{I_{c0}}\right) \qquad [13.3]$$

Thus subtracting from equations (13.1) and (13.2):

$$\phi - E0 = B_1 \mathrm{Log}\left(\frac{I_a}{I_{corr}}\right) = -B_2 \mathrm{Log}\left(\frac{I_c}{I_{corr}}\right) \quad [13.4]$$

But when x is close to 1, $x - 1 \approx \mathrm{Ln}(x)$. Thus, when I_a and I_c are close to I_{corr}:

$$\phi - E0 = \frac{B_1}{\mathrm{Ln}(10)} \times \left(\frac{I_a}{I_{corr}} - 1\right) = -\frac{B_2}{\mathrm{Ln}(10)} \times \left(\frac{I_c}{I_{corr}} - 1\right) \quad [13.5]$$

With the following definitions:

$$\text{constant } B = \frac{B_1 B_2}{(B_1 + B_2)\mathrm{Ln}(10)} \quad [13.6]$$

and

$$\text{polarisation resistance } R_p = \frac{B}{I_{corr}} \quad [13.7]$$

equation (13.5) reduces to:

$$\text{external current } I_x = I_a - I_c = \frac{\phi - E0}{R_p} \quad [13.8]$$

Equation (13.8) is known as the Stern–Geary equation (Stern and Geary, 1957) and enables the polarisation resistance and thus the corrosion current to be measured by applying an external voltage ϕ close to the rest potential $E0$ and measuring the resulting external current I_x. This is known as linear polarisation resistance measurement because of the linear relationship in equation (13.8).

A correction is needed because, as may be seen in Fig. 13.3, the circuit also flows through the concrete resistance. This must be measured separately and subtracted from the polarisation resistance. There is also an effect of the double-layer capacitance of areas of the bar that are not corroding. This causes a high initial current to flow but may be avoided by waiting 30 s after applying the external voltage before measuring the current.

13.3.2 Experimental procedure

Samples containing a mild steel bar were placed in salt solution and the initial corrosion rates were measured by linear polarisation resistance measurements. The steel was then polarised to + 100 mV relative to a standard calomel electrode for 28 days and the corrosion rate was measured again. The resistivity measurements described in Section 8.4.2 were used to correct for the concrete resistance.

13.4 Correlating transport measurements with corrosion

13.4.1 Sample testing

Samples were prepared using the mix designs and curing conditions given Section 8.2. The corrosion current was measured and measurements were made of the properties known to influence it (the predictor properties). These predictors were all transport properties except for the lime content and the cube strength. The testing programme is summarised in Table 13.1.

In addition to the carbonation strain measurements described in Section 8.4.1, the carbonation depth was measured by breaking the samples and spraying phenolphthalein indicator solution on the exposed surface to show the areas of reduced alkalinity. The lime content was measured by thermogravimetric analysis of ground samples. The area of the calcium hydroxide peak which occurs at around 450 °C was recorded (Cabrera and Claisse, 1991). Two readings were obtained for each sample condition for each experiment.

Table 13.1 Summary of experimental programme

Predictor measurements		
Chloride transport	Concentration (Cl conc)	Measured in sample after gravity assisted ingress (see Section 8.4.3)
Carbonation (see Section 8.4.1)	Strain (Strain 18)	Measured on mortar prisms with LVDT
	Prism depth (Depth 18)	Measured with phenolphthalein at 18 days exposure
	Mortar depth (Depth 28)	Measured with phenolphthalein at 28 days exposure
Oxygen transport	Permeability ($K(O_2)$)	Measured on sections on mortar cores (see Section 8.5)
Vapour transport	(Vapour)	Measured on thin discs of paste (see Section 8.6)
Electrical conductivity	(Conductivity)	Measured between steel and solution on corrosion samples (see Section 8.4.2)
Lime content	(Lime)	Measured with thermogravimetric analysis of paste samples
Compressive strength	(Cube strength)	Measured on 100 mm cubes

Predictor measurements are as shown. Corrosion current was measured at the start of the testing programme and at 28 days.

13.4.2 Statistical analysis

Initial calculations

For a statistical interpretation of regression and analysis of variance, it is assumed that the data are normally distributed. The results obtained for corrosion currents were very clearly non-normal and thus unsuitable for analysis. Equation (13.4) indicates that the rest potential is proportional to the log of the corrosion current (and this was observed for this data). This logarithm was found to be normally distributed and was therefore used as the fundamental parameter and, on this basis, it was used for the analysis.

Regression

The purpose of the regression analysis was twofold:

1. to construct a model for predicting corrosion current from the measured predictor properties, thereby identifying which properties provide the best indication of corrosion;
2. to assess the size of the effect of each predictor property on corrosion current.

A particular property may be highly correlated with corrosion current yet may have little actual effect on it. This is the distinction between the correlation coefficient and the regression coefficient or, in simple terms, the difference between how well the line fits the data and how steep the slope of the line is.

Using standard stepwise regression techniques (Draper and Smith, 1998), it was found that several of the predictor properties were highly correlated with the corrosion current. However, having fitted one of these properties as a single predictor, the model could not be improved by the addition of a second or further predictors. This phenomenon is due largely to the high correlations existing among the transport properties themselves. Nonetheless, a comparison of the single predictor models is instructive.

The *t*-ratio was used to assess the significance of the correlation between corrosion current and each transport property. Using the regression coefficients (or slopes) to compare the size of the effect of each predictor on corrosion current is complicated by the different units of measurement adopted for each predictor. This difficulty has been overcome by calculating the change in corrosion current predicted by each single predictor model *over the range of samples tested*. The validity of this method of comparison relies on the careful design of the experiment in selecting the range of values for each predictor to reflect the full range of normal site conditions.

It should be noted that, for each model used, a thorough residual analysis was conducted to check for the possibility of non-linearity or heteroscedasticity. A normal probability plot was used to test for normality of residuals. In the case of oxygen permeability, these diagnostic checks indicated that a logarithmic transformation of the predictor was necessary.

13.4.3 Results

The effects of the predictors and their *t*-ratios are given in Table 13.2 for the initial corrosion current and Table 13.3 for the 28 day corrosion current. The effects are shown in Figs 13.4 and 13.5 (note that the scales are different). In these figures, the predictors are labelled using the abbreviations from Table 13.2.

Table 13.2 Effect of predictors on initial corrosion current

Property	Effect	*t*-ratio
SF concrete		
Strain 18	NS	
Cl conc.	1.124	3.13
Log $K(O_2)$	NS	
Cube strength	1.596	–5.31
Depth 18	NS	
Depth 28	NS	
Conductivity	1.061	3.86
Lime	1.689	6.05
Vapour	0.798	2.39
PC concrete		
Strain 18	NS	
Cl conc.	0.611	2.92
Log $K(O_2)$	0.456	2.28
Cube strength	0.584	–2.64
Depth 18	NS	
Depth 28	NS	
Conductivity	0.57	3.38
Lime	NS	
Vapour	NS	

Note:
The 5% critical *t*-value is 2.032.
The 1% critical *t*-value is 2.728.
The 0.1% critical *t*-value is 3.601.
NS = not significant.

Table 13.3 Effect of predictors on 28 day corrosion current

Property	Effect	*t*-ratio
SF concrete		
Strain 18	0.595	2.27
Cl conc.	0.550	2.22
Log $K(O_2)$	0.803	3.98
Cube strength	NS	
Depth 18	NS	
Depth 28	NS	
Conductivity	0.641	3.51
Lime	NS	
Vapour	0.586	2.77
PC concrete		
Strain 18	4.303	5.17
Cl conc.	3.577	5.80
Log $K(O_2)$	3.533	6.72
Cube strength	3.431	−4.98
Depth 18	2.921	3.02
Depth 28	2.574	6.79
Conductivity	2.572	4.45
Lime	2.564	2.98
Vapour	1.806	2.30

Note:
The 5% critical *t*-value is 2.032.
The 1% critical *t*-value is 2.728.
The 0.1% critical *t*-value is 3.601.
NS = not significant.

13.4.4 Discussion

The cube strength was the only predictor which had a negative coefficient, i.e. high strength indicated low corrosion as expected. The effect of oxygen transport as a predictor is not justified directly in this instance because the corrosion was shown to be anodically controlled. This was checked using equation (13.3). It may be seen from the right hand side of this that if ϕ_{c0} and I_{c0} remain constant, the rest potential will decrease linearly as the corrosion current increases. This was observed for this data (Cabrera and Claisse, 1995) indicating that the cathode conditions were the same for all samples. However, oxygen transport remains a good general measure of transport in the concrete.

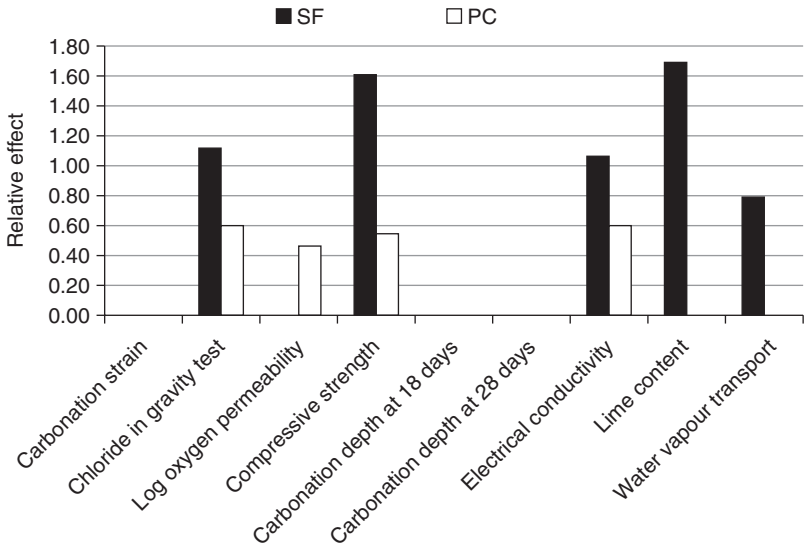

13.4 Effect of transport properties on initial corrosion current. The effect is the slope of the regression line and is divided by the range and thus dimensionless.

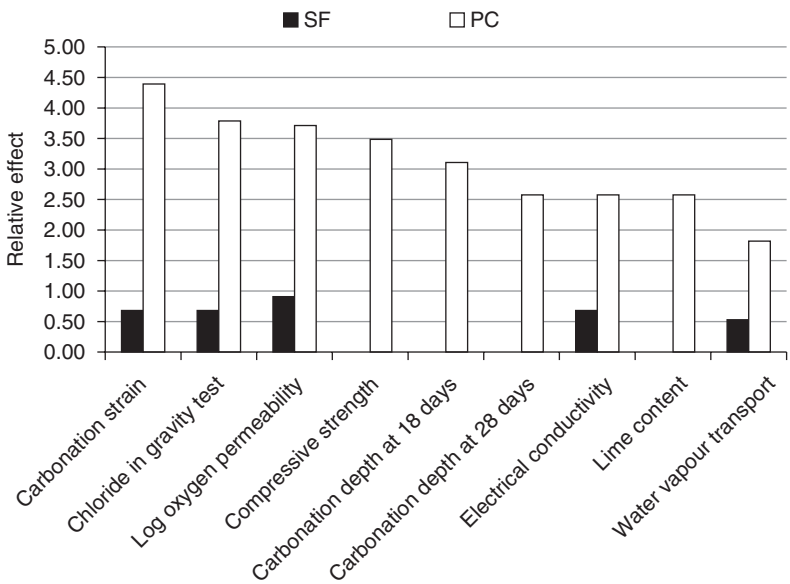

13.5 Effect of transport properties on 28 day corrosion current.

The initial current

For the Portland cement (PC) mixes, five of the nine predictors were not significant. None of the measurements of carbonation (Strain 18, Depth 18 and Depth 28) or the vapour transport or the lime content were significant. The most significant predictor was the electrical conductivity because none of the transport properties will have been significant before exposure. The remaining significant predictors are chloride transport (Cl conc.), oxygen permeability ($\log K(O_2)$) and cube strength which are only significant because they measure the general 'quality' of the concrete. The effect of the four significant predictors on the corrosion current is very similar implying that changes in any of them would indicate the same change in corrosion current.

For the SF mixes, the lime content becomes the most significant predictor and also has the greatest effect. The mechanism of conduction of direct current discussed in Chapter 10 suggests that it is substantially controlled by the amount of lime (hydroxyl ions) present. The high significance of the lime content is therefore due to a combination of its effect on the electrical conductivity and its depletion as the pozzolanic reaction of the SF proceeds and the transport properties decrease. This high significance implies that the pozzolanic reaction is not depleting the lime sufficiently to affect the alkalinity of the steel because this would cause corrosion to increase as the lime content decreased giving a negative *t*-ratio. The high significance and effect of the cube strength (greater than all of the remaining transport properties) was unexpected.

The 28 day current

The PC mixes generally performed as expected with every predictor being significant. Having been insignificant for the initial current, the carbonation strain has become the second most significant predictor and the oxygen permeability the most significant. The conductivity remains significant but has been overtaken by many transport properties. Figure 13.5 shows the effects in decreasing order indicating that the carbonation strain has greatest effect followed by the chloride transport next. Because the exposure took place in chloride solution, the chloride transport would have been expected to be greatest, but all of these properties are highly correlated.

The SF mixes showed significantly lower changes in corrosion current because their corrosion currents were generally significantly lower. An important observation was that, in contrast to the result for the initial current, the cube strength was not significant as a predictor. This implies that producing high strength mixes with SF is not a route to durability of embedded steel in a chloride environment. The lime content was also not

significant. The failure of the two measures of carbonation depth to work as predictors was caused by the very low (and often nil) depths observed.

13.5 Predictive models for corrosion

Equation (12.1) is used as the basis for a number of models that are used to predict chloride ingress into concrete and, from it, the durability of structures.

Software packages such as Life-365 (http://www.nrmca.org/research_engineering/Life365.htm) use equation (12.1) and take no account of ion–ion interactions. These packages are used to predict the life of structures and influence design decisions such as the depth of cover to the reinforcement of the w/c ratio of the mix. The package is set up so recommended values of the diffusion coefficient are given for different mixes, however, it would be possible for users to input their own values if experimental data was available.

In Chapter 12, the limitations of this approach were shown to be significant. These limitations are most apparent when different mixes are compared which have different concentrations of other ions which can carry current. SF is a good example of this because the strong pozzolanic reaction depletes the lime and thus the hydroxyl ions.

The first approach to overcoming this could be to use a different test. 'Simple gravity' diffusion tests are discussed in Chapter 12 and shown to be ineffective if the other ions are not modelled. A further test type is the Nordtest chloride migration test.

13.5.1 The Nordtest NT Build-492 test

This test, shown in Fig. 13.6, is similar to the ASTM C1202 test described in Chapter 10 in that a voltage is used to drive chlorides into the sample (NTBUILD, 1999). However, the results are obtained by cutting up the sample and measuring the chloride content at different depths at the end of the test. The results are then analysed using an integrated form of the Nernst–Planck equation (1.26). No account is taken of the ion–ion interactions.

Figures 13.7 and 13.8 show the effect of ion–ion interactions on this test. They may be seen to be very significant. The concentration is completely changed by the ion–ion interactions. Thus any diffusion coefficient obtained directly from equation (1.26) will be incorrect.

13.5.2 Predictions with the ASTM C1202 test

The ASTM C1202 test is not normally used to calculate a diffusion coefficient (although some authors have used equation 10.8). The result is normally

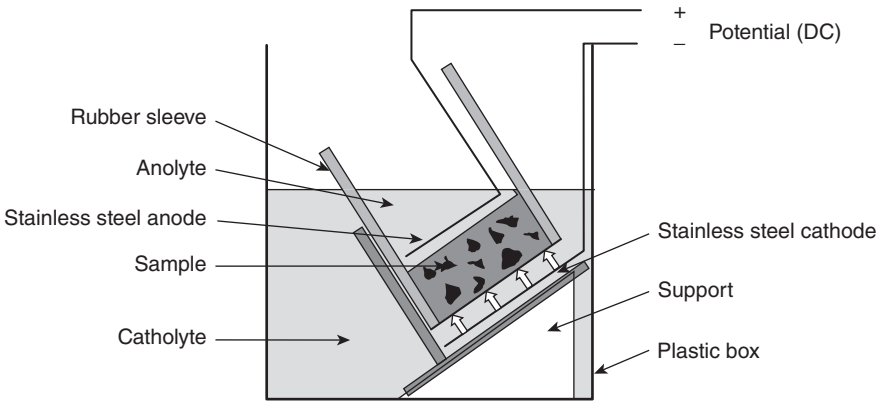

13.6 Arrangement of the migration test (NT Build-492).

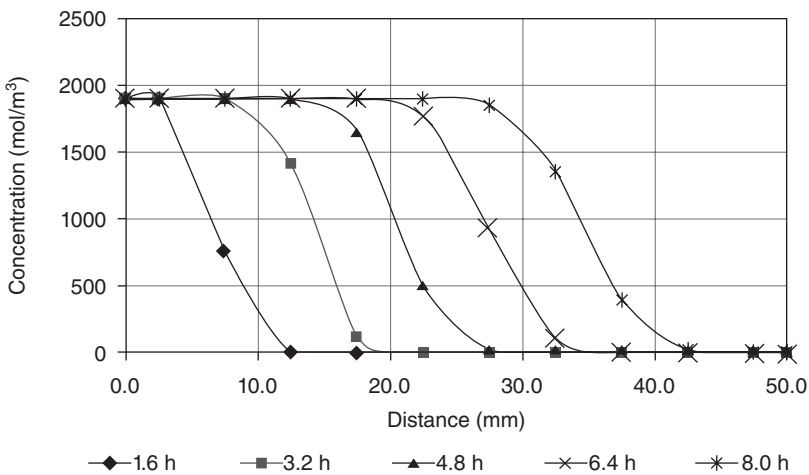

13.7 Modelled results for the NT Build-492 test using the Nernst–Planck equation (13.1).

simply given as charge passing. In some project specifications, a maximum charge passing of 1000 C is specified and the mix design is left to the contractor with no further checks for durability.

Figure 13.9 shows results for the mixes A and B described in Chapter 8 after 28 and 90 days of curing. The results from the gravity diffusion test are compared with those from the ASTM C1202 migration test. The pozzolanic mixes generally have coulomb values below 1000 and the CEM1 mixes above (the only SF mix above 1000 C was from 28 days of cold curing so the pozzolanic reaction would not have progressed). This data indicates that the ASTM C1202 test is not suitable for this purpose.

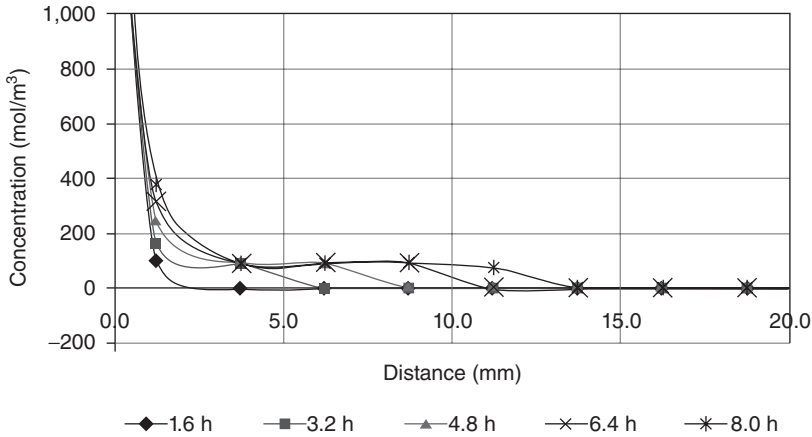

13.8 Modelled results for the NT Build-492 test with ion–ion interactions.

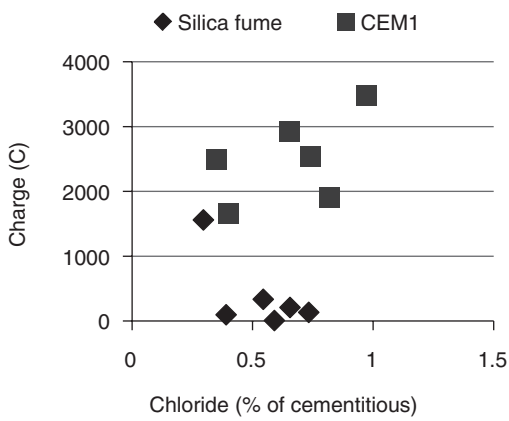

13.9 Comparison of charge passing with data for a simple diffusion test for mixes with w/c = 0.3 and 20% silica fume replacement.

13.5.3 Discussion

For modelling concrete durability, it has been noted that neither the simple diffusion test nor the durability models take account of ion–ion interactions. It may also be seen that the simple diffusion test has a good resemblance to the geometry of an exposed concrete surface on site. It may therefore be indicated that results from the test may be used in the model, subject to concerns about changing conditions which may affect adsorption or ionic concentrations. It is indicated that the use of coefficients from electrical tests in these durability models should only be attempted if numerical simulations are used to correct for the effect of the ion–ion interactions.

Any test can be used for site quality control purposes provided it is only used for comparative purposes on similar mixes. Thus the ASTM C1202 test could be used very effectively for this purpose provided initial tests were carried out on samples which were known to be of adequate quality. Provided the contractor did not start adding more pozzolan in the mix, any sample giving results as low as the initial tests could confidently be confirmed to be satisfactory.

13.6 Conclusions

- The corrosion of steel in concrete is controlled by the transport processes, but the relationship is complex.
- The electrical conductivity and the chloride transport were the only two predictors of corrosion which were significant for all situations and the conductivity was more significant than the chloride transport in three out of four.
- All measurements of diffusion in concrete, with or without applied voltages, are significantly affected by ion–ion interactions.
- For the comparison of mixes with different cementitious materials in them, a simple diffusion test should be used unless computer modelling is used to correct the results of electrical tests.
- The electrical tests are suitable for quality control purposes.
- For modelling the life of structures, a diffusion coefficient which includes some 'adjustment' for ion–ion interactions (such as that obtained by applying Fick's law to a simple diffusion test) could be used (if the model itself also uses Fick's law without corrections for ion–ion interactions).

13.7 References

Cabrera J G and Claisse P A (1991) The effect of curing conditions on the properties of silica fume concrete, in Swamy R N (ed.), *Blended Cements in Construction*, Elsevier, London.

Cabrera J G and Claisse P A (1995) Corrosion measurements on reinforcement in silica fume concrete, *Arabian Journal for Science and Engineering*, **20** (2), pp. 259–267

Draper N R and Smith H (1998) *Applied Regression Analysis (3rd edn)*,Wiley, New York.

NTBUILD-492 (1999) *Concrete, mortar and cement-based repair materials: Chloride migration coefficient from non-steady-state migration experiments*, Nordtest, Espoo.

Stern M and Geary A L (1957) Electrochemical polarisation. theoretical analysis of shape of polarisation curves, *Journal of the Electrochemical Society*, **104** (1), pp. 56–63.

14

Applications using measured values of the transport properties of concrete II: modelling the effect of gas pressure

DOI: 10.1533/9781782423195.235

Abstract: Cementitious barriers remain the primary containment mechanism for nuclear waste disposal in the UK. This chapter reports on a major programme in which the movement of gas in a nuclear waste repository was modelled using both analytical methods and a computer model. The purpose of the model was to predict cracking. Cracks would be a significant problem because they would permit harmful species to escape without being exposed to binding sites on the cementitious matrix. The measurement of the permeability of the materials was reported in Chapter 6. Calculations are presented to show the effect of the gas pressure on cracking within the repository.

Key words: nuclear waste, gas generation, crack generation, repository, hoop stress.

14.1 Introduction

The strategy adopted by many countries for the disposal of low and intermediate level radioactive wastes requires an engineered repository placed at considerable depth underground. Typically, such a repository will lie below the water table and hence will become water saturated relatively soon after the cessation of operations and closure. The majority of disposal strategies, including that adopted by the UK, require that the waste packages be surrounded by a backfilling material. The most commonly adopted types of backfilling material are based on either hydraulic cements or clay materials such as bentonite. Much of the remainder of the engineered structure of a repository may also be constructed of materials based on hydraulic cements; in particular structural concretes. The disposal strategy in the UK envisages a cement-based material for backfilling. Consequently, the properties of such cementitious materials are important both in the design of the repository and in the safety assessment.

Gas will be generated within a radioactive waste repository by several mechanisms. The principal such mechanisms are the anaerobic corrosion of steel reinforcement and containers (to generate hydrogen), the degradation of organic components in the waste (to yield carbon dioxide and methane) and the radiolysis of water (yielding hydrogen and oxygen). The majority

of the gas generated will be hydrogen, methane or carbon dioxide. The local pressure within the repository will rise above the ambient hydrostatic pressure to a value determined in the steady state by the relative rates of gas generation and release due to migration out of the immediate repository structure into the geological environment. A sufficient rise in internal pressure may result in stresses large enough to damage the repository structure and hence may compromise the containment strategy. In addition, gas-driven water flow, in the form of bulk water or bubbles, has the potential to short-circuit the repository containment by carrying contaminated water direct to the geological environment without prior conditioning of the water to high pH. Thus, data for, and the understanding of, the migration of gases within potential repository construction materials are required in order that the likelihood of such an eventuality can be determined and, if required, allowed for in the repository design.

Cementitious materials may be used for three main purposes in the UK repository: structural components, backfilling of the repository vaults and the encapsulation of materials within the actual waste packages. The materials selected for study in this work were chosen to be typical of those which may be adopted for each of these three applications. The structural concretes studied were relatively conventional materials based on either sulphate resistant Portland cement (SRC) or a mixture of ordinary Portland cement (PC) and pulverised fuel ash (PFA), together with both fine and coarse limestone aggregates. The waste encapsulation material was represented by a grout based on a 1:9 mixture of PC and blast furnace slag (GGBS) containing no aggregate.

The cementitious backfilling material requires a high porosity both to provide a high capacity for the sorption of radionuclides and to readily condition the chemistry of the mobile water in the repository. Two materials of this type, differing in composition and compressive strength, have been studied in this work. They are referred to in this chapter as preliminary backfill grout and reference backfill grout.

14.2 Background: mechanisms of gas migration

The mechanisms of gas migration are described in Chapter 1. In this chapter, the main mechanism is advection. During the operating phase when the repository is open to the atmosphere the pressures are low, but the results in Section 8.5.5 indicate that the Knudsen effect will not be significant. After closure the pressures will increase to match the hydraulic pressure of the surrounding groundwater making Knudsen flow even less significant.

The migration of gases within the pore structure of the cementitious materials intended for use in repository construction is likely to be complicated by the presence of pore water. Under fully water-saturated

conditions the pores will be effectively blocked and, for lower gas pressure gradients, the only plausible mechanism of gas migration will be the aqueous phase diffusion of gas molecules which have become dissolved in the water. It is currently not known whether the conditions within a repository will result in completely water-saturated material or whether some air will be trapped. At a sufficient excess internal pressure difference, the gas should be able expel a proportion of the pore water from the porosity of even fully-saturated material, allowing migration in what is effectively a small volume fraction of open porosity as discussed in Chapter 6.

14.3 The effects of stress generation in cementitious materials

14.3.1 Simple analytical model of crack generation

The effects of the stress generated by gas pressurisation were studied using a simple model of a spherical gas source in spherical repository. The model is illustrated schematically in Fig. 14.1. The ultimate effect of stress will be a failure of the backfill resulting in the formation of a crack. If the region

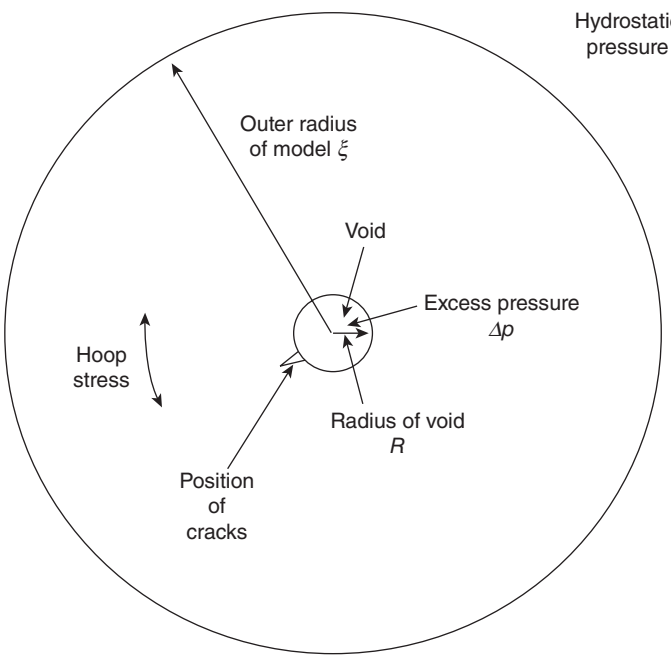

14.1 Illustration of the spherical repository approximation used as the basis for the model of stress and crack generation in backfill.

of gas generation shown in Fig. 14.1 is considered to be a void then backfill failure at the void surface will occur if the tangential hoop stress exceeds the tensile strength of the backfill. Hence, in the model the crucial stress for determining the failure of the material is considered to be the tangential hoop stress at the surface of the void.

The relationship between the tangential hoop strain at a particular radius r and the radial and tangential hoop stresses acting at that position is given by Roark and Young (1975):

$$\text{tangential hoop strain} = \frac{1}{E}[(1-\nu)S_\theta - \nu S_r] \qquad [14.1]$$

where:

S_r and S_θ are the radial and tangential hoop stresses, respectively, and
ν and E are the Poisson's ratio and Young's modulus for the backfill material.

The tangential hoop strain at a particular radius is also equal to the ratio of the radial displacement at that point to the radius.

Analytical solutions exist for the tangential hoop stress and radial stress at a given radius for a spherical pressure vessel (Roark and Young, 1975). The repository model can be considered to be equivalent to such a situation and hence the equations for the stresses at radius r and the radial displacement of the inner surface y are:

$$S_r = \frac{-\Delta P R^3(\xi^3 - r^3)}{r^3(\xi^3 - R^3)} \qquad [14.2]$$

$$S_\theta = \frac{\Delta P R^3(\xi^3 + 2r^3)}{2r^3(\xi^3 - R^3)} \qquad [14.3]$$

$$y = \frac{\Delta P}{E}\left[\frac{(1-\nu)(\xi^3 + 2R^3)}{2(\xi^3 - R^3)} + \nu\right] \qquad [14.4]$$

where:

ΔP is the excess pressure in the void (compared to the hydrostatic pressure in the medium surrounding the repository) and
R and ξ are the radii of the void and the repository, respectively.

The above equations are derived for the particular case where the porosity of the repository construction material is zero.

The radial displacement of the inner surface of the repository, that is the surface of the void, can be derived from equations (14.2)–(14.4) by putting the radius at which the stress is to be calculated r equal to the void radius R. It can be shown that if the outer radius ξ is more than an order of magnitude greater than the void radius. Equations (14.2)–(14.4) can be

further simplified by assuming that the outer radius is effectively infinite. The dimensions of a repository are likely to be of the order of tens of metres whilst the voids will be of the order of a few tens of centimetres. Hence, the assumption that the outer radius is effectively infinite is reasonable for this model of stress generation. The radial displacement of the void surface y_v is then given by:

$$y_v = \frac{\Delta P R(1+\nu)}{2E} \qquad [14.5]$$

Dividing the radial displacement of the void surface, given by equation (14.5), by the radius of the void and equating to the tangential hoop strain given in equation (14.1) produces an expression for the tangential hoop stress at the void surface:

$$S_\theta = \frac{1}{(1-\nu)}\left[\frac{\Delta P(1+\nu)}{2} + \nu S_r\right] \qquad [14.6]$$

For the zero porosity case, the radial stress can be derived from the equations given previously. This gives a radial stress equal in magnitude to the excess pressure in the void, although negative in sign. The tangential hoop stress obtained from equation (14.6) is then equal to half the excess pressure. This is a standard result for a pressure vessel.

The effect of the porosity of the backfill material has been included into the model by modifying the value used for the radial stress:

$$S_r = -(1-\varepsilon)\Delta P \qquad [14.7]$$

where ε is the fractional porosity of the material. This approach is rather simplistic but, as discussed below, it can be shown to be a good approximation for the conditions applicable to the behaviour of a repository. Substituting the equation for the radial stress into the expression for the tangential hoop stress given in equation (14.6) gives:

$$S_\theta = \frac{\Delta P}{2}\left[1 + \frac{2\nu\varepsilon}{(1-\nu)}\right] \qquad [14.8]$$

This expression can be used to calculate the hoop stress using appropriate parameters. The backfill is considered to fail if the calculated stress exceeds the tensile strength of the material.

14.3.2 Numerical solution for non-zero porosities

The analytical solution for the tangential hoop stress at the surface of the void is an approximation which takes limited account of the effect of the

backfill porosity. The validity of this approximation was tested using a numerical approach.

The numerical model explicitly considered the inward and outward forces acting on a spherical shell within the backfill, centred on the gas-generating inclusion, with an inner radius r and an outer radius $r + \mathrm{d}r$. The inward force F_i and outward force F_0 are, respectively:

$$F_i = 4\pi r^2(\varepsilon\, \mathrm{d}P - S_r) \qquad [14.9]$$

and

$$F_0 = 4\pi(r + \mathrm{d}r)^2\left[\frac{2S_\theta \mathrm{d}r}{r} - (S_r + \mathrm{d}S_r)\right] \qquad [14.10]$$

where:

$\mathrm{d}P$ is the pressure difference across the shell and
$\mathrm{d}S_r$ is the change in radial stress across the shell.

In a stable situation these forces will be equal. Equating the two forces gives:

$$\mathrm{d}S_r = \frac{S_r r^2}{(r + \mathrm{d}r)^2 - 1} + \frac{2S_\theta \mathrm{d}r}{r} - \varepsilon \mathrm{d}P \qquad [14.11]$$

The radial strain is equal to the rate of change of radial displacement with radius, that is strain is given by $\mathrm{d}y/\mathrm{d}r$. The standard definition of radial strain gives:

$$\text{radial strain} = \frac{1}{E}(S_r - 2\nu S_\theta) \qquad [14.12]$$

Equations (14.9)–(14.12) were used to determine the radial displacement of the void surface by iterating until a constant value of radial stress was obtained. The boundary conditions imposed on the procedure were that the radial stress at the void surface was equal to the excess pressure, modified by porosity, and that at infinite radius was zero. The radial displacement was then used to calculate the tangential hoop stress.

The numerical solution was used to obtain the hoop stress at the void surface and the value compared to that obtained using the analytical approximation. It was found that the difference between the two solutions was negligible and the analytical equation, combined with a description of the pressurisation of the void given in Section 14.3.3, was adopted for subsequent calculations.

14.3.3 Pressurisation of the void

Gas is considered to be generated within the void in the material. The excess pressure produced by the gas generation will depend on the rate at which

the gas can flow through the material. The volumetric flow rate within the backfill material at a radius r, denoted dV/dt, is determined by the pressure at that position P_r and the gas generation rate Q, measured at the hydrostatic pressure P:

$$\frac{dV}{dt} = \frac{QP}{P_r} \qquad [14.13]$$

The volumetric flow rate is also given by the Darcy equation (equation 1.9), provided that the value of the pressure gradient used is that at the appropriate radius. Combining equations (1.9) and (14.13) and rearranging gives an equation for the pressure gradient at radius r:

$$\frac{dp}{dr} = \frac{eQP}{AKP_r} \qquad [14.14]$$

where A is the area of the spherical shell of radius r. This expression can be integrated between the void radius R and the outer radius of the repository ξ. This gives an expression for the pressure produced in the void P_v:

$$P_v^2 - P^2 = \left[\frac{1}{R} - \frac{1}{\zeta}\right]\frac{QeP_{atm}}{2\pi K} \qquad [14.15]$$

If it is assumed that the outer radius is effectively infinite, equation (14.15) can be simplified and rearranged to yield an equation for the difference between the pressure in the void and the hydrostatic; pressure, the excess pressure ΔP used in previous equations:

$$\Delta P = \frac{QeP_{atm}}{2\pi KR(P_v + P)} \qquad [14.16]$$

Substituting the expression for ΔP given in equation (14.16) into equation (14.8) gives an expression for the tangential hoop stress generated at the void surface by a given void pressure P_v:

$$S_\theta = \frac{1+2\nu\varepsilon}{1-\nu}\frac{QeP_{atm}}{2\pi KR(P_v + P)} \qquad [14.17]$$

This equation is used to calculate the tangential hoop stresses in the discussion in Section 14.4.

14.4 Sensitivity to material properties and conditions

The sensitivity of the tangential hoop stress, calculated using the analytical approximation given in equation (14.17), to the material parameters required by the model was investigated. The effect of a particular parameter was assessed by fixing all remaining parameters at typical values and varying

the parameter of concern over an appropriate range. The typical parameters were selected to reasonably approximate the reference backfill grout in a water-saturated condition. It is apparent from the analytical approximation that the calculated stress in this model is independent of the Young's modulus of the material. The gas viscosity was assumed to be equal to that of argon at a value of 2.2×10^{-5} Pa s.

The tangential hoop stress at the void surface calculated from the typical values of the model parameters is 238 kPa. The compressive strength of the reference backfill grout is 6.0 MPa. If the tensile strength is assumed to be one tenth of the compressive strength, that is 600 kPa, then the tensile strength is not exceeded by the hoop stress for the typical conditions and the reference backfill grout will not crack.

14.4.1 Gas generation rate

The anticipated maximum gas generation rate is approximately one repository volume of gas per year, measured at standard temperature and pressure. The model is intended to represent the venting of gas from a single waste drum with an approximate volume of 1 m^3. Hence, the typical value of the generation rate was taken to be 1 m^3 per year at standard temperature and pressure. The range of generation rates was specified as 0–5 m^3 per year. The variation in stress with gas generation rate is shown in Fig. 14.2. The stress is increased as the gas generation is increased.

14.4.2 Hydrostatic pressure

The majority of current radioactive waste disposal strategies envisage the placement of a repository at a depth of up to 1000 m below ground level. This indicates a potential range of hydrostatic pressures of between 100 kPa and 10 MPa if the repository is fully saturated by the groundwater. Figure 14.2 demonstrates that the stress is inversely dependent on the hydrostatic pressure and hence the lower pressure of 100 kPa was adopted as the typical value to represent a plausible worst case. The reduction in stress with increasing hydrostatic pressure is attributed to the compressibility of the gas. As the pressure increases, the volumetric flow rate is decreased. This behaviour implies that a repository will be more susceptible to gas-generated cracking before resaturation by groundwater after closure as the effective hydrostatic pressure will be lower.

14.4.3 Fractional porosity

The data given in Table 6.2 indicates a range of fractional porosities of between about 0.1 and 0.6 for the experimental materials. The relationship

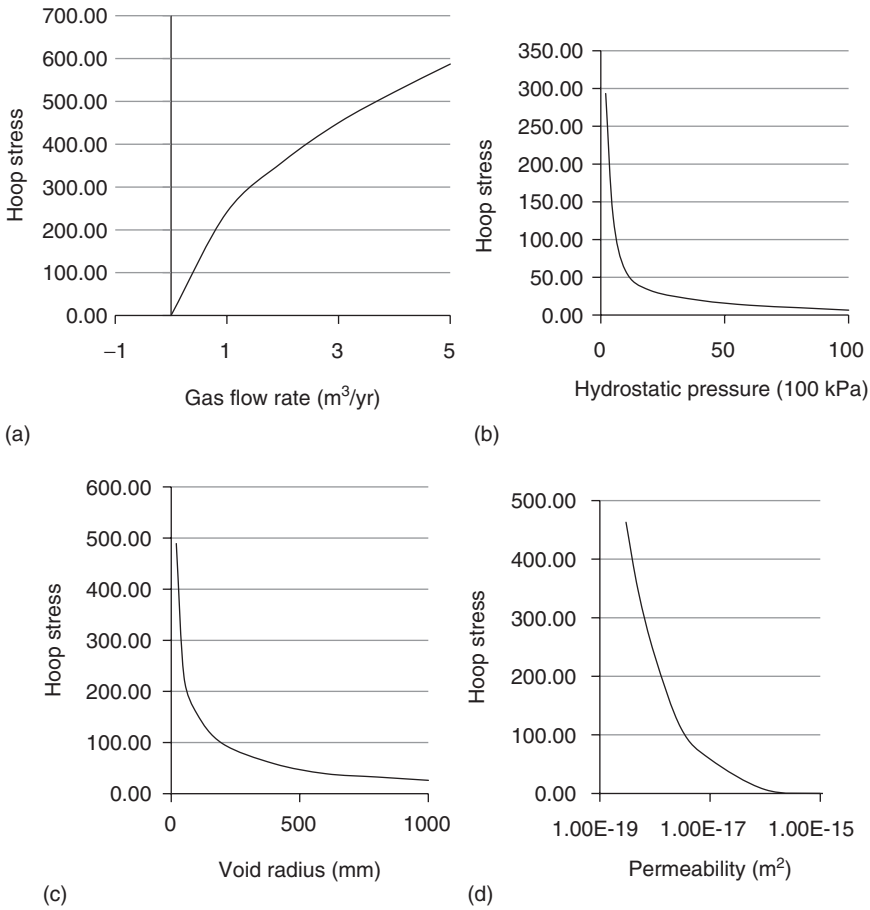

14.2 Variation in spherical hoop stress in kPa at the void surface with (a) gas generation rate, (b) hydrostatic pressure, (c) void radius and (d) backfill permeability coefficient, calculated from the analytical solution to the stress generation model.

between the measured values of fractional porosity and that available for gas flow is not known. The typical value was taken as 0.5, close to the values given for the backfill grouts in Table 6.2. The analytical solution demonstrates that gas-generated stress is linearly dependent on the fractional porosity of the material, assuming constant permeability. The stress increases by a factor of 0.5 as the porosity is varied between zero and unity. The effect of porosity on the stress may not be adequately modelled by the analytical approximation and the dependence of stress on porosity may not be as simple as indicated here.

14.4.4 Void radius

The model is intended to simulate the effects of gas vented from waste drums. It is expected that any vent will be of the order of the size of the drum; approximately 0–1 m in dimension. The typical value of 0.05 m was selected to represent a vent of 100 mm diameter in the drum. Figure 14.2 demonstrates that the stress generated at the surface of the void is strongly dependent on the void radius. The requirement for a void dimension is a limitation in the overall model, and Fig. 14.2 shows that the value of the void radius is crucial in determining the level of stress.

14.4.5 Poisson's ratio

The expected value of the Poisson's ratio for an ideal material is 0.5. The values for real materials tend to be between about 0.2 and 0.4 and hence a range of 0–0.5 was investigated. The typical value was taken to be 0.2. The stress increased by a factor of two as the Poisson's ratio was varied between 0 and 0.5. Variation in this parameter is not of primary importance in determining the stress.

14.4.6 Permeability coefficient

As has been discussed previously, the repository is likely to become water saturated at some stage after closure and hence the gas permeability will be influenced by the presence of water. Figure 14.2 demonstrates that the stress is strongly dependent on permeability for permeability coefficients below about $10^{-16}\,m^2$. Table 6.5 shows that the permeability coefficients for water-saturated materials are likely to lie below this value and hence will be crucial in determining the stress. The value of the permeability coefficient used as the typical value was $10^{-18}\,m^2$, somewhat below the measured permeability coefficient for the reference backfill grout in the 100 % relative humidity (RH) conditioned state.

14.5 Behaviour in a repository

The comparative performance of the cementitious materials studied in this work is summarised in Fig. 14.3. As discussed above, the crucial parameters in determining the calculated level of tangential hoop stress at the void surface are the void radius and the permeability coefficient of the surrounding material. Figure 14.3 shows the calculated stress for permeability coefficients between 10^{-22} and $l0^{-14}\,m^2$ for voids of 0.02, 0.1 and 0.5 m radius using the typical values for the remaining parameters. The measured ranges of the permeability coefficients for the cementitious materials are

also illustrated, plotted at stress values equal to the estimated tensile strength of each material based on one tenth of the compressive strength. If the tensile strength of the material at an appropriate permeability is exceeded by the calculated stress then the material is predicted to fail by cracking at the void.

In Fig. 14.3, the variation in tangential hoop stress at the void surface for three different void radii is plotted against permeability coefficient. The estimated tensile strengths for the materials investigated in this work are also plotted against the range of the permeability coefficients. A material

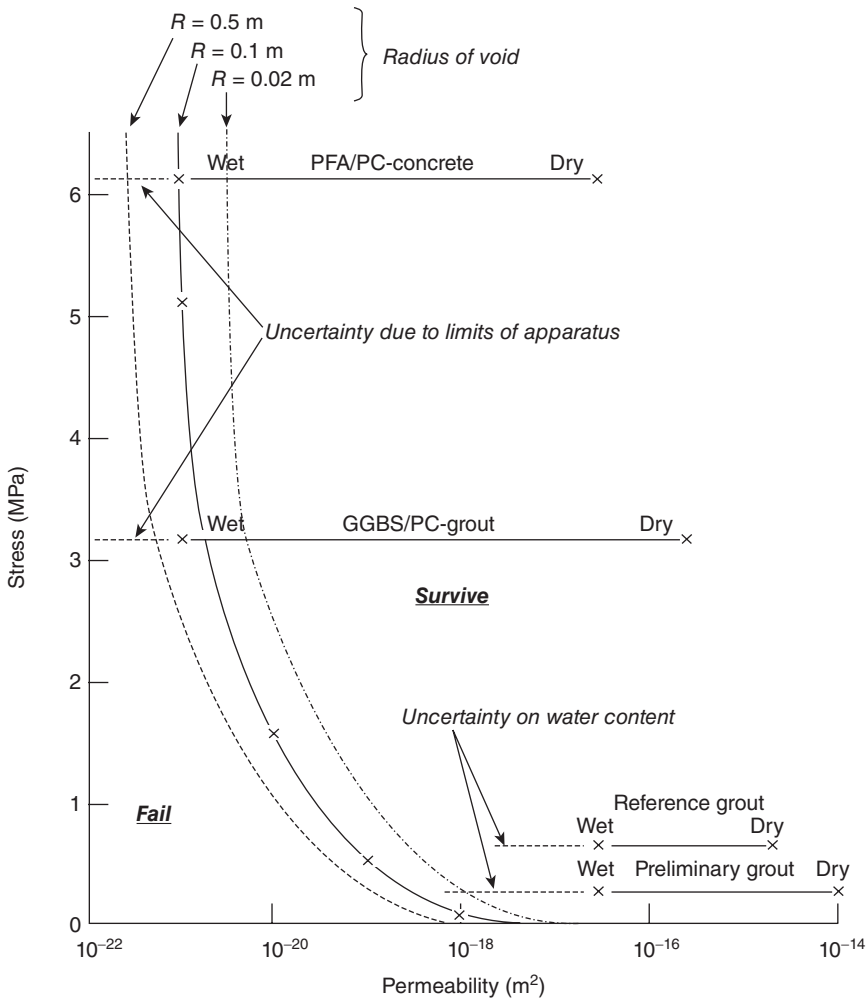

14.3 Summary of the conclusions of the stress generation model.

is considered to crack if the calculated stress exceeds the tensile strength, as shown by the regions labelled 'survive' and 'fail' (crack).

Figure 14.3 indicates that the two backfill grouts can adequately disperse gas and hence will not fail. In contrast, the PFA/PC concrete and the GGBS/PC grout appear to have insufficient permeability in the saturated state to prevent cracking. The simplicity of the model and the uncertainty in some of the parameters, in particular the permeability coefficients, Poisson's ratios and tensile strengths, require that these conclusions are tentative. In particular, the possibility of the formation of high pH 'boulders' in the backfill surrounded by carbonated layers with low permeability has been postulated (Claisse and Unsworth, 1996).

14.6 Conclusions

A simple model of the development of cracking in cementitious materials in repositories has been developed. The model identifies the gas permeability coefficient as a crucial parameter in determining the likelihood of cracking through gas generation in voids. Initial calculations indicate that the backfill grouts studied in this work should be able to release gas at a sufficient rate to avoid cracking.

14.7 References

Claisse P A and Unsworth H P (1996) The engineering of a cementitious barrier, in Bentley S P (ed.), *Engineering Geology of Waste Disposal*, Engineering Geology Special Publication No.11, Geological Society, London, pp. 267–272.

Roark T and Young C (1975) *Formulas for Stress and Strain* (5th edn), McGraw Hill, New York.

15

Applications using measured values of the transport properties of concrete – III: predicting the transport of liquids through concrete barriers for waste containment

DOI: 10.1533/9781782423195.247

Abstract: This chapter describes measurements of the transport of liquids through concrete barriers for waste containment. A computer model (which is described in Chapter 2) was used and the results were used to relate laboratory observations with site trials. Confidence limits for the results were obtained by running the model with successive data sets representing extreme values of the input data. The observed results from the site trials generally fell within the expected limits but there were some notable exceptions. It was concluded that transport modelling of real landfills is not an exact science.

Key words: landfill, leachate migration, cementitious barriers, diffusion permeability, site trials.

15.1 Introduction

15.1.1 The concrete waste containment barrier

Concrete barriers were designed as alternatives to conventional systems used as landfill liners such as bentonite enhanced sand and high density polyethylene (HDPE) membranes. The concretes were made from mineral wastes and were expected to be cheaper and more effective than current systems.

Interest in concrete as a barrier for lining landfills has arose for the following reasons:

- Current liner technology based on HDPE membranes and bentonite-enhanced sand is expensive and its production and installation involves a high environmental impact.
- HDPE membranes are easily damaged after installation. A concrete barrier provides a relatively hard concrete surface to permit operation of vehicles and to prevent damage from large items of waste compacted onto it and is also relatively resistant to damage from fires.
- The concretes which are used for these barriers are made from waste materials which would otherwise go into landfills.

A landfill liner (barrier) should be physically strong enough to allow vehicular access during the operational phase, and provide adequate containment of leachate during the post-closure period. In order to satisfy both these operational and long-term requirements, a range of composite barrier materials were evaluated. These included: low cost, chemically conditioning, cementitious media (such as concretes containing metallurgical slags, spent foundry sands and/or demolition waste as an aggregate, blended cements containing waste materials such as fly ash, cement kiln dust and slag) and non-swelling clays.

The properties of an ideal barrier system are:

- low permeability – less than 10^{-9} ms^{-1};
- high cation exchange capacity;
- the ability to chemically condition leachate through sacrificial action;
- construction from inexpensive materials;
- tolerance of deformation during service without barrier failure through brittle cracking;
- the ability to promote self-sealing of cracks;
- ease of construction;
- sufficient strength to support a refuse vehicle during operation – a cube strength of 5 N/mm^2 is adequate.

15.1.2 The alkaline barrier

During the 1980s, a very large research programme was carried out in the UK to develop designs for repositories for nuclear waste (see Chapter 14). The design which was developed to the greatest extent was the repository for intermediate and low level waste. This repository was required to have a predictable performance in a deep saturated geological environment over a timescale of up to a million years. The design essentially involved placing the waste in concrete containers and placing these containers in an excavated underground cavern. This cavern was then to be backfilled with a relatively soft cementitious grout (Claisse, 1989).

One of the achievements of the nuclear programme was to analyse and define the performance which was actually required of the concrete when used for this application. This performance requirement is quite different from the requirements for concrete in normal construction and led to the development of some very unusual concrete mixes.

The barrier design used conventional engineering materials, but its method of operation was far from conventional for an engineering structure because it is essentially sacrificial (Claisse and Unsworth, 1996). The main function of the barrier was to condition the chemistry of the repository to high pH by dissolving alkalis in the groundwater. The alkalis are free

sodium, potassium and lime and, subsequently, the calcium silicate hydrate which forms the structure of the hardened cement. At the high pH values, the harmful species from the waste which are permeating through the barrier are adsorbed onto the cement matrix and immobilised. Clay-based liners were considered for the nuclear repository, but concrete was chosen as the best option for the UK. The nuclear programme was stalled in the 1990s by the refusal of planning permission for the test facility at Sellafield in Cumbria.

The novel concrete barrier concept for conventional landfills is based on the theory that the pollution of soils and watercourses by the release of leachate may be prevented by adoption of a composite barrier liner. This will not only chemically condition the waste, but is designed to be self-sealing through secondary mineralisation and will retain heavy metal ions through ion exchange, surface sorption, filtration and precipitation.

15.1.3 The three layer barrier concept

In the design considered in this book, three layers are envisaged such that the clay-based hydraulic barrier is sandwiched between two layers of cementitious materials (see Fig. 15.1). These concretes for the liner are made with a range of waste materials which would otherwise have to be disposed of in the landfill.

Each of the layers has different properties, so that any defects, such as cracks, are likely to form at different locations in different layers, thus limiting the creation of connected pathways through the barrier. The clay may be a natural material or, for some applications, the concept of an

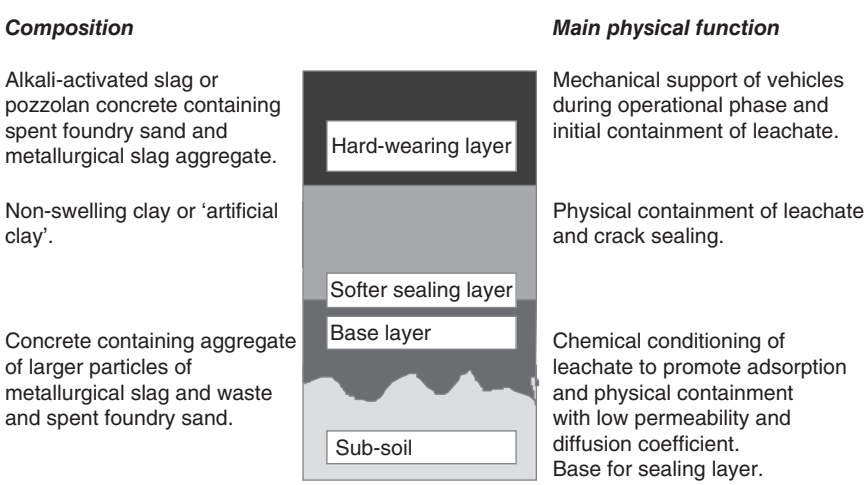

15.1 The new composite landfill liner.

'artificial pourable clay' made from a setting mix based on waste gypsum or ash has been developed.

15.1.4 Transport mechanisms

The degree of containment will depend on the transport properties of the barrier. The properties considered for modelling purposes are the permeability, diffusion coefficient and capacity factor. The capacity factor is used to give an approximation for the chemical containment and the diffusion coefficient measures ion transport, but the most significant property has been found to be the permeability which measures fluid transport (see Chapter 1). The permeability of concrete and mortar was measured in the high pressure cell described in Section 4.2.

For a nuclear waste repository in which a cementitious barrier is used, the main mechanism of loss of radionuclides is caused by flowing groundwater. This flow may be present in the area before the repository is built or it may be caused by the heat generated in the repository. In order to operate for a long time the chemical barrier depends on other barriers to limit the flow of groundwater through it. This is normally achieved by positioning the repository in a geology with a very low permeability. In this situation, the permeability of the repository itself can be shown not to have a significant effect on the flow of water through it. In the non-nuclear landfills which are considered in this chapter, the hydraulic head on the barrier is caused by standing leachate in the bottom of the cell. European guidelines require leachate extraction in order to limit this to a depth of 1 m above the liner but, in order to guarantee effective containment, a possible head of 10 m has been considered in the design.

15.1.5 Vertical barriers

In most current landfill designs, the sides of the cells slope, typically at 30° to the horizontal. This enables conventional machines to work and compact the mineral layers. In order to provide maximum deposition volume on restricted sites, a number of vertically sided cells have been built, but the technology for this has been very expensive. The proposed novel barrier system would be well suited to this application because the two concrete layers could be built as conventional concrete walls and then the pourable clay placed between them as the waste level rose to contain the resulting fluid pressures.

15.1.6 The research programme

The work reported here formed part of a major industry-based project on a novel composite barrier system, which used metallurgical waste materials

for the cementitious liners in the landfill barriers. This work included carrying out three large-scale site trials to demonstrate the construction of the system. The trials consisted of cells approximately 8 m wide, which were designed to contain leachate to a depth of 1 m.

Transport modelling was used to predict the performance of the barriers. The processes of advection, diffusion and adsorption were included in the model. Four elements were studied: sodium, potassium, calcium and sulphur. These elements are not generally of concern in the environment, but it was not possible to use toxic elements such as mercury because the work involved large quantities of leachate in field-scale trials.

15.2 The computer model

15.2.1 The basis of the model

A computer model was written to simulate the transport processes (the details are discussed in Chapter 2). This model was used both to obtain transport properties from the laboratory results and to predict the results from the site trials. In each application, the calculations are identical. The only differences are in the exact output given and the length of time that a run simulates. The model is based on physical transport processes (diffusion and advection) with linear adsorption and uses the following assumptions:

1. The transport processes which are considered here are advection and diffusion and they are limited by adsorption. These are discussed in Chapter 1.
2. The following mechanisms are assumed not to be significant: thermal migration, electromigration, osmosis, electro-osmosis, capillary suction.
3. The barrier is assumed to be saturated when the leachate first comes into contact with it.
4. The layers of the barrier are assumed to be homogeneous. In particular, 'boulders' are assumed not to form. These would be regions surrounded by impermeable layers of carbonates, chloroaluminates or magnesium compounds which do not contribute to the transport or adsorption.
5. The properties of the barrier are assumed not to change with time or the amount of transport that has taken place through it, other than the gain or loss of ions due to the transport processes.
6. The adsorption processes are assumed to reach equilibrium within each time step.

15.2.2 Treatment of tolerances

The input data for the modelling of the full-scale barriers (e.g. layer thickness) is assumed to be normally distributed. For the purpose of

modelling, it is divided into three outcomes, an expected outcome and one high and one low. Studying the normal probability function shows that to give each outcome equal probability the expected outcome must include all results within 0.43 standard deviations of the population mean. The means of the high and low outcomes have been calculated to be 1.1 standard deviations above and below the sample mean. The standard deviation has been estimated as a coefficient of variation V = standard deviation/mean. Thus three outcomes were modelled, and these are shown in Table 15.1.

For the diffusion coefficient and the permeability, the treatment is slightly more complex in that the distribution of results form a highly skewed distribution when measured on a linear scale. On a logarithmic scale they are, however, more normally distributed and the three different outcomes have therefore been obtained by dividing up the distribution of the log of the parameter. The three outcomes for this case are shown in Table 15.2 where V is the coefficient of variation of the sample on a logarithmic scale.

Typical values for the parameters are shown in Table 15.3. From this it may be seen that, although V for permeability appears low at 2 %, it represents a range of +60 % and –36 % on a linear scale. The 5 % for diffusion gives an increase of 460 % on a linear scale. Because the populations were skewed on a linear scale, the mean outcome from this analysis was not the outcome with the highest probability (as would be expected from a normal distribution).

Each of these outcomes was modelled for each input parameter for which there was significant uncertainty. Thus, for example, where four different input parameters had significant uncertainty, 81 simulations were carried out and the 10^{th} and 90^{th} percentiles of the resulting population were used to calculate the degree of uncertainty of the model predictions.

Table 15.1 Probabilities for parameters with a linear distribution

Outcome	Mean value	Probability
High	Sample mean × $(1 + 1.1V)$	0.33
Expected	Sample mean	0.33
Low	Sample mean × $(1 - 1.1V)$	0.33

Table 15.2 Probabilities for parameters with a logarithmic distribution

Outcome	Mean value	Probability
High	Sample mean$^{(1 - 1.1V)}$	0.33
Expected	Sample mean	0.33
Low	Sample mean$^{(1 + 1.1V)}$	0.33

Table 15.3 Typical values and ranges for the measured parameters

Parameter	Typical value	Scale	Coefficient of variation (%)	Low value	High value
Capacity factor	5	Linear	50	2.25	7.75
Permeability	10^{-9}	Logarithmic	2	6.4×10^{-10}	1.6×10^{-9}
Diffusion coefficient	10^{-12}	Logarithmic	5	2.2×10^{-13}	4.6×10^{-12}
Layer thickness	300	Linear	15	250.5	349.5

The coefficients of variation for the input data obtained in the laboratory work were obtained by studying several series of replicate samples and also analysing the optimisation of the data from the through diffusion tests.

Some variables, such as layer thickness in multilayer barriers, were in sets in which varying each one had a similar effect. Reducing the thickness of one layer by 20 mm will have a similar effect to reducing another layer. In these situations only the variation of one of the variables was modelled.

15.3 Laboratory testing

Tests were carried out on samples taken from the mixes at the time of the pours for the site trials.

15.3.1 Mix designs

The mix designs are shown in Table 15.4. The designs were chosen to make use of available industrial wastes and give an adequate strength (5 MPa) and permeability (10^{-9} m/s) (Ganjian *et al.*, 2004).

15.3.2 Diffusion tests

The diffusion cells were used to examine mass transport in reactive systems. An aggressive solution, simulating an acetogenic leachate typical of the early stages of landfill evolution (this is given in Table 9.1), was allowed to react with the sample, whilst concentration changes due both to diffusion and reactive transport were monitored in the cells.

This diffusion test was intended to measure both the diffusion coefficient and capacity factor of species partitioned between a solution and a porous sample. The basis of the test was a divided cell with the sample in the centre.

Table 15.4 Composition of mixes used in the three trial cells

	Proportions used	
	kg/m^3	% by mass
Composition of top layer mortar for cell No.2		
Ferrosilicate slag sand (<5 mm)	1575	65.9
CKD – 60%	490	20.5
Lagoon ash – 40%	325	13.6
Water	200	
Composition of top layer concrete for cell No.3		
Ferrosilicate slag (<150 mm to dust)	0	
Limestone (<20 mm)	715	29.8
Ferrosilicate slag sand (<5 mm)	1105	46
CKD – 60%	340	14.2
Lagoon ash – 40%	240	10
Water	220	
Composition of lower layer concrete for cell No.2		
Chrome alumina slag (<40 mm)	1175	49.6
Chrome alumina slag (<5 mm)	720	30.4
Green sand	100	4.2
CKD – 60%	165	7
Sodium sulphate solution (l)	165	
Composition of lower layer concrete for cell No.3		
Chrome alumina slag (<40 mm)	1175	50.3
Chrome alumina slag (<5 mm)	720	30.8
Green sand	110	4.7
PC – 5.2%	25	1.1
CEM1 42.5N to BSEN 197-1		
CKD – 69.8%	185	7.9
Lagoon ash – 25%	120	5.2
Water	240	

Artificial leachate was placed on one side and deionised water on the other. Chemical analysis was used to track changes with time on each side.

The apparatus was a modified ASTM C1202 test (see Chapter 10). The C1202 test has an applied electric field and in this work the same cells were used without the field but with extra reservoirs on the top. Using an electric field would have accelerated the tests but made interpretation very uncertain.

Two symmetric poly methyl methacrylate ('Perspex') chambers with fluid reservoirs of 85 mm diameter and about 47 mm depth were made with extra liquid storage reservoirs of 50 ml on top of the chambers. Figure 15.2 shows the arrangement of cells and the specimens between them. The specimens were 100 mm diameter discs approximately 10 mm thick.

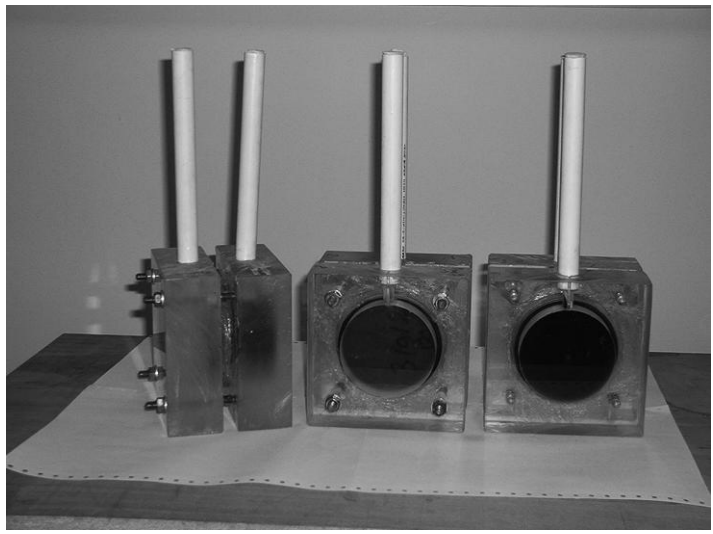

15.2 Diffusion cells.

The specimen cells were sealed by using rubber gaskets on each side of the specimen, tightening the bolts and applying silicone rubber round the specimen and inner face of cells. The apparatus was kept in a temperature controlled room at 20 °C. Periodically, 10 ml of liquid was taken out from the reservoirs and the chemical composition was analysed using inductive coupled plasma (ICP) analysis. Synthetic leachate was used on one side of the sample and de-ionised water on the other. The capacity factor and diffusion coefficient values were calculated from the diffusion test results using an optimisation routine with the computer model.

The modelled input–output and experimentally measured (real) input–output concentrations from the diffusion cell are plotted for two typical examples in Figs 15.3 and 15.4. The results show that, for the limited data used, the model optimisation gave a very good agreement between the modelled values and the experimental values. This was achieved by the progressive changing of the capacity factor and diffusion coefficient using the optimisation routine. In Fig. 15.3, increasing either parameter increases the transport into the sample and will thus increase the rate of decline of the input concentration. The output concentration will, however, change more if the diffusion is increased but the adsorption is decreased. In Fig. 15.4, a high initial concentration in the sample (measured by pore fluid expression and input into the model) gives a rising concentration on both sides of the sample. The derived results for diffusion and adsorption are given in Table 15.5.

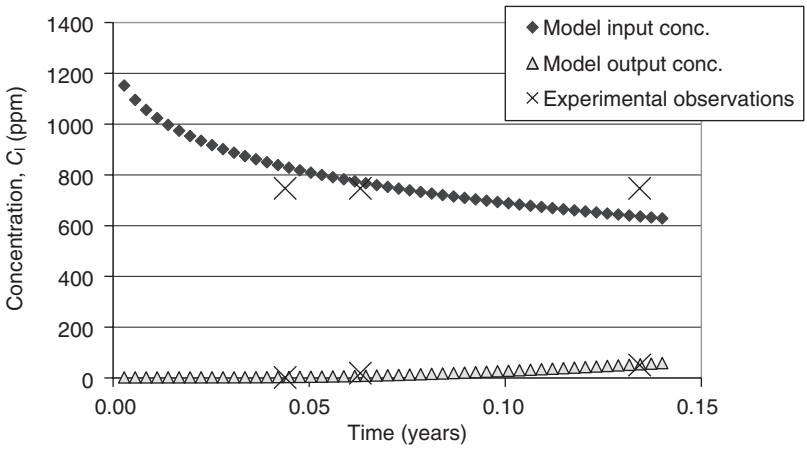

15.3 Concentrations from laboratory diffusion testing for calcium.

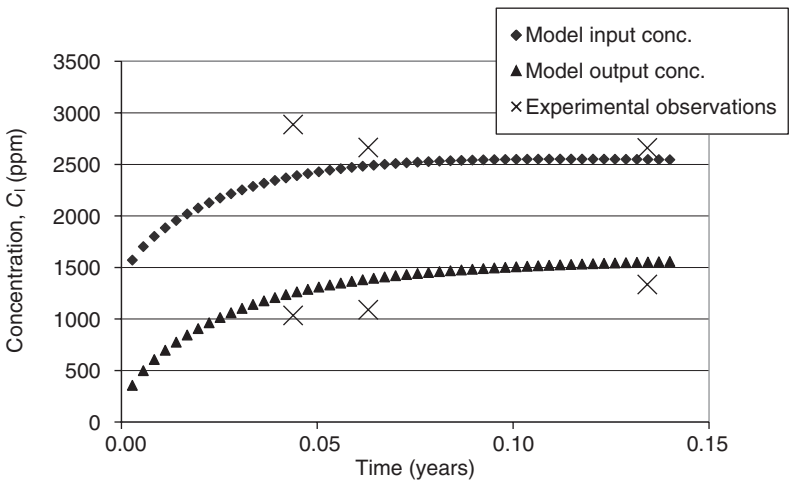

15.4 Concentrations from laboratory diffusion testing for potassium.

Table 15.5 Capacity factor (α) and diffusion coefficient (D) values for the four major elements in the trial cells

Chemical element	Top layer mix Cell 2 & 3 (porosity = 12%)		Bottom layer mix Cell 2 (porosity = 9%)		Bottom layer mix Cell 3 (porosity = 9%)	
	α	D (m^2/s)	α	D (m^2/s)	α	D (m^2/s)
Calcium	7.74	3.7×10^{-10}	0.5	1.77×10^{-10}	0.09	1.35×10^{-10}
Sodium	0.43	1.19×10^{-10}	0.09	10^{-14}	1	4.58×10^{-13}
Potassium	0.86	1.07×10^{-10}	1.02	1.71×10^{-12}	1	6.73×10^{-12}
Sulphur	1	2.07×10^{-12}	1.37	10^{-14}	27.67	2.93×10^{-14}

Table 15.6 Characteristics of the mixes used in the site trial cells

	7 days strength (MPa)	28 days strength (MPa)	Intrinsic permeability to water at 28 days (m/s)	Intrinsic permeability to leachate at 28 days (m/s)
Cell 2 top	1.1	1.7	4.5×10^{-9}	5×10^{-9}
Cell 2 base	4.4	6.9	2.3×10^{-9}	4.5×10^{-9}
Cell 3 top	0.9	1.3	1.2×10^{-8}	7.5×10^{-9}
Cell 3 base	2.8	6.0	1.2×10^{-8}	6.2×10^{-9}

15.3.3 Permeability tests

The permeabilities of the specimens were determined using a continuous high-pressure flow experiment described in Section 4.2. Measurements were made after one sample volume of liquid had passed through the concrete or mortar specimens. Assuming an average permeability of 10^{-9} and a maximum leachate head of 1 m above the liner, this corresponds to 16 years of exposure in service. The results are given in Table 15.6.

15.3.4 Pore fluid concentrations

Samples of pore fluid were expressed under pressure from samples of the different mixes using a cell similar to an OPI-CAD cell (http://www.cad-inst.com/en, http://www.claisse.info/Lab%20Testing/Chemical%20Testing.htm) and the concentrations obtained from them using ICP analysis. This cell works by applying very high pressures to a confined sample using a compression test machine. As the volume of the sample is reduced, a small amount of pore fluid flows out through a pipe in the bottom of the cell.

15.4 Site trials

15.4.1 Introduction

Two cells were constructed on a licensed landfill operation site at Risley, Cheshire, UK in Winter 2000 with different cementitious composite mineral waste materials. This landfill site received both domestic and industrial waste.

The purpose of the cells was as follows:

- to provide validation data for the modelling of the performance of the barriers in service;
- to demonstrate a construction method;

- to demonstrate that the novel mixes could be made in industrial quantities (150 tonnes of concrete were used in the three test cells);
- to provide samples for on-site workability testing and long-term physical testing in the lab;
- to provide samples for mineralogical analysis when the cells were dismantled.

15.4.2 Layout and construction methods of the cells

A typical test cell is shown schematically in Fig. 15.5. The barrier was made up of two layers of concrete with a layer of clay between them. These inverted pyramid shape cells measured 8 m wide and contained waste to a maximum depth of 1.1 m. The slopes of the cells were 30° and the cells contained 5.4 m^3 of waste. Table 15.7 gives the dimensions and volume of

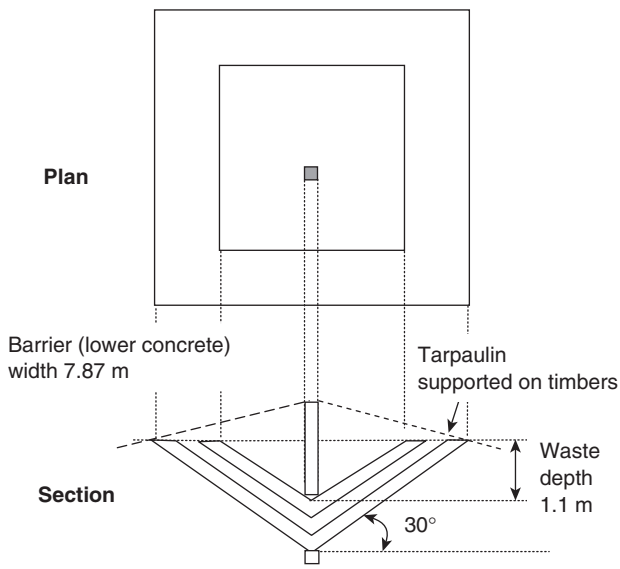

15.5 Typical trial test cell layout.

Table 15.7 Dimensions and volume of each layer of test cells

	Thickness (m)	Depth to lowest point (m)	Width (m)	Volume (m^3)
Waste	–	1.1	3.84	5.4
Upper concrete	0.2	1.33	4.65	4.16
Clay	0.5	1.9	6.66	18.61
Lower concrete	0.3	2.25	7.87	18.28

each layer in the test cells. The excavation was carried out with an excavator which was also used to place the concrete and mortar mixes designed for the different cells. The concrete layers were placed and levelled by the excavator. The compaction of concrete layers was carried out by two poker vibrators and the compaction of clay layer was carried out using the outside surface of the excavator's bucket.

15.4.3 Observations from the construction

During the construction of cell numbers 2 and 3, the mix proportions actually used were different to what was designed in the laboratory due to some practical problems encountered in the batching plant and placement of some of materials (inaccurate weighing of different materials and partial hydration of cement kiln dust (CKD) while stored at the plant). The mixes actually made were tested and showed higher permeabilities than the mixes designed initially in the laboratory.

15.4.4 Emplacement of waste and leachate

Due to size and shape constraints of the cells, shredded waste was used. It was placed and compacted up to the top level of the test cells. A leachate which provided the most aggressive solution representing the leachates found in the landfill was obtained from the leachate treatment plant for the site and the cells were filled 100 mm below the top giving a 1 m head at the deepest point. The cells were covered with a tarpaulin rain cover to prevent rainwater ingress and contain odour.

15.4.5 Instrumentation and sampling

Two types of sampling lines were used between the layers of the cell liners using 3 mm plastic tubes in both. In one type, the ends of the 3 mm plastic tubes were glued inside porous stone discs of 60 mm diameter. In the other type, the layer was drilled and the 3 mm plastic tubes ends were sealed in place in the set concrete with sponge around the end of the line. The sampling lines were placed as an array in the various liner materials and levels. Liquid samples were obtained by applying a vacuum to the lines.

15.4.6 Operation of vacuum lines

On the end of the extract lines, there was a sponge or a stone to form a void. If there was gas in adjacent pores or cracks, etc., samples could be extracted easily with a vacuum. If there was no gas or other pathway, the flow up the line had to be from advection from a spherical region around

the void. Solving the equation for permeable flow into a spherical void, the velocity of flow up the pipe V_F is given by:

$$V_F = \frac{4khr_1}{r_0^2} \quad \text{m/s} \qquad [15.1]$$

where:

k is the coefficient of permeability (10^{-9} m/s)
h is the head of water corresponding to the atmospheric pressure (m)
r_1 is the radius of the void (10 mm) and
r_0 is the bore radius of the pipe (1.5 mm).

The outer radius of the integral is insignificant provided it is much greater than r_1. Using the values in brackets gives a calculated flow of 640 mm per hour. Flow rates of approximately this value were observed.

15.4.7 Modelling transport in the test cells

Cell 3 needed to be refilled after 12 months. The reason for this was inadequate compaction of the clay layer leading to an increased permeability. The effective indicated permeability was calculated as follows:

total volume of the leachate leaked $\cong 4.54\,m^3$
surface area of pyramid in bottom of clay layer = $25.3\,m^2$

Thus

indicated permeability $k = 5.2 \times 10^{-9}$ m/s

This corresponds to nearly the same permeability as a bentonite-enhanced sand liner and indicates satisfactory performance even when very poor construction practice was evident, but it did affect the modelling considerably. The permeability calculated from these site observations was therefore used for the clay layer.

15.4.8 Comparison between model and observations

The capacity factors and diffusion coefficients from the diffusion tests on the top and bottom mixes and the initial concentrations of different elements in site leachate and the mixes (from pore pressed solutions, see Table 15.8) were used to verify the modelled concentration against measured values. These are shown in Figs 15.6–15.11 for calcium, sodium and potassium for cells 2 and 3, respectively. On these graphs, error bars are shown between the 10th and 90th percentiles from the probability calculations at ages of 2 and 4 years (in Figs 15.9, 15.10 and 15.11 these have been offset slightly for clarity). The coefficients of variation used for these are shown in

Table 15.8 Initial liquid concentrations used in models for site trials (mg/l)

Elements	Site leachate	Cell 2			Cell 3		
		Top layer	Clay layer	Bottom layer	Top layer	Clay layer	Bottom layer
Calcium	344	4	350	1214	4	350	14
Sodium	2300	450	450	10802	450	450	2157
Potassium	4730	15193	300	1761	15193	300	761
Sulphur	770	2000	500	549	9294	500	50

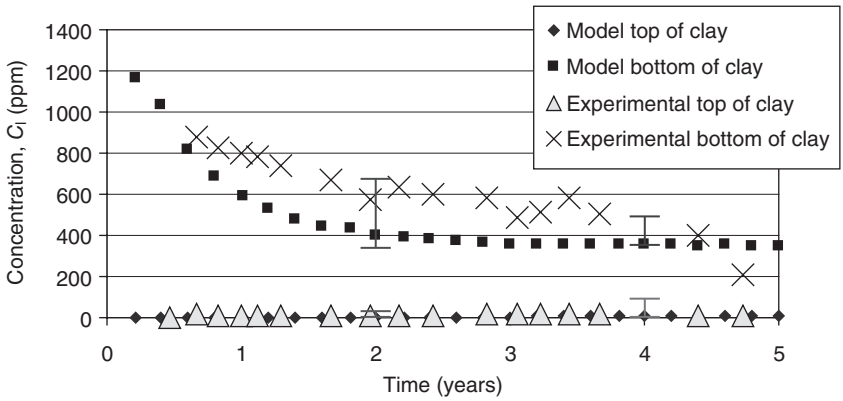

15.6 Concentrations of calcium in site trial cell 2.

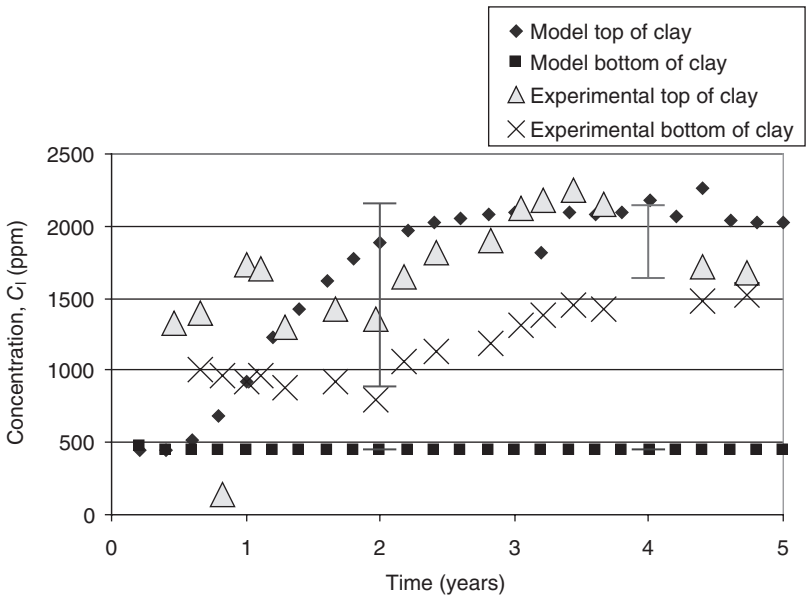

15.7 Concentrations of sodium in site trial cell 2.

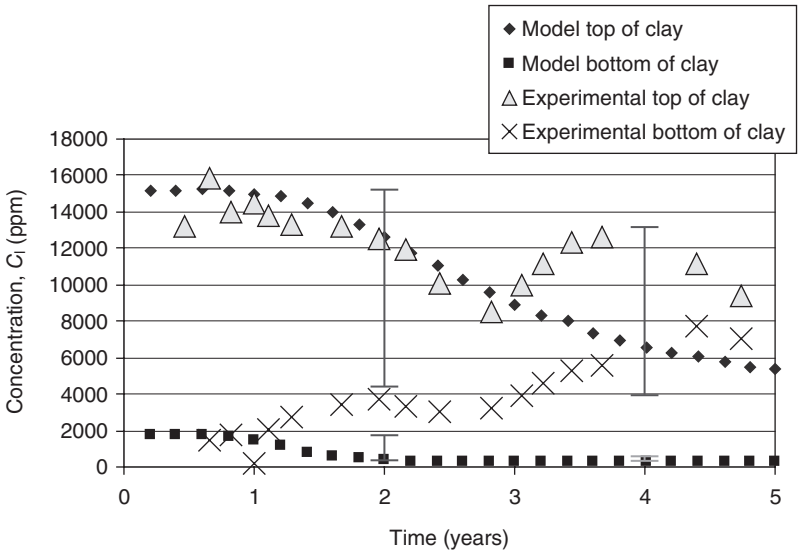

15.8 Concentrations of potassium in site trial cell 2.

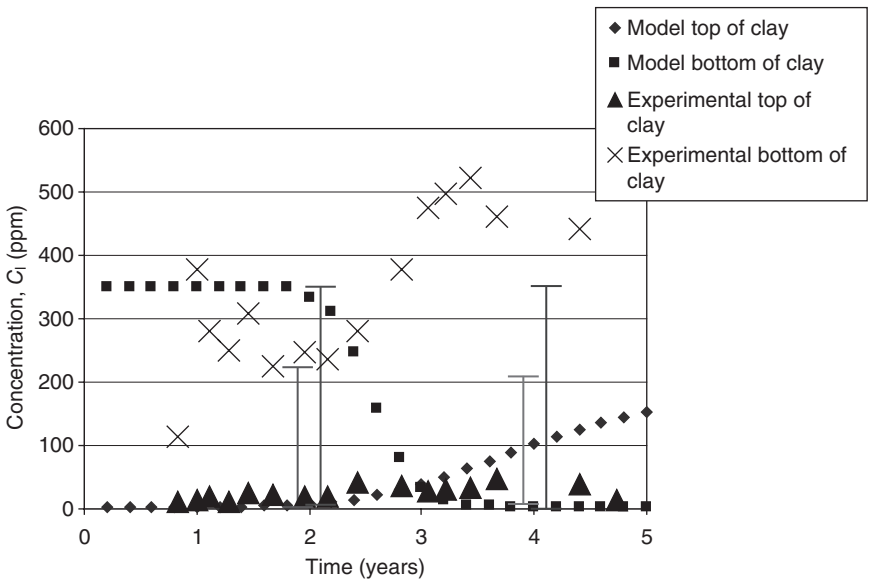

15.9 Concentrations of calcium in site trial cell 3.

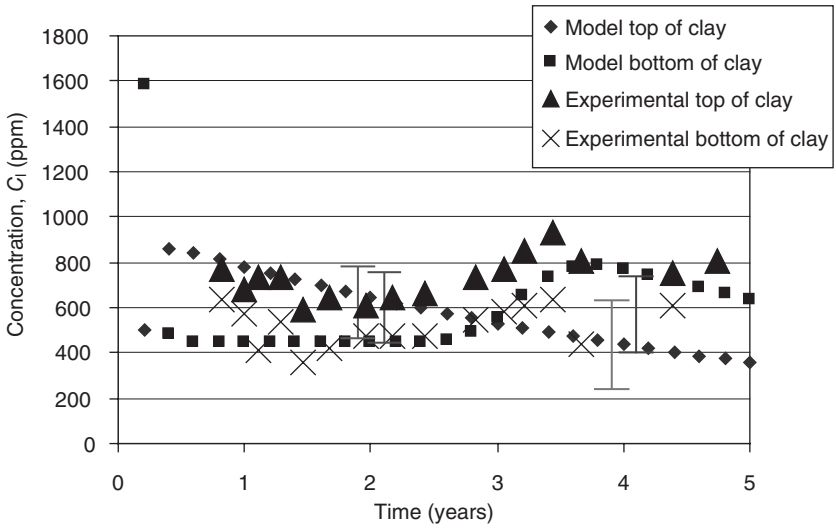

15.10 Concentrations of sodium in site trial cell 3.

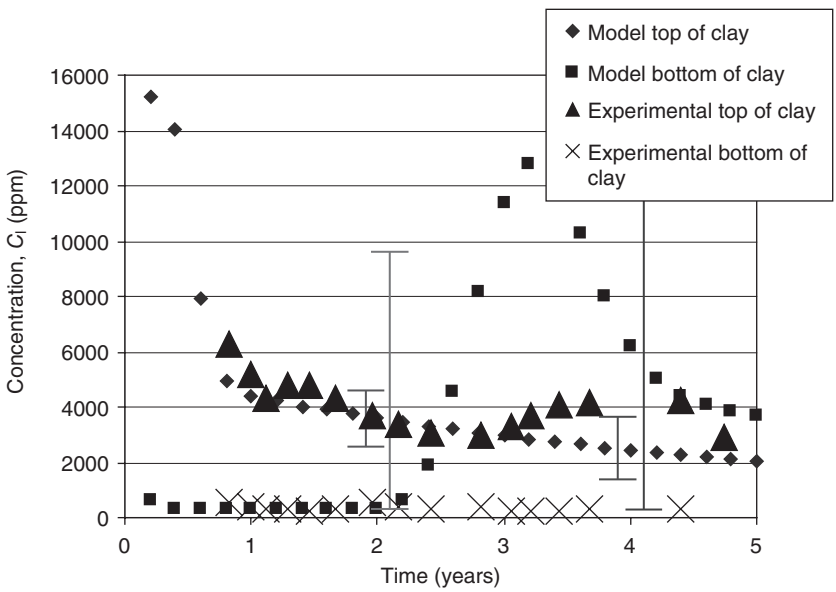

15.11 Concentrations of potassium in site trial cell 3.

Table 15.9 Coefficients of variation for parameters used in the modelling

Parameter	*V*%	Distribution used
Capacity factor	50	Linear
Diffusion coefficient	4	Logarithmic
Permeability	3.165	Logarithmic
Layer thickness	15	Linear

Table 15.9. The observed concentrations which are shown in the graphs are based on the average from up to four different samples taken in different parts of the cells. For some of these, a considerable spread of results was recorded.

In Fig. 15.6, the fall in calcium concentration at the bottom of the clay in cell 2 is somewhat slower than predicted, but the error bars (which included a range of permeabilities in their calculation) allow for this and cover the range of observed data. The very slow rise at the top of the clay is well predicted.

In Fig. 15.7, the rapid rise of the sodium concentration at the top of the clay follows the predictions within the range of the error bars. Some instability in the model may be seen at 3–4 years. This could be solved at the expense of increasing the run time but is not considered relevant within the accuracy of the whole model. The results at the bottom of the clay are not explained at all. There is an unexplained source of sodium (possibly in the shredded waste).

For the potassium in Fig. 15.8, the decline at the top of the clay lies just within the error bars, but there is again an unexplained trend at the bottom.

In cell 3, Fig. 15.9 shows the calcium rising at the bottom of the clay. The model shows it falling and the error bars show that no changes in the input data led to a predicted increase. The agreement at the top of the clay is, however, good with a rise occurring as predicted but somewhat earlier.

In Fig. 15.10, the observed data from both sets lie within the range given. The rise and fall predicted for the bottom of the clay appears to be occurring in the site data at a lower level than expected but within the error bars. The observed increase at the top of the clay after 3 years is not predicted.

In Fig. 15.11, the expected increase in potassium at the bottom of the clay has not occurred; however, the error bars give a very wide range due to uncertainty about the time when this will occur. The data for the top of the clay lies within the error bars.

The transport processes in landfills are associated with a high degree of uncertainty. The processes modelled here used real landfill leachate which was undergoing biological reactions throughout the experiment and took place in a site environment with all of the associated uncertainty. The

combination of these factors with the uncertainty associated with the stated assumptions in the model has given rise to some unexpected events. Nevertheless, this is a useful exercise to indicate likely trends in a real environment. Long-term results which will involve transport processes far closer to the steady state are actually likely to be more accurate.

15.5 Reducing transport in cracked concrete

15.5.1 Cracking and other preferential flow paths

This section describes a programme to measure the effect of cracking in concrete on the permeability. It also describes a method used to seal the cracks in waste containment barriers and experiments carried out to confirm that this method works. It is concluded that cracking will not cause failure. The modelling of the transport processes provided a good prediction of the movement of some species in the site trials.

Cracking could be caused by drying or thermal effects or the imposed stresses on the barrier and would permit transport regardless of the properties of the concrete. The solution to this is to use composite systems of concrete and clay, and their performance has been demonstrated experimentally in the work described here.

A possible cause of premature chemical failure is the formation of impermeable 'boulder-like' pieces with preferential flow paths for water around them. These boulders could develop impermeable surface layers through the formation of carbonates, chloroaluminates or magnesium compounds in a similar manner to that observed at the surface of existing concrete structures in hostile environments. If this occurred, the alkaline buffering and sorption capacity of the interior of the boulders would be lost. In this way the total buffering and sorption capacity of the repository would be substantially reduced.

In the plans for nuclear waste, it is envisaged that almost all of the cementitious material will be in the form of a soft grout (see Chapter 14). This material has been chosen to comply with various operational criteria including being readily pumpable into small spaces between the packages and having a low strength. These requirements have the effect that the formation of hard impermeable boulders will be strongly inhibited. For non-nuclear waste, the strength of the concrete was also kept as low as possible.

15.5.2 Action of sulphates

Penetrating sulphates react with hardened concrete and produce reaction products which have a volume which is greater than the available pore

space (Claisse and Unsworth, 1996). In normal structures, this causes expansion of the matrix which continues until the critical stress is developed and cracks form. It is of note, however, that in a deep nuclear waste emplacement the effect is harmless because there is no void space in the whole repository and all compressible wastes are super-compacted to save space. The entire system is also subject to long-term compression from the surrounding rock and this will prevent any expansion and the resulting compressive stresses may even be beneficial. For non-nuclear applications with typical waste emplacement at depths possibly greater than 20 m, the expansive stresses would be sufficient to cause cracking, but the cracks would not open and would remain sealed with reaction product. In the event of any dissolution of this product, the multilayer barrier design described below would make the cracks fill with clay which would be extruded from the inter-layer.

15.5.3 Trial 1

Cracked samples were investigated using the high pressure cell described in Section 4.2.2. In the first test, a 100 mm diameter mortar disc 33.4 mm thick was cracked by applying small loads using a compression test machine. Fibre reinforcement was used in the sample to prevent it from falling apart. The cracks induced in the disc were clearly visible by naked eye and were measured between 0.5 mm and 1.2 mm wide (see Fig. 15.12).

15.12 Narrow cracks induced in the fibre-reinforced mortar disc.

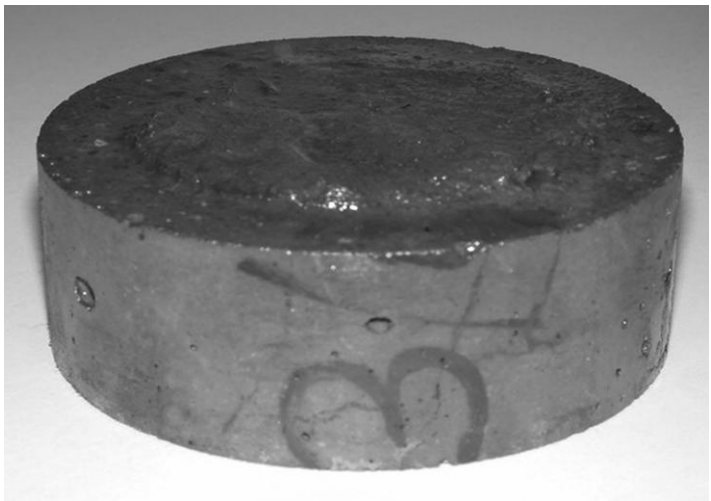

15.13 Cracked sample after clay has sealed the cracks.

15.5.4 Trial 2

A 55 mm thick metal spacer ring packed with clay from the trial site was placed on the top of the cracked disc. A two-layer test was then carried out on the high pressure cell apparatus using the synthetic leachate with fluorescein dye. After running the high pressure cell for about 1 h at 95 bar pressure, liquid started to leach out showing the fluorescein colour. When left for another 5 h at 95 bar the leaching stopped. About 0.8 sample volumes of liquid were collected during this period. No more leaching was observed when the cell was continuously run at the same pressure for another 24 h (see Fig. 15.13).

15.5.5 Trial 3

In trial 3, hairline cracks (about 0.2 mm wide) were induced in mortar samples (similar to cell number 2 bottom layer mix) and clay (passing 5 mm mesh sieve) was packed inside the sample (see Fig. 15.14). A mortar disc (similar to the cell number 2 top layer mix) was then placed on top of the clay and cracked mortar (Fig. 15.15). The thicknesses of the three layers were proportional to those in the site trial cells. Running this multi-layered sample at 100 bar for 3 days showed no leaching from it at all. After dismantling, it was noticed that the top mortar had disintegrated under the high pressure leachate flow, but no trace of leachate could be found in the bottom cracked mortar. These experiments therefore indicated that, under

15.14 The set-up of bottom layer mix and compacted clay with silicone rubber round the rim and inside wall to prevent ingress of leachate from rim and interfaces.

15.15 Multilayer sample with partially compacted clay inside it.

the expected high saturation pressures, the clay would effectively seal cracks in the concrete.

15.6 Conclusions

- Transport through concrete barriers may be modelled using simple computer programmes that apply the basic transport equations directly.
- Site trials showed that the model provided a useful estimate but revealed some unexplained data
- Experimental work has indicated that minor cracking will be sealed by the clay. No barrier can withstand the effect of gross failure of the substrate. This would cause major cracks to form and should be avoided.

15.7 References

Claisse P A (1989) *New grouts for backfilling of ILW/LLW repository excavations*, Harwell Report AERE M 3696.

Claisse P A and Unsworth H P (1996) The engineering of a cementitious barrier, in Bentley S P (ed.), *Engineering Geology of Waste Disposal*, Engineering Geology Special Publication No.11, Geological Society, London, pp. 267–272.

Ganjian E, Claisse P A, Tyrer M and Atkinson A (2004) Selection of cementitious mixes as a barrier for landfill leachate containment, *ASCE Journal of Materials in Civil Engineering*, **16** (5), pp. 477–486.

Conclusions, recommendations and guidance for measuring transport properties of concrete

The state of the art

It is concluded that, in the century since the transport processes were first analysed, much progress has been made but much remains to be done. It is clear that the tests that measure these processes should give true values for the basic properties such as permeability and diffusion coefficient and that models which predict performance should use them.

The process of using diffusion coefficients to measure durability is a good example of where progress needs to be made. It has been shown that none of the tests in current use gives a true measure of the diffusion coefficient because they rely on the solution of Fick's law for a single ion. The durability models use the same solution so it can be argued that they are using the available data as well as they can. However, the influence of other ions may be completely different in the test sample and the structure which is being modelled so the answer will not be accurate.

Similarly, ISAT and Figg tests may be used to obtain an indication of durability. However, they do not yield data suitable for use in models and they are influenced by factors which may not affect durability.

Two solutions are proposed in this book: the additional pressure measurements for the Figg test discussed in Chapter 5 and the additional voltage measurements in the electrical tests discussed in Chapter 10. Both of these require further work before they are suitable for general industrial use, but they show that progress can be made towards developing this subject from a sound scientific base.

Recommendations and guidance

Practitioners who are measuring transport properties as indicators of durability or for any other purpose are advised to proceed as follows:

- Always use more than one test. The tests that you are using may give unreliable results such as the low results from the rapid chloride test when used with pozzolanic mixes.
- Obtain fundamental parameters such as the permeability or the intrinsic diffusion coefficient from your test. The methods in this book give guidance for this.
- Use the fundamental properties to compare the results from your different tests.
- These tests are not accurate so exact agreement is unlikely, but systematic differences between the results from the tests should be investigated.

Appendix 1: List of papers for the experimental data and derivations

The paper numbers refer to the list at www.claisse.info/publish.htm where the full text of many of the papers is available.

Paper number	Chapters/ Sections	
2	6 14	Harris A W, Atkinson A and Claisse P A, Transport of gases in concrete barriers. *Waste Management*, 12, pp. 155–178, 1992.
4	3.5	Dhir R K, Shabban I, Claisse P A and Byars E, Preconditioning in situ concrete for permeation testing, part 1: Initial surface absorption. *Magazine of Concrete Research*, 45, No.163, pp. 113–118.
5	13.2–13.4	Cabrera J G, Claisse P A and Hunt D N, A statistical analysis of the factors which contribute to the corrosion of steel in PC and silica fume concrete. *Construction and Building Materials*, 9, No. 1, 1995, pp. 105–113.
7	3.2 3.4.1 4.3 4.4	Claisse P A, Elsayad H I and Shaaban I G, Absorption and sorptivity of cover concrete. *ASCE Materials Journal*, 9, No. 3, 1997, pp. 105–110.
9	3.3 3.4.2 3.6 4.6	Claisse P A, Elsayad H I and Shaaban I G, Test methods for measuring fluid transfer in cover concrete. *ASCE Materials Journal*, 11, No.2, 1999, pp. 138–143.
10	8.1–8.7	Cabrera J G and Claisse P A, Oxygen and water transport in cement-silica fume pastes. *Construction and Building Materials*, 13, 1999, pp. 405–414.
13	8.3–8.7	Claisse P A, Cabrera J G and Hunt D N, Measurement of porosity as a predictor of the performance of concrete with and without silica fume. *Advances in Cement Research*, 13, No.4, 2001, pp. 165–174.
17	5.1–5.4	Claisse P A , Ganjian E and Adham T A, Vacuum-air permeability test for in-situ assessment of cover concrete. *Cement and Concrete Research*, 33, No. 1, 2003, pp. 47–53.

Paper number	Chapters/ Sections	
18	5.4–5.5	Claisse P A, Ganjian E and Adham T A, *In situ* measurement of the intrinsic permeability of concrete. *Magazine of Concrete Research*, 55, No. 2, 2003, pp. 125–132.
22	1.1–1.5 2.4 13.2	Claisse P A, Transport properties of concrete. *Concrete International*, 27, No. 1, 2005, pp. 43–48.
23	7	Claisse P A, Elsayad H I and Ganjian E, Water vapour and liquid permeability measurements in mortar samples. *Advances In Cement Research*, 21, No. 2, 2009, pp. 83–89.
24	9	Ganjian E, Claisse P, Tyrer M and Atkinson A, Factors affecting measurement of hydraulic conductivity in low strength cementitious materials. *Cement and Concrete Research*, 36, No. 12, 2006, pp. 2109–2114.
25	15.1–15.3	Claisse P, Ganjian E, Atkinson A and Tyrer M, Measuring and predicting transport in composite cementitious barriers. *ACI Materials Journal*, 103, No. 2, 2006, pp. 113–120.
32	15.4–15.5	Claisse P and Ganjian E, Transport processes for harmful species through concrete barriers made with mineral wastes. *Construction and Building Materials*, 23, No. 5, 2009, pp. 1837–1846.
35	10.7	Lizarazo Marriaga J and Claisse P, Effect of non-linear membrane potential on the migration of ionic species in concrete. *Elecrochemica Acta*, 54, No. 10, 2009, pp. 2761–2769.
37	11 12	Lizarazo-Marriaga J and Claisse P, Determination of the concrete chloride diffusion coefficient based on an electrochemical test and an optimization model. *Materials Chemistry and Physics*, 117, No. 2–3, 2009, pp. 536–543.
38	10.1–10.6	Claisse P A, Elsayad H I and Ganjian E, Modelling the rapid chloride permeability test. *Cement and Concrete Research*, 40, No. 3, 2010, pp. 405–409.
45	12	Lizarazo-Marriaga J and Claisse P, Modelling concrete chloride penetration in concrete using electrical voltage and current approaches. *MatRes – Materials Research*, 14, No. 1, 2011, pp. 31–38.
Conference 64	13.5	Claisse P and Lizarazo Marriaga J, The effect of other ions on chloride migration in concrete. *3rd International Conference on the Durability of Concrete Structures*, Queens University Belfast, 16–18 September 2012.

Appendix 2: Notation and abbreviations

Notation

A	area (m^2)
a	regression parameter
b, β_1 and β_2	constants for the Klinkenberg equation
B, B_1 and B_2	Tafel constants
c	concentration (mol/m^3)
C	concentration (kg/m^3)
C_l	concentration of ions per unit volume of liquid (kg/m^3)
C_s	total concentration per unit volume of the solid (kg/m^3)
Ct_i	thickness of cell i (m)
D	diffusion coefficient (m^2/s)
D_a	apparent or effective diffusion coefficient (m^2/s)
D_i	intrinsic diffusion coefficient (m^2/s)
DD	dry density (mass/bulk volume) (kg/m^3)
E	electric field (V/m)
e	viscosity (Pa s)
e_0	electronic charge (C)
E	Young's modulus (Pa)
$E0$	rest potential (V)
F	flux ($kg/m^2/s$)
F_a	Faraday constant = 9.65×10^4 C/mol
F_v	volumetric flux (m^3/s)
F_i	inwards force (N)
F_0	outwards force (N)
g	gravitational constant = 9.81 (m/s^2)
h	head of water (m)
I	Current (A)
I_a, I_c	anode and cathode current (A)
I_{a0}, I_{c0}	anode and cathode exchange current (A)
I_{corr}	corrosion current (A)
ISA	initial surface absorption ($m^3/m^2/s$)
ISA_{10}	ISA value at 10 min ($m^3/m^2/s$).
J	flux ($mol/m^2/s$)
K	intrinsic permeability (m^2)
K_B	Boltzmann constant (J/K)
k	coefficient of permeability (m/s)
K_g	gas intrinsic permeability of concrete (m^2)
K_l	water intrinsic permeability of concrete (m^2)
K_v	vapour intrinsic permeability for the vapour (m^2)
K_∞	intrinsic permeability at infinite pressure (m^2)
L	length (mm)

M	mass (kg)
m	atomic/molecular mass (kg)
n	number of mols
n	regression parameter
P	pressure (Pa)
P_{atm}	atmospheric pressure (Pa)
P_i	initial vacuum (Pa)
P_m	mean pressure (Pa)
P_{10}, P_{20}	initial low and high pressures (Pa)
P_v	pressure in void (Pa)
P_r	pressure at radius r (Pa)
Q	gas generation rate or volumetric flow (m^3/s)
Q	charge (C)
R	gas constant = 8.31 (J/mol/K)
R	resistance (Ω)
R	void radius (m)
RH	relative humidity
r	radius of the pores (m)
s	surface tension (N/m)
S	sorptivity ($m\,s^{-0.5}$)
SG	specific gravity (mass/net volume) (kg/m^3)
S_r	radial hoop stress (Pa)
S_θ	tangential hoop stress (Pa)
T	temperature (K)
t	time (s)
t_i	transference number for ion i
u_i	mobility of species i in the pore fluid ($m^2/s/V$)
V	coefficient of variation
V	volume (m^3)
V_F	Darcy velocity for the fluid (m/s)
V%	coefficient of variation %
V_0	volume of drilled hole (m^3)
V'	ratio of the reservoir volumes ($V1/V2$)
W_F	ratio of the water vapour volume to the volume of the same mass of water as a liquid
x	distance (m)
X	distance across permeation block (m)
X_s	radius of hemisphere (m)
x_0	radius of drilled hole (m)
x_1	separation of drilled holes (m)
y	displacement (m)
z	valence of an ion
α	capacity factor
β	$2KS\alpha A^2/re$
γ	$6\pi l x_0^2$
γ_v	radial displacement of the void surface (m)
γ	surface tension of the mercury (N/m)
δ	$(8\pi lKs)/re$
ε	permittivity ($C^2/N/m^2$)
ε	porosity
κ	inverse Debye length (m^{-1})
ν	Poisson's ratio

ρ	density (kg/m^3)
ρ	electrical resistivity (Ωm)
σ	electrical conductivity (Ωm)$^{-1}$
λ	mean free path (m)
ϕ	voltage (V)
ϕ_{a0}, ϕ_{c0}	anode and cathode exchange voltage (V)
ϕ_p	membrane potential (V)
φ	contact angle of the mercury with the pore surface
ξ	outer radius of repository (m)

Abbreviations

ANN	artificial neural network
ASTM	American Society for Testing and Materials
CAT	cover concrete absorption test
CC	curing condition
CKD	cement kiln dust
DD	dry density (mass/total volume)
GAV	gas accessible volume
GGBS	ground granulated blastfurnace slag
HDPE	high density polyethylene
Hg	mercury (intrusion)
HP	high pressure (test)
ICP	inductive coupled plasma
ISA or ISAT	initial surface absorption (test)
LVDT	linear voltage displacement transducer
LWC	low water concrete
M	molar (concentration mol/litre)
N	normal (concentration mol/litre)
MIP	mercury intrusion porosimeter
NS	not significant
NTBUILD	Norwegian standard for building
PC (or OPC)	Portland cement
PFA	pulverised fuel ash
ppm	parts per million
RH	relative humidity
SCE	saturated calomel electrode
SF	silica fume
SG	specific gravity (mass/net volume)
SRC	sulphate resisting cement
SV	sample volume
w/b	water to binder ratio
w/c	water to cement ratio

Index

This page intentionally left blank

This page intentionally left blank